UNIVERSIDAD COMPLUTENSE DE MADRID
FACULTAD DE CIENCIAS FÍSICAS

TESIS DOCTORAL

Improved Techniques for PET Imaging

Técnicas Mejoradas para Imagen PET

MEMORIA PARA OPTAR AL GRADO DE DOCTOR

PRESENTADA POR

Alejandro López Montes

Directores

Joaquín López Herraiz
José Manuel Udías Moinelo

Madrid

Universidad Complutense de Madrid

Facultad de Ciencias Físicas

Tesis Doctoral

Improved Techniques for PET Imaging
Técnicas Mejoradas para Imagen PET

Memoria para optar al grado de Doctor
Presentada por:

Alejandro López Montes

Directores:
Joaquín López Herraiz
José Manuel Udías Moinelo

Madrid, 2021

Agradecimientos

Para empezar
diré que es el final.
(M. Clan)

Y aquí estamos, casi 5 años después de empezar esta aventura. He de decir que, tras hacer balance de lo vivido, me llevo muchas más experiencias buenas que malas de esta fase de mi vida y que, si tuviera que volver a recorrer, haría con gusto, siempre y cuando pudiera volver a hacerlo en tan buenas compañías.

Gran parte de la culpa de que decidiera tomar este camino la tiene José Manuel Udías, quien confió en mí para iniciarme en el mundo de la ciencia y la investigación. Sin él, no estaría escribiendo estas líneas ahora mismo. Muchas gracias por abrirme las puertas a este mundo y por toda la labor que realizas para que cada día haya más doctores nucleares en este país. Gracias por enseñarme tanto, sólo espero un día poder llegar a saber la mitad de todo lo que tú sabes.

Después llegó Joaquín López Herraiz a mi tesis y, aunque lo intentara, no podría decir ni una sola palabra mala sobre él, porque no la encontraría. Gracias por tanto. Sin tu apoyo y tu fe en mí estoy seguro de que nunca habría llegado aquí. Por apoyarme en los momentos más oscuros y ser capaz de sacarme adelante cuando pensaba que no había salida, por enseñarme tanto del mundo de la investigación que no habría conocido sin ti y por sembrar en mí la pasión por la ciencia. Te diría que nunca cambiaras pero una de tus muchas virtudes es que siempre estás en constante cambio, en constante mejoría, así que en vez de eso te diré que sigas cambiando, que sigas avanzando y convirtiéndote cada día más en el brillante investigador y mentor que hoy ya eres. Te has convertido en un referente y un ejemplo para mí, tanto en el campo de la investigación como en el personal así que gracias una vez más.

Una de las mejores cosas que tiene el GFN son sin duda sus gfnitos. Trabajar rodeado de gente maravillosa te hace crecer y aprender cada día. No es fácil encontrar un ambiente donde cada uno de tus compañeros y compañeras te apoya siempre y en todo momento y donde sabes que puedes contar con cualquiera de esas personas para que te ayuden cuando haga falta y con quienes cada minuto invertido merece la pena. Por eso quiero agradecer a cada uno de ellos su apoyo, compañía y sobre todo amistad. A Amaia y a Pablo, con quienes he recorrido este camino de principio a fin y que dentro de muy poco estarán dando también sus últimos pasos en este camino del doctorado, me alegro mucho de poder haber compartido con vosotros esta experiencia, los dos os habéis convertido en excelentes investigadores, aunque lo más importante es que los dos sois unas personas maravillosas, gracias por tantos momentos compartidos, sólo espero poder seguir compartiendo muchos más a vuestro lado. A las mejores gallinitas del corral GFN, Paula, Vicky y Mailyn, por recogernos cuando aún éramos polluelos y enseñarnos a convertirnos en auténticos gfnitos, sois de esas amistades a las que ni el tiempo ni la distancia pueden vencer. A los que, aunque hace tiempo que no están presentes en el grupo, en realidad siempre lo estarán, gracias, Esther y Jacobo por ser unos referentes, por enseñarme y guiarme desde la distancia y por convertiros en mentores y amigos. A Jaime y Víctor, con quienes no sólo he compartido estos años sino todos los de la carrera, gracias por todos estos años y gracias por todos los que estoy seguro de que vendrán, gracias por esos momentos de despacho y por guiarme en el apasionante mundo de Fortran y de Gnuplot. A los que llegaron después, Fer, Víctor Jr, Clara, Miguel... agradecerles todo el tiempo juntos, con vosotros he compartido camino, despacho, congresos y amistad, ahora recae en vuestras manos recoger a las nuevas generaciones de gfnitos. A los nuevos (y no tan nuevos) miembros del grupo, Andrea, Murias y toda la nueva generación de gfnitos con quienes no he tenido la suerte de pasar tanto tiempo debido a la pandemia, os deseo lo mejor en vuestras carreras. A Silvia y Javi, gfnitos adoptivos y grandes amigos, a ellos y a todos los maravillosos compañeros y compañeras con quienes tuve la suerte de hacer el Máster de Física Nuclear, nunca olvidaré ese año ni a todas las personas con las que lo compartí, estoy seguro de que nos cruzaremos una y otra vez y que aún nos quedan muchas más cosas por vivir juntos. Agradecer también a tantos otros con los que he tenido la suerte de poder compartir una parte del viaje, Ober, Vadym, Fran, Pedro, Carlos, Pauline, Aidana... espero que nuestros caminos se vuelvan a cruzar en algún momento. Por supuesto, quiero agradecer a Samuel, Luis Mario, Raúl y Dani, que son una parte esencial e imprescindible del grupo y de quienes he tenido la suerte de aprender y de compartir tiempo con ellos. Por último a Laura, José María, Óscar, Cristina, Armando, José Luis y a tantos otros profesores que he tenido, porque de todos ellos me llevo cosas, de su pasión bien por la ciencia o bien por la docencia, cuando no por ambas, gracias.

An essential part of science that I really appreciate are the collaborations between groups. They have allowed me to know really valuable people which, sometimes, even have become friends. I have had the luck to work and to learn from many of them and I have known people who I really admire. Thank you Christoph and all the group in Jülich, Chuck and Jan from MSKCC in New York, Jorge, Maurizio and all the PET team from Siemens, thank you Andreu, thank you Alex, Hunor, Lalith, Ivo and all the people from Vienna that I have had the chance to know and to work with. Thank you also Alex, Wojtek and Jeffrey for trusting me to join you in the next stage of my life.

Pero no todo en esta vida es trabajo y hay una persona que ha recorrido este camino mano a mano conmigo, sufriéndome en todo momento, que me ha apoyado en todo y para todo, que se ha convertido en una parte imprescindible de mi vida y sin la cual no sería quien soy hoy. Una persona con quien tengo la inmensa suerte de compartir mi vida y mis días y con quien espero compartir todo lo que la vida nos depare. Gracias Oli por todo. Gracias por convertir los momentos buenos en aún mejores y los malos en no tan malos. Por quererme y acompañarme en este camino que no siempre ha sido fácil y, pese a todo, animarme a seguir haciendo lo que me gusta. Te quiero.

A mis padres, a quienes les debo todo. Les debo la vida, mi educación y el allanarme el camino para que pudiera ir cumpliendo metas. Sé que sin ellos y sin su apoyo y ayuda nada de esto sería posible. A mis abuelos Francisco y María, que me han criado como si fuera un hijo y que se han desvivido por que yo tuviera las oportunidades y las facilidades que ellos nunca tuvieron. Espero abuelo que, estés donde estés, sepas que gracias a ti y todo lo que la abuela y tú habéis hecho puedo estar aquí hoy. A mi hermana, Clara, porque siempre ha creído en mí y me ha querido y apoyado y al resto de mi familia porque todos ellos han contribuido de una forma o de otra a mi educación y mi formación, os quiero.

Por último, hay un gran número de personas a las que agradecer, que se han ganado un hueco en mi vida y que me han ayudado a llegar a donde estoy. A las mejores amigas que pudiera imaginar, esas amistades con quienes has vivido tanto que sabes que serán para toda la vida, gracias por tanto Rocis y Alba, os quiero. A tantos amigos y amigas que han compartido este viaje conmigo, David y Patri (familia y amigos así que gracias por partida doble), mis Migueles, Sandra, Mario, Leti, Edu, Carmen, Natalia, Pablo, Marta y tantos otros, algunos de los cuales he tenido la suerte de conocer hacer poco y otros que me llevan acompañando ya muchos años, gracias.

Seguro que me dejo a muchas otras personas, porque cuando echas la vista atrás te das cuenta del gran número de personas que han estado muy presentes en tu vida y que, de una forma u otra, han sido un pilar para llegar hasta el día de hoy. Así que gracias una y otra vez. A todas esas personas les dedico esta tesis.

Contents

List of Figures

List of Tables

Summary

Introduction

Positron Emission Tomography (PET) is a medical imaging technique based on the administration of molecules of biological interest labelled with a radionuclide which decays β^+ emitting positrons. These positrons are annihilated with an electron emitting, most of the times, two photons, in opposite directions which are detected in coincidence in a scanner (usually with detectors arranged in a ring form). Then the position of the source inside the body can be determined from the directions given by the two detection points of each coincidence, reconstructing the image of the uptake of the radio-labelled drug in the organism. These images provides important functional information of the body of the patient.

Motivation and objectives

In the last years, the technological advances, especially in computational sciences, has boosted the development of new techniques that can be applied in the field of medical imaging and specifically in PET. Many approaches were unachievable due to their high computational cost, but the improvements on capabilities of the computers has opened the door to the inclusion of many of them.

With the evolution (or revolution) of the GPUs thanks in part to the video-game industry, some methods, usually considered too slow to be used in tomographic image reconstruction and correction such as Monte Carlo methods or 3D iterative reconstruction, have shown to be feasible and to provide good results without compromising a reasonable computational time and requirements. Furthermore, Artificial Intelligence, specially Deep Learning techniques, has shown a great potential in the field of medical imaging, specially for some corrections where they can provide fast and accurate results improving in many cases the state of the art methods. Also, the CPUs and RAM memories have seen an evolution that lead us to propose new reconstruction methods based on the pseudo-inverse of the system matrix, an approach that although theoretically proposed in many works, had been dismissed due to the big size of the matrices. All these new techniques may lead to new applications in PET like multiplexed PET, able to provide the reconstructed image of two separated radionuclides injected together in the same acquisition. For this method, fast corrections that can be included during the reconstruction workflow are needed.

In this thesis, we make use of all these technological improvements to propose new methods which presents very promising applications for PET imaging.

Monte Carlo Simulation

In order to be able to simulate experiments, Monte Carlo (MC) simulators were introduced in the field of medical imaging. They have a huge impact, from planning future experiments to test reconstruction methods or corrections. They have become a powerful tool to model and solve very complex problems with more accuracy than most of analytic algorithms.

The most relevant uses of MC tools in PET are their direct use for reconstruction using MC simulations for the forward projections in the reconstruction process, perform accurate corrections to PET acquisitions as scatter or background due to spurious coincidences in non-standard PET radionuclides, testing configurations and scanner designs, and testing image reconstruction algorithms. The main disadvantage of these methods compared to other analytical methods for image corrections are the required time of computation, however, the use of GPU acceleration can provide fast enough simulations able to out-stand analytical methods. One chapter of this thesis is dedicated to present the results of a MCGPU-PET code developed in collaboration with a group in the Food and Drug Administration (FDA) and its potential use for PET images correction, specially for scatter and background due to spurious coincidences.

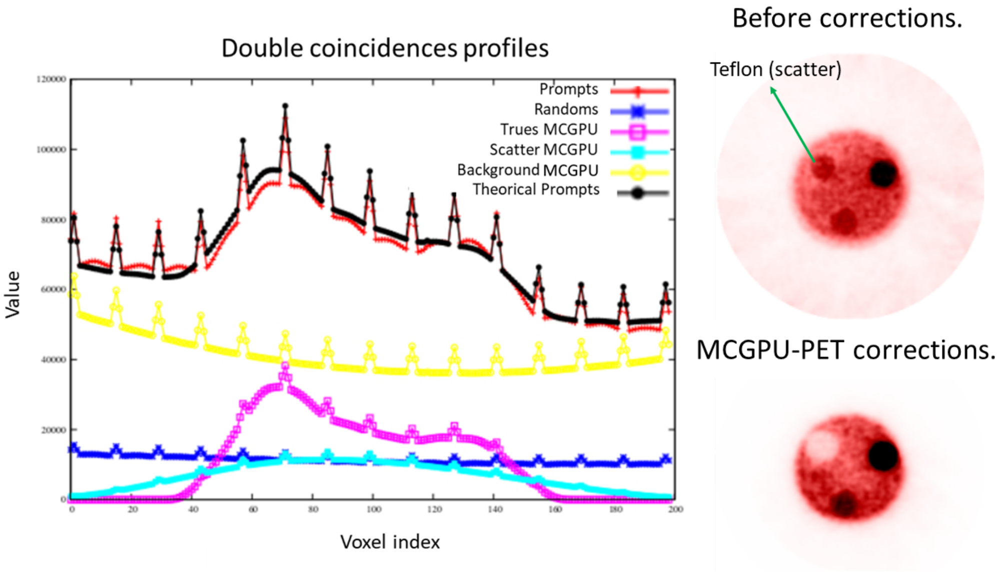

Figure S1: MCGPU-PET based scatter and spurious background corrections. The use of realistic and accurate Monte Carlo simulations provides a flexible method to perform a large variety of data corrections in PET

Pseudo-inverse Reconstruction

Reconstruction algorithms in tomographic image are usually classified into analytical and iterative methods. Analytical methods use models and assumption to obtain a mathematical expression to reconstruct the image of an object from its projections. Iterative methods on their side, have proved to provide better results than analytical methods since they can take into account the most important physical effects included in the emission, transport and detection of PET radiation and also they may include non-linear algorithms and a priory information into the reconstruction workflow.

We propose an alternative reconstruction method based on the pseudo-inverse of the System Response Matrices (SRM) [López-Montes et al., 2020], which can be very fast yet yielding good-quality images. The reconstruction problem is separated into two independent reconstructions. First, the axial part of the SRM is pseudo-inverted (PINV), and used to rebin the acquired 3D data in the axial direction into 2D datasets with resolution recovery. The resulting 2D datasets can be reconstructed with standard analytical methods or with another in-plane pseudo-inverse algorithm. Overall, the proposed two-step PINV reconstruction yields good-quality images at a rate of several frames per second, compatible with real time applications. Furthermore, PINV methods can provide the projections of the 3D image collapsed along specific directions directly, accelerating the reconstruction even further, reaching up to 10 frames per second.

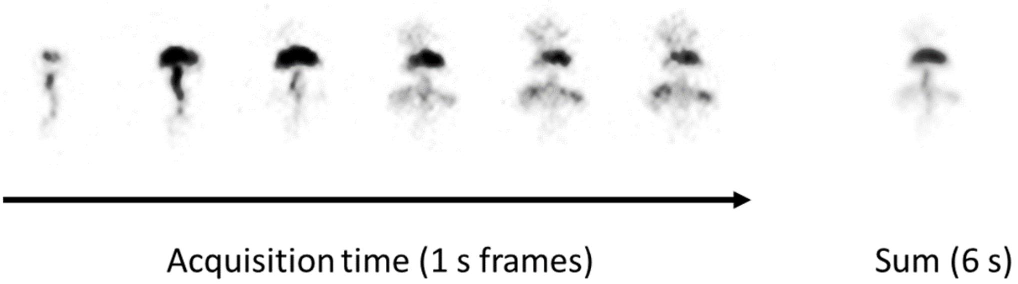

Figure S2: Real-Time PET reconstruction using pseudo-inverse method.

Deep-Learning based Positron Range Correction

Positron Range (PR) is one of the main limiting factors in current PET imaging, specially in PET oriented to animals where a few millimeters can be determinant. This effect is a consequence of the emission energy of the positron and the path traversed by it until the annihilation. It depends also on the density of the surrounding medium, with less positron range effect in high density mediums. This effect is particularly important for certain radionuclides such as ^{68}Ga, ^{76}Br, ^{82}Rb, ^{86}Y or ^{124}I where the initial energy of the positrons is very high.

Many correction approaches have been proposed to remove the blurring caused by the PR on PET reconstructed images. Most of the current methods are inaccurate and introduce additional noise to the reconstruction images or are computationally expensive and require important modifications on the reconstruction workflow.

We propose a deep-learning based PRC method (Deep-PRC) [Herraiz et al., 2021] applied as a post-processing step to the reconstructed PET images. Our goal was to develop a fast and accurate PRC method for 3D PET imaging, that provides PET images for medium and large range radionuclides rivaling in spatial resolution to the ones reconstructed with the standard short-range ^{18}F radionuclide avoiding introducing noise to the images.

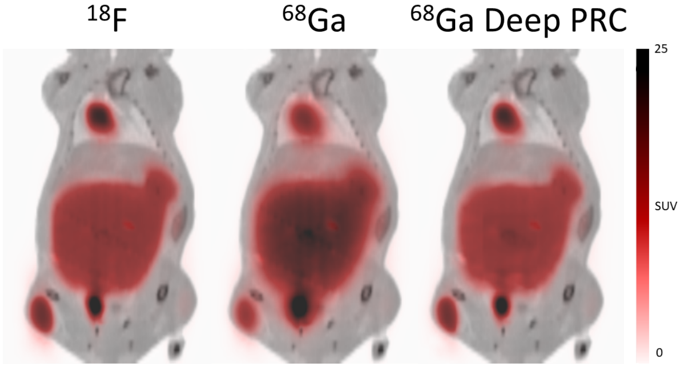

Figure S3: Deep-PRC results.

	Recovery (%)			Noise (%)		
	Heart	Bladder	Tumor	Heart	Bladder	Tumor
^{18}F	100.00	100.00	100.00	2.00	3.75	3.39
^{68}Ga	67.41	53.49	60.50	4.03	4.96	4.08
^{68}Ga Deep PRC	95.19	96.16	97.46	2.52	3.96	3.02

Table S1: Quantification of Deep-PRC results.

Multiplexed PET

In this section, we evaluated the simultaneous use of a variety of non-standard radionuclides, emitting additional prompt-γ rays together with a standard β^+ emitter as ^{18}F in several scanners. Multiplexed PET allows us to the separate the images of two different radionuclides used in the same acquisition. The method is based on the identification and reconstruction of triple coincidences created by non-standard radionuclides. While most common PET emitters generate only two photons, both coming from the annihilation of the positron emitted, some non-standard radionuclides emit additional prompt-γ rays. Thus, we can identify double coincidences, produced by emitted positrons, coming from both radionuclides, and triple coincidences, where one of the additional γ rays emitted by the non-standard radionuclide, is detected in coincidence with the photons from the annihilation.

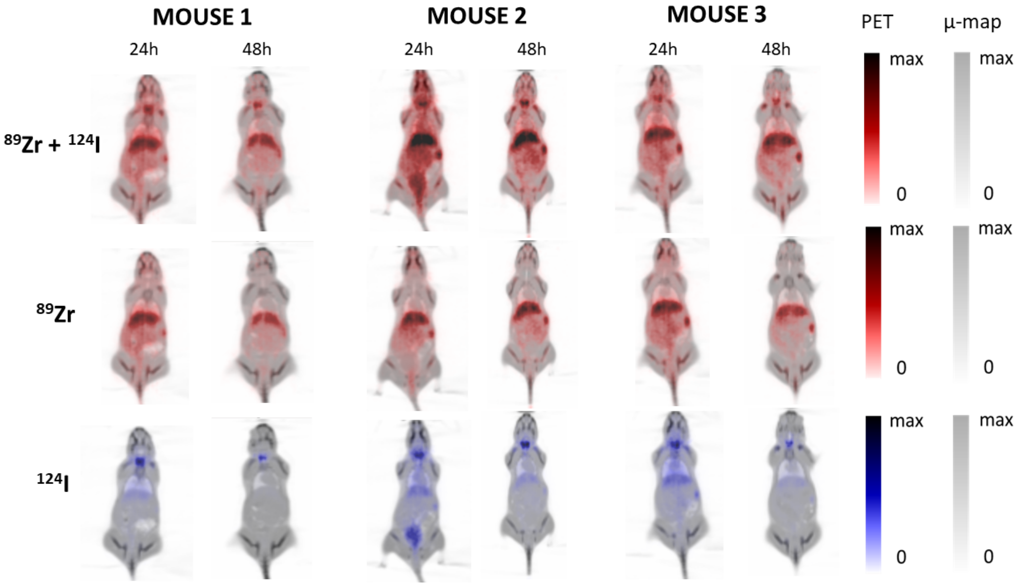

Figure S4: Example of mPET results of mice experiments of simultaneous imaging of ^{89}Zr and ^{124}I.

Conclusions

In this thesis, we exploited the technological advances in computer sciences to improve the image quality in tomographic image reconstruction and to propose new algorithms that may be used for cutting edge PET applications such as real-time PET or mPET.

In general, the results presented in this thesis, open the possibility for new lines of resarch that may exploit the use of these new techniques.

Resumen en español

Introducción

La Tomogafía por Emisión de Positrones (PET por sus siglas en inglés) es una técnica de imagen médica basada en la inoculación de moléculas de interés biológico marcadas con radionúclidos que se desintegran β^+ emitiendo positrones. Estos positrones se aniquilan en el medio circundante cuando encuentran un electrón emitiéndose como resultado dos fotones en direcciones opuestas que pueden ser detectados en coincidencia en un escáner (generalmente con sus detectores distribuidos en forma de anillo). Con esta información, la posición de la fuente dentro del cuerpo puede ser determinada a partir de las direcciones dadas por los dos puntos de detección de cada coincidencia, reconstruyendo la imagen de captación del medicamento marcado radiológicamente dentro del organismo. Estas imágenes proporcionan información funcional sobre el cuerpo del paciente.

Motivación y objetivos

Durante los últimos años, el avance de las tecnologías, especialmente en computación, han permitido el desarrollo de nuevas técnicas que pueden ser aplicadas en el campo de la imagen médica, y en concreto del PET. Muchos enfoques eran inalcanzables debido a los importantes costes computacionales que suponían, pero con las mejoras en las capacidades de los ordenadores se ha abierto la puerta a la inclusión de muchos de ellos.

Con la evolución (o revolución) de las GPUs gracias en parte a la industria de los videojuegos, algunos métodos, habitualmente considerados demasiado lentos para usarlos en la reconstrucción de imagen tomográfica o en correcciones en las imágenes reconstruidas, como los métodos de simulación Monte Carlo o los métodos de reconstrucción iterativa 3D, han demostrado ser adecuados y capaces de producir buenos resultados sin comprometer un tiempo razonable de computación. Por otro lado, la Inteligencia Artificial, y en especial las técnicas de Deep Learning, han demostrado un gran potencial en el campo de la imagen médica, especialmente para algunas correcciones donde pueden producir resultados de forma rápida y precisa mejorando en muchos casos a los métodos más usados. Además, las memorias RAM y CPUs también han visto una evolución que nos lleva a proponer nuevos métodos de reconstrucción de imagen basados en la pseudo-inversa de la matriz del sistema, un enfoque que, aunque teóricamente propuesto en muchos trabajos, se había descartado para casos reales debido al gran tamaño de las matrices. Todas estas técnicas, nos pueden llevar a la aparición de nuevas aplicaciones en PET como el PET multiplexado, capaz de generar las imágenes reconstruidas de dos emisores β^+ separados inyectados juntos en la misma adquisición. Para este método, son necesarias correcciones rápidas que puedan ser incluidas durante el proceso de reconstrucción.

A lo largo de esta tesis, aprovechamos todos estos avances tecnológicos para proponer nuevos métodos que presentan aplicaciones realmente interesantes para la imagen PET.

Simulación Monte Carlo

Para poder simular experimentos, los métodos Monte Carlo (MC) fueron introducidos en el campo de la imagen médica. Tienen un amplio impacto, desde planificación de experimentos futuros hasta testeo de métodos de reconstrucción o corrección de imágenes. Se han convertido en una herramienta poderosa para modelizar y resolver problemas muy complejos con mejor eficiencia y precisión que la mayor parte de algoritmos analíticos.

Los usos más importantes de herramientas MC en PET son su uso directo para reconstrucción, usando los simuladores MC para las proyecciones en el proceso de reconstrucción, obtener correcciones precisas para adquisiciones PET como coincidencias debidas a la dispersión de uno de los fotones o a un fondo causado por coincidencias espúrias al usar emisores PET no estándar, probar nuevos diseños y configuraciones en escáneres o probar algoritmos de reconstrucción de imagen. La principal desventaja de estos métodos comparados con otros métodos analíticos para la corrección de imágenes es el tiempo de computación requerido, sin embargo, el uso de aceleración basada en GPU puede producir simulaciones lo suficientemente rápidas que pueden mejorar los métodos analíticos. Uno de los capítulos de esta tesis está dedicado a presentar resultados de un código de libre distribución, MCGPU-PET, desarrollado en colaboración con un grupo en Washington DC y su potencial uso para la corrección de imágenes, especialmente para dispersión y las coincidencias espúrias al usar radionúclidos PET no estándar.

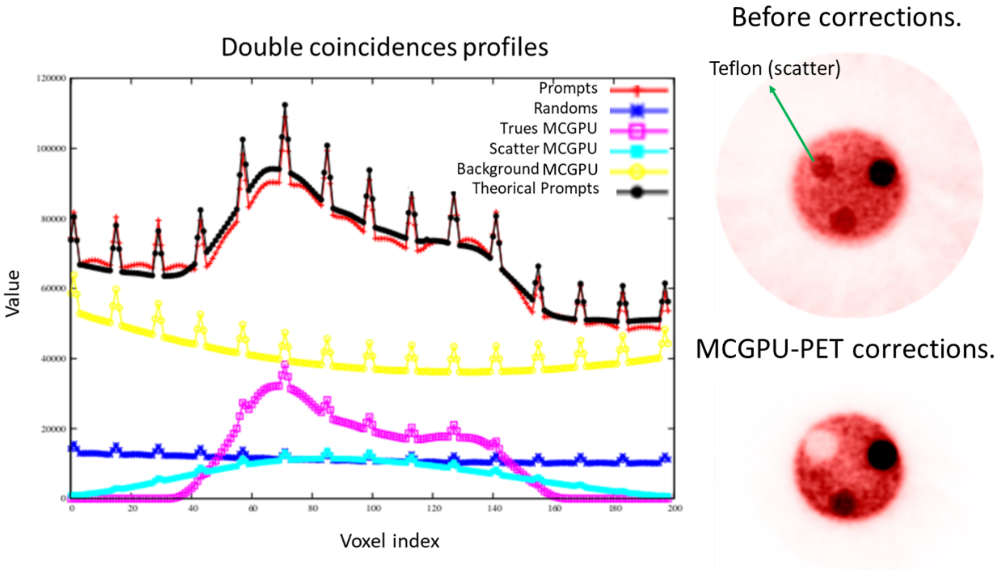

Figura R1: Correcciones de dispersión y de fondo de coincidencias espúrias usando MCGPU-PET. El uso de simulaciones Monte Carlo realistas y precisas supone un método flexible para llevar a cabo una gran variedad de correcciones en PET.

Reconstrucción Pseudo-Inversa

Los algoritmos de reconstrucción de imagen en imagen tomográfica, generalmente se clasifican en métodos analíticos e iterativos. Los primeros usan modelos y suposiciones para obtener expresiones matemáticas para reconstruir la imagen de un objeto a partir de sus proyecciones. Los métodos iterativos, por su parte, han demostrado que pueden proporcionar mejores resultados que los métodos analíticos ya que nos permiten tener en cuenta los efectos físicos más importantes que involucran la emisión, transporte y detección de radiación PET, además de permitir la inclusión de algoritmos no lineales e información a priori en el proceso de reconstrucción.

Proponemos un método alternativo de reconstrucción de imagen basado en la pseudo-inversa de las matrices de respuesta del sistema (SRM) [López-Montes et al., 2020], que puede ser muy rápido además de producir imágenes de buena calidad. El proceso de reconstrucción se separa en dos reconstrucciones independientes. Primero, la parte axial de la SRM es pseudo-invertida (PINV) y usada para rebinear los datos 3D adquiridos en la dirección axial produciendo conjuntos de datos 2D y permitiendo la recuperación de resolución. Los conjuntos de datos 2D pueden ser después reconstruidos usando métodos estándar de reconstrucción analítica o con otra pseudo-inversa de la matriz de respuesta transaxial. En general, el método propuesto proporciona imáagenes de buena calidad a una ratio de varias actualizaciones por segundo, tiempos compatibles para aplicaciones en tiempo real. Además, los médotos PINV pueden producir las proyecciones de las imágenes 3D colapsadas a lo largo de direcciones específicas directamente, acelerando la reconstrucción más aún, llegando a obtenerse hasta 10 actualizaciones por segundo.

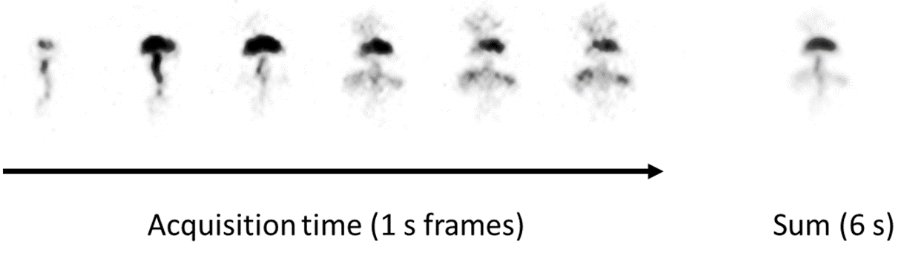

Figura R2: Reconstrucción PET en tiempo real usando el método de la pseudo-inversa.

Corrección al Rango del Positrón con Deep Learning

El rango del positrón es uno de los principales factores limitantes actualmente en imagen PET, especialmente en PET preclínico orientado a pequeños animales donde unos pocos milímetros pueden ser determinantes. Este efecto es consecuencia de la energía de emisión del positrón y la trayectoria recorrida por él hasta la aniquilación. Depende igualmente de la densidad del medio circundante, con menos efecto en medios de alta densidad. Este efecto es especialmente importante para ciertos radionúclidos como ^{68}Ga, ^{76}Br, ^{82}Rb, ^{86}Y o ^{124}I, donde la energía inicial del positrón es muy alta.

Ha habido muchas propuestas para eliminar este emborronamiento causado por el rango del positrón en imágenes PET. La mayor parte de los métodos actuales son imprecisos e introducen ruido adicional en la imagen o son demasiado costosos desde un punto de vista computacional y requieren importantes modificaciones en el proceso de reconstrucción.

Proponemos un método basado en deep learning para la corrección de rango del positrón (Deep-PRC) [Herraiz et al., 2021] aplicado como un post procesado de la imagen reconstruida. Nuestro objetivo era desarrollar un método rápido y preciso para imagen PET 3D que proporciones imágenes para radionúclidos con un rango medio y largo capaces de compararse en resolución espacial con otros de rango corto como el ^{18}F sin introducir ruido adicional en la imagen.

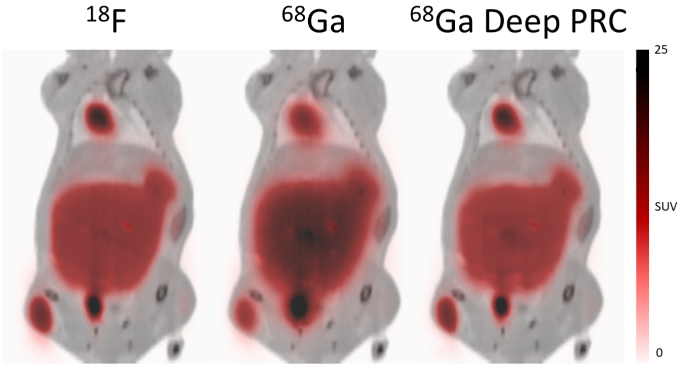

Figura R3: Resultados usando Deep-PRC.

	Recovery (%)			Noise (%)		
	Heart	Bladder	Tumor	Heart	Bladder	Tumor
^{18}F	100.00	100.00	100.00	2.00	3.75	3.39
^{68}Ga	67.41	53.49	60.50	4.03	4.96	4.08
^{68}Ga Deep PRC	95.19	96.16	97.46	2.52	3.96	3.02

Tabla R1: Cuantificación para resultados usando Deep-PRC.

PET Multiplexado

En esta sección, proponemos el uso simultáneo de emisores PET no estándar que emitan rayos prompt-γ adicionales junto con emisores β^+ puros como el ^{18}F. El PET multiplexado (mPET) nos permite separar las imágenes de los dos radionúclidos usados en la misma adquisición. Este método está basado en la identificación y reconstrucción de coincidencias triples creadas por los emisores no estándar. Mientras que los radionúclidos estándar sólo producen dos fotones, los dos procedentes de la aniquilación del positrón, algunos radionúclidos emiten rayos γ adicionales de forma simultánea con el positrón. Entonces podemos identificar las coincidencias dobles, producidas por los positrones emitidos procedentes de ambos radionúclidos y coincidencias triples donde uno de los rayos adicionales se detecta en coincidencia con los fotones de la aniquilación.

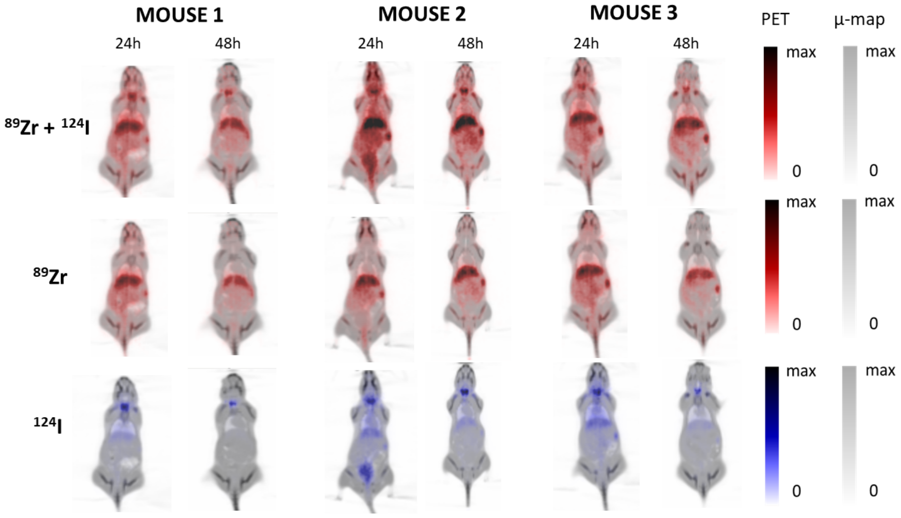

Figura R4: Resultados de mPET para experimentos con ratones.

Conclusiones

Durante esta tesis, fuimos capaces de explotar los avances tecnológicos en computación para mejorar la calidad de imagen en reconstrucción de imagen tomográfica y de proponer nuevos algoritmos que pueden ser usados para aplicaciones punteras en PET como el PET en tiempo real o para mPET.

En general, los resultados presentados en esta tesis, abren la posibilidad a nuevas líneas de investigación que pueden explotar el uso de estas nuevas técnicas.

1 Introduction

1.1 Introduction to medical imaging

Nowadays, it is difficult to conceive a world without medical imaging techniques. They are widely used, and some techniques have surpassed medical purposes. Since 1895, when the German physicist Wilhelm Conrad Röntgen discovered X-Rays, being awarded with the first Nobel Price in Physics in 1901 for this discovery, the world of medical imaging has seen many revolutions and a constant evolution which has driven us to the current outlook of the field [Bradley, 2008].

X-Rays firstly introduced the possibility of taking photographs of the inside of a human body, sending photons which cross the tissues to a greater or lesser extent depending on the density of the tissues crossed by these photons. They are later detected at the other side of the object, showing a projection of the density of the materials in the path of the photons.

One of the most important revolutions arrived with the development of tomographic medical imaging, which started with the works of the Austrian mathematician Johann Radon, who described mathematically the projections over lines produced by an extensive object described by a function $f(x, y)$. This projections can be described through the Radon transform [Deans, 1985] which is intimately related with the data acquired by the scanners [Roger L. Easton,], being possible to find an inverse operator for this transform, and thus to obtain an image of the object from the projections over lines of it [Herman, 2009].

This principle was used by the physicist Allan McLeon Cormad in 1967 and the engineer Godfrey Newbold Hounsfield in 1972 to propose what we know currently as Computed Tomography or just CT. It is a tomographic extension of X-Rays consisting on the acquisition of X-Rays projections from different directions to be able to obtain a three dimensional image of the body of the patient. These 3D images are presented as cross sections of the object [Bradley, 2008].

In the decade of the 1950's, new modalities, based on the injection of radionuclides made their appearance in the world of medical imaging. We know these techniques, included in the field of nuclear medicine, as molecular imaging and includes mainly two techniques:

- **Positron Emission Tomography (PET)** was first proposed in 1950 by Brownell and Sweet [Davis et al., 2020] [Nutt, 2002] [Phelps, 2002] for tumor detection in brain. This technique is the main topic of the present thesis. PET consists on the inoculation of a radionuclide which emits positrons in its decay, these positrons are annihilated with the electrons of the body and, consequently, two photons with an energy of 511 keV each are emitted in opposite directions. These photons are further detected in the scanner in a very short lapse of time (detected in coincidence). The direction given by the two detection points gives information about the place where the annihilation took place.

- **Single Photon Emission Tomography (SPECT)** based on the injection of radionuclides emitting single photons in their decay which can be detected by a scanner and which direction can be determined using collimators [Davis et al., 2020]. One of the main disadvantages comparing to PET is the need of the collimators which reduce significantly the sensitivity of the scanner.

While CT provides mainly anatomical and structural information of the body, molecular imaging provides functional information. Therefore, PET and SPECT are usually combined with CT in PET/CT or SPECT/CT images which provide both anatomical and functional information (see figure 1).

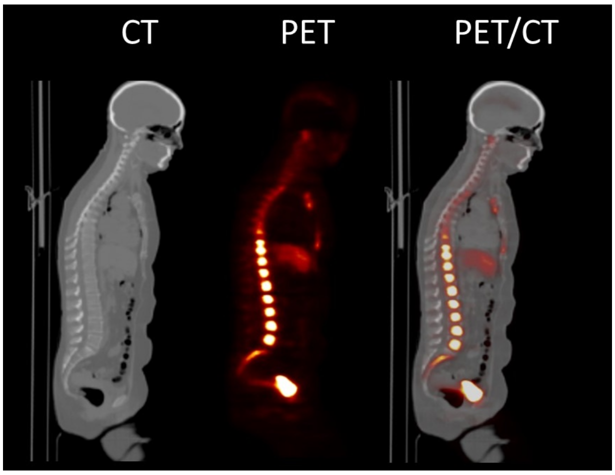

Figure 1: (Left) Computed Tomography image (CT). (Center) Positron Emission Tomography image (PET). (Right) Combined PET/CT.

Years later, in the decade of the 1970's, many other medical imaging techniques were included [Bradley, 2008]. Among them, we want to highlight Ultrasound Computed Tomography (USCT), based on the properties of acoustic waves and their reflection (or transmission) [Pérez Liva, 2017] in the change of medium, and Magnetic Resonance Imaging (MRI), based on the use of magnetic fields and their interaction with the alignment of the spins of the nucleons (mainly protons in hydrogen atoms). These two techniques present the advantage, compared to the modalities previously discussed, that they do not use ionizing radiation. [Brahme, 2014]

1.2 Fundamentals of Positron Emission Tomography

Positron Emission Tomography (PET) is a medical imaging technique based on the administration of molecules of biological interest labelled with a radionuclide which decays β^+ emitting positrons [Cal González, 2015] [Abushab, 2013] [Vicente Torrico, 2013] [Cherry and Dahlbom, 2006] [Brahme, 2014] [Selivanov, 2002] [Bendriem and Townsend, 2003]. Simplifying, these positrons are annihilated with the electrons of the medium, emitting, in most cases, two photons, in opposite directions which are detected in coincidence in a scanner (usually with detectors arranged in a ring form). Then the position of the source (the radionuclide) inside the body can be determined from the directions given by the two detection points of each coincidence, reconstructing the image of the uptake of the radio-labelled drug in the organism. These images provide important functional information [Brahme, 2014]. A simplified and schematic representation of a PET acquisition is presented in figure 2.

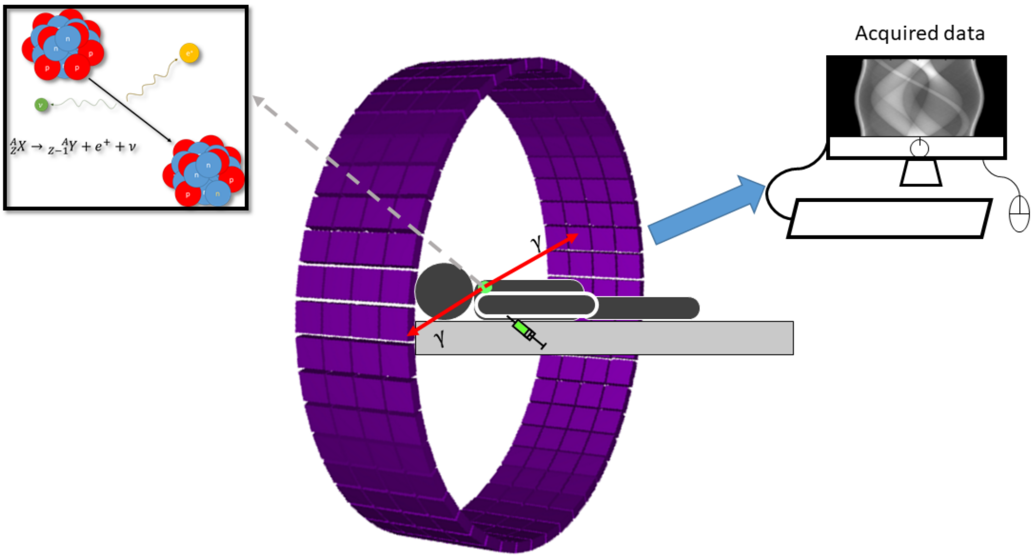

Figure 2: Schematic representation of a PET acquisition.

For clinical purposes, the main field in which PET is used, is oncology. Since tumors have an accelerated metabolism, cancerous cells generally consume glucose at a higher rate that healthy cells [Pauwels et al., 1998]. Thus, using glucose labelled with, generally, ^{18}F, [Reske and Kotzerke, 2001] medical doctors can observe the distribution of the glucose in the organism and detect tumors if there are more presence of glucose in certain region in which it should be lower. Other fields of the medicine where PET is commonly used are cardiology or neurology.

1.2.1 Nuclear decay

Nuclei, can be differentiated between stable and unstable isotopes. The stability or instability of them depends mainly on the configuration of the protons and neutrons inside each nucleus. Only a small number of all the known nuclei are stable [Henning, 2012] and most of them decay into other nuclides, usually generating a cascade of decays until achieving a stable state.

A common way to show all the known nuclei, and its principle mode of decay, is through the chart of nuclei or Segré Chart, represented in figure 3.

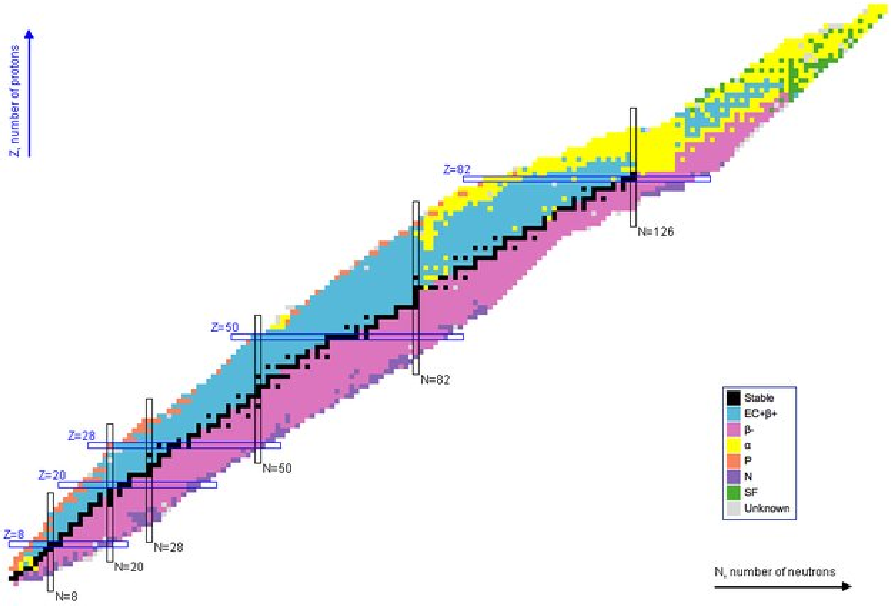

Figure 3: Schematic view of the Segré Chart of Nuclei. Image from [Henning, 2012]

Attending to the decay mode, and if the nucleus has an excess of protons or neutrons, different particles can be emitted during the decay process [Knoll, 2010] [Krane et al., 1987]:

- **Spontaneous fission:** some very unstable nuclei produce fission spontaneously resulting into two different nuclei.
- **Proton/neutron emission:** in some cases, nuclei can decay by emitting a proton or a neutron, depending on which of them is in excess inside the nucleus. Protons emitted this way are easily detected due to their charge. Neutrons can also be detected although it is more difficult since they have no electrical charge.
- α **emission:** in these processes, the nucleus decays to another emitting two protons and two neutrons, forming a nucleus of ${}^4_2He$.

$$ {}^A_Z X \rightarrow {}^{A-4}_{Z-2} Y + {}^4_2 He \qquad (1)$$

This nucleus of helium emitted is known as α particle. For each nucleus decaying in this mode, the α particle has a fixed and unique energy. Due to the high charge

(+2e) and mass of these particles, they usually are very likely to interact with the matter around and lose their energy very soon [Knoll, 2010].

- β^- **decay:** in this process, an electron (β^- particle) is emitted as a result of the internal conversion of a neutron into a proton. To preserve lepton number into the nuclear reaction, also an anti-neutrino is emitted during the process. Opposite to α emission, in this case, two different particles are emitted in the decay. This results into a continuous spectrum of energies for the electron and the anti-neutrino, which maximum and minimum energies are determined by the decaying nucleus. An example for the electron energy spectrum is represented in figure 4.

$$^A_ZX \rightarrow ^A_{Z+1} Y + e + \bar{\nu} \tag{2}$$

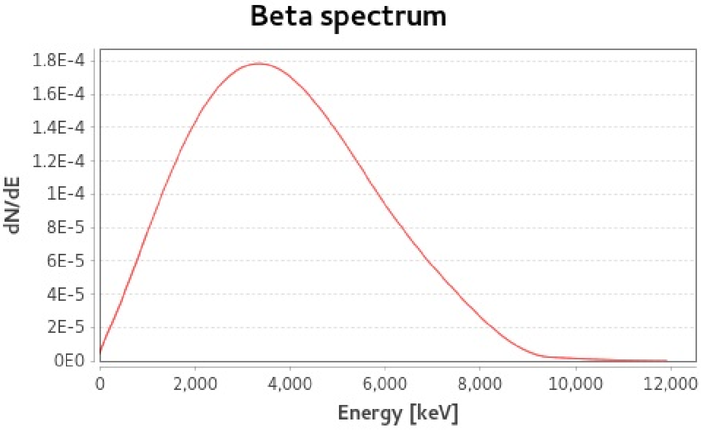

Figure 4: Schematic representation for the β^- particle for ^{14}N [NDS, 2020]

- β^+ **decay:** in this type of β decay, the particle emitted is not an electron, but a positron, due to the internal conversion of a proton into a neutron inside the nucleus. In consequence, also a neutrino is emitted in this kind of decays. The emission of positrons in β^+ decays is the main physical principle in which PET is based, thus this process is the base of this thesis. Similar to the case of β^- decay, the total energy of the decay is shared between the positron and the neutrino, resulting into a continuous spectrum of energy for both particles.

$$^A_ZX \rightarrow ^A_{Z-1} Y + e^+ + \nu \tag{3}$$

- γ **emission:** in general, after a nuclear decay, the final state of the new nucleus is not the ground state but a excited state instead with an excess of energy. During the desexcitation of the nucleus to achieve the ground state, γ particles (photons) are emitted, with fixed energies corresponding to the energy gaps between the initial and the final state in each desexcitation. The lapse of time between the nuclear decay and the nuclear desexcitation of the resulting nucleus, depends on each state of each nucleus. When the mean lifetime of the excited states is very short we can consider that the γ rays are prompt emitted with the decay, in other cases, we can find delayed γ emissions.

$$^{A}_{Z}X^{*} \rightarrow ^{A}_{Z} X + \gamma \tag{4}$$

The total number of decays that are produced in a lapse of time in a radioactive source is known as total activity (A) of the source. It can be also defined as the total probability of decay in a time t inside a sample with N nuclei at that time, being λ the probability of decay of a single nucleus.

$$A(t) = \frac{dN(t)}{dt} = \lambda \cdot N(t) \tag{5}$$

The International System units for activity are known as Bequerel (Bq) and correspond to one decay per second. In nuclear physics, it is extended the use of Curie (Ci) as activity unit. $1Ci$ correspond to $3.7 \cdot 10^{7}$Bq [Knoll, 2010] [Krane et al., 1987]. For some application in nuclear sciences, the only object of interest are the decays producing a certain type of particles, for instance positrons. It is common to talk about β^{+} activity to refer only to the β^{+} decays of the particle, or even activity due to positrons if only the β^{+} decays producing positrons are important for the study.

The activity of a radioactive source decays exponentially according to λ. That conclusion can be also achieved solving the differential equation (5). Considering A_0 as a reference activity in a time $t = 0$, the activity in a time t is:

$$A(t) = A_0 \cdot e^{-\lambda \cdot t} \tag{6}$$

The half life ($T_{1/2}$) of the nucleus can be defined as the time elapsed when the activity is exactly the half of the initial or reference activity ($A(t) = A_0/2$). From 6, it can be shown that:

$$T_{1/2} = \frac{\ln 2}{\lambda} \tag{7}$$

The mean life (τ) can be defined as the average time that each nucleus remains in the sample before the decay. Mathematically it is the inverse of λ.

$$\tau = \frac{1}{\lambda} \tag{8}$$

1.2.2 Physics of PET: positron emission and annihilation

β^{+} decay occurs in proton-rich nuclei where an internal conversion of one of the protons of the nucleus into a neutron is produced, emitting as a result a positron and a neutrino to preserve lepton number [Griffiths, 2008]. This process is schematized in figure 5.

$$p \rightarrow n + e^+ + \nu \tag{9}$$

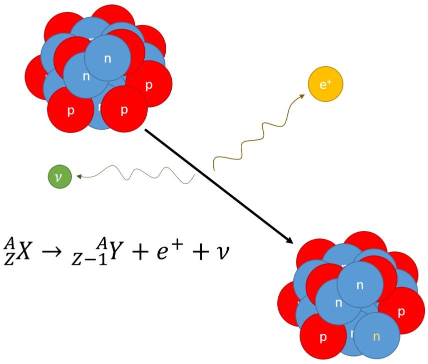

Figure 5: Scheme of a β^+ decay

It is important to notice that β^+ decay does not always imply the emission of a positron. Sometimes, the nucleus captures an electron of an inner layer of the atom. This process is known as **electron capture** [Cal González, 2015] [Krane et al., 1987]. It is important to consider this effect when looking at the activity of an acquisition since not all the activity might produce positrons. The branching ratios for each radionuclide should be considered to take into account the probability of emitting a positron or capturing an inner electron [NDS, 2020] [Krane et al., 1987]

$$p + e^- \rightarrow n + \nu \tag{10}$$

Depending on the initial state of the father nucleus and final state of the produced nucleus, the total energy shared by the positron and the neutrino is determined. Thus, the initial energy of emission of the positrons is characteristic for each radionuclide. In figure 6 some of the energy spectra for positrons in several common PET emitters are shown.

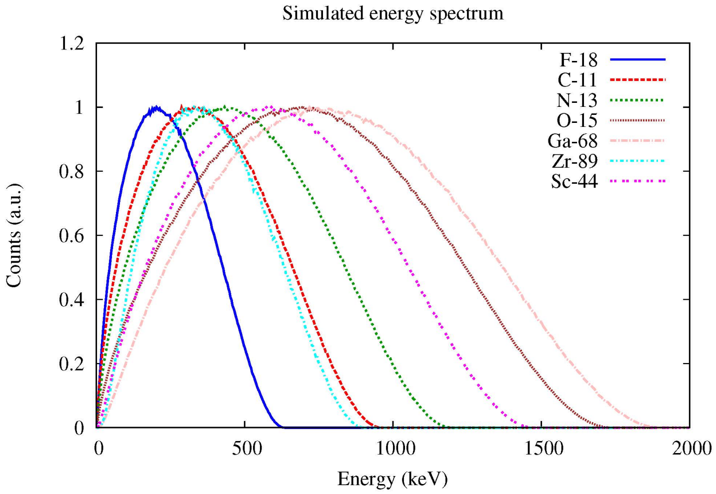

Figure 6: Energy spectrum for positrons in some frequent PET emitters

The positrons emitted in a β^+ decay lose progressively their energy when they interact mainly with electrons of the surrounding medium [Knoll, 2010]. When it has lost most of its energy, the positron is annihilated with an electron, resulting most of the time into two 511 keV photons emitted approximately in opposite directions due to energy and momentum conservation [Knoll, 2010] [Cal González, 2015] [Cherry and Dahlbom, 2006].

In general, before the annihilation, the positron and the electron form a system known as positronium with a very short half life [Griffiths, 2008]. This positronium ends with the annihilation of the positron and the electron producing two (para positronium) or three (ortho positronium) gamma rays. Some recent works propose also the use of the annihilation produced by the ortho positronium for some PET scanners [Moskal et al., 2019] but, for our purposes, we will only focus on the case of the annihilation producing two photons. A simplification of this process is presented in figure 7. Note that the 3-γ decay of the positronium is considered to happen only around 0.5% of the positron emissions [Cassidy, 2018] [Griffiths, 2008].

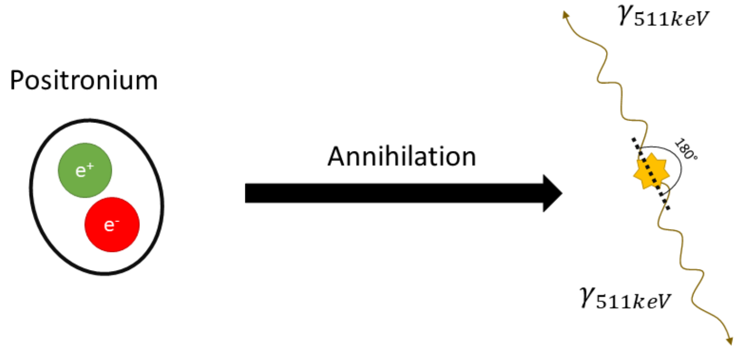

Figure 7: Schematic representation of the annihilation process from the positronium.

The distance between the emission and the annihilation points is known as Positron Range (PR) [Cal González, 2015] [Cherry and Dahlbom, 2006] [Brahme, 2014] and it is one of the main limitations for spatial resolution in PET imaging. Positron range increases with the initial energy of the emitted positrons, thus, nuclides that emit more energetic positrons will present higher positron range effects. It also depends on the media surrounding the positron emitter, in general the PR decreases with the increasing of the electronic density of the medium [Herraiz et al., 2021].

At the moment of the emission, the positron or the electron may keep a small part of their moment. It produces an effect of non-collinearity due to which the angular difference between the two photons may differ from 180º [Cherry and Dahlbom, 2006]. It is in general a small effect in terms of angular difference (with a maximum around 0.5º) but it becomes an important effect specially for PET scanners with a large radius [DeBenedetti et al., 1950] [Shibuya et al., 2007].

These effects, affecting the image quality will be further discussed in next sections.

1.2.3 Interaction of the photons with the matter

The main goal in a PET acquisition is to detect in coincidence the two photons emitted in the annihilation of the positrons [Brahme, 2014] [Cherry and Dahlbom, 2006]. Once these photons are emitted, they travel through the medium surrounding them until they reach the scanner (or going outside the field of view). During their path they can suffer interactions with the particles they find. In this section, we are summing the main possible interactions of the photons with the matter. Also, these interactions are the basis of photons detection in the scanner [Knoll, 2010] [Krane et al., 1987].

- **Photoelectric absorption.** Photons can be absorbed by the atoms, losing all their energy which is further spent in the ejection of one of the external electrons of the atom to the medium. Due to the energy conservation law, the ejected electron will have a kinetic energy (T_{e^-}) which results of the subtraction of the initial energy of the photon (E_γ) minus the bounding energy (B) that the electron had with the atom [Knoll, 2010],

  $$T_{e^-} = E_\gamma - B \tag{11}$$

  This effect is particularly important when the energy of the photons is relatively low. The probability of suffering a photoelectric absorption also grows with the electron density of the medium [Knoll, 2010].

  In a PET acquisition, for 511 keV photons, this effect has an important contribution. It is the main effect inside the scanner to detect photons. Also, it can make that one of the emitted electrons vanishes in the medium between the emission point and the scanner, resulting in the lose of effective coincidences in the acquisition (attenuation). The effect becomes more important in high density tissues.

- **Rayleigh scattering.** It is a process of coherent scattering in which the photon does not lose energy at all [Knoll, 2010], but its direction is slightly modified. As it does not involve an energy loss of the photon, it is many times neglected in many physical applications. However, in the case of PET, the change in the direction of the photon may result into a possible lose of information in the determination of the annihilation point in the image. The probability of this kind of interactions increases for media with atoms with high electronic densities (high Z).

- **Compton scattering.** It is one of the main forms of interaction of photons coming from the annihilation of the positron (511 keV). In this process, the photon lose part of its initial energy (E_γ) when it is deflected at a certain angle (θ) by an electron of an atom of the medium. The energy of the photon after the scatter ($E_\gamma^{'}$) is given by [Knoll, 2010] [Cal González, 2015] [Vicente Torrico, 2013]:

  $$E_\gamma^{'} = \frac{E_\gamma}{1 + \frac{E_\gamma}{m_{e^-}c^2}(1 - \cos\theta)} \tag{12}$$

  The angular distribution of the photons can be described using the formula of Klein-Nishina [Knoll, 2010].
  The probability of suffering a Compton scattering increases with the effective Z

of the atoms in the medium. In the case of PET acquisition, scattering effects play an important role in the deterioration of the images and are one of the main contributions that should be properly corrected. This will be properly discussed in section 1.4.

- **Pair production.** For high energy photons (more than 1.022 MeV which is twice the energy in rest for electrons and positrons), pair production might take place. During this process, the photon disappears and produces a pair electron-positron preserving the total energy and momentum of the initial photon. As consequence, the emitted positron will be further annihilated with an electron in the medium and will produce the corresponding 511 keV annihilation photons. In general, these processes are not observed in a PET acquisition since the photons involved in these cases are 511 keV photons that cannot produce pairs [Knoll, 2010] [Cal González, 2015] [Vicente Torrico, 2013]. However, as we will discuss in the next section, some non-standard radionuclides for PET emit additional gamma rays which energies are sometimes high enough to produce pairs. However, even in those cases its contribution is low comparing to the rest of physical effects and, thus, it is neglected in the reconstruction process.

In general, in a PET acquisition, these interactions result into two different contributions, attenuation and scatter. They will be discussed in section 1.4. In figure 8 the probabilities of each kind of interaction as a function of the energy of the photon and atomic number of the medium is schematically represented.

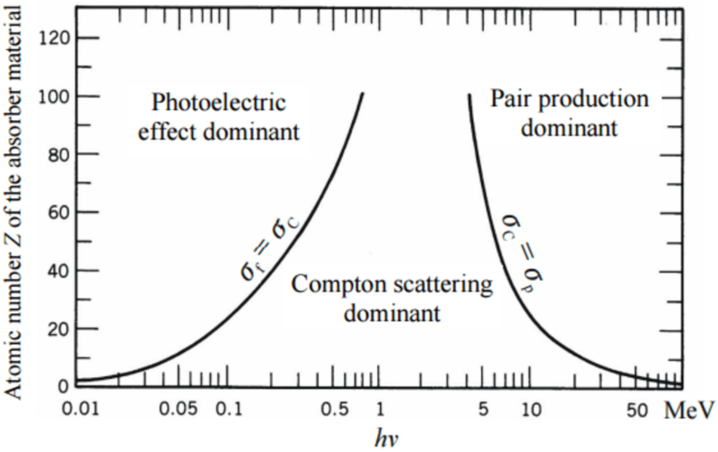

Figure 8: Predominance of the different interactions of the photons with the matter as a function of the energy and the atomic number [Evans and Evans, 1955]

1.3 PET radionuclides

There are a wide number of β^+ emitters used in PET nowadays depending on the purpose and nature of the study. In this section, we discuss some of the most common radionuclides used in PET and other less used that are obtaining more visibility in the last years.

Standard nuclides for PET, are commonly pure β^+ emitters, and thus, there are not other gamma rays coming from the radionuclide apart from those coming from the annihilation of the positrons. Moreover, in general, they have relatively short half lives which is a good point for the patients since they do not need to stay in the hospital more than some hours until the nuclides have decayed several half lives. Besides, they are generally part of molecules of biological interest or have good chemical properties that make them suitable to label common molecules such as glucose. They also can be easily produced in cyclotrons although due to their short half lives, many times too short to carry them to other places, an in-site cyclotron is needed. The most commonly used are:

- ^{18}**F** is the most commonly used nuclide for PET imaging by far [Hess et al., 2014], specially in oncology for tumor imaging [Reske and Kotzerke, 2001]. It is generally produced in cyclotrons, using stable ^{18}O as target [Cherry and Dahlbom, 2006]. Its half life (around 2 hours) [NDS, 2020] makes it ideal for a good number of studies since it is suitable for many biological processes and furthermore it can be transported from the production place to other hospitals and research centers. [Pauwels et al., 1998] [Cherry and Dahlbom, 2006]. The main properties of the β^+ decay of ^{18}F are presented in figure 9.

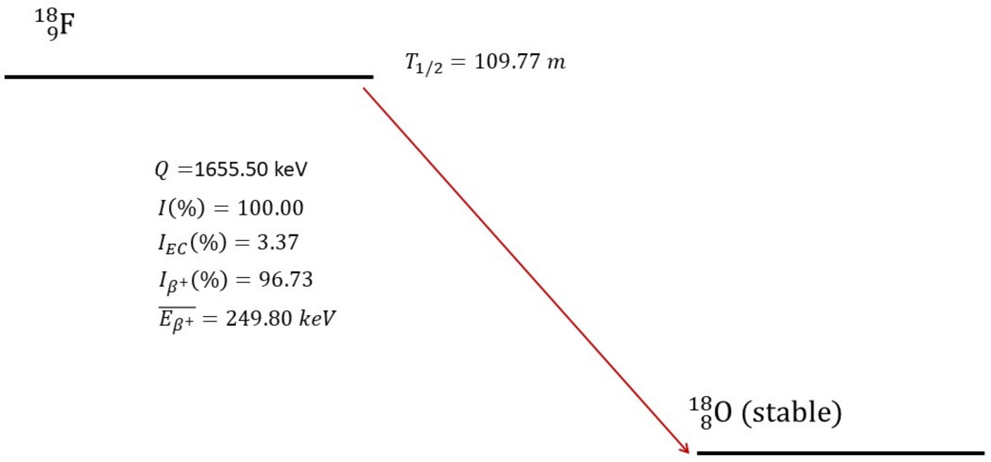

Figure 9: Schematic representation of the decay plot for ^{18}F

It is commonly used as ^{18}F-FDG, labelling glucose [Reske and Kotzerke, 2001] [Pauwels et al., 1998] [Rudd et al., 2002]. It is frequently used for the detection of a large variety of tumors since the metabolism of cancerous cells is accelerated compared to healthy tissues and, thus, the uptake of glucose is higher than in normal cells [Gambhir et al., 2001]. Other fields where ^{18}F-FDG plays a crucial role are cardiology, where it is frequently used to study the myocardial viability after a heart attack [Gambhir et al., 2001], or to study heart disease [James et al., 2011]. Also, this molecule is commonly used in neurology to study different pathologies such as dementia, Alzheimer's disease or epilepsy [Gambhir et al., 2001] [Hess et al., 2014].

Other molecules where ^{18}F is used are, for instance, ^{18}F-NaF (sodium fluoride) used for bone studies or for atherosclerotic plaques [Joshi et al., 2014], ^{18}F-Fluorodihydroxyphenylalanine (DOPA) used for some kind of cancers and also for hyperinsulinism [Bastianello et al., 2017] [Timmers et al., 2009], ^{18}F-Fluoro-Dopamine (FDA) also used for some tumors as Pheochromocytoma and Paraganglioma [Timmers et al., 2009] or ^{18}F-flutemetamol for Alzheimer's disease [Vandenberghe et al., 2006].

- ^{11}**C** has a half life considerably shorter than ^{18}F, with only 20 minutes. This implies the need to have an in-site cyclotron. However, it is widely used to study different biological processes. For instance, ^{11}C-Acetate, is a well known tracer in cardiology, where it is used to study myocardial metabolism and perfusion [Grassi et al., 2012] and also in oncology to study some kind of tumors [Grassi et al., 2012], specially for prostate cancer [Oyama et al., 2002], where it has been shown to be even more suitable than ^{18}F-FDG, but also in other tumors such as liver [Ho et al., 2003]. Other molecules involving ^{11}C and used in PET are ^{11}C-choline for several kind of tumors [Yamamoto et al., 2008] [Hara et al., 1997] [Reske et al., 2006], ^{11}C-PIB for Alzheimer's disease [Rabinovici et al., 2007] [Edison et al., 2008] or ^{11}C-methionine for tumors like gliomas [Herholz et al., 1998]. The main properties of the β^+ decay of ^{11}C are presented in figure 10.

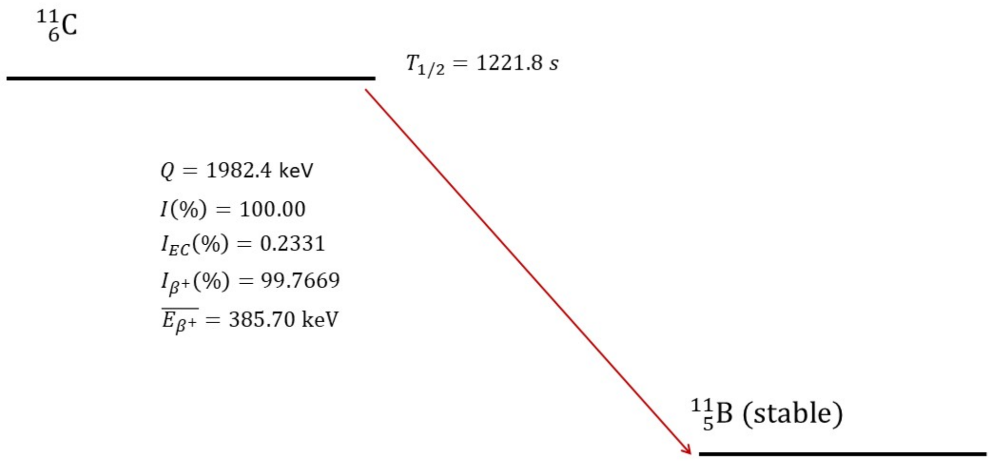

Figure 10: Schematic representation of the decay plot for ^{11}C

- ^{13}**N**: its half life is even shorter than ^{11}C with less than 10 minutes [NDS, 2020], thus, it is essential an in-situ generator. This radionuclide is commonly used in cardiology as ^{13}N-NH$_3$ since ammonia is implied in myocardial blood flow [Choi et al., 1999]. There are numerous works proposing different applications related to myocardial blood flow and involving ^{13}N and PET [Herzog et al., 2009a] [Yamagishi et al., 2003] [Fiechter et al., 2012] [Slomka et al., 2012]. Also, ^{13}N has been proposed as ^{13}N-N (just as nitrogen), whether inhaled or injected, to study lung diseases [Wellman et al., 2010] [Melo et al., 2010]. In figure 11 we show a simplified schematic model of the decay of ^{13}N.

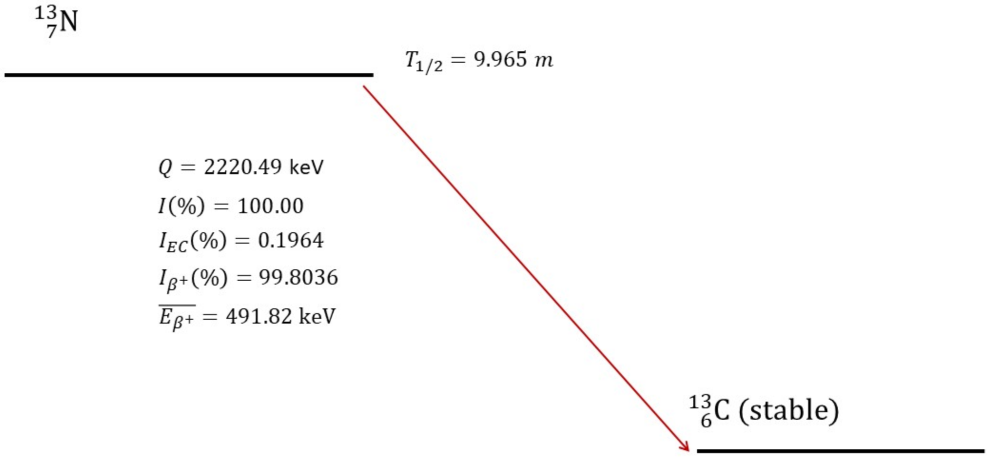

Figure 11: Schematic representation of the decay plot for ^{13}N

- ^{15}**O** presents some interesting properties such as the possibility of labelling common molecules, as ^{15}O-H$_2$O, ^{15}O-CO$_2$ or ^{15}O-O$_2$. It is specially used labelling these molecules to study brain functionalities or injuries [Coles et al., 2006] [Hugdahl et al., 1999] [Hugdahl et al., 2000] [Hamdy et al., 1999] [Boecker et al., 1998] [Muzik et al., 2013] . The bad points of this nuclide are its short half life (only 2 minutes) and its relatively high positron range. In figure 12 we show a simplified schematic model of the decay of ^{15}O.

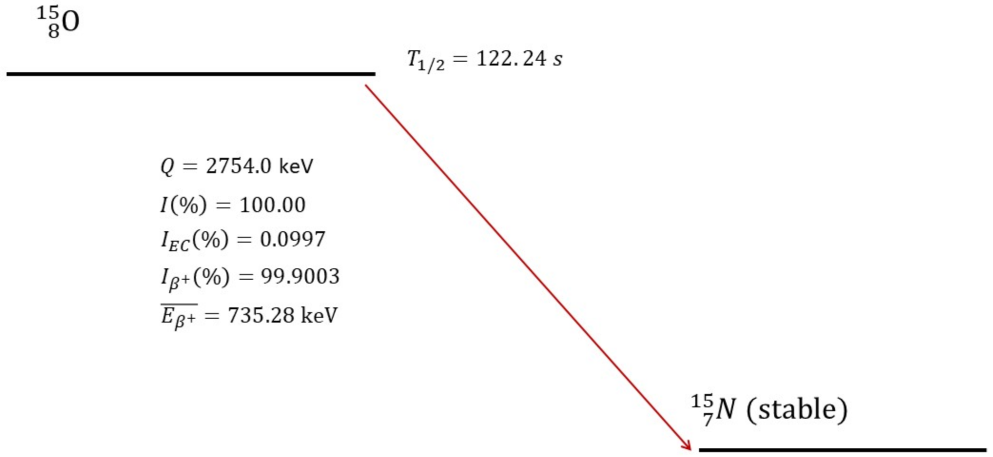

Figure 12: Schematic representation of the decay plot for ^{15}O

Also, in recent years, some non-standard PET emitters, have been proposed for PET due to their properties and the new possible uses that they present [Conti and Eriksson, 2016] [Hao et al., 2010] [Braad et al., 2015]. These radionulcides present some interesting challenges since, in general, they have higher positron range effects and other prompt γ rays are sometimes emitted with the positrons, introducing a spurious background of coincidences. There is a growing list of more non-standard β^+ emitters that are being used in PET, but the aim of this section is to discuss the main physical properties of interest for PET (positron emission probability, positron range, additional prompt γ rays, half life, etc) and the main uses that have been proposed in the literature for some of the most popular of these radionuclides.

- ^{44}**Sc** has been studied [Roesch, 2012] [Filosofov et al., 2010] [Hernandez et al., 2014] [Alliot et al., 2015] [Lima et al., 2020] as a candidate which presents some interesting properties. The half-life of ^{44}Sc is close to 4 hours. For this reason, it can be used to study long term biological processes. Furthermore, ^{44}Sc decay mode is mostly β^+ (94.27%).

  In the decay process of ^{44}Sc, there are some additional gamma rays, being the most probable of them (99.88%) an additional gamma ray with an energy of 1157 keV. The positron range of ^{44}Sc is not too high compared to other non-standard PET emitters, although it is not negligible.

^{44}Sc has been proposed for labelling peptides, useful in the detection of some kind of tumors [Hernandez et al., 2014] [Pruszyński et al., 2012] [Lau et al., 2019] [Domnanich et al., 2017b]. Also, in combination with other radionuclides as ^{47}Sc it has been proposed for theragnostics [Domnanich et al., 2017a] [Umbricht et al., 2017] [Müller et al., 2014].

^{44}Sc is also interesting as it can be produced either in ^{44}Ti/Sc generator [Filosofov et al., 2010] or irradiating natural ^{44}Ca in cyclotrons [Hernandez et al., 2014].

In figure 13 we show a simplified schematic model of the decay of ^{44}Sc.

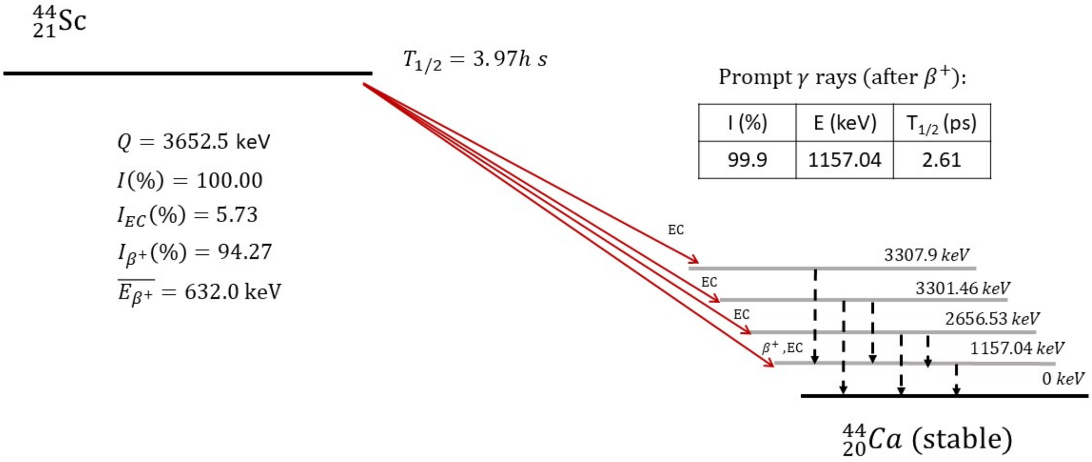

Figure 13: Schematic representation of the decay plot for ^{44}Sc

- ^{52}**Mn** has been proposed in several works as a good candidate for positron emission tomography due to several reasons [Wooten et al., 2017]. One of them is that it can be used for PET/MR imaging as traceable nuclide in combination with a para-magnetic contrast agent based on stable manganese [Brandt et al., 2019]. Furthermore, manganese, in its divalent state, has been shown to be a unique tool for tracing neuronal pathways as it is taken up and transported by neurons, being able to cross synapses [Napieczynska et al., 2017]. ^{52}Mn has been also used as ^{52}Mn-oxinate for labeling cells and liposomal medicines, allowing to get images of labelled cells and nano-medicines for long periods of time due to ^{52}Mn long half-life [Gawne et al., 2018].

Another advantage of ^{52}Mn is that it can be easily produced by irradiating natural ^{52}Cr [El Sayed et al., 2019] with protons accelerated in cyclotrons or other accelerators [Buchholz et al., 2013] [Buchholz et al., 2015]. ^{52}Mn decays to stable ^{52}Cr emitting positrons with a probability of around 30% and also a cascade of prompt gamma emission [Herraiz et al., 2013]. The long life of ^{52}Mn, around 5.5 days, makes it ideal to label slow tracers such as antibodies. Furthermore, its isomer, ^{52m}Mn with a much shorter half-life of around 20 minutes, can be used for shorter studies.

Besides, its mean positron emission energy is even lower than in the case of ^{18}F. This results into a lower positron range. This fact present an important advantage comparing with most of non-standard radionuclides which positron range is larger and should be considered. In figure 14 we show a simplified schematic model of the decay of ^{52}Mn including some of the most probable prompt-γ rays emitted with the positron.

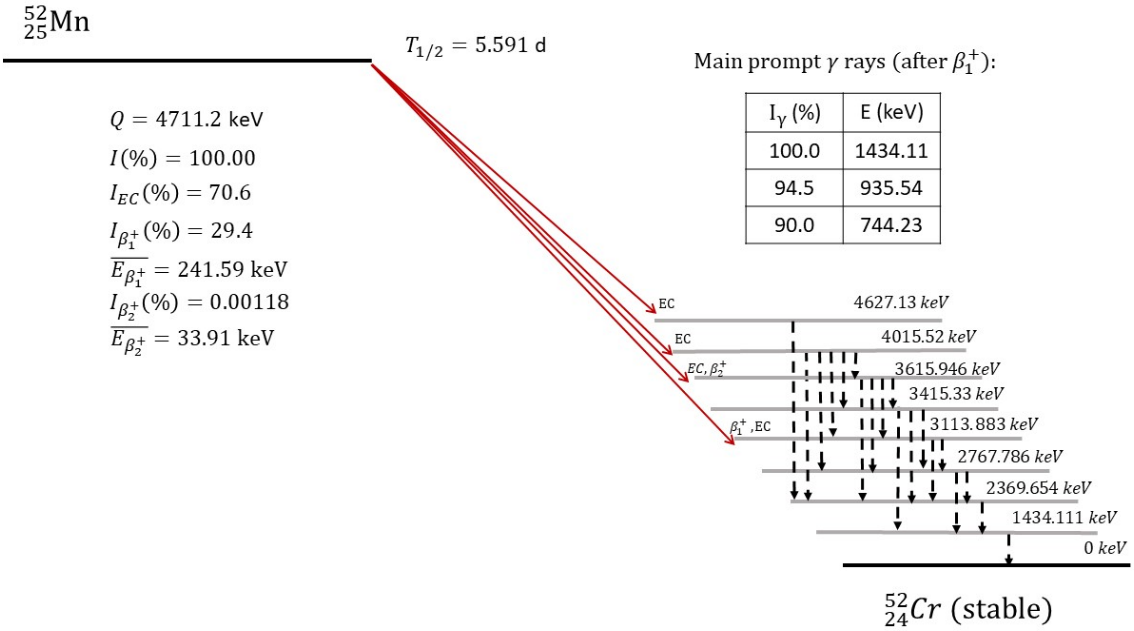

I_γ (%)	E (keV)
100.0	1434.11
94.5	935.54
90.0	744.23

Figure 14: Schematic representation of the decay plot for ^{52}Mn

^{52m}Mn is a meta stable state of ^{52}Mn that can also decay β^+ (it can also decay to ^{52}Mn). For the branch of its β decay to ^{52}Cr, its half life is much shorter than ^{52}Mn (around 20 minutes) which open the possibility of using also ^{52m}Mn for shorter biological processes in PET imaging. It also emits additional prompt gamma rays being by far 1434 keV the more probable (other probabilities are negligible). However, in the case of ^{52m}Mn, the positron range is considerably larger than for ^{52}Mn. In figure

15 we show a simplified schematic model of the decay of ^{52m}Mn.

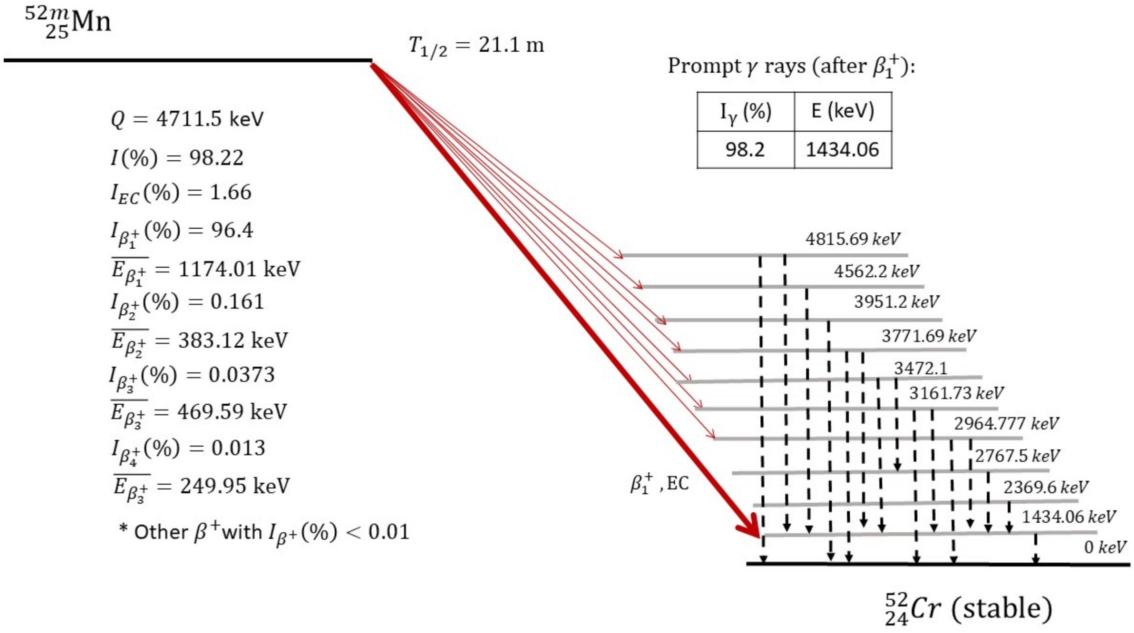

Figure 15: Schematic representation of the decay plot for ^{52m}Mn

- ^{64}**Cu** has interesting applications for labelling antibodies. Immuno-PET has became one of the most used techniques for tumor detection due to their specificity. ^{64}Cu is commonly used for this purpose labelling different antibodies [Voss et al., 2007] [Anderson et al., 1997] [Tamura et al., 2013] [Lesniak et al., 2016] [Yuan et al., 2006]. Also, it has been proposed, labelling nano-particles, as a contrast agent for magnetic resonance, producing good signal for both PET and MR imaging [Glaus et al., 2010].

  ^{64}Cu decays β^+ to stable ^{64}Ni with a probability of 61.5%. It can also decay β^- to stable ^{64}Zn with a probability of 38.5%. Its half life of 12 hours makes it suitable for a good number of studies. It also has a relatively short positron range. This information is shown in a simplified and schematic representation in figure 16.

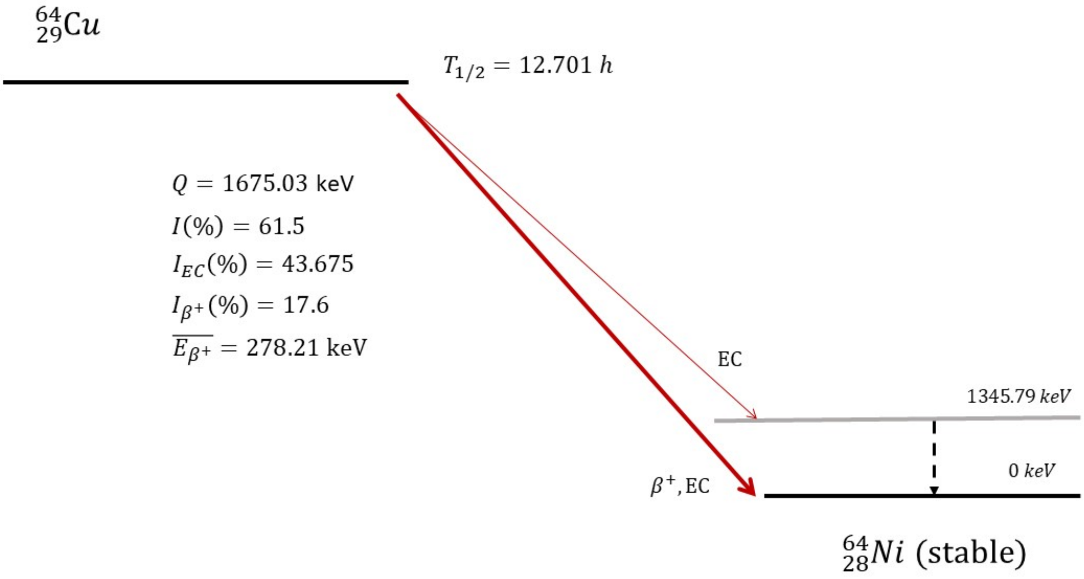

Figure 16: Schematic representation of the β^+ decay plot for ^{64}Cu

- ^{68}**Ga** has good chemical properties that make them ideal for labelling many molecules. Furthermore, it can be easily produced from its parent nucleus ^{68}Ge which decays with EC to ^{68}Ga with a very large half life (271 days) being able to obtain ^{68}Ga from it without the need of a cyclotron [Fani et al., 2008] [Maecke H.R., 2007].

  It is generally used as ^{68}Ga-PSMA to detect prostate cancer [Afshar-Oromieh et al., 2014] [Eiber et al., 2016] [Eiber et al., 2015]. It is also used labelling peptides as ^{68}Ga-DOTA for the detection of some kind of tumors with no high metabolic activity being much more sensible to them than other common radionuclides as ^{18}F-FDG [Gabriel et al., 2007] [Irene Virgolini, 2010]. It has been also proposed for labelling nano-particles [Hofman et al., 2011].

  Despite of its growing popularity, it presents some challenges for resolution recovery, particularly due to its high positron range which makes that its resolution seems to be worse than other β^+ emitters. [Herraiz et al., 2021]. It also may emit prompt gamma rays although with a very low probability (around 3%) as represented in figure 17. Notice that this representation is a simplified model of the decay of ^{68}Ga and some low probability states may not appear.

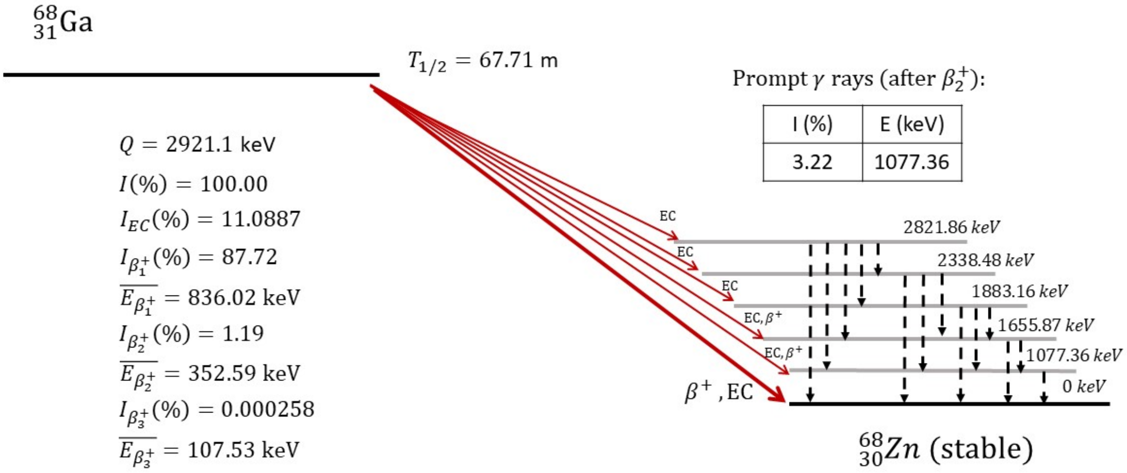

Figure 17: Schematic representation of the decay plot for ^{68}Ga

- ^{76}**Br** this radionuclide, as most of the rest of the ones discussed in this section, can decay to a high number of different states with non-negligible probabilities. Their complete decay details can be consulted in the bibliography [NDS, 2020]. In this section we will only focus on their main applications and some of their most relevant physical properties.
  ^{76}Br decays β^+ to stable ^{76}Se with a half life of 16.2 hours. The probability of emitting a positron in its decay is around 55.71%, decaying also with EC with a probability of 44.29%. Many different prompt γ rays can be emitted in the decay of ^{76}Br, being the energy of the most probable γ ray of 559 keV. Some works has studied the effect of the additional gamma rays in a ^{76}Br [Lubberink et al., 2002] on PET images.
  In the literature, ^{76}Br has been used for multiple purposes, from labelling drugs against tuberculosis [Ordonez et al., 2019] to a wide number of tumors where the specificity of the molecules that can be labelled with ^{76}Br can be very useful [Hanaoka et al., 2015] [Watanabe et al., 2010] [Bruehlmeier et al., 2003] [Rossin et al., 2007] [Gardelle et al., 2001].

- ^{82}**Rb and its isomer** ^{82m}**Rb** are mainly used as an alternative to ^{13}N in places where there are no cyclotrons to study myocardial blood flow [El Fakhri et al., 2005] [El Fakhri et al., 2009] [Manabe et al., 2009] [Nesterov et al., 2014]. ^{82}Rb decays to ^{82}Kr with a high probability of positron emission (more than 80%), it has a short half life of only 1.2575 min, but its isomer ^{82m}Rb with a much longer half life (around 6.47 hours) can be also used for some purposes, despite the much lower probability of emission of a positron in ^{82m}Rb compared with ^{82}Rb. Some effects that should be considered is that ^{82}Rb has a large positron range with reduces the spatial resolution of the PET images if no PR correction is used and that it can emit additional prompt gamma rays.

- ^{86}**Y** is a radionuclide that has gained popularity in the field of immuno-PET for labelling monoclonal antibodies [Lövqvist et al., 2001] [Schneider et al., 2009] [Nayak et al., 2011] [K Nayak and W Brechbiel, 2011]. Although it is very suitable for antibodies labelling, it has some challenging properties as its non-negligible positron range and the large number of prompt γ rays that it emits which generate an important and undesirable spurious background in the images. Besides, it emits positron with a probability around 33%, being the rest of the decays EC. Its half life of 14.74h is sometimes too short for some biological processes for antibodies in humans [Deri et al., 2013].

- ^{89}**Zr** is becoming one of the reference radionuclides for immuno-PET in the last years since it presents ideal physical and chemical properties for this purpose [Deri et al., 2013] [Verel et al., 2003] [Vugts et al., 2013] [Sham et al., 2014] [Gaykema et al., 2013] [Makris et al., 2014]. Its long half life of 78.41 hours is suitable for immuno-PET. Furthermore, although its probability of emitting positrons is 22.74%, the energy of the emitted positrons is not high, and thus, positron range effects are not too drastic. Furthermore, although additional γ rays can be emitted after the decay, they are not in coincidence with the positron (they are delayed γ emission instead of prompt), and, thus, they not introduce the spurious background that other non-standard PET emitters do. In figure 18 we show a simplified schematic model of the decay of ^{89}Zr.

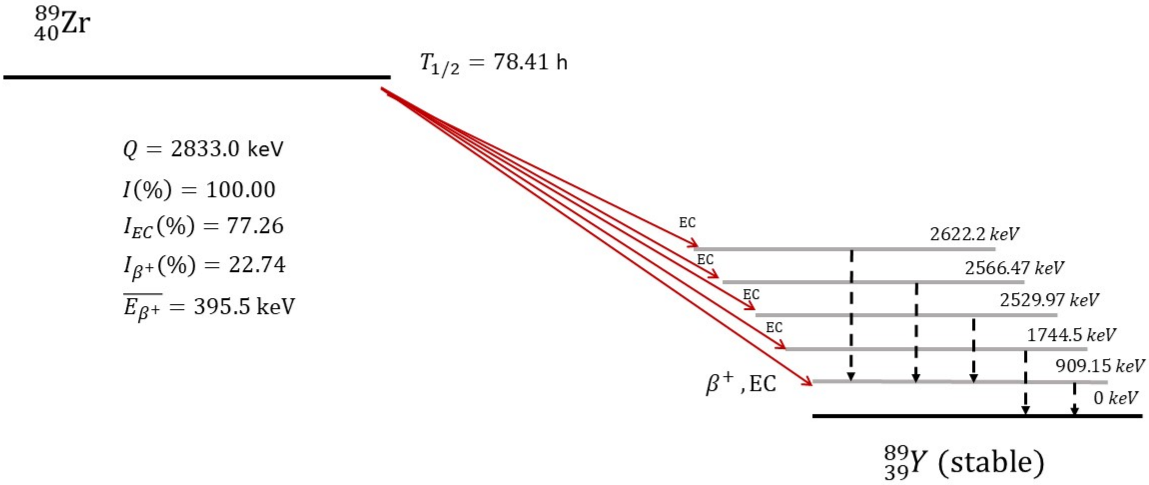

Figure 18: Schematic representation of the β^+ decay plot for ^{89}Zr

- ^{94}**Tc** and more commonly its isomer ^{94m}Tc are interesting non-standard radionuclides for PET [Herraiz et al., 2013] [Gagnon et al., 2011]. ^{94m}Tc can be produced by irradiating natural molybdenum (^{94}Mo) in cyclotrons [Christian et al., 1995] [Rösch and Qaim, 1993]. Also, it is more likely to emit positrons ($> 70\%$) than ^{94}Tc ($< 11\%$). The main disadvantages of ^{94m}Tc are its great positron range and prompt γ emissions together with the positrons.

- ^{124}**I** is currently, together with ^{89}Zr, one of the reference radionuclides for immuno-PET [Deri et al., 2013] [Pratt et al., 2020]. It has a very long half life that makes it ideal to study long biological processes as most of the immuno-PET studies focus on [Carrasquillo et al., 2011] [O'Donoghue et al., 2011] [Schwartz et al., 2012] [McBride et al., 2006]. Moreover, as iodine itself is mostly absorbed in the thyroids, it has been used as a perfect tracer for thyroid cancer and together with ^{131}I (used for radiotherapy) in its treatment to study dosimetry and residual after treatment [Freudenberg et al., 2004] [Freudenberg et al., 2007] [Freudenberg et al., 2011] [Jentzen et al., 2008] [Sgouros et al., 2004]. It should be considered that ^{124}I only emits positrons with a probability of 22.74%, being the rest EC. Furthermore, the energy of the most probable emitted positrons is considerably high, and, thus, positron range effects are important when using ^{124}I for PET imaging. Also, the prompt gamma emissions play an important role on the degrading of ^{124}I PET images. In figure 19 we show a simplified schematic model of the decay of ^{124}I. Some of the states which the ^{124}I may decay to are not represented because of ther low probability or low relevance for PET purposes.

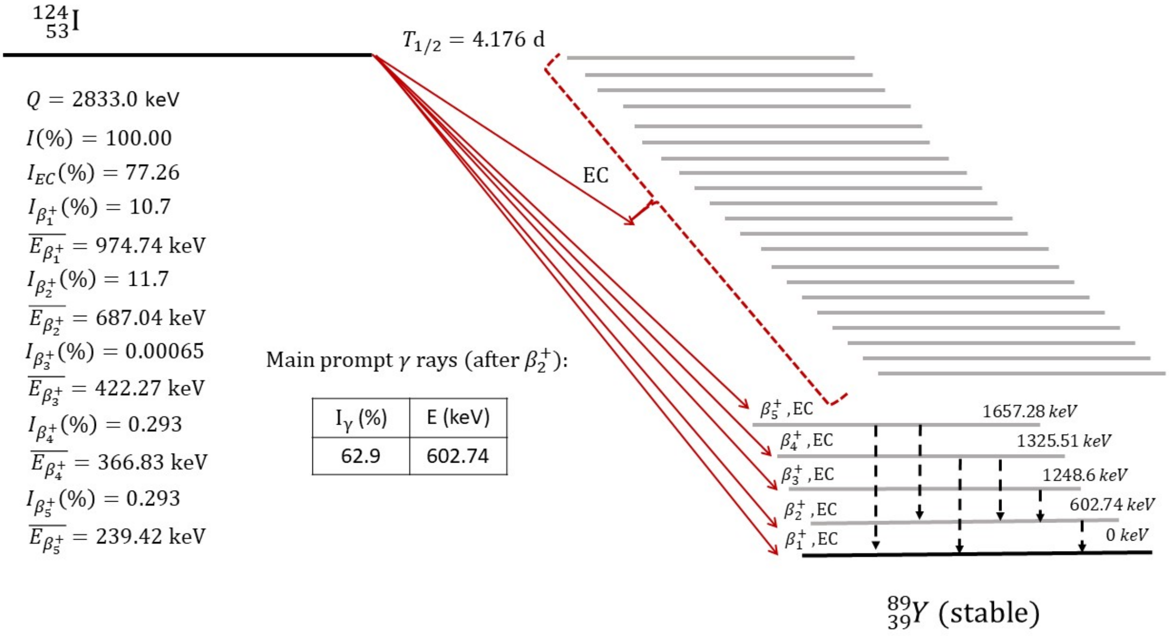

Figure 19: Schematic representation of the β^+ decay plot for ^{124}I

1.4 PET scanners

1.4.1 Radiation detectors properties

A radiation detector is a device that can generate a measurable electric signal when a ionizing particle reaches the detector. According to the features of a detector, some properties can be considered. In this section, we will discuss some of them that are appreciable for PET scanners. [Knoll, 2010] [Krane et al., 1987]

- **Energy response**. Most current detectors are able to determine the energy of the incident particle. The energy spectrum observed in a detector depends mainly on the type of incident radiation (α, β or γ) and the detector used [Knoll, 2010]. In this thesis we will focus on the energy response for γ particles since it is the main interest on a PET scanner. In a γ spectrum, there are some regions easily identifiable as shown in figure 20. One of them is the photo-peak, produced when the total (or almost the total) energy of the photon is absorbed in the detector, producing a signal corresponding to the total emitted energy of the γ ray. The photon may also suffer a Compton scattering event before being absorbed by the detector, producing the Compton's continuous. These effects are shown in figure 20. There are also other effects as back-scatter or pair production effect (for γ rays with enough energy) that can also be observed in γ spectra [Knoll, 2010].

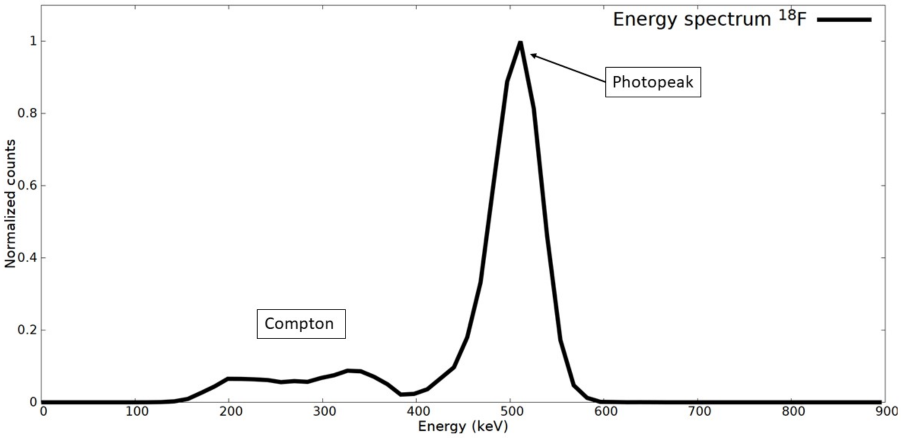

Figure 20: Example of a γ energy spectrum for ^{18}F in a typical detector used in a PET scanner

According to the capability of the detector to resolve two peaks with different energy, the resolution of the detector is defined [Knoll, 2010]. It is a relative magnitude and it is calculated as the Full Width at Half Maximum ($FWHM$) of the peak divided by the mean energy of that peak [Knoll, 2010].

$$R(\%) = \frac{FWHM}{E} \tag{13}$$

Typical energy resolution range for crystals used in PET detectors is around 15-30% for the 511 keV peak [Weber et al., 2003], although it is very variable for different materials. It is typical in PET scanners to consider energy windows to determine if a count is given by an annihilation photon or not. Some of the most typical energy windows used in PET are 350-700 keV or even narrower windows of 450-650 keV.

- **Efficiency**. Another important feature of radiation detectors is the number of counts that they can gather considering the emitted activity [Knoll, 2010]. This efficiency (ε) has two contributions, one of them is a geometrical contribution that depends on the solid angle that the detector covers, the other is an intrinsic efficiency that depends on the material and properties of the detector. In a PET scanner, efficiency is given as the number of coincidences given for a certain injected activity. Common units for it in PET are kcps/MBq (kilo counts per second per mega becquerel). This is one of the most important properties of a scanner, since for higher efficiencies, the scanning time or the injected activity can be reduced without affecting the quality of the images. Indeed, the efficiency of the scanner is one of the studied parameters in the performance of PET scanners.

- **Dead time**. It is defined as the time that the device needs between one detection and the following to be processed as separate counts. It can be a relevant effect in PET, specially when the activity of the source is high and several events can occur at approximately the same time [Knoll, 2010] [Cal González, 2015]. If two or more photons are detected at the same time, they might be processed as a single event with a total energy being the sum of all the deposited energy by the photons. This effect is known as pile-up and may result in a lost of information since the event can be recorded with an energy greater than the upper threshold for energy [Cal González, 2015] [Vicente Torrico, 2013] [Abushab et al., 2016]. We can also talk in terms of temporal resolution to determine the capability of a detector to resolve two different counts in a certain time [Knoll, 2010].

1.4.2 Types of radiation detectors. Detectors for nuclear medical applications.

There are different kinds of detectors used for radiation. Depending on the purpose, some of them are preferred to others. Usually, radiation detectors are classified into [Knoll, 2010] [Cal González, 2015] [Vicente Torrico, 2013] [Abushab et al., 2016] [Cherry and Dahlbom, 2006]:

- **Gas-filled detectors:** the main principle of these detectors consists on a tube or a chamber, filled with a gas, that can be easily ionized by the particles that reach the detector. When this happens, the charged particles generated by the ionization are accelerated and gathered generating an electric signal. If the ions generated are just detected, the detector is known as ionization chamber and were some of the first detectors used in history. If the potential applied in the detector is higher, the electrons produced in the ionization are accelerated enough to produce secondary ionizations, magnifying the signal and being able to detect lower radiation levels than ionization chambers. For some gaseous detectors, known as proportional counters, the amplitude of the signal detected is proportional to the energy of the incident particle, however, for applied voltages higher than certain value, the avalanche generated by each particle is such that the signal is not proportional anymore to the energy of the incident particle. This is known as Geiger-Mueller region, and the counters that use that potential region are known as Geiger-Mueller or just Geiger counters. [Knoll, 2010] [Cal González, 2015] [Vicente Torrico, 2013]
- **Solid-state detectors:** they consist on a semi-conductor material, generally silicon based detectors or germanium based detectors. The internal structure of semi-

conductor materials make them ideal to detect radiations very precisely. They have an energy band structure, in which the electrons can populate two main bands, valence and conduction bands. Between them, there is a gap of forbidden energies which is small enough to be skipped by electrons when a relatively small perturbation (as a ionizing particle) gives energy to the material. The amount of electrons that reach the conduction band, and thus, the amplitude of the electric signal generated, is directly proportional to the energy given by the incident particle [Knoll, 2010]. This kind of detectors have in general very good energy resolution but poor efficiencies for PET purposes. Furthermore they use to be expensive so they are not used for PET scanners, although they are very useful for other purposes.

- **Scintillation detectors:** the main principle of these detectors is the production of light inside scintillating materials when a ionizing particle deposits its energy on them. When this happens, the detector is excited, and then, during the desexcitation, it emits photons in the range of visible light approximately. The wavelength of the emitted light depends on the scintillating material. After the emission, the light is driven using reflection properties until it reaches a photodetector, where this light signal is converted into a measurable electric signal [Knoll, 2010] [Cal González, 2015] [Vicente Torrico, 2013]. Thus, a scintillation detector is composed of least two different components:
    - **Scintillation crystal:** Depending of the material used, it is common to classify scintillation detectors into organic and inorganic detectors. Organic scintillators are based into transitions in the energy levels of a single molecule, they can be either solid, liquid or even gaseous since the transitions do not rely on the state of the material [Knoll, 2010]. Inorganic scintillators, however, base their light emission properties in the crystalline lattice of the material [Knoll, 2010], thus, they are solid and forming ionic crystals. In general, inorganic scintillators are more sensitive that organic detectors, and thus, they are usually preferred in PET. Some common materials used as inorganic scintillators in PET are NaI (Sodium Iodide), BGO (Bismuth Germanate), LSO (Lutetium Oxyorthosilicate), LYSO (Lutetium-Ytrium Oxyorthosilicate), GSO (Gadolinium Orthosilicate) or LuAP (Lutetium Aluminium Perovskite) [Cal González, 2015] [Knoll, 2010].

      One of the main important properties of a scintillation crystal for PET is their stopping power, which determines the probability of detecting a particle that reaches the detector, for greater effective atomic number (Z_{eff}) and material density it is more likely that an incident particle leaves its energy inside the crystal per unit of volume [Knoll, 2010].

      Another important property for scintillators is their time resolution, given mainly by their decay time, defined as the time needed to reduce the light intensity emitted by the crystal a factor e from its maximum [Knoll, 2010].

Crystal	**d(g/cm^3)**	**Z$_{eff}$**	**t$_{decay}$(ns)**	**Light(γ/MeV)**	**Ref.Index**	**λ_{max}(nm)**
NaI	6.7	51	230	38000	1.85	415
BGO	7.1	74	300	8200	2.15	480
LSO	7.4	66	47	25000	1.82	420
LYSO	5.37	54	53	30000	1.81	420
GSO	6.7	59	56(90%)/400	9000	1.85	440
LuAP	8.3	65	17	17000	1.94	365

Table 1: Most important properties of some of the most commonly used scintillation inogranic crystals in PET [Vicente Torrico, 2013] [Cal González, 2015] [Knoll, 2010] [Pepin et al., 2004] [Petrosyan et al., 2003]

There are two contributions to the time response of a scintillation detector, their activation time, which is usually fast (few ns or less) and a decay time ($ns - \mu s$) which is much slower and determines the time resolution of the crystal [Knoll, 2010].

Regarding other interesting properties of these detectors, the light production yield determines the amount of light that a scintillator emits per unit of energy deposited by the ionizing particle on it. The refractive index of the crystal determines how easily the light emitted is transported until the photodetector. For smaller refractive index, the transport is easier [Knoll, 2010].

The wavelength of the emitted light may be an important factor to avoid the self-absorption of the emitted light. It is also remarkable that some crystals based mainly on lutetium (LSO, LYSO, LuAP) involve an intrinsic emission due to lutetium activity that can generate a background in PET images [Cal González, 2015].

An ideal scintillation detector for PET would have a high electron density (effective atomic number), a short decay time, a good light yield production and a small refractive index. In table 1 we show the properties for some of the most important inorganic crystals used in PET.

- **Photodetector:** it converts the light emitted by the scintillator into a measurable electric signal. Historically, the most common used photodetector was the Photomultiplier Tube (PMT), but currently they are being replaced by other devices, based on semi-conductors such as Avalanche Photo-Diodes (APD).

  Usually, PMTs consist on a vacuum enclosure, in which, due to photoelectric effect, the incident photons are absorbed in a photocathode, and as a result, electrons are emitted into the inside of the PMT. Then, these electrons are accelerated due to an internal electric field produced by several dynodes connected each one to a higher voltage than the previous dynode. When the electrons get to each dynode, they produce secondary electron emissions, getting more electrons in each dynode. Finally, the electrons get to the anode, where the signal is gathered to be processed. A schematic representation of a scintillator crystal coupled to a PMT and its main funcioning is shown in figure 21. The gain of the PMT is the relationship between the total number of electrons gathered in the anode and the number of electrons produced in the photocathode. Typical gains for PMTs are between 10^5 and 10^8 [Knoll, 2010] [Cal González, 2015] [Vicente Torrico, 2013]. PMTs are usually too big comparing to the crystal size in a PET scanner, and one single photomultiplier gets the signal of several crystals. Thus they need to be adapted, using an array of independent anodes to determine the position of the PMT where the light interacted with it, these adapted PMTs are known as Position-Sensitive Photomultipliers (PS-PMT) [Anger, 1969] [Cal González, 2015] [Vicente Torrico, 2013].

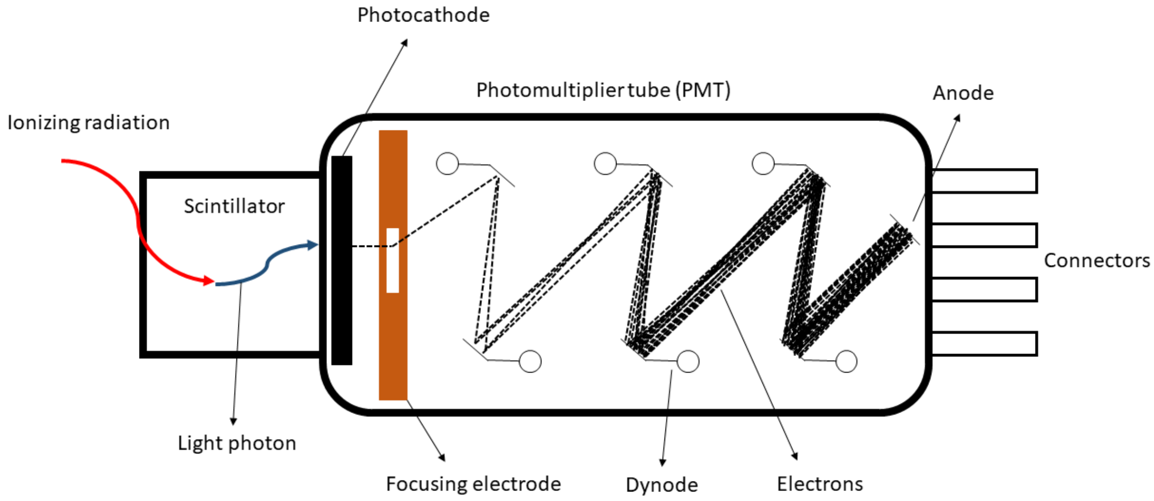

Figure 21: Schematic representation of the operation of a scintillator crystal coupled to a photomultiplier tube (PMT)

Some of the disadvantages of PMTs in PET scanners are that they are sensitive to magnetic field, being not suitable for combining PET with magnetic resonance (PET-MR). Also, their big size, much bigger than the crystals used in PET is a disadvantage.

PMTs are currently being replaced in PET by other photodetectors based on semiconductors which presents some interesting properties for PET, specially their small size comparing to PMTs and the fact that they can be used in presence of magnetic fields [Knoll, 2010] [Vicente Torrico, 2013] [Cal González, 2015]. The most commonly used photodector based on semiconductors for PET are silicon photomultipliers (SiPM), composed of an array of avalanche photodetectors (APDs) working on Geiger mode [Knoll, 2010]. An APD is a device that can produce an electric signal from an optical photon. The process is based on the creation of electron-hole pairs into the semiconductor material in a similar way to solid state detectors with the difference that in this case the energy of the photons is much lower. When the optical photon coming from the scintillator gets the APD, it may deposit its energy into it, making that one of the electrons of the valence band of the semiconductor jumps into the conduction band, leaving a hole into the valence band, both the electron and the hole are considered as charge carriers. In the case of APDs, a voltage is applied such that it accelerates the resulting electrons enough to produce secondary electron-hole pairs. For higher applied voltages, we find an effect similar to the gas-filled detectors working in the Geiger-Mueller region, producing an avalanche of electrons that is not anymore proportional to the applied voltage. At this point, a huge number of electrons can be produced from a small initial signal. SiPMs are arrays of small APDs working on the Geiger mode [Knoll, 2010].

1.4.3 Evolution and state of the art of PET scanners

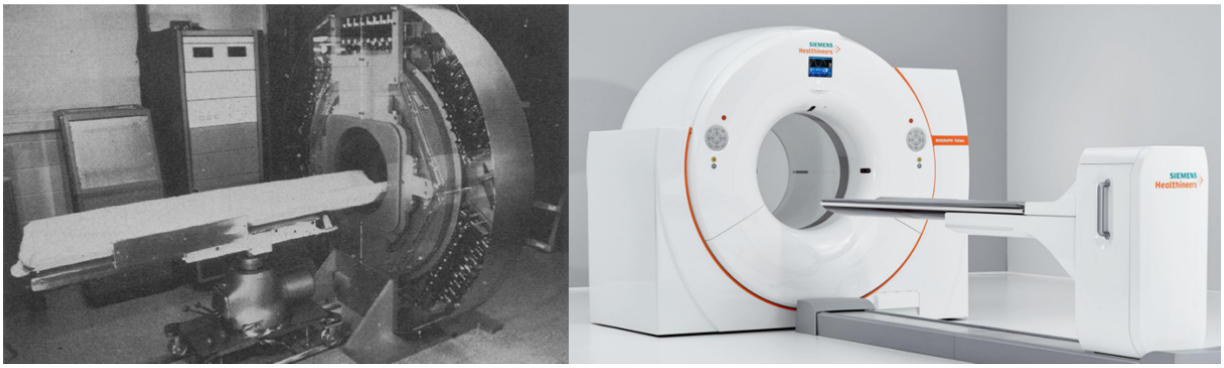

Figure 22: (Left) Photograph of PET III, first human scanner [Phelps et al., 1976]. (Right) Photograph of Biograph Vision PET/CT scanner [Siemens, 2019b]

Since the origins of PET in the initial years of the decade of the 1970's, PET scanners have constantly evolved, improving the resolution and quality of PET images and also the sensitivity of the scanners. The first scanner that was successfully used for PET was named PET II, developed in 1973 by Phelps et al. [Phelps, 2002]. It consisted on a circumference of NaI detectors and was used for small animals and phantoms [Phelps, 2002]. The first human PET scanner was PET III (see figure 22), developed some years later, in 1975 [Phelps et al., 1976]. Initially, NaI crystals were preferred and PMTs were used in the scanner designs and they consisted on a single ring of detectors. With the development of new materials and technologies, PET scanners grew, covering a larger field of view (FOV), specially a larger axial FOV (FOV_z) including several rings of detector instead of only one. Also, other scintillators as BGO and later lutetium based scintillators as LSO or LYSO replaced NaI crystals, improving considerably the sensitivity and efficiency of the scanners. Also scintillation crystals progressed to smaller sizes, making possible to improve the spatial resolution of the scanners from the 10-20mm of the first PET scanner to the 1mm spatial resolution of current preclinical PET scanners [Goertzen et al., 2012]. In table 2 we show some of the most commonly used PET scanners from 1972 to 2020 and some of their features.

Name	Year	#crys	Mat.	diam.	FOV_z	Use	res.	ε
PET II	1972	24×1	NaI	5	2.5	Precl.	25	2
PET III	1975	48×1	NaI	50-100	5	Clin.	12	3.25
ECAT	1978	66×1	NaI	100	3.8	Clin.	9.12	–
ECAT III	1983	512×1	BGO	100-400	3	Clin.	4	–
931-08/12	1987	512×4	BGO	102	10.8	Clin.	5.5/5.9	–
MicroPET	1997	240×8	LSO	17.2	1.8	Precl.	2.3/2.2	-
ECAT EXACT HR+	1997	576×32	BGO	82.7	15.5	Clin.	4.5/4.1	3.8
Biograph TPTV	2007	624×52	LSO	80	21.6	Clin.	4.1/4.7	8.1
INVEON	2009	320×80	LSO	16.1	12.7	Precl.	1.46/1.15	24.3
Argus	2009	$234 \times 26 \times 2$	LYSO/ GSO	11.8	4.8	Precl.	1.5	3.5
LabPET 12	2009	$192 \times 48 \times 12$	LYSO/ LGSO	16.2	11.25	Precl.	1.65	7
Biograph mMR	2011	448×64	LSO	65.6	25.8	Clin.	4/4.1	13.3
Biograph mCT	2015	624×52	LSO	84.6	22.5	Clin.	4.4/4.4	10.0
SuperArgus 6R	2018	$312 \times 78 \times 2$	LYSO/ GSO	18	15	Precl.	1.2/1.8	25.0
Molecubes β-Cube	2018	$9 \times 5 \times 5$	LYSO (monolyth)	7.6	13	Precl.	1.06/1.1	7.5
Biograph VISION	2020	760×80	LSO	82	26.1	Clin.	3.6/3.5	16.4

Table 2: Some features of different PET scanners through the years. Name of the scanner, year of publication/commercialization, total number of crystals (transaxial × axial), material of the scintillators, total diameter of the scanner (cm), axial field of view of the scanner (cm), main use (preclinical/clinical), spatial resolution (mm) transaxial/axial, total efficiency of the scanner kcps/MBq. These data have been collected from different publications of the performance for the different scanners and repositories. [Goertzen et al., 2012] [Constantinescu and Mukherjee, 2009] [Jakoby et al., 2007] [Adam et al., 1997] [Chatziioannou et al., 1999] [Spinks et al., 1988] [Hoffman et al., 1982] [Phelps et al., 1976] [Phelps et al., 1976] [Udias et al., 2018] [Krishnamoorthy et al., 2018] [Vicente Torrico, 2013] [Cal González, 2015]

Currently, new scanners for humans are focused in larger axial field of view, improving sensitivity and being able to acquire full body scans in a single acquisition. This may improve image quality and contributes to reduce the time that the patient need to stay in the scanner [Cherry et al., 2018] [Badawi et al., 2019].

In the field of preclinical scanners, the technology used is usually on the cutting-edge PET techniques since animals as mice are much smaller than humans and thus, the resolution needed to make useful studies in animals is much higher than for humans. Nowadays, new materials and techniques to improve PET images have been developed as the inclusion of monolythic crystals instead of separated crystals in the detector [Krishnamoorthy et al., 2018] or the use of several crystal layers to improve the determination of the depth of interaction of the particles in the scanner [Udias et al., 2018].

1.5 PET acquisitions

1.5.1 Data gathering in PET

There are different ways of gathering the information of the detected events on a PET scanner. Depending on the purpose or the information needed, some of these ways are preferred. Here, we describe the most commonly used.

- List mode files:

  This mode is the most complete way of gathering the data collected by a PET scanner [Fahey, 2002] [Cal González, 2015]. Almost every modern PET scanner includes a list mode acquisition mode. It usually includes detailed information including the position of the detection (coordinates of the crystal which detects the photon), time of detection (or a time stamp to order events), sometimes the energy of each event, time of flight information, etc. It is important to notice that the format and the information included in the list mode file depends on the manufacturer of the scanner, finding huge differences between scanners. This is inconvenient since for each scanner, the user may need a different software to read the data in this mode. Depending on the way of gathering events in the list mode file, we can talk about list of singles or list of coincidences.

  - List of singles: a single event is each one of the events that get the scanner. They can be gathered independently of the rest of events in a singles list mode. It is the most detailed way of gathering events in PET but it is also computationally expensive.
  - List of coincidences: if, after one event detected in the scanner, other detection occurs in a different crystal of the scanner in a short period of time (typically some ns), we can say that both events are detected in the same time window and that they conform a coincidence. PET imaging is based on the detection in coincidence of the two photons emitted in the annihilation of a positron. For that reason it is frequent to gather the events paired in coincidences instead of in single mode, this can be useful since it takes up less disk space than single mode.

- Histogram of LORs (or HistoLOR):

  In a PET acquisition, each coincidence can be assigned to the imaginary line connecting both detectors involved in the coincidence, which is known as Line Of Response or just LOR. Thus, one common way of gathering the coincidences is with a histogram of LORs, which includes the information of the number of coincidences coming from each LOR. Although it is not as detailed as list mode where you can get more information of each coincidence, it is a compact way to organize the information and it is a very useful tool for image reconstruction algorithms. In the case of histograms of LORs, a single program dedicated to this format, could interpret and reconstruct data from different scanners, with the only requirement of specifying the position of each one of the crystals involved in each LOR. This make this method, sometimes, more suitable than list mode acquisition.

- Sinograms:

  Sinograms are a very common way to gather data in some modalities of tomographic medical imaging, as Positron Emission Tomography (PET) or Computed Tomography (CT). They are just a special way of histograming the data.

  In PET, a sinogram, is a type of histogram in which each LOR is characterized with some parameters, some of them concerning to the transaxial coordinates of the LOR and others concerning to the axial components [Defrise and Kinahan, 1998]. It is very useful since in a sinogram, data can be shown in a very visual representation where we can see the projections over different directions of the data. Moreover, this format is especially important when the reconstruction algorithm is based on Radon transforms, which indeed, use these projections to achieve the final image.

  The transaxial parameters are the orthogonal distance from the LOR to the center of the scanner, ρ, which represents the radial coordinate of the sinogram, and the angle between the LOR and a reference axis of the system of coordinates (in general the one considered as x axis in the system of reference of the scanner), this is known as the angular coordinate of the sinogram and usually represented by θ. The name of sinogram, comes from the aspect of representing these histograms considering the ρ and θ coordinates, looking like a sine function (see figure 23).

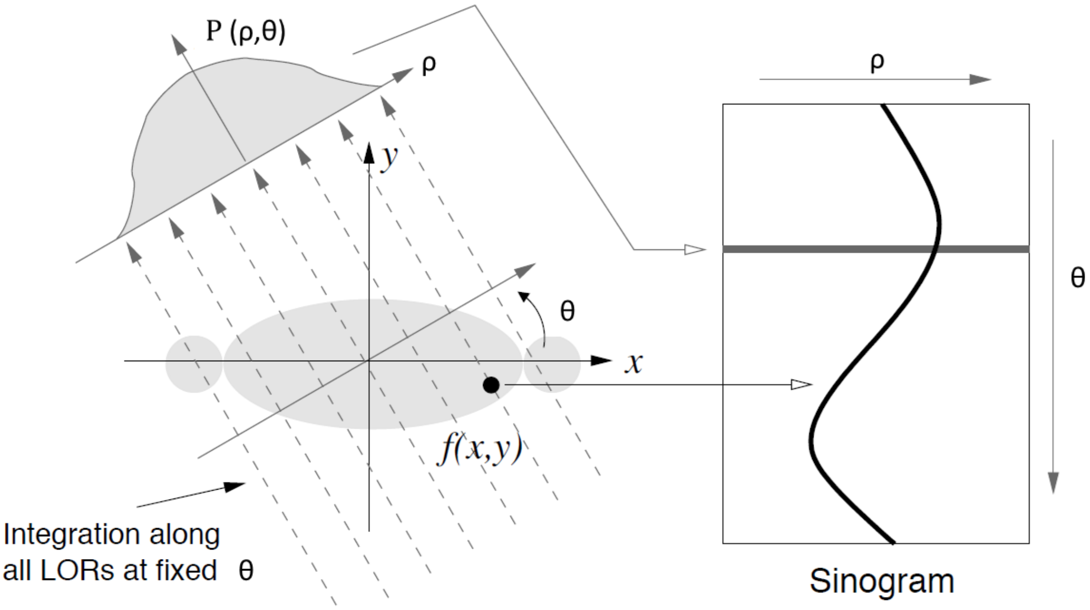

Figure 23: Schematic representation of a sinogram from [Alessio et al., 2006a]

The axial parameters of the LOR can be given by the axial coordinates of the crystals involved in the coincidence z_1, z_2. Another frequent notation uses the mean height of the LOR, in other words, the average axial point between z_1 and z_2, here represented by z_m and the axial slope of the LOR ($z_2 - z_1$), represented by Δ (can be positive when $z_2 > z_1$ or negative else-wise). We will say that every LOR with the same Δ parameter constitute a segment, each LOR of the segment with z_m coordinate is known as a slice of the segment. Usually the user can limit the maximum slope of the LOR dismissing the coincidences coming from LORs which Δ coordinate is higher than certain threshold known as **Maximum Ring Difference (MRD)**. Of course, this reduces the statistics of the acquisition but can be very useful to avoid axial blurring when using certain reconstruction algorithms or to reduce the size of the data. Furthermore, it is very common when working with sinograms to mash up some LORs with the same transaxial coordinates and slightly different axial coordinates into one common slice of a segment. This contributes to reduce significantly the size of the data while hardly affecting the quality of the images when the mashed up is not too sharp. The **span** parameter determines the number of different slices that would be mashed into the same. It should be an odd number and greater than 1. Span equal to 1 would mean not mash up at all and, in general, is not recommended. Sinogram slices with $\Delta = 0$ or mashed into a slice with $\Delta = 0$ will be referred as direct sinograms while the rest will be referred as oblique sinograms.

Sinograms are the most common format used by reconstruction algorithm due to their simplicity and connection with the projections of the image into different views (angles).

1.5.2 Axial rebinning

Axial rebinning is very useful as it reduces a sinogram with different segments (i.e. inclinations) to a set of direct slices that can be reconstructed separately using 2D image reconstruction algorithms, much faster and easier to implement than fully 3D algorithms. [Liu et al., 1999] [Brahme, 2014] [Alessio et al., 2006b]

One simple way of performing axial rebinning is assigning each oblique sinogram to the direct sinogram with the same z_m coordinate. This is one of the simplest techniques of axial rebinning known as **Single Slice Rebinning (SSRB)** [Daube-Witherspoon and Muehllehner, 1987]. This is essentially the same case of using a span factor $span = 2 \cdot MRD + 1$. SSRB present some important inaccuracies that should be considered, especially when the activity is located far from the center of the scanner. There are other techniques for axial rebinning more accurate than SSRB such as **Fourier Rebinning (FORE)** [Defrise et al., 1997] [Liu et al., 1999], based on the Fourier Transform of the sinogram. In the Fourier domain, the planar distance t of a point to the center of the scanner, can be estimated from the angular and radial frequencies of the sinogram ($t = \frac{\omega_\theta}{\omega_\rho}$), and considering also the medium height and the slope of the slice, the axial emission point associated to the oblique sinogram can be achieved:

$$z_{new} = z_m + t \cdot \Delta \tag{14}$$

Then, the direct sinogram with the same z coordinate as z_{new} is updated with the information of the corresponding oblique sinograms.

Other alternatives for axial rebinning are iterative or **pseudoinverse rebinning**. Pseudoinverse rebinning is one of the main contributions presented in this thesis [Lopez-Montes et al., 2017] [López-Montes et al., 2019] [López-Montes et al., 2020], while iterative rebinning is also presented as a slower but sometimes more accurate alternative.

However, if good quality images are required, in general it is recommended to select a moderate parameter for the span factor and use 3D iterative reconstruction algorithms. Currently, axial rebinning is only used if fast reconstructed images are needed but historically it has an important repercussion since most of the first reconstruction methods were limited to 2D acquisitions and axial rebinning allows to reduce a 3D PET acquisition to a set of 2D direct sinograms that can be regarded and reconstructed as independent 2D acquisitions.

1.6 Types of event in PET acquisitions

1.6.1 True events. Prompt and random coincidences

As we described in previous sections, each positron annihilation, produces mainly two photons emitted in opposite directions. If these two photons are detected in coincidence in the scanner, we can talk about true coincidences, since both photons came from the same annihilation and thus from the same point of the image. But not all the coincidences acquired in the scanner come from true events. When the first photon reaches the scanner, then a time window is opened and if another photon gets the scanner during the time that this window is still open, a coincidence is generated. However, it may happen that the second photon comes from a different annihilation. This is known as random coincidence and results into a background of **random coincidences** introduced to the image, reducing the image quality (see figure 24). The number of random coincidences detected in an acquisition, depends mainly on the scanner features and on the activity in the object. For higher activity, the amount of random coincidences grows since the probability that two non-related annihilation photons are detected in coincidence is higher [Brasse et al., 2005]. In a PET acquisition, we do not know if an acquired coincidence is a true or a random coincidence. Therefore, to denote these events, we use the term **prompt coincidences** and includes both true and random coincidences.

In order to estimate the amount and the distribution of the random events, it is common the use of delayed time widows. That is, besides the normal time window opened when the first photon arrive the scanner, an additional time window is opened, but some time after the first coincidence get the scanner (depends on the scanner configuration but typically some μs or ms after the first coincidence). Every coincidence detected in the delayed window with the first photon will be a random coincidence since there will not be any correlation between the two photons. In general, random coincidences are more or less uniformly distributed and smooth. Once they are estimated they can be subtracted to prompt coincidences to obtain true coincidences.

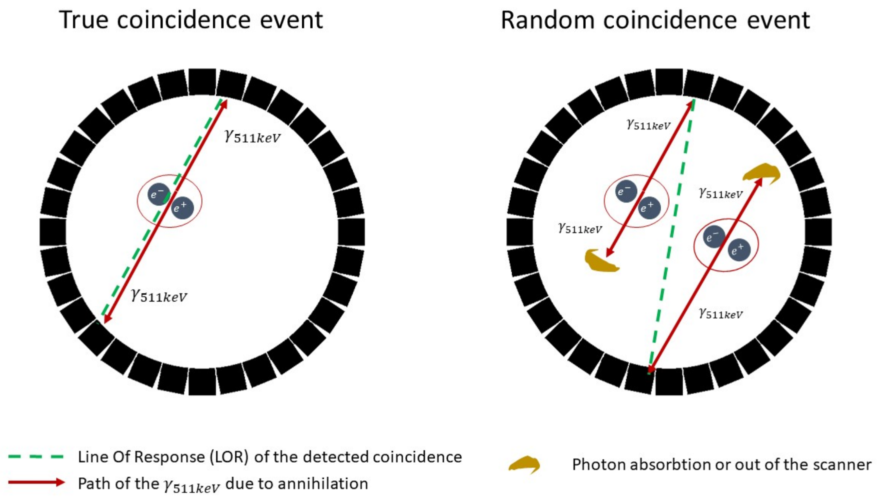

Figure 24: Schematic representation of true and random coincidences

1.6.2 Triple and multiple coincidences.

Some radionuclides used in PET, may emit additional gamma rays after the positron emission. If these gamma rays are emitted a few picoseconds after the positron, we refer to them as prompt gamma rays as they can be detected in coincidence in the scanner with the photons resulting from the annihilation of the positron. When, in the same time window, more than two different photons are detected, we talk about multiple coincidences. In the particular case of three different photons, it is considered as a triple coincidence. Multiple coincidences are generally neglected and they are not used in the reconstruction of the PET images. They are considered to introduce a background of spurious coincidences due to the coincidences gathered between one of the photons of the annihilation and one of the additional gamma rays [Cal-González et al., 2013] [Lage et al., 2015].

As we saw in standard double PET coincidences, also random coincidences are detected in triple coincidences. One or even both coincidences of a triple event can be produced as a result of a random detection of non-correlated photons (see figure 25). These triple random coincidences can be also estimated using delayed time windows as we did with double coincidences.

Standard PET nuclides, do not emit additional gamma rays, however, triple coincidences can still be found. All of them are random triple coincidences since not all the LORs gathered in that coincidence window can result from the same decay [Lage et al., 2015] .

It should be noticed that, as in the case of true and random coincidences, during the PET acquisition, when a triple coincidence is gathered, we do not know if it is a true or a random triple coincidence. We can talk about prompt triple coincidences. Delayed time

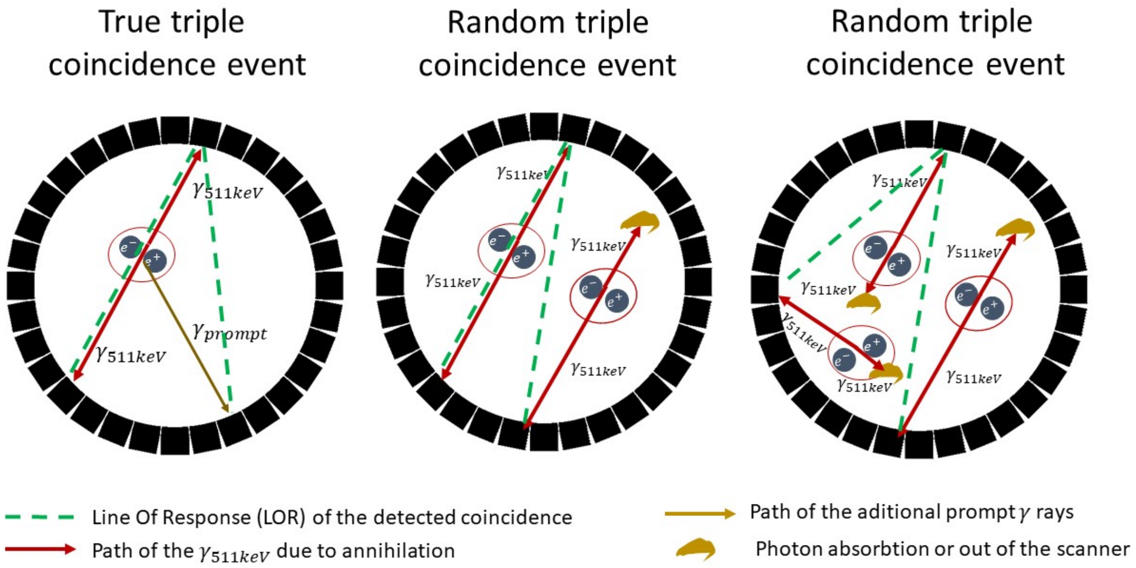

Figure 25: Schematic representation of true and random triple coincidences

windows can be used to estimate the amount and distribution of random triple coincidences as we did in random coincidences.

In multiple coincidences, we may differentiate as we do with triple coincidences between true multiple coincidences and random multiple coincidences.

1.7 Data correction and uncertainties in PET.

In a PET acquisition, there are different sources of uncertainties affecting the image quality. Some of the most relevant effects considered in data correction are detailed in this section.

1.7.1 Positron range (PR)

Positron range (PR) is one of the main limiting factors in current PET imaging [Cal González, 2015] [Carter et al., 2020] [Herraiz et al., 2021], specially in PET dedicated to small animals where an additional blurring of a few millimeters can be crucial. As we indicated in previous sections, this effect is a consequence of the emission energy of the positron and their path until the annihilation. It depends also on the density of the surrounding medium, with less positron range effect in high density mediums. This effect is particularly important for certain radionuclides such as ^{68}Ga, ^{76}Br, ^{82}Rb, ^{86}Y or ^{124}I where the initial energy of the positrons is very high. As an example, we present in figure 26 a simulation the annihilation points of two point sources, one with ^{18}F (short PR) and other with ^{68}Ga (large PR) in two different tissues, lung with low density and water with higher density than lung. Also, in figure 27, we can appreciate the effect of PR into a PET image of a simulated mouse, the blurring introduced in the images by large PR emitters can be clearly appreciated.

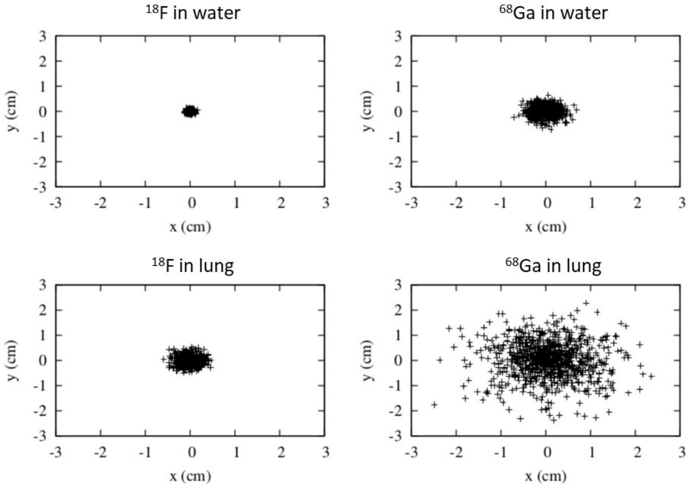

Figure 26: Annihilation points produced by a point source of ^{18}F and ^{68}Ga in different tissues. It can be clearly appreciated a higher dispersion if the case of low density materials as lung and for nuclides as ^{68}Ga where the initial energy of the positrons is much higher than for ^{18}F.

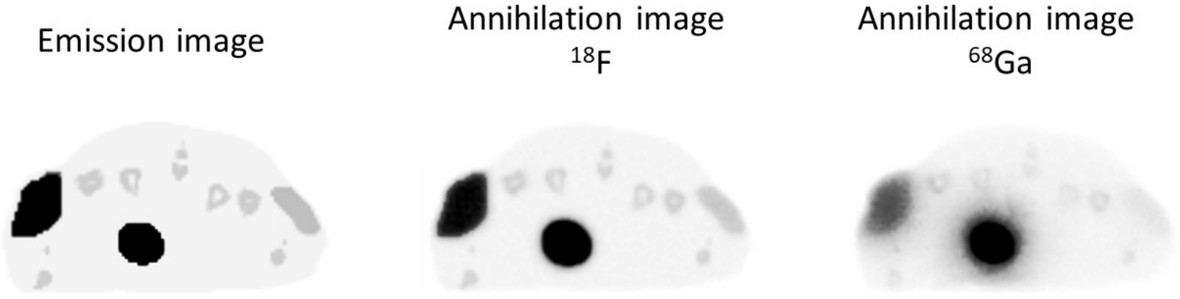

Figure 27: Blurring introduced in the image due to PR effect for some radionuclides.

Positron range can be corrected in several ways. There are methods which simply consider the blurring produced by positron range effects modeling it with convolution kernels and trying to achieve the original resolution using deconvolution. In general these methods are fast but they usually increase noise in the image which supposes an important disadvantage. Other more accurate methods, include the effect of the PR during the reconstruction workflow. These methods use to be slow and need to be adapted for every distribution of the object, since the PR depends mainly on the object where the emission of the positron takes place. In this thesis, a new method will be discussed which is based on neural networks and can provide a fast and accurate way of correcting PR effects [Herraiz et al., 2021] [Cal González, 2015]. The modelling of the PR can be also consider just the radionuclide and not the emission medium which can be enough for some purposes but may lead to important inaccuracies when correcting some PR effects. Therefore, it is useful to model the PR considering properly the medium and the inhomogeneities inside it.

1.7.2 Non-collinearity

When one of the particles in the annihilation conserve part of its linear moment at the instant of the annihilation, we can observe that the angular difference between the emitted photons may differ from 180º up to 5º [Cherry and Dahlbom, 2006] [DeBenedetti et al., 1950] [Shibuya et al., 2007] (see figure 28). This effect has important consequences in a PET acquisition since it can cause an incorrect assignment of the LOR to the actual path of the photons. It can be reduced limiting the radius of the scanner and, thus, despite not being very critical in the case of small scanners dedicated to animals, the effect can be considerable when using scanners with great radius [Bolwin et al., 2017]. It can be considered during the reconstruction assuming and modeling the effect by adapting the LORs to include the possibility of non-collinearity in the annihilation.

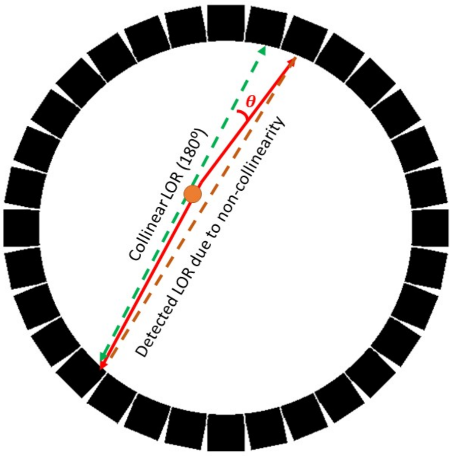

Figure 28: Schematic representation for non-collinearity in a positron annihilation with an angle θ differing from 180 degrees difference

1.7.3 Attenuation

Photons coming from the annihilation process, may suffer absorption or scattering processes during their path to the detector, resulting in loss of coincidences. If a photoelectric effect takes place, one of the photons can be absorbed by the medium, never reaching the detector and losing a true coincidence as consequence. Similar effects can occur if the photon suffers a Compton scattering with one of the electrons of the medium and its deviation is such that it never gets to one of the detectors of the scanner [Krane et al., 1987]. All these effects can be considered together as attenuation effect. We can define the probability of losing a photon in each cm of the path as the linear attenuation coefficient ($\mu[cm^{-1}]$) [Kinahan et al., 1998]. If we denote the number of detected photons in a certain direction (x) as N and the number of photons that would be detected in the same direction in absence of attenuation as N_0, they can be related as:

$$N = \int N_0 \cdot e^{-\mu(x) \cdot x} dx \tag{15}$$

In general the linear attenuation coefficient is a function of the energy of the photon and the density of the medium which determines the probability for a photon to be absorbed or deflected in a medium. Regarding the energy of the photon, for PET purposes it is assumed that we are going to detect 511 keV photons resulting from the annihilation, so for attenuation correction, linear attenuation coefficients are selected for that energy. As, in most cases, PET images are combined with other modalities as CT [Burger et al., 2002] or MR [Wagenknecht et al., 2013], the information of the density of the material, and thus, the linear attenuation, in the object to study can be approximately known. It is common to use a μ-map and use its projection into the data space to correct the attenuation in the data. More recently, some works are proposing the use of neural networks to correct attenuation in PET images without the need of the corresponding CT or MR images [Liu et al., 2018].

1.7.4 Scatter

This effect is particularly important in PET since it can introduce a non-uniform background in the images that can affect the image quality and quantification, making that part of the activity in hot regions is displaced to cold regions [Watson et al., 1996]. This is produced when one (or both) photon of the annihilation, suffers a Compton scattering and it changes its path, being finally detected in a crystal different to the expected one. This is represented in a simplified way in figure 29. The energy of the resulting photon is given by equation 12, thus, the effect of scattering can be reduced using narrower energy windows to avoid the inclusion of scattered events at the cost of losing statistic as less coincidences (non scattered true coincidences between them) are detected. However due to the limited energy resolution of PET scanners, even with narrow energy windows the effect of scattering is still important, specially in the case of big scanners where the effect is much more notable. It is common to talk in terms of scatter fraction to determine the percentage of scattered events over true coincidences. Scattering has an important dependence on the object being particularly important in the case of high density tissues such as bone.

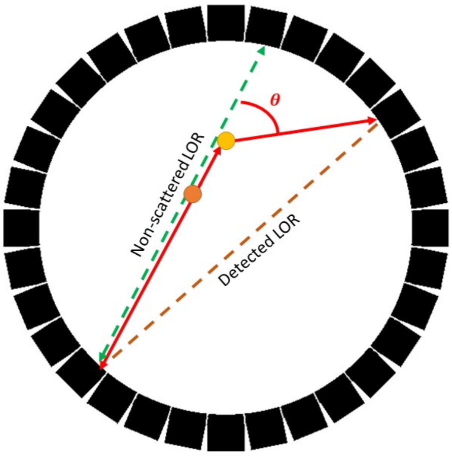

Figure 29: Schematic representation for scattering in PET images. The photons can be deflected a certain angle θ resulting into the assignation of the coincidence to a different LOR.

In some cases, the scatter fraction can get the 30% or event the 50% of true coincidences [Watson et al., 1996], so its correction can be critical to achieve good quality images and a correct quantification in PET. Many authors [Watson et al., 1996] [Castiglioni et al., 1999] [Zaidi and Montandon, 2007], agree with the opinion that the most correct way of correcting scatter is using detailed models of particle transportation (usually Monte Carlo simulators) to estimate this effect. However, until very recently, this models used to be very slow and computationally expensive and most times were not suitable for reconstruction workflows. Thus, some analytical methods that are still being used were developed. The most used one is known as Single Scatter Simulation (SSS) [Watson et al., 1996], which, using the attenuation map, simulates a stack of scattering points and simulates the scattering effect given by them. Although this method is very useful and broadly used for PET imaging, it presents some important inaccuracies. In recent years, many works are proposing the use of deep learning techniques for scatter correction which can be fast and accurate [Qian et al., 2017] [Berker et al., 2018]. Also, the inclusion of acceleration techniques as the use of graphics processor units (GPUs), has made possible that techniques based on Monte Carlo simulations to be fast enough to be considered as a good alternative to SSS. One of the sections of this thesis is focused on a new Monte Carlo simulator based on GPU able to correct scatter and other effects fast and accurately.

1.7.5 Spurious background due to additional prompt gamma rays

When using radionuclides emitting prompt gamma rays together with the positrons in the beta decay, some coincidences can be produced by one of the photons of annihilation and the additional gamma ray which was emitted in a random direction with no correlation with the γ rays of the annihilation process (see figure 30). This may result in the inclusion of a background of spurious coincidences that affects the quality of the images [Cal-González et al., 2013] [Andreyev et al., 2014] [Sitek et al., 2011] [Conti and Eriksson, 2016].

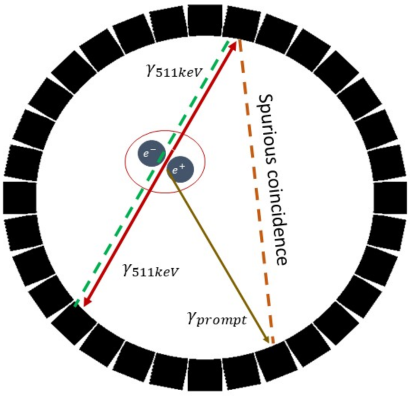

Figure 30: Schematic representation for the spurious coincidences detected due to additional prompt gamma rays.

There are many methods proposed to correct this effect [Herraiz et al., 2014a] [Beattie et al., 2003] [Watson et al., 2008].This background may be also corrected by simulating the spurious coincidences produced when the direction of emission of one of the photons is randomly distributed. The MC-GPU simulator proposed in this thesis can simulate this background coincidences and further correct them.

1.7.6 Normalization

PET data acquired in real scanners have not an ideal sampling since not all the crystals in the scanner present exactly the same behaviour or sometimes some of them do not work properly. This results in inhomogeneities between the detection rates that do not rely on the emission and annihilation process but on the efficiency or properly work of the detectors. Also, geometrical factors as the limited axial FOV that makes that the detectors in the center of the axial FOV gather much more coincidences than those in the edges may affect the normalization. In order to avoid artifacts in the images caused by these factors, in almost every PET acquisition, a normalization of the data is required. To do so, many authors propose the use of an acquisition with known activity and distribution that should be homogeneous in every detector. Typically, a small cylinder or an annulus (an empty cylinder with the activity uniformly distributed in the external ring) centered on the FOV of the scanner is used. Then, the total number of coincidences in each crystal is gathered, and, assuming that it should be the same for each one of them, the normalization factors are achieved and then applied to the rest of acquired data [Bai et al., 2002] [Badawi and

Marsden, 1999] [Defrise et al., 1991].

Another component usually considered in the normalization factors is the normalization of the activity, since due to nuclear decay and the scanner efficiency, not all the activity injected in the body is gathered by the scanner. Thus, it is very frequent to include a normalization factor to the measured activity to match the injected one [Defrise et al., 1991]. Moreover, during the acquisition, the radionuclides are constantly decaying, being the activity reduced, specially for short half-lives radionuclides. Thus, a correction decay factor should be also included in the workflow. This factor can be obtained from the nuclear decay during the acquisition time ($T = t_f - t_0$). Being $N(T)$ the number of nuclear decays during the acquisition time (5):

$$N(T) = \int_{t_0}^{t_f} A_0 \cdot e^{-\lambda t} \cdot dt = \frac{A_0}{\lambda} \cdot (e^{-\lambda t_0} - e^{-\lambda t_f}) = \frac{A_0}{\lambda} \cdot e^{-\lambda t_0}(1 - e^{-\lambda T}) \tag{16}$$

If the activity were assumed as constant ($\bar{A}$) during the acquisition time, the expected number of decays during this time would be:

$$N(T) = \int_{t_0}^{t_f} \bar{A} \cdot dt = \bar{A} \cdot T \tag{17}$$

And, thus, the measured activity could be calculated as $\bar{A} = \frac{N}{T}$. However, since during this time, the activity is not constant due to nuclear decay rule, a decay correction factor (D_f) should be added to match the real measured activity:

$$A_0 = \frac{\lambda \cdot N(T)}{e^{-\lambda t_0}(1 - e^{-\lambda T})} = \bar{A} \cdot \frac{\lambda \cdot T}{e^{-\lambda t_0}(1 - e^{-\lambda T})} = \bar{A} \cdot D_f \tag{18}$$

1.7.7 Depth of interaction (DOI)

In general, the Depth Of Interaction (DOI) in the crystals cannot be determined. The ionizing particles can travel through the detector crystal until they leave their energy inside it, although commonly, every event detected in a single crystal is assigned to the same point. This may produce an incorrect consideration of the path of the photons when assigning the coordinates of the LORs (see figure 31). To correct this effect, many scanners, specially in the preclinical field, use several layers of detectors in which is called a phoswhich system. Each layer is made of different scintillator composition with different properties in order to be able to determine whether the coincidence took place in one layer of scintillator crystals or in other [Udias et al., 2018] [Ito et al., 2011] [Miyaoka et al., 1998] [Tsuda et al., 2004]. Other works propose methods to correct the DOI based on simulations [Galve, 2016] or on deep learning techniques [Sanaat and Zaidi, 2020].

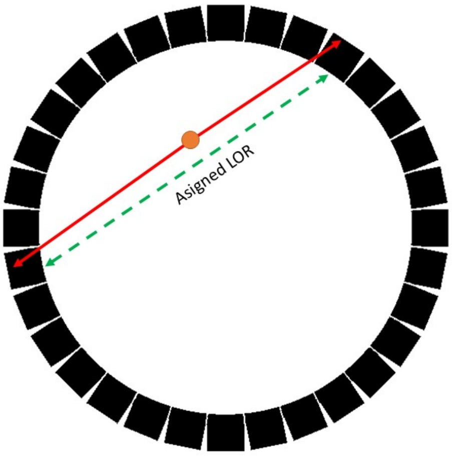

Figure 31: Schematic representation for the depth of interaction in a PET scanner.

1.7.8 Intrinsic activity of lutetium

Currently, lutetium based detectors (LSO, LYSO and LuAP mainly) are preferred to other materials due to their good properties for PET (high efficiency and light production and low decay time) [Conti et al., 2017] [Wei, 2015]. However, approximately 2.6% of natural lutetium is ^{176}Lu, which decays β^- to stable ^{176}Hf emitting a cascade of γ particles that can be detected by the scanner itself, resulting into a background of self-coincidences that may affect the image quality [Conti et al., 2017] [Wei, 2015]. Some simulators may include this effect, being able to consider it into the reconstruction process and correcting it [Lopez-Montes et al., 2019].

1.8 Metrics in PET

In order to study the accuracy of PET images, some metrics are commonly defined. They are needed to have an objective method to compare images and to study the quality of scanners, reconstruction methods or corrections to the images. There are several metrics that can be used. To show the performance of PET scanners it is common to follow those given by the National Electronic Manufacturers Association (NEMA) [National Electrical Manufacturers Association, 2007] [National Electrical Manufacturers Association, 2008]. Although NEMA metrics are focused into the objective comparison between different scanners, we will use also these metrics in some chapters of the thesis to compare between reconstruction methods.

Some of the common performance metrics in PET and that are used in this thesis are:

- **Spatial resolution:** it can be defined as the minimum distance between two point sources to be distinguished. It is frequently calculated using the FWHM (Full-Width at Half Maximum) or the FWTM (Full-Width at Tenth Maximum) of the profile of a reconstructed image with a point source in it. It can be used to compare scanners or reconstruction methods.

- **True, scatter and random fractions:** this metric is focused into the comparison of scanner configurations, since depending on the manufacturing of the scanner and the activity of the acquisition, the rate of scatter and random events may differ. It is common to talk about the **scatter fraction (SF)**, **random fraction (RF)** or **true fraction (TF)** of an acquisition. Other commonly used concept is the **Noise Equivalent Count Rate (NECR)**, which can be defined as the square of the total true coincidences (regarding as true coincidence non scattered nor random coincidences) divided by the total number of coincidences gathered by the scanner. It should be noticed that this metric does not include the possibility of spurious coincidences due to additional prompt γ rays. As the use of non-standard β^+ emitters is growing considerably in PET [Conti and Eriksson, 2016], this possibility should be also considered and, thus, we will talk also about spurious background fraction (SBF) in the case that a γ emitter is used.

- **Sensitivity and efficiency of the scanner:** the sensitivity of a scanner can be expressed as the rate of true coincidences for a given positron activity. The efficiency can be expressed as the percentage of coincidences detected divided by the number of γ annihilation emissions. Both magnitudes express similar concepts although, according to NEMA standards, sensitivity is preferred for scanner comparisons.

- **Image Quality (IQ):** comparing technological features of a scanner as the sensitivity or the spatial resolution they can achieve is relatively easy and objective to do, but in general, when PET images have to be compared, the metric used are more controversial and it is difficult to find an objective way of comparing images obtained with different scanners or reconstruction methods. For instance, although spatial resolution seems to be a good metric to study image quality, many times a smoother and lower resolution image is preferred if the noise in the image is too high and may result into losing details or lead to errors in the interpretation of the images. Because of this, NEMA standards propose the use of certain phantoms, known as IQ NEMA phantoms to study the image quality in PET. These phantoms are specially designed to study noise-resolution compromise and also to test some of the main important corrections to PET images as attenuation or scatter correction. IQ NEMA phantoms usually comprises a uniform region filled with a known activity to study uniformity (noise and image fluctuations) and several rods or spheres with different sizes filled with different activity to study resolution recovery. They also include empty regions surrounded by hot activity regions to test attenuation and scatter corrections. In this thesis we will use mainly two IQ NEMA phantoms: one of them dedicated to small animals scanners and included in NEMA NU-4 2008 report [National Electrical Manufacturers Association, 2008] (see figure 32) and other one dedicated to human scanners included in NEMA NU-2 2007 report (see figure

33) [National Electrical Manufacturers Association, 2007]. However, NEMA phantoms are not always suitable, and for certain studies as detailed scatter correction of for more complex studies, some other phantoms are preferred. There are many different phantoms available for different studies related to the image quality. Some examples are the Defrise disk phantom, suitable to evaluate axial resolution, the Derenzo phantom, consisting on different rods with different sizes to test image resolution, the bladder phantom, consisting on a very hot region surrounded by a uniform slightly hot region (several orders of magnitude lower), which is very useful to determine the proper scatter correction in the images as well as many other phantoms simulating real tissues or animals as the brain phantom, many rat and mice phantoms as Digimouse phantom or Moby (for mice) and Roby (for rats) phantoms. Some of them will be shown in this thesis.

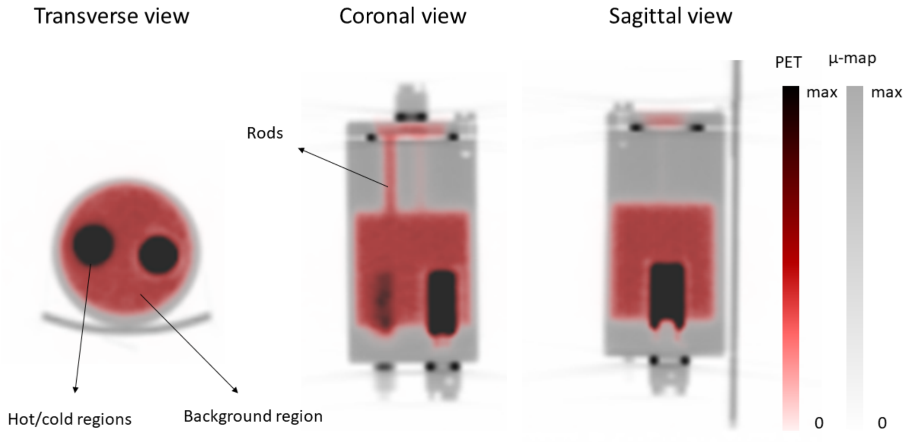

Figure 32: IQ-NEMA phantom acquisition in an Inveon PET/CT scanner according to the NEMA NU-4 2008. [National Electrical Manufacturers Association, 2008]

.

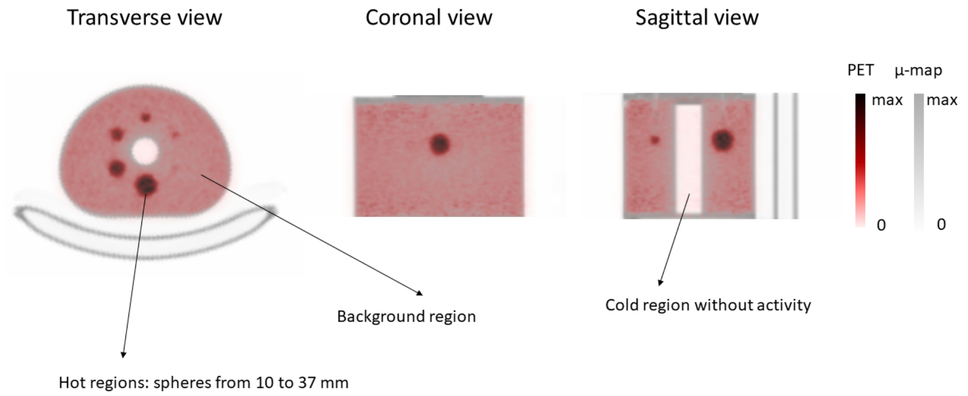

Figure 33: IQ-NEMA phantom acquisition in a Biograph Vision PET/CT scanner according to the NEMA NU-2 2007. [National Electrical Manufacturers Association, 2007].

1.9 Time-of-Flight PET

With the development and improvement of PET scanners, time resolution has become good enough to be able to determine which one of the γ rays of the coincidence got the scanner first and the time difference between the two γ rays. This fact can be used in PET reconstruction to improve images. The method to use the information about the time of arrival of each photon is known as Time Of Flight PET or TOF-PET [Conti, 2009] [Lewellen, 1998] [Moses, 2010] [Vandenberghe et al., 2016] [Moses and Derenzo, 1999] [Jakoby et al., 2011]. TOF-PET was first proposed and developed in the decade of the 1980's, but it was in the 2000's with the inclusion on new scanners with lutetium based detectors when it began to be widely used in PET because of the good timing resolution of these new crystals. The main purpose of the use of this technique is to improve the determination of the position of the activity in the image, being able to improve resolution and image quality. In the last years, some other crystals as lantane bromide ($LaBr_3$) with very good time resolution has been proposed for PET although lutetium based crystals are still preferred due to their higher stopping power and efficiency.

1.10 Multimodal PET imaging

PET images can be combined with other modalities that provide the anatomical information that PET does not provide. This information is basic for some of the most important corrections for PET images as attenuation correction or scatter correction.

- **PET/CT imaging**: it is probably the most extended multimodal technique for PET. CT can provide fast, and with good enough resolution anatomical information than can complete the metabolic information given by PET. Besides properly locating inside the body the activity shown in PET images, it can be used for some corrections to PET images, mainly attenuation correction and sometimes also scatter correction. CT imaging provides a map of the attenuation of X-rays in the tissues inside the organism, being able to identify different organs between them [Basu et al., 2011] [Kapoor et al., 2004]. This map is commonly given in Hounsfield Units (HU) in honour of one of the discoverers of the technique Godfrey Newbold Hounsfield, which results from a linear transformation of the attenuation coefficients of the materials:

$$HU = 1000 \times \frac{\mu_t - \mu_{H_2O}}{\mu_{H_2O} - \mu_{air}} \tag{19}$$

Where μ_t is the attenuation coefficient for each tissue.

Thus, the μ-map of the linear attenuation coefficients of the body can be approximately obtained using a linear transformation of the given CT. This information is essential in PET image reconstruction since non-corrected attenuation PET images present important inaccuracies that may affect the interpretation of these images. The attenuation coefficients depends on the material and also on the energy of the photons used in the CT. For the μ-map used for PET, it is interesting to consider the attenuation coefficients for 511 keV photons, being approximately $0.096cm^{-1}$ for water.

- PET/MR imaging Nuclear Magnetic Resonance (NMR) or just MR is a medical imaging technique based on the response of the different tissues of the body to a external magnetic field. MR imaging is based on the energy difference between the two states of spin of the protons in the body, generally in hydrogen atoms present, for example, in water molecules, in the presence of a magnetic field [Torigian et al., 2013]. This energy difference can be given by:

$$\Delta E = \gamma \cdot \hbar \cdot B_z \tag{20}$$

If a radio-frequency field, perpendicular to the magnetic field, is applied to that system, it will produce that some nuclei go from one state to the other, finally returning to the ground state in a time known as relaxation time. This time is different for each medium where the protons are, being able to differentiate the tissues through the detection of the change of the spin state of the nuclei with the corresponding energy emission.

One of the most important advantages of MR is that it is not necessary the use of ionizing radiation, however, some contrast agents are commonly used, some of them with high toxicity in the organism [Hasebroock and Serkova, 2009] [Bower et al., 2019].

From the last 90's, some works proposed the use of simultaneous PET and MR imaging to achieve a complete, anatomical and metabolic, information of the body [Shao et al., 1997]. Some current scanners use combined PET/MR techniques [Herzog et al., 2011] [Delso et al., 2011]. This became possible with the introduction of SiPMs since former PMTs are highly sensitive to magnetic fields. One of the main limitations of MR for PET purposes compared with CT is that MR imaging does not provide an attenuation map, needed in PET to correct attenuation effects. Thus, other techniques have been introduced to obtain this μ-map from the MR images, from the segmentation into different tissues using the MR images and after the assignment of the corresponding attenuation coefficients to each tissue to the use of Neural Networks trained with CT and MR images being able to achieve continuous and accurate μ-maps from MR images [Bezrukov et al., 2013]. Other of the effects that MR has in PET images is the reduction of the transaxial PR effect, but with sometimes an increased blurring in the axial direction [Herzog et al., 2010].

- PET/US imaging: recent works have proposed the combined use of PET/CT and ultrasound imaging to achieve improvements in motion correction for PET including the heart beat that can be tracked with the use of US imaging [Perez-Liva et al., 2020] [Perez-Liva et al., 2018].

1.11 Monte Carlo simulations in medical imaging. PET oriented simulators

In order to be able to simulate further experiments, Monte Carlo (MC) simulators were introduced in the field of medical imaging [Andreo, 1991]. They have a huge impact, from planning future experiments to test reconstruction methods or corrections. They have became a powerful tool to model and solve very complex problems with more efficiency and accuracy than most of analytic algorithms [Zaidi, 1999].

Monte Carlo methods are used in many fields of science and technology. They are based on the generation of random numbers [James, 1980] (or pseudo-random numbers) and, in many cases, on the simulation of the probabilities that are found for certain events in real systems [Kalos and Whitlock, 2009]. Thus, in PET, for example, they can simulate the probability of emission of certain activity of a radioactive source [España et al., 2009] [Santin et al., 2003], furthermore, they can simulate the probabilities that the emitted particles interact with the matter and even simulate secondary particles emission resulting from these interactions [Jan et al., 2004] [Lopez-Montes et al., 2019]. In order to consider these probabilities, they use probability density functions, which, together with the generation of random numbers is one of the most important considerations regarding MC codes [Zaidi, 1999] [Cal González, 2015].

In general, we can say that one of the aims of Monte Carlo simulators in medical imaging is to replicate the results that we could find in real experiments but without the cost of the experiments [Zaidi, 1999] [Andreo, 1991].

There is a large number of Monte Carlo simulators used in medical imaging, since for this particular case, the utility of these methods is drastic. They are commonly used to test new scanners and improve their designs, planning for radiotherapy treatments, study the viability of clinical and preclinical acquisitions, testing reconstruction methods, etc. Some of the most important and commonly used MC tool-kits adapted for medical imaging purposes are Geant4 [Agostinelli et al., 2003], PENELOPE [Salvat et al., 2006] [Salvat et al., 2008] [Sempau et al., 2003] and EGS code system [Rogers and Bielajew, 1984] [Mackie et al., 1988] [Ford et al., 2006] [López-Sánchez et al., 2019].

One of the main limiting factors of MC simulators is the computational cost and the time required to perform accurate and low-noise simulations. For that reason, some techniques are proposed to reduce the statistical error of the calculations. These techniques are known as variance reduction techniques [Zaidi, 1999] and make possible to reduce the time required to obtain low-noise simulations. Furthermore, in recent years, with the development of GPU's, its use has been proposed for parallel acceleration, being able to reduce drastically the required computational time [Badal and Sempau, 2006] [Badal and Badano, 2009] [Sharma et al., 2018] [Bosman et al., 2021] [Ghammraoui et al., 2014] [Xie et al., 2020] [Bert et al., 2012].

In the field of PET imaging, there are some MC tools that have been specifically adapted to PET [Buvat et al., 2002]. Currently, the most commonly used in PET is GATE (Geant4 Application for Tomographic Emission) [Jan et al., 2004] [Santin et al., 2003] [Strulab et al., 2003] [Bert et al., 2012], based on Geant4 code. Also, some codes based on PENELOPE code are frequently used, as PeneloPET [España et al., 2009] [Lopez-Montes et al., 2019] [Abushab, 2013] [Cal-González et al., 2014] [España et al., 2007] [Liu et al., 2011] [Liu and Zhao, 2014], developed at the Nuclear Physics Group of the Complutense University of Madrid (UCM).

The most relevant uses of MC tools in PET are their direct use for reconstruction using MC simulations for the forward projections in the reconstruction process [Aguiar et al., 2010] [Rafecas et al., 2004b], perform accurate corrections to PET acquisitions as scatter [Levin et al., 1995] [Castiglioni et al., 1999] [Holdsworth et al., 2001] [Barret et al., 2005] or background due to spurious coincidences in non-standard PET emitters [Cal-González et al., 2014] [De Beenhouwer et al., 2009], testing configurations and scanner designs, and testing image reconstruction algorithms [López-Montes et al., 2020]. The main disadvantage of these methods compared to other analytical methods for image corrections are the required time of computation, however, the use of GPU acceleration can provide fast enough simulations able to out-stand analytical methods. Chapter 4 is dedicated to the MCGPU-PET code developed in collaboration with Andreu Badal, main developer of MCGPU [Badal and Badano, 2009] [Badal et al., 2018].

1.12 Basics of Multiplexed PET

Multiplexed PET is a technique that allows obtaining separated images of two different radionuclides acquired together in the same acquisition [Andreyev and Celler, 2011] [Herraiz et al., 2014b] [Fukuchi et al., 2021]. One way to achieve this separations is via the identification and reconstruction of triple coincidences created by non-standard radionuclides [Cal-González et al., 2014] [Andreyev et al., 2014]. While standard β^+ emitters as ^{18}F just produce two photons, both coming from the annihilation of the positron emitted, some non-standard PET radionuclides emit additional prompt gamma rays. Thus, we can identify double coincidences, produced by emitted positrons, coming from both radionuclides, and triple coincidences, where one of the additional gamma rays emitted by the non-standard radionuclide, is detected in coincidence with the photons from the annihilation. We should consider, that due to undesirable effects as inter detector scatter and random triple coincidences, we can find triple coincidences due to standard radionuclides activity [Cal-González et al., 2014]. All these effects should be considered and corrected to obtain an optimum reconstruction of triple coincidences.

One of the keys for radionuclides separation in multiplexed PET, is the correct identification and further reconstruction of triple coincidences [Sitek et al., 2011] [Andreyev et al., 2014] [Andreyev and Celler, 2011]. There are several approaches to reconstruct triple coincidences. In this thesis, we will consider that every triple coincidence consists on one line of response coming from the annihilation of the positron, and another line coming from the coincidence produced by one of the photons of the annihilation and one of the additional gamma rays. We can gather both coincidences and reconstruct the image considering that only one of the lines is a real coincidence. The other line of response will introduce a spurious background which should be considered and corrected during the reconstruction. Once both double and triple coincidences are identified and reconstructed, the radionuclides separation can be done considering that the triple images are only produced by the non-standard β^+ emitter, while the double coincidence image will be a combination of both radionuclides. We have to consider also a sensitivity factor for triples, depending on the non-standard β^+ emitter considered and position and attenuation dependant.

Once double and triple images have been obtained, the images of each one of the radionuclides can be separated. This can be done using an iterative approach using, for instance, a ML algorithm until convergence of the separation [Wang et al., 2006] [Sitek et al., 2011] [Parot et al., 2013] [Andreyev et al., 2014]. It should be considered that the triple and double sensitivity may differ, not only in the global number of coincidences but also in normalization and uniformity sampling of each one. Thus, triples image need to be corrected by sensitivity before the radionuclide separation. After that the radionuclides separation can be performed assuming that double coincidences are a combination of both radionuclides while triple coincidences are only produced by the non-standard β^+ emitter.

1.13 Artificial Intelligence in PET. Deep learning techniques

In recent years, Artificial Intelligence (AI) has experimented a huge development. Although many of these techniques were proposed several years ago [McCarthy, 1998] [Mitchell et al., 2013] [Nilsson, 2014] [Dick, 2019], with the advances in computing capability, the evolution (or maybe revolution) of GPUs and Tensor Processor Units (TPUs) have provided the tools need to fully exploit the possibilities that AI presents.

AI techniques, allow computers to solve many problems without human guidance. The most important techniques in AI in the recent years, are those related to solve complex models via the update of the model parameters. These techniques are included into Machine Learning (ML) techniques. The main difference between a classical approach and ML is that, in a classical approach, a model with a determined structure and parameters is proposed to explain some experimental data, in the case of ML, there is not a specific model, but we let the system to be explained by any model, then, the parameters of this model are fitted using a good number of known cases (train dataset) and are tested with other data that were not used into the training of the model (test dataset). The main reason argued by the detractors of this technique is that it is some kind of a black box with a non-easy interpretation of the meaning of each parameter of the model. This is even more important in the case of Deep Learning (DL) techniques. DL is a technique of ML which aims to work in a similar way of human neurons do. Each input is processed by many layers each one containing different neurons that look for specific patterns or features of the image, giving as a result an output of a general view of the whole problem. The structure containing these layers and neurons is known as Neural Network (NN) [Goodfellow et al., 2016] [LeCun et al., 2015]. Some of the most important applications of DL are classification, segmentation, or pattern recognition networks.

In the field of medical imaging, and more specifically for PET, ML and DL techniques have been proposed and introduced in the last years [Gong et al., 2019]. Working with images, a technique of DL using convolutions is particularly important, this is known as Convolutional Neural Networks (CNN) and are the main base of processing images using DL. CNN have been proposed in PET for different purposes as positron range correction [Herraiz et al., 2021], attenuation correction from MRI [Liu et al., 2018], scatter correction [Qian et al., 2017] [Berker et al., 2018], DOI correction in monolithic crystals [Sanaat and Zaidi, 2020] or even PET reconstruction [Reader et al., 2020] where it can be used to denoise images, to improve low resolution images or even to obtain direct reconstructed images from sinograms.

One of the points that makes that DL methods have gained such a popularity is the possibility of using predefined architectures, with some pre-trained parameters, working in a similar way for some similar problems. For example, some of the most commonly used architectures in medical imaging are VGG-16 [Kang et al., 2018], Res-NET [Sato et al., 2019], and specially for pixel to pixel relationships (being both input and output images), U-NET architecture (see figure 34) [Ronneberger et al., 2015] [Zhou et al., 2018].

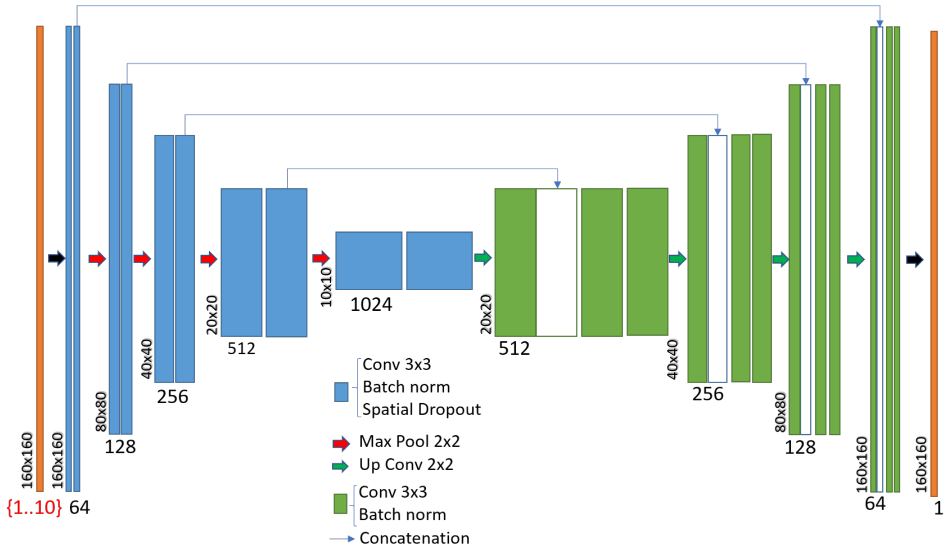

Figure 34: Example of a U-NET architecture [Herraiz et al., 2021]. It represents schematically the convolutional layers of the network until achieving a compact information of the input image followed by several deconvolution or up-sampling operations to recover again an image with a similar shape of the input one.

2 Basics of Tomographic Image Reconstruction

2.1 System Response

In PET, and in other tomographic medical imaging modalities such as CT, the reconstruction problem can be reduced to a linearized version of the actual problem: the data (Y) are related to the image (X) of the radiotracer distribution in the case of PET or the photon absorption in the case of CT, via the System Response Matrix (SRM). In this thesis, for convenience, this matrix will be usually denoted just as A.

$$Y = A \cdot X \tag{21}$$

The SRM usually contains the probability that a decay at a voxel with coordinates (x, y, z) in the image space is detected in a specific LOR [Herraiz et al., 2006] [Kao et al., 2008] [Qi and Leahy, 2006] [Rafecas et al., 2004a]. For 3D acquisitions, the SRM is usually too large (of the order of Terabytes) to be kept in the memory of current computers. Sometimes, these huge, although very sparse, matrices are handled with sparse methods [Zhou and Qi, 2011], or the storage requirement is reduced by exploiting symmetries [Herraiz et al., 2006].

SRMs can be obtained using Monte Carlo simulations [Cabello and Rafecas, 2012] [Rafecas et al., 2004a] [Herraiz et al., 2006], estimated with analytical expressions [Reader et al., 2003], or even measured experimentally [Panin et al., 2006].

In general, the main goal of image reconstruction in PET is to be able to solve the linear equation system (21) and to obtain the image X from the data Y. Thus, the objective is to solve the inverse problem:

$$X = A^{-1} \cdot Y \tag{22}$$

However, the inverse of the SRM is not generally achievable [López-Montes et al., 2019] [Natterer, 2001] [Brahme, 2014] [Cherry and Dahlbom, 2006] and other alternatives are used to approach the solution of X.

In the reconstruction methods for tomographic images, it is common to talk in terms of two different mathematical spaces: the data space and the image space. The SRM, then, is understood as the mathematical operator to pass from the image space to the data space. In PET literature, the process to pass from the image space to the data space is known as forward-projection, while the process to pass from the data space to the image space is known as back-projection. Thus, the goal of image reconstruction is to find a proper back-projection operator that provide a good solution for the reconstruction process. This can be achieved in a single step, finding a good operator that gives the solution of the system, or in a iterative approach, approximating to the solution step by step until achieving a good convergence [Natterer, 2001]. From the matrix point of view, a good forward-projection operator is the proper SRM. Many back-projection operators can be used. The inverse of the SRM is one of them, although the transpose of the SRM also can act as back-projection since it passes from the data space to the image space:

$$\begin{aligned} &X \xrightarrow{A} Y; Forward - projection \\ &Y \xrightarrow{A^{-1}} X; Back - projection \\ &Y \xrightarrow{A^{T}} X; Back - projection \end{aligned} \tag{23}$$

2.2 Analytical methods

The first methods used to reconstruct PET images were based on the inverse of the Radon transform. The Radon transform gives the projections over certain radial (ρ) and angular (θ) views of an extensive object described by a function $f(x, y)$: [Natterer, 2001] [Easton Jr, 2010]. This projections, to which we refer as sinograms, can be expressed as:

$$R(\rho, \theta) = \int_{-\infty}^{\infty} \int_{-\infty}^{\infty} f(x, y)\delta(\rho - (x \cos\theta + y \sin\theta))dxdy = \lambda_\theta(\rho) \tag{24}$$

Another possible notation for ρ is $\rho =< \vec{r} \cdot \vec{n} >= x \cos\theta + y \sin\theta$, which implies a 2D representation of the 1D line [Easton Jr, 2010]. This notation is key to understand the process of back-projection of the data from the Radon space (data space) to the image space.

Also, it can be shown that, allowing negative values for ρ, for a parallel beam geometry like the one considered in PET, $\lambda_\theta(-\rho) = \lambda_{\theta+\pi}(\rho)$, and thus, for $\theta \in (0, \pi)$, all the data set is contained [Barrett, 1984].

This method allows to find an analytical expression of the SRM, which, although presents some inaccuracies, can be inverted to obtain the image from the data through the inverse of the Radon transform [Easton Jr, 2010] [Natterer, 2001] [Cherry and Dahlbom, 2006]. One of the key points of the Radon transform is the Central Slice Theorem, which states that the 1-D Fourier Transform of a given projection of the object obtained with the Radon Transform is equivalent to select a slice of the 2-D Fourier Transform of the object.

$$F_{1D}(\omega, \theta_0)_{\rho \to \omega}[\lambda_{\theta_0}(\rho)] = F_{2D}(k_{x_0}, k_{y_0})_{(x,y) \to (k_{x_0}, k_{y_0})}[f(x, y)] \tag{25}$$

Note that we are using a notation such that $(k_x, k_y) = (\omega \cos\theta, \omega \sin\theta)$ in the Fourier domain and, thus, $\omega = \sqrt{k_x^2 + k_y^2}$. Then, a central slice of the 2D Fourier spectrum can be represented by $(k_{x_0}, k_{y_0}) = (\omega \cos\theta_0, \omega \sin\theta_0)$.

Now, the key is to find an operator that can provide $f(x, y)$ from the sinogram projections. This operator can be known as the inverse of the Radon transform (R^-1). This can be achieved following different approaches although in the case of image reconstruction, the most commonly used is using the Filtered Back-projection (FBP) algorithm. This algorithm is based on the back-projection of the data of the sinogram from the Radon space to the image space. The back-projection for each angular view of the sinogram consists on the distribution ("smear") of the coincidences in that view all over the LOR. Then all the back-pojected views are summed (integrated) among all the angular views:

$$BP(x, y) = \int_0^{\pi} \lambda_\theta(x\cos\theta + y\sin\theta)d\theta \tag{26}$$

However, the back-projection of the data generated by a point source centered in the point (x_0, y_0) (it can be shown as $f(x, y) = \delta(x - x_0, y - y_0)$ function) does not return exactly the point source (x_0, y_0) but a blurred image of it, with the form $\hat{f}(x, y) = \frac{1}{\sqrt{(x-x_0)^2+(y-y_0)^2}} = \frac{1}{r-r_0}$ [Natterer, 2001] [Easton Jr, 2010] [Barrett, 1984]. This blurring should be compensated with the introduction of filters. Thus, the result of the backprojection could be interpreted as a convolution of the original function with a blurring kernel with radial symmetry [Barrett, 1984] [Herman, 1995]:

$$BP(x, y) = \hat{f}(x, y) = f(x, y) ** \frac{1}{|r|} \tag{27}$$

Thanks to the central slice theorem, we can study the effect of that convolution in the Fourier space using Fourier transform theory, and thus, it can be shown that [Barrett, 1984]:

$$F_{2D}\left(\frac{1}{|r|}\right) = \frac{1}{|\omega|} \tag{28}$$

This terms appears as a consequence of passing from polar to Cartesian coordinates in the frequency domain. It has an effect on highlighting low frequencies ($|\omega| << 1$). This is interesting since, in the field of images, the low frequencies of the Fourier transform of the image are associated to a smooth version of the image while the small details of the images are associated to the high frequencies of the Fourier domain. Thus, without a filter we expect to observe a smoothed version of the image. This can be appreciated in Figure 35 [Easton Jr, 2010].

Thus, using both the Central slice theorem and the properties of convolutions in Fourier domain, we can finally get the filter needed to recover the original image from the backprojection [Barrett, 1984] [Herman, 1995]:

$$f(x, y) = \int_0^{\pi} \mathcal{F}^{-1}_{1D(\omega\to\rho)}(|\omega| \cdot \mathcal{F}_{1D(\rho\to\omega)}(\lambda_\theta(\rho)))d\theta \tag{29}$$

This last equation is a form of the inverse of the Radon transform. Notice that $|\omega|$ can be seen as a filtering function, known as Ramp-filter [Zeng, 2015] in image reconstruction field. Other filter can be more suitable for some reconstruction problems, thus, we could generalized the filter $|\omega| \rightarrow h(\omega)$ where $h(\omega)$ is a filter function. Thus, a more general expression for equation 29 would be:

$$f(x, y) = \int_0^\pi \mathcal{F}^{-1}_{1D(\omega \rightarrow \rho)}(h(\omega) \cdot \mathcal{F}_{1D(\rho \rightarrow \omega)}(\lambda_\theta(\rho)))d\theta \tag{30}$$

In Figure 35, we show the effect of different filters (and no filtering) using the FBP algorithm.

To sum up, the algorithm of FBP is based on a first 1D Fourier transform of each angular view of the data (Radon space → Fourier space), followed by a filter in the Fourier domain, after what we perform the inverse 1D Fourier transform back again to the data space (Fourier space → Radon space). After that, only a back-projection of the data (Radon space → Image space) is needed. Note that all this process can be done in the space domain, applying the filters as convolutions, this variant is commonly known as Convolution Back-Projection (CBP) [Natterer, 2001]. However, in general the use of the filters in the Fourier domain, FBP, is preferred to CBP since it is less computational expensive [Natterer, 2001].

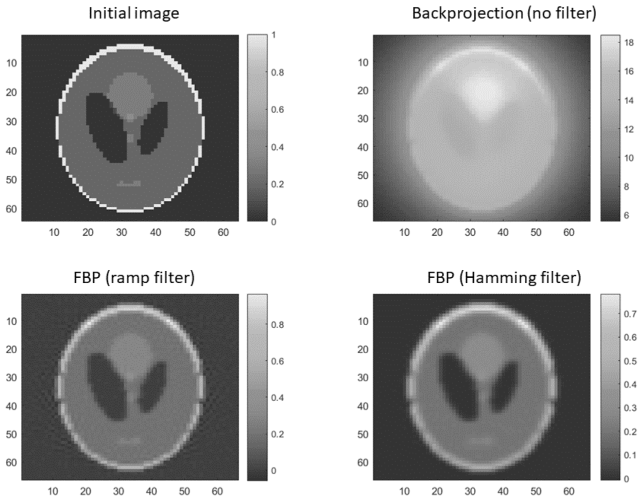

Figure 35: Different filters for FBP and their effect in the image.

Other expressions could be found for the inverse of the Radon transform. A simple one could be simply using the Central slice theorem and using the 2D inverse Fourier transform in polar coordinates. This would lead us to a similar expression to equation (29) where the Ramp-filter would appear in this case as the Jacobian determinant to pass from Cartesian coordinates (k_x, k_y) to polar coordinates (ω, θ) [Easton Jr, 2010] [Barrett, 1984]. Although this expression could be used as well for image reconstruction (as Direct Fourier Reconstruction [Brahme, 2014] [Natterer, 2001] [Easton Jr, 2010]), in general FBP is preferred since it is easier to implement from a computational point of view and filters can be also easily interpreted.

Analytical methods have important limitations, which is the main reason because why they have been replaced by other reconstruction methods such as iterative methods.

First of all, for the derivation of all previous expressions, we have assumed the data and the image to be continuous functions, while in the case of a real acquisition it is not correct. Thus, we need a discrete version of the expressions of the inverse of the Radon transform to obtain the image from the data.

$$f(x,y) = \sum_{i=1}^{\pi} \mathcal{F}^{-1}_{1D(\omega\rightarrow\rho)}(h(\omega)\cdot\mathcal{F}_{1D(\rho\rightarrow\omega)}(\lambda_{\theta_i}(\rho)))\Delta\theta_i \tag{31}$$

Now assuming $\mathcal{F}$ transform and $\mathcal{F}^{-1}$ to be the discrete version of Fourier transforms.

However, there is a more important problem regarding the discrete nature of the data, which is that, due to the physical separation of the blocks of detectors of a scanner, to assure the homogeneity and consistency in the distance between the radial and angular views of the sinogram, some gaps without counts are left between some bins of the sinogram. These gaps produce an effect of incompleteness of the data which is not accounted for the formulation of FBP or other analytical methods. This produce important artifacts in the image (see figure 36). To solve this, several approaches have been proposed. The simplest methods are based on the interpolation of the missing data using "inpainting" techniques. This simple approach is sometimes enough since the size of the gaps is generally small and a good interpolation could be good enough to estimate missing data. There are other more sophisticated inpainting methods, many of them based on a first reconstruction of the image, interpolating data, and a further projection of the reconstructed image to estimate the missing data. Other proposed methods exploit the properties of sinograms in the frequency (Fourier) domain to estimate the data for the gaps [Herraiz et al., 2011] [Herraiz et al., 2008]. Independently of the method used, it involves an additional step prior the reconstruction which makes the process more computationally expensive.

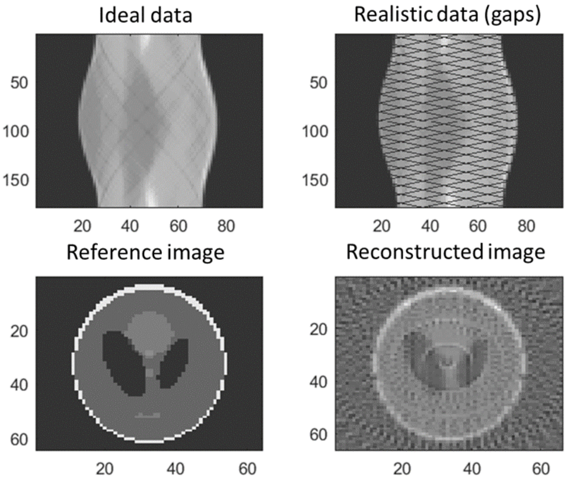

Figure 36: Effect of incompleteness of the data over the images reconstructed with FBP. Artifacts can be clearly appreciated in the reconstructed image.

Other important limitation is the ill-posed of the reconstruction problem, being the solution very sensitive to small perturbations in the data. In a PET acquisition, some of these perturbations are produced by the noise introduced in the image by random, scattered and background coincidences. All these effects summed to the intrinsic probability of positron emission in each pixel of the image, ruled by Poison statistics, introduce a random fluctuation of the expected number of counts in each LOR of the sinogram. This noise has an important impact on the quality of the reconstructed image that should be corrected. This correction is achieved using appropriate filters (see equation 30) able to recover less noisy images from noisy data [Cherry and Dahlbom, 2006]. In general, the filters work by reducing the contribution of the noise which is dominant over the image information at high frequencies in the Fourier domain. This can be done just ignoring all the contributions over certain frequency with the Ramp-filter or using more sophisticated functions which reduce the contribution to the images of these frequencies as done for example with Hamming filter [Easton Jr, 2010] (see figure 37).

Related to filtering high frequencies and to the nature of the Fourier analysis of the image, we can find the appearance of negative values inside the reconstructed image. A PET image can be assumed to be strictly positive but, when trying to recover some details of the image, specially sharp regions, the Fourier analysis introduce fluctuations which can introduce higher values on some pixels that they should have. These higher values need to be compensated by negative ”wings” in the image [Easton Jr, 2010]. In general, this ”wings” have a low amplitudes and in the final image the negative values are many times set to zero, but it may introduce some inconsistencies from the mathematical and quantitative point of view.

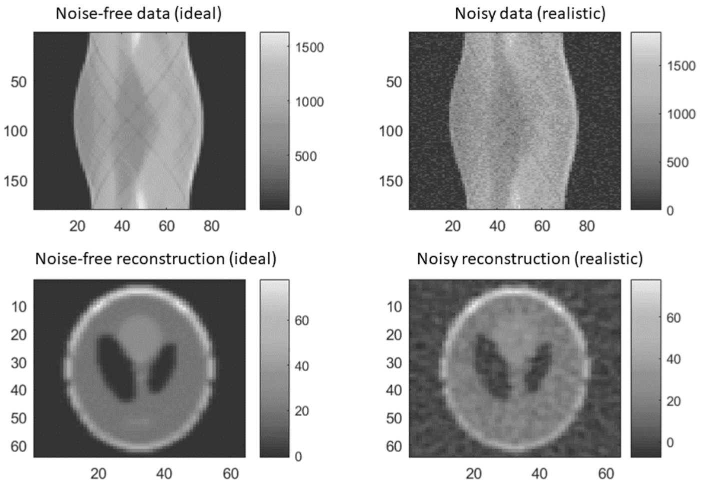

Figure 37: Effect of noise in the data in FBP reconstruction. Hamming filter has been applied to the noisy reconstruction.

Finally, another limitation of FBP and most analytical reconstruction algorithms is that they are derived for 2D data (only in-plane reconstruction), however, PET data are usually gathered in 3D mode, including axial information. Some works have proposed the use of extension formulas from 2D to 3D algorithms (as 3D-Reprojection algorithm [Kinahan and Rogers, 1988]) but, many times, it is just preferred a combination of axial rebinning techniques (discussed in section 1.5.2) as SSRB, FORE or iterative or pseudo-inverse rebinning followed by a slice by slice 2D reconstruction using FBP, which often provide similar result at a much less computational cost that fully 3D analytical methods.

All these limitations are the main reason because of which analytical methods have been progressively replaced by iterative methods.

2.3 Iterative methods

Although these methods were proposed some decades ago, they have progressively been introduced into the image reconstruction field with the improvement of computers. The main idea of iterative reconstruction is to approximate progressively to the desired solution of certain problem [Iriarte, 2017] [Cherry and Dahlbom, 2006] [Natterer, 2001] [Brahme, 2014] [Alessio et al., 2006a]. In general, the initial point is a generic image of ones or zeros which would be updated iteratively until the desired convergence. A schematic representation of an iterative reconstruction is presented in figure 38. The main goal is to minimize the error between the observed data and the forward-projected data of the image. The function that we minimize, usually referred as cost function [Cherry and Dahlbom, 2006] and the function used to update the image determine the algorithm used in the approach to the solution [Cherry and Dahlbom, 2006] [Brahme, 2014] [Natterer, 2001]. In general, they improve the images provided by analytical methods for several reasons. First of all, they can consider the main physical and geometrical (as inter detector gaps) effects in a PET acquisition into the SRM [Rafecas et al., 2004a] [Qi and Leahy, 2006] [Herraiz et al., 2006] [López-Montes et al., 2020]. Moreover, they are in general more robust to noise than analytical methods, and they can be used for fully 3D PET image reconstruction [Alessio et al., 2006a] [Defrise et al., 2005] [Frese et al., 2003]. Other important advantage of iterative methods is that they can easily include non-linear considerations into the reconstruction workflow, as filtering negative values in the images in each iteration. For all these reasons and thanks to the advances in computational technology, iterative methods are currently the main technique for PET image reconstruction.

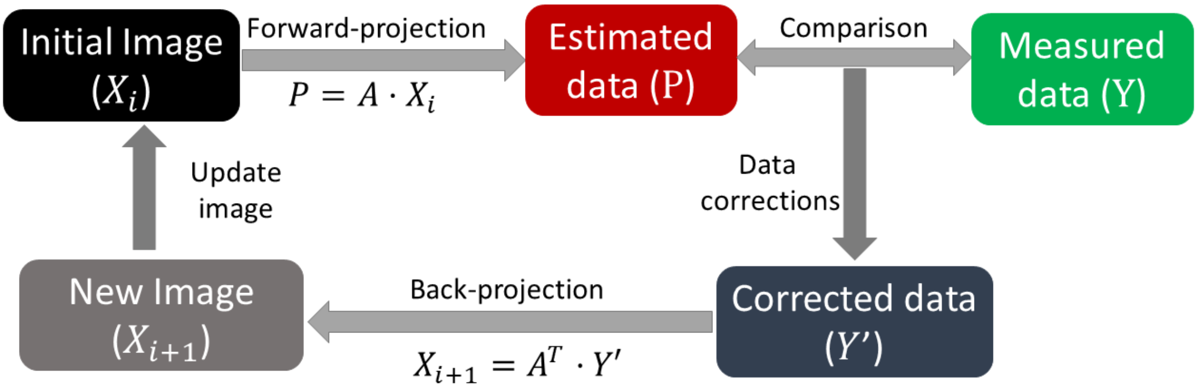

Figure 38: Iterative reconstruction schematic representation. In each step, a forward projection of the initial image is performed to obtain an estimation of the data which is compared to the actual data, the way to compare and correct the estimated data to match the measured data depends of the selected algorithm. After that, the corrected data are back-projected to the image space and the new image becomes the initial image for the next iteration. This process is continued until convergence or until the result is satisfactory.

In this chapter we will discuss some of the most commonly used algorithms for iterative reconstruction in PET imaging.

2.3.1 Algebraic reconstruction

The tomographic image reconstruction can be considered as an optimization problem with the goal of minimizing the differences between the measured data and the projections obtained from the estimated image. Thus, we could approach the solution looking for the global minimum (or at least local minimum) of the problem. This can be done step by step moving in the opposite direction of the gradient. This is in known as gradient descent method [Lemaréchal, 2012] [Leitão and Svaiter, 2016]:

$$X^{n+1} = X^n - \omega \nabla f(X) \tag{32}$$

Where $f(x)$ is the function that we want to minimize and ω a relaxation factor to assure the convergence of the method. One of the most common approach is trying to solve the least squares problem [Merriman, 1877] (LSP), it is, trying to find the solution that minimize the $L2$ norm of the system:

$$f(X) = (||AX - Y||^2)/2 \tag{33}$$

Thus:

$$\nabla f(X) = \frac{\partial f(X)}{\partial X} = A^T \cdot (AX - Y) \tag{34}$$

This solution naturally leads to the known as Landweber method [Landweber, 1951]:

$$X^{n+1} = X^n - \omega A^T (AX - Y) \tag{35}$$

In this case, the factor $\omega \in (0, 2/\sigma_1^2)$, with σ_1 the greatest singular value of the matrix to assure the convergence of the algorithm. Notice that if the matrix is normalized to the Euclidean norm ($\sigma_1 = 1$), $\omega = 1$ is valid for the relaxation factor and the algorithm can be reduced to:

$$X^{n+1} = X^n - A^T (AX - Y) \tag{36}$$

Another well known algorithm in mathematics that also minimize the LSP is Kaczmarz method [Kaczmarz, 1937], which direct application to image reconstruction is known as Algebraic Reconstruction Technique (ART) [Gordon et al., 1970]:

$$x_i^{n+1} = x_i^n + a(i,j) \cdot \frac{y_j - \sum_i a(i,j) \cdot x_i^n}{\sum_i a(i,j)^2} \tag{37}$$

This method update the image for each individual LOR (j). A complete iteration of ART is achieved when all the LORs have been considered once. Some years later after this method were proposed, a generalization of it that accelerate the reconstruction using a simultaneous update of the image using all the LORs at the same time were proposed with the name of Simultaneous Algebraic Reconstruction Technique (SART) [Andersen and Kak, 1984], and it is still one of the mainly used algorithms in image reconstruction (specially CT image reconstruction [Jiang and Wang, 2003] [Yan, 2010]).

$$x_i^{n+1} = x_i^n + \frac{\sum_j^{NV} a(i,j) \cdot \frac{y_j - \sum_i a(i,j) \cdot x_i^n}{\sum_i a(i,j)}}{\sum_j^{NL} a(i,j)} \tag{38}$$

Where NV is the total number of voxels of the image and NL the total number of LORs. We can express this algorithm in a matrix notation, easier to follow and compare to other algorithms:

$$X^{n+1} = X^n + \frac{A^T \cdot \frac{Y - A \cdot X^n}{A \cdot \mathbb{1}_{(NV,1)}}}{A^T \cdot \mathbb{1}_{(NL,1)}} \tag{39}$$

Sometimes, a relaxation factor is included to control the convergence of the algorithm in a similar way that it was introduced for Landweber iterations. This relaxation factor, plays a similar role to the different filters (for example Hamming filter) in the FBP reconstruction [Andersen and Kak, 1984] [Nikazad et al., 2017].

$$X^{n+1} = X^n + \omega \cdot \frac{A^T \cdot \frac{Y - A \cdot X^n}{A \cdot \mathbb{1}_{(NV,1)}}}{A^T \cdot \mathbb{1}_{(NL,1)}} \tag{40}$$

Note that, for a normalized matrix (A), the results given by Landweber algorithm and SART will be the same [Yan, 2010]. Furthermore, note also that the linear solution provided using purely SART or Landweber algorithms would be equivalent to the solution of FBP. However, using an iterative approach let us to introduce some a priory knowledge as positive constraints which converts the method into a non-linear problem. Moreover, the introduction of realistic system matrices allow these iterative methods to outperform FBP, being able to consider inter-detector gaps (solving the need to interpolate missing data in FBP) and to include physical effects using techniques as Gaussian TORs instead of ideal LORs in the SRM that take into account the possibility that the emission point differs from the points of an ideal line connecting the detectors. Finally, although a whole 3D SRM would be unachievable for current computers, the use of symmetries in the computation of the SRM allow us to perform a fully 3D reconstruction using iterative methods, suppressing the problem of axial rebinning inaccuracies with the cost, of course of increasing reconstruction time.

2.3.2 Maximum Likelihood - Expectation Maximization (MLEM)

This method is based on the use of the maximization estimator for a maximum likelihood problem [Dempster et al., 1977]. Thus, lets assume that, since the probability that a emission occurs at a certain point is ruled by the nuclear probabilities of decays, all the process follows a Poisson distribution [Cherry and Dahlbom, 2006] [Shepp and Vardi, 1982]. This means, if we denote by x_i the activity in a pixel i of the image the probability of $n_i = k$ number of decays take place in this pixel is:

$$P(n_i = k) = e^{x_i} \cdot \frac{x_i^k}{k!} \tag{41}$$

Now, lets denote by $y_j(x_i)$ the number of coincidences produced in the LOR j from the voxel i. This value is unknown in the reconstruction problem, but we do know the number of coincidences detected in certain LOR j, summed all over the pixels, weighted by the probability that a pixel i produces a coincidence in the LOR j. These probabilities are indeed the elements of the SRM (A), which we denote as $a(i,j)$:

$$y_j = \sum_{i=1}^{NV} y_j(x_i) = \sum_{i=1}^{NV} a(i,j) \cdot x_i \tag{42}$$

Note that this representation is an equivalent representation of the matrix equation (21)

Furthermore, the number of emissions in each pixel i detected in each LOR j ($y_j(x_i)$) follow independent Poisson distributions (41) [Shepp and Vardi, 1982]. Thus, the maximum likelihood function can be expressed as [Shepp and Vardi, 1982]:

$$L(x|y) = \prod_i \prod_j \frac{e^{-a(i,j)\cdot x_i} \cdot (a(i,j) \cdot x_i)^{y_j(x_i)}}{y_j(x_i)!} \tag{43}$$

The maximization of this likelihood function is often done in terms of $l = \ln L$, since [Dempster et al., 1977]:

$$l(x|y) = \ln L = \sum_i \sum_j (-a(i,j) \cdot x_i + y_j(x_i) \cdot \ln(a(i,j) \cdot x_i) - y_j(x_i)) \tag{44}$$

And, then:

$$\frac{\partial l(x|y)}{\partial x_i} = \sum_i \sum_j (-a(i,j) + a(i,j) \cdot \frac{y_j(x_i)}{a(i,j) \cdot (x_i)}) = -1 + \sum_j a(i,j) \cdot \frac{y_j}{\sum_i a(i,j) \cdot x_i} \tag{45}$$

From this solution, and applying Karush-Kühn-Tucker conditions [Bazaraa et al., 2013] [Shepp and Vardi, 1982] for the optimal solution of a non-linear problem, it can be found a good estimator to the solution of the MLEM which can be achieved iteratively as:

$$x_i^{n+1} = x_i^n \cdot \sum_j a(i,j) \cdot \frac{y_j}{\sum_i a(i,j)_i} \tag{46}$$

Note that all this derivation has been done assuming that the probability matrix (SRM) has been normalized to $\sum_j a(i,j) = 1$. In any other case, this expression should be replaced with [Alessio et al., 2006a] [Defrise and Kinahan, 1998]:

$$x_i^{n+1} = \frac{x_i^n}{\sum_j a(i,j)} \cdot \sum_j a(i,j) \cdot \frac{y_j}{\sum_i a(i,j)_i} \tag{47}$$

Moreover, if the matrix is properly normalized, this algorithm can be expressed in a matrix form as:

$$X^{n+1} = X^n \bullet A^T \left(\frac{Y}{A \cdot X} \right) \tag{48}$$

Where $\bullet$ indicates element by element array multiplication. The fraction $\frac{Y}{A \cdot X}$ refers also to a element by element array division.

Some important considerations regarding this method are the pure positivity of the solution, since the coefficients or the SRM are assumed to be non-negative as well as the number of counts in each LOR gathered in Y. It is also important to note that the initial value for X, X^0 should not include 0 values. Moreover, strictly 0 values will not appear (except for empty LORs) in the solution, finding instead very close to 0 values. This is one of the main controversial points of MLEM for some authors, however, since this method allows to consider the Poisson nature of the emission image, it usually provides better images that other algorithms, which make MLEM the preferred iterative algorithm in PET imaging [Alessio et al., 2006a].

One of the limitations of this method is the slow convergence of the algorithm, which involves a high computational cost and a long time to get a good solution compared to other algorithms. For that reason, a variation of the method was proposed in 1994 [Hudson and Larkin, 1994]. In that work an acceleration of the convergence was proposed via the use of subsets (SB), it is, to use only a part of the data to update the image in several sub-iterations, being a total iteration when the whole dataset has been used. The modification of the algorithm for subsets would be [Alessio et al., 2006a]:

$$x_i^{n+1} = \frac{x_i^n}{\sum_{j \in SB} a(i,j)} \cdot \sum_{j \in SB} a(i,j) \cdot \frac{y_j}{\sum_i a(i,j)_i} \tag{49}$$

This method is known as Ordered Subsets Expectation Maximization (OSEM).

2.3.3 Image Space Reconstruction Algorithm (ISRA)

Another algorithm based on ML is ISRA, firstly proposed by Margareth Daube-Witherspoon and Muehllehner [Daube-Witherspoon and Muehllehner, 1986], it takes the same initial point of MLEM, deducing the expression for the corrections to achieve the ML solution [Shepp and Vardi, 1982]. However, in this case, the corrections are done in the image space instead of in the data space. The provided solution is similar to the obtained with MLEM but it involves a lower number of calculations when the number of LORs is high, and, for that reason, some authors have proposed it as an alternative to MLEM [Archer and Titterington, 1995] [De Pierro, 1993]. A matrix representation of the algorithm would be:

$$X^{n+1} = X^n \cdot \frac{A^T Y}{A^T A X^n} \tag{50}$$

Assuming a normalized matrix where $\sum_{i,j} a(i,j) = 1$

In figure 39 we present the reconstruction of the same image using different reconstruction algorithms.

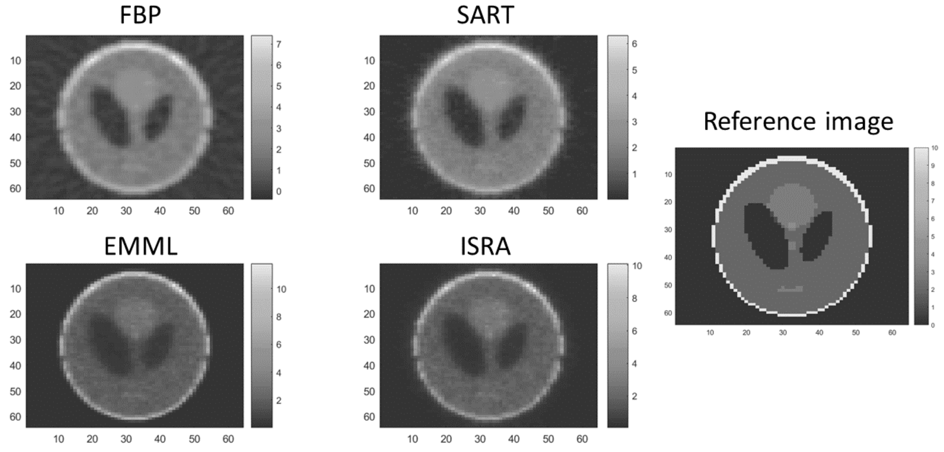

Figure 39: Comparison of different methods of image reconstruction.

2.3.4 Regularization and improvements on iterative reconstruction

One of the key points of iterative reconstruction is to decide in which iteration the solution is acceptable, it is, to set the end point of the algorithm. In general, low number of iterations provide smoother solutions but with low image resolution, high resolution images can be achieved increasing the number of iterations, however, due to the presence of statistical noise, if too many iterations are used, the variability of the points in the image grow, resulting in noisy images which are not desired due to their difficult interpretation [Guo and Renaut, 2011]. This is a consequence of the ill-posed nature of the reconstruction problem since, for example, the measured data are affected by statistical noise due to the stochastic nature of the nuclear emission, in addition to other effects affecting the image as random or scattered coincidences. Then, even in the case of a perfectly corrected PET data, some statistical fluctuations will be found, thus, a more proper representation of the measured data would be:

$$Y = A \cdot X + n \tag{51}$$

Where n represents the statistical noise. Thus, during the reconstruction workflow we are actually trying to fit noisy data. This noise, as we said in the analytical methods reconstruction section, is particularly important at high frequencies of the image spectrum where the contribution of the noise is sometimes even higher than the contribution of the image itself. In the case of analytical methods, this was dealt by suppressing or reducing the contribution of high frequencies in the Fourier domain with the use of filters. In the case of iterative reconstruction, the number of iterations act as a first regularization of the algorithm, and thus, the goal is to find the point where the compromise between resolution and noise is satisfactory. Other approaches are the use of post processing filters, as Gaussian filtering the result to obtain smoother images. Some other techniques have been proposed to improve images reconstructed with iterative methods, some of the most commonly used are those to explore Bayesian methods including a priory or a posteriori information [Alessio et al., 2006a]. Maybe the most common of these methods is the Maximum A Posteriori (MAP) method [Qi et al., 1998] [Cheng et al., 2012] which allows to control the variance and fluctuations at high number of iterations reducing the variability of the solutions and allowing to achieve improved resolution avoiding noisy images.

On the other hand, an important improvement on iterative reconstruction appeared in recent years with the improvement of the Time Of Flight (TOF) information of the scanners, specially for clinical scanners. This information can be used into iterative reconstruction algorithm to improve the quality of the images since they allow to narrow down the emission point from the data information [Conti, 2010] [Conti and Bendriem, 2019] [Rezaei et al., 2014]. It is common to separate each LOR in TOF bins with the information about the crystal that was reached by the first photon, then the reconstruction can be done projecting the image considering the TOF bins which contribute to determine better the position of the activity source.

3 Materials and methods

3.1 Scanners used in this thesis

In this thesis, we have worked with several preclinical and clinical PET scanners. In this section, we describe the main features of the scanners used which data are analyzed and presented in the different sections of results of the thesis.

3.1.1 Super-Argus PET/CT scanner

This scanner developed by Sedecal consists on several rings of 24 blocks of detectors with arrays of 13×13 ($1.55 \times 1.55mm$) detectors per block. It is designed for small animals as mice and rats with a scanner diameter of $17.5cm$. A phoswhich system is included to correct data by Depth Of Interaction (DOI), thus, each crystal is conformed by two layers with different materials, LYSO and GSO the first and second layer respectively with 7 mm length LYSO layer and 8 mm length the GSO one. The different time and light response of each material allows to determine whether the coincidences took place in one layer or in the other being able to reconstruct with DOI considerations improving the quality of the reconstructed images [Udias et al., 2018]. Several versions with different number of rings are available. In this thesis, we have used two versions: 4-rings and 6-rings versions with axial FOVs of 10 and 15.2 cm each one [Udias et al., 2018]. A schematic representation of the Super-Argus scanner 6 rings version is shown in figure 40.

We used data in list mode format as well as in sinogram format. Sinograms commonly used in Super-Argus scanner had 168 angular views and a variable number of radial bins for different transaxial FOVs, from 99 radial bins (corresponding to 76.725 mm FOV) to 225 radial bins (corresponding to 174 mm FOV). Different axial compression (span factor) and MRD were also used.

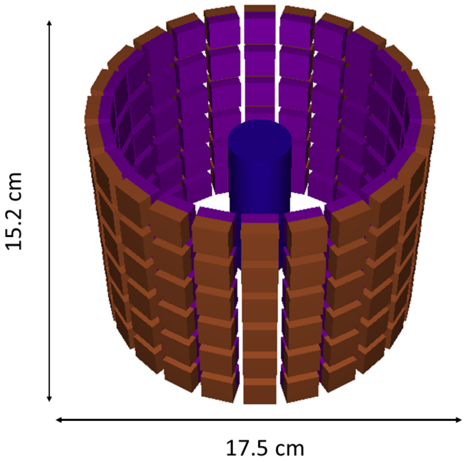

Figure 40: Schematic representation of Super-Argus scanner (6 rings version) with a small cylinder inside (blue) using gview3d (auxiliary program distributed with the code of PENELOPE [Sempau et al., 2003]).

Super-Argus acquisitions were provided by collaborators at Instituto de Investigación Sanitaria Gregorio Marañón (Madrid, Spain). Acquisitions and simulations with Super-Argus geometry were used in this thesis to study the performance of this scanner and to test pseudo-inverse reconstruction method in it.

Also, in this thesis, some studies on the most important features of the scanner were done, as the NEC studies and the Scatter Fraction of the scanner following the NEMA-4-2008 standards for both mouse-like and rat-like phantoms [Udias et al., 2018]. The results of these studies are presented in figures 41 and 42.

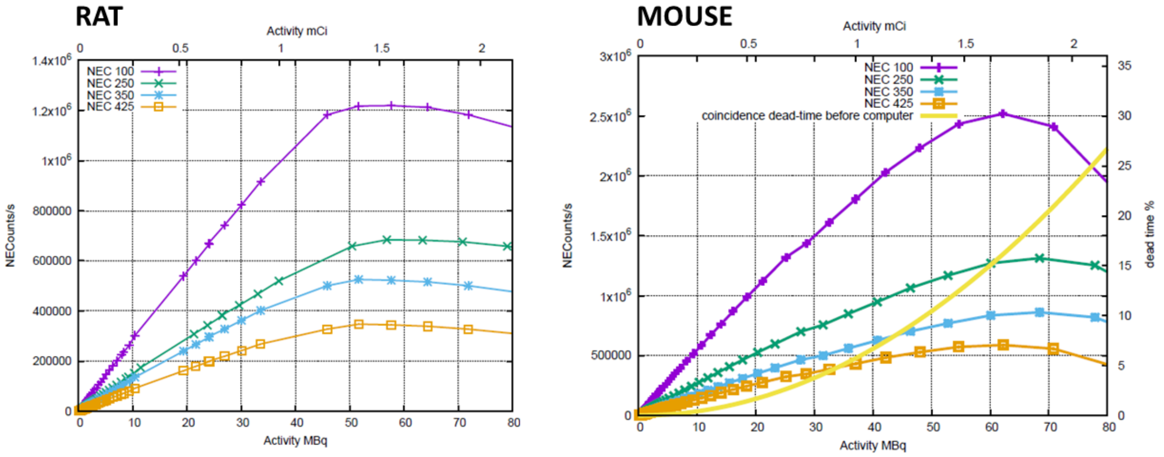

Figure 41: Study of the Noise-Equivalent Count Ratio for Super-Argus PET/CT scanner (6 rings version) for rat-like (left) and mouse-like (right) phantoms for different energy windows (100-700 keV, 250-650 keV, 350-640 keV, 425-600 keV).

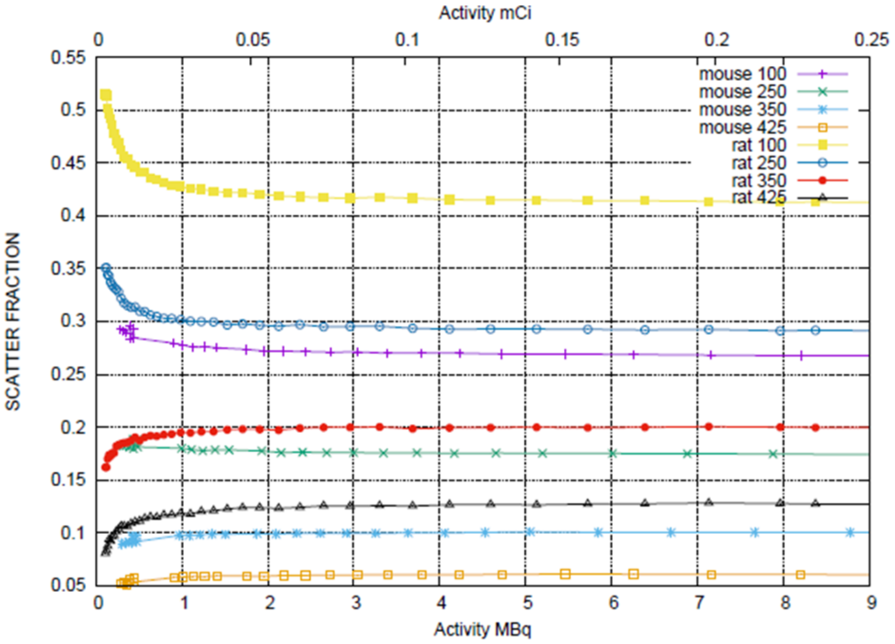

Figure 42: Study of the scatter fraction (SF) for Super-Argus PET/CT scanner following NEMA-4-2008 standards for rat-like and moue-like phantoms for different energy windows (100-700 keV, 250-650 keV, 350-640 keV, 425-600 keV).

We also show a sensitivity study for the Super-Argus PET/CT scanner in figure 43.

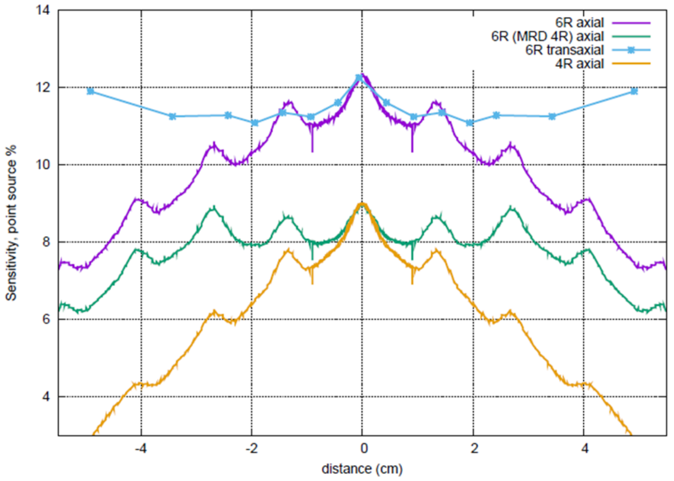

Figure 43: Study of the sensitivity (axial and transaxial) for Super-Argus PET/CT scanner in its 4-rings and 6-rings version.

In figure 44 we show a reconstructed image of a gated cardiac mouse where the myocardium can be clearly appreciated [Udias et al., 2018].

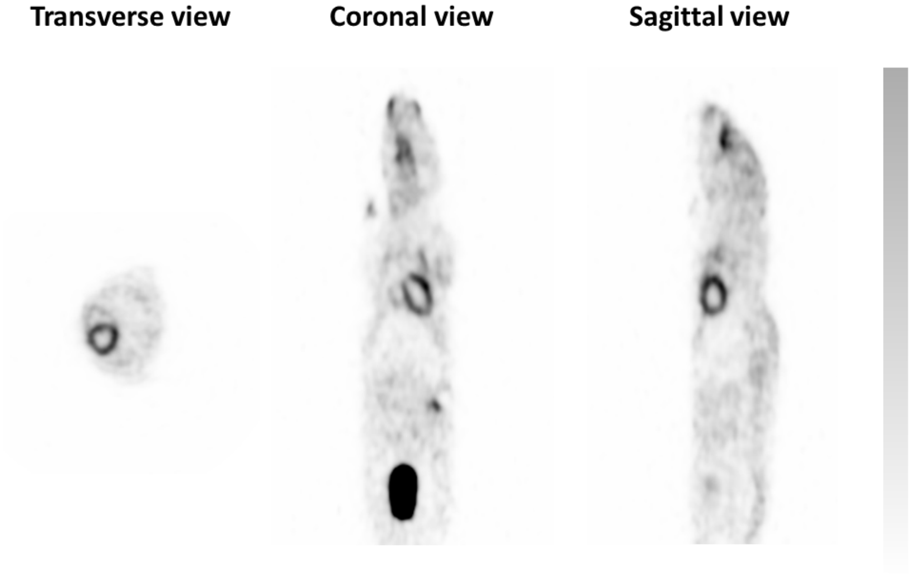

Figure 44: Small Mouse, 220 uCi ^{18}F-FDG, Acquired for 10 minutes, 30 minutes after injection gated study (8 gates). Shown Gate 7th. 3DOSEM, 3x8 updates

3.1.2 Inveon PET/CT scanner

This preclinical scanner was commercialized by Siemens Medical Solutions. It consists on 4 rings of 16 detector blocks of 20×20 LSO crystals coupled to PSPMTs. Crystal's pitch is $1.59 \times 1.59 \times 10$ *mm* [Constantinescu and Mukherjee, 2009]. The diameter of the scanner is 12 *cm* while the axial FOV is around 12.7 *cm*.

Inveon scanner has also a CT insert with an axial FOV of 10 *cm* which simultaneous acquisitions with PET were used to determine corrections such as attenuation, scatter and spurious background corrections.

We analyzed list mode files generating sinograms of 147×168 radial and angular views respectively, with a radial bin size of 1.59 *mm*. Axial compression was set to a span factor of 11 and a MRD of 79 (all slopes considered) to give a total number of 1293 sinograms.

We obtained acquisitions from collaborators at Memorial Sloan Kettering Cancer Center (MSKCC) in New York to test mPET techniques on different radionuclides and configurations. Also, we participated in a collaboration with the Medical University of Vienna, during which we were able to acquire simultaneous ^{44}Sc and ^{18}F in an IQ NEMA phantom. The results of these experiments are presented in the results section dedicated to mPET.

We also used some of these acquisitions to test and evaluate the use of pseudo-inverse reconstruction. MCGPU-PET for scatter and spurious background estimation were used to apply corrections on Inveon acquisitions.

We used simulations with the geometry of an Inveon scanner (see figure 45) to study a method for positron range correction based on deep learning techniques.

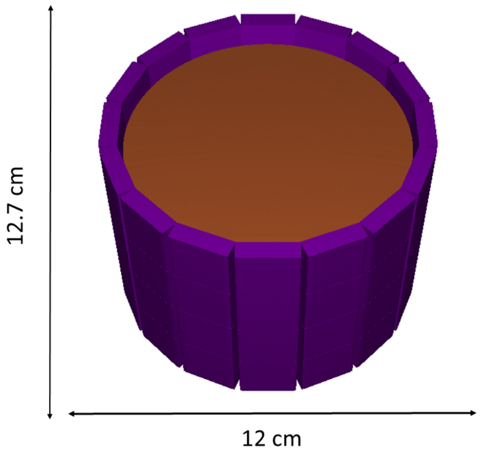

Figure 45: Schematic representation of the Inveon PET/CT scanner with a cylinder inside (brown) using the gview3d program.

3.1.3 Clinical scanners

- **Biograph TPTV PET/CT scanner**: in this thesis, we used its 4 rings version, with 48 blocks of 13×13 ($4 \times 4mm$ pitch) LSO crystals in each ring. The radial diameter of the scanner is $80cm$ and the axial FOV is around $22cm$. A schematic representation of the scanner using gview3d software (distributed as an auxiliary program of PENELOPE code [Sempau et al., 2003]) is shown in figure 46.

  In the thesis we used sinograms of acquisitions of ^{18}F in a IQ NEMA phantom in Medical University of Vienna. Sinograms had 336×336 radial and angular views and an axial compression with a span factor of 11 and a MRD of 38, leading to a total of 559 sinograms. Scatter correction was done using SSS algorithm and attenuation correction was taken into account via the aligned CT within the PET acquisitions. The acquisitions were used to test pseudo-inverse reconstruction method on a clinical scanner.

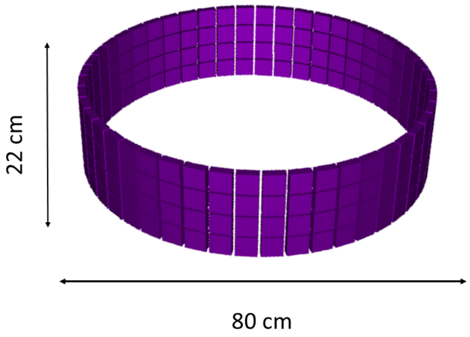

Figure 46: Schematic representation of Biograph TPTV PET/CT scanner.

- **Biograph mCT PET/CT scanner**: this scanner is a bigger and improved version of Biograph TPTV scanner. It is conformed by 4 rings with 48 detectors blocks, each one formed by a 13×13 LSO crystals array with a pitch of $4 \times 4 \times 20$ mm. It covers 84 cm diameter and an axial FOV of 22.1 cm [Rausch et al., 2015] [Jakoby et al., 2011].

  List mode files were processed to obtain sinograms with 400 radial bins and 336 angular views. Span factor was set to 11 and MRD to 49, leading to 621 total sinograms. Reconstructed images are $400 \times 400 \times 109$ bins with a cubic voxel with side of 2 mm.

  Acquisitions from mCT were obtained from collaborators at Siemens Medical Solutions and were used in order to test scattered and spurious background corrections for ^{124}I and ^{18}F acquisitions.

- **Biograph mMR PET/MR scanner**: another Biograph family scanner, this time combining PET and MRI, this scanner has 8 rings of detectors with 56 blocks each one. the blocks in mMR are composed of 8×8 arrays of LSO crystals coupled to SiPMs. The pitch of the crystals is $4 \times 4 \times 20mm$ [Delso et al., 2011] [Karlberg et al., 2016].

  We processed list mode files to get sinograms with 344 radial bins and 242 angular views. Span was set to 11 and MRD to 63 leading to a total of 837 sinograms. Reconstructed images are $344 \times 344 \times 127$ cubic voxel images with a voxel side of 2 mm.

  We used acquisition from Biograph mMR to test MCGPU-PET corrections on a clinical PET/MR scanner.

- **Biograph Vision PET/CT scanner**: this is one of the most recent PET scanners available of the Biograph Siemens scanners. It is formed by 38 blocks of detectors, each one with an array of 20×10 LSO crystals with a pitch of around $3.3 \times 3.3 \times 3.3$ mm. The arrays are coupled to SiPMs. There is a total of 8 rings of blocks which lead to an axial FOV of 26.4 cm. The diameter of the scanner is 82 cm. The axial and transaxial resolution of the scanner is better than the rest of Biograph scanners, achieving around 3.6 and 3.5 mm transaxial and axial resolution respectively [Van Sluis et al., 2019].

  List mode files were analyzed and sinogram of double and triple coincidences were gathered. Sinogram size was 520×399 radial and angular views, using a span factor of 11 and a MRD of 79, leading to 815 total sinograms. Reconstructed images are $440 \times 440 \times 159$ bins with 1.65 mm side cubic voxels.

  MCGPU-PET corrections and radionuclide separation for non-standard β^+ emitters were tested in this scanner in this thesis.

- **3TMR-BRAINPET PET/MR**: in this thesis, we also used BrainPET scanner acquisitions. This is a PET scanner dedicated to brain with a 3T MR insert. The scanner consists of 32 blocks of 12×12 squared crystals of 2.5 mm pitch arranged in 6 rings, covering an axial FOV of around 19 cm. It is located at the research center of Jülich, in Germany (see figure 47) [Herzog et al., 2009b] [Herzog et al., 2011] [Caldeira et al., 2018].

  List files were processed to obtain sinograms with 199×224 radial and angular views respectively. Span factor was set to 11 with a MRD of 79, resulting into 1203 total sinograms. Reconstructed images were $256 \times 256 \times 153$ with cubic voxels of $1.25mm$ side.

  BrainPET acquisitions were used to study radionuclides separation with ^{52}Mn and ^{18}F for multiplexed PET reconstruction. Also, simulations with the geometry of BrainPET were performed to study the triple and multiple coincidences rate.

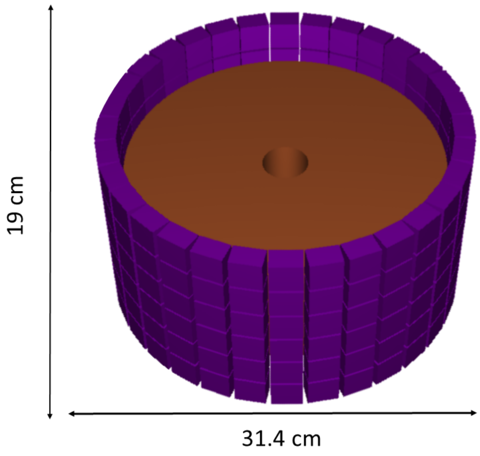

Figure 47: Schematic representation of 3TMR-BrainPET using gview3d.

3.2 List-mode files analyzer

Different scanners were used in this thesis. Each one of them usually requires a specific software to read and analyze the coincidences detected by the scanner. A single code, which can read and process list files from some of the most usual scanners, clinical and preclinical, has been developed in the group, and it is described in this chapter. The scanners that are supported by the tool developed in this thesis are:

- **Clinical scanners:**
  - Siemens Biograph scanners: including True Point (also True Point – True View), mCT, mMR and Vision.
  - 3TMR-BrainPET PET/MR scanner.
- **Preclinical scanners:**
  - Inveon PET/CT scanner.
  - SuperArgus PET/CT scanner.

3.2.1 Inputs and outputs

The code uses publicly available information of the list files for the Biograph [Siemens, 2019a] and BrainPET scanners to obtain sinograms in a format that can be easily read, for the Super-Argus scanner we used private information provided by the manufacturer, for the Inveon scanner, we obtained the information from published works [Bindseil, 2013] [Lee et al., 2013].

An input file specifying the main features of the scanner and the acquisitions is required. This file contains information about the name of the scanner (as each scanner requires a different format for reading the coincidences file), the number of crystals in the scanner, the number of radial bins, axial compression parameters (span and MRD), energy window if that information is included in the list mode file and the number of neighbour coincidences to search triple coincidences (to include non consecutive triple coincidences, specially important when the activity of the source is very high). Also a working directory and the name of the coincidences file are required.

The code produces the following output files from the input list of coincidences:

- **Sinograms:**
  - Double coincidences sinogram: in this sinogram, prompt double coincidences are gathered as they are written into the list file. These coincidences are not corrected by random, scattered or spurious background coincidences. However, triple coincidences are not included in this file, but instead in triple sinograms. In general, this is the information provided in the sinograms given by most scanners.
  - Random coincidences sinogram: the code uses a delayed coincidence window to estimate the random coincidences detected by the scanner.
  - Triple coincidences sinogram: when a triple coincidence occurs (double coincidence plus a second coincidence produced by the additional gamma ray emitted by the radionuclide), during the process, two different coincidences sharing a vertex (the same crystal involved) and with a small time difference between them are observed. We can assume these kind of events as triple coincidences.
  - Triple random coincidences sinogram: triple coincidences, produced by the simultaneous detection of three different gamma rays, may come from different sources. When the three gamma rays come from the same emission (positron annihilation, plus an additional prompt gamma ray), they are considered as a true triple, however, the additional gamma ray could come from a random coincidence, which is considered as a true-random or a random-true depending on the true coincidence is the first or the second to be gathered. In these cases, usually the coincidence does not come from a true triple, but from a true double in coincidence with a random double. That is why usually, there is a contribution to triple prompts similar to the prompt double sinogram, and other similar to random double sinogram. We consider both types of coincidence as random triple and the code generates a different output for each. Finally, it may occur that both coincidences forming a triple coincidence come from two random events, these contribution is gathered in another sinogram.
  - Bad triples: when looking for triple coincidences, one should look into events arriving to the detector simultaneously, but sometimes, between the two coincidences forming a triple, other events are gathered. These contributions are particularly important when the activity of the source is high. To remedy this,

we look also into several events after the first one to look for another sharing a vertex that can be considered as a triple coincidence. This has to be done carefully, because if one looks too far, two different true double coincidences that randomly share a vertex, could be considered wrongly as a triple coincidence.

- **Other output files:**
    - sinogram_info.txt: contains the main information about the sinogram written.
    - time.txt: contains the information of the time stamps during the read of the list file. It is written every fixed number of time stamps. It includes also the number of prompt and random double and triple coincidences gathered until each time stamp.
    - Total_counts.txt: contains the information about the total counts of each type gathered in the sinograms. It also considers the counts that are geometrically outside the sinograms and, thus, are not included into them. It is a useful tool to check the information inside the sinograms without opening them.

3.2.2 Sinogram format

In this thesis, we follow a commonly used criteria to generate the sinograms. Considering:

- Crystals in the same ring (row) can be numerated from 0 to the total number of crystals in each ring (row) -1. Being X_1 and X_2 the corresponding number of each one of the crystals involved in a coincidence.
- Axial crystals can be numerated from 1 to the total number of rows, being Z_1 and Z_2 the axial number of each one of the crystals involved in a coincidence.
- ρ, θ and $sino$ coordinates are discretized in the sinogram, obtaining ρ, θ and $sino$ bins. The number of coincidences in each bin is gathered in the sinogram.

Considering the previous criteria, a coincidence in a LOR with coordinates (X_1, Z_1, X_2, Z_2) is stored in the sinogram bin $(\rho, \theta, sino)$. Where:

- n_ρ = number of radial bins (specified as an input).
- n_θ = number of angular bins (determined by the half of the number of crystals).
- $\theta = (X_1 + X_2 + n_\theta + 1) module(2n_\theta)/2$
- $\rho = sign(|X_2 - X_1 - n_\theta|) + n_\rho/2$
- $sign = -1$ for $(X_1 < \theta$ or $X_2 > n_\theta + \theta)$ and $sign = 1$ else.
- $sino = Z_1 + Z_2 - 1 + offset_{slice} + offset_{segment}$ the number of sinogram.
- $offset_{slice} + offset_{segment}$ are determined by the MRD and span factor.

The number of segments (odd number) is determined by the parameters chosen for MRD and span by the relation:

$$nseg = 2 \cdot floor(MRD/span) + 1 \tag{52}$$

The total number of sinograms (ns) can be determined by the input parameters by:

$$ns = nz + (nseg - 1) \cdot (nz - 1 - span \cdot ((nseg - 1)/2)) \tag{53}$$

3.3 MC PET simulations

3.3.1 PeneloPET

PeneloPET is a Monte Carlo simulation tool [España et al., 2009] [Lopez-Montes et al., 2019] for PET based on PENELOPE [Salvat et al., 2008], a code for the MC simulation of coupled transport of electrons, positrons and photons which includes the main physical interactions of the particles with the matter allowing complex materials and geometries definitions. It is suitable for the range of energies between 100 eV and 1 GeV.

PeneloPET was first released in 2009 by the Nuclear Physics Group at Complutense University of Madrid. Since the first release, some features have been improved and added, making PeneloPET more user-friendly, faster and with improved physical considerations which make the simulations more realistic and useful. These new features include improved simulations for positron range for different materials and radionuclides [Cal-González et al., 2013], a detailed simulation for self coincidence detection [Conti et al., 2017] including the case of the inner activity of the crystals of the scanner as well as the possibility of simulating non-pure beta emitters and multiple gamma emissions [Cal-González et al., 2014], incorporating the possibility of including detailed decay cascades for the nuclei and providing more realistic simulations.

In this thesis, some improvements have been done to the PeneloPET code, including a library with many examples for geometries similar to the main current PET scanners, both for preclinical and clinical PET (see figures 48 and 49), also, new non-standard β^+ emitters as ^{52}Mn have been added to the database of PeneloPET, including the detailed cascade of particles emission and the positron range for these radionuclides. All these improvements were included into a new version of PeneloPET released in 2019 [Lopez-Montes et al., 2019].

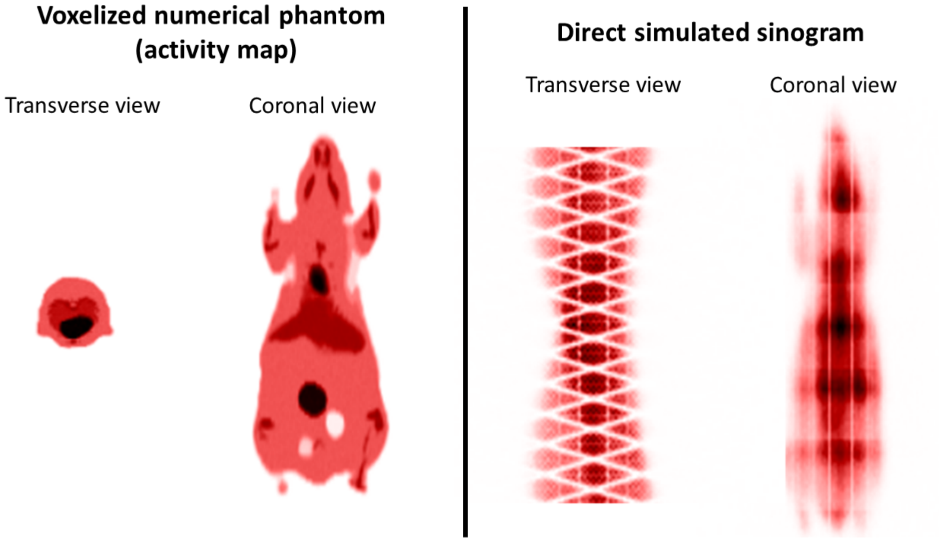

Figure 48: Mouse numerical phantom included with PeneloPET v3.0, simulation using Super-Argus geometry.

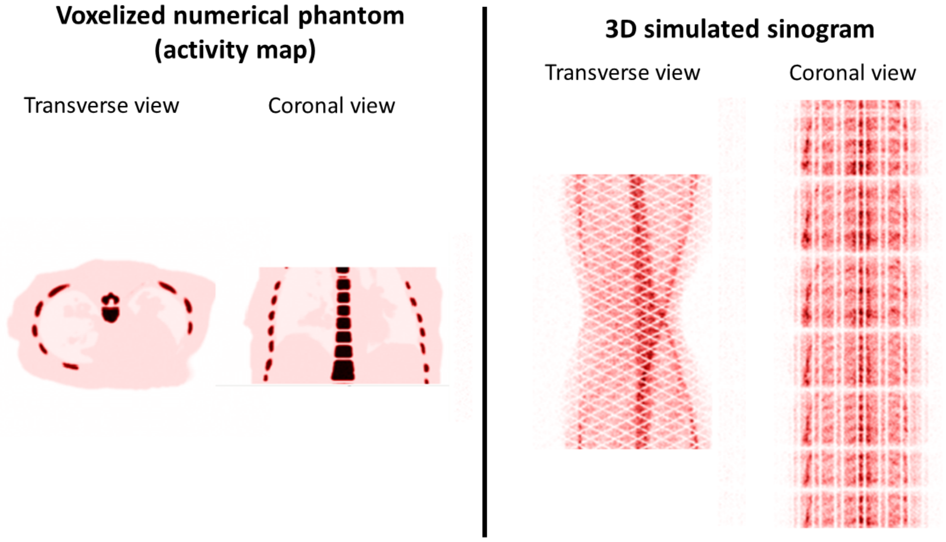

Figure 49: Human torso numerical phantom included with PeneloPET v3.0, simulation using Biograph TPTV PET/CT clinical scanner.

3.3.2 MCGPU-PET

MCGPU-PET is a GPU based Monte Carlo simulator oriented to PET [Badal et al., 2018]. It is based on a existing version of a MC-GPU oriented to X-rays [Badal and Badano, 2009] [Sempau et al., 2011]. MGGPU-PET is based on the libraries and particle transport calculations of PENELOPE [Salvat et al., 2006] and it uses a massive parallelization using GPU to drastically improve the simulation time [Badal and Badano, 2009] [Sempau et al., 2011] [Badal and Sempau, 2006].

MCGPU-PET may simulate realistic PET acquisitions including all the important physics during the emission and transportation of the particles to the scanner, represented in this simulator by a phase space at certain radius from the center of the FOV. MCGPU-PET does not simulate the interactions of the particles inside the scanner. If needed, this contribution can be simulated using analytical kernel convolutions or using the results of the simulations of MCGPU-PET in other MC simulator.

This simulator is suitable to estimate scatter and spurious background contributions due to the low time required to obtain realistic simulations. Usually, scatter coincidences are estimated using analytical techniques as SSS, although fast, SSS is not always as accurate as needed. For that reason, MC simulators have been proposed to obtain realistic and accurate estimations of the contribution of scattered events, however, they are not generally used due to the high computational time required. MCGPU-PET allows to perform realistic and accurate simulations of scatter in really short times, which makes it ideal to obtain scatter coincidences estimations. On the other hand, spurious background estimation models have been proposed using analytical kernels [Beattie et al., 2003] or just even assuming a background similar to random coincidences [Watson et al., 2008] and adjusting the tail of the radial sinogram profiles to match random, scatter and spurious background coincidences. These methods, although useful in some cases, introduce some inaccuracies as using 2D kernels instead of 3D that would increase the computational time or assuming some models that are not exact. MCGPU-PET can simulate fully 3D acquisitions in several seconds and allows to include the main important physical effects to obtain realistic estimations of the contribution of spurious background when using certain non-standard β^+ emitters.

MCGPU-PET can provide list mode files or 3D sinograms allowing to select sinogram parameters as radial bins or axial mashing (span factor and MRD). Both list files and 3D sinograms, include information about true and scattered coincidences. Also, another simulation mode has been included to estimate spurious background coincidences. In it, instead of annihilation events with two photons generated in opposite directions, events in which one of the photons is emitted in a random direction are simulated instead. These events differ from random events since the emission point is the same for both photons while in random coincidences this does not occur. Random coincidences are not simulated in the current version of MCGPU since most scanners include their own random coincidences estimation using delayed time windows.

In this thesis, some important contributions have been included into MCGPU-PET as the inclusion of 3D sinograms for PET or the improvement of the information included in the list mode files. Also, MCGPU-PET has been broadly tested for different scanners and configurations, including both clinical and preclinical cases and for a wide number of different radionuclides to test the estimation of spurious background and scattered events contributions. We present some of the most important results using MCGPU in the results section.

3.3.3 Other MC simulators used in this thesis

Some other MC simulators have been used for different purposes. In order to simulate the positron range (PR) of different radionuclides, the MC tool penEasy [Sempau and Andreo, 2006] has been used. Some modifications were made to the code since we are interested in obtaining the blurred images with a realistic PR effect for different radionuclides and activity distributions. For our case, the inputs for this adapted version of penEasy were the 3D images of the activity distribution together with the density and material information of the tissues and the output consisted on the 3D blurred activity distribution images with the PR effect. PenEasy can simulate properly the PR in heterogeneous tissues, being able to consider the path travelled by the positrons from the emission point to the annihilation one.

Also, the energy distributions of the studied radionuclides were set as inputs for this penEasy version. We obtained these distributions using another MC simulator, PenNuc [García-Toraño et al., 2019] which considers properly the energy spectrum for different nuclear emissions.

3.4 GPU-based iterative reconstruction (GFIRST)

We used an adapted version of the GPU-based PET fully 3D reconstruction code GFIRST [Herraiz et al., 2006] based on OSEM-EMML algorithm. This tool has been also adapted for the different scanners used in the thesis, including the posibility of reconstructing doubles and triple coincidences. Triple coincidences can be reconstructed using VLORS or standard sinograms with a background subtraction. Due to the lower statistics of triples coincidences in the acquisitions comparing with the double, standard, coincidences, in the reconstruction code, a filter guided by double coincidences is applied to triples, achieving improved noise-resolution rate in the triple images while not affecting the reliability of the images. Also, the code is adapted to include corrections to the data such as random, scatter and spurious background subtraction.

4 MCGPU-PET

In this section, we present the contributions of this thesis related to the MCGPU-PET open source code simulator. Mainly some important features were added to the simulator as the generation of 3D sinograms, some modifications in the outputs and the inclussion of new physical effect as non-collinearity to the code. Moreover, we validated the code and some of its potential applications for PET image correction.

4.1 MCGPU-PET code description

MCGPU-PET is an open source code developed in collaboration between UCM-GFN and the US Food and Drugs Administration (FDA) group. The code is based on a pre-existing version of a MCGPU oriented to X-rays and developed by Andreu Badal and collaborators at the US FDA [Badal and Badano, 2009]. The models for the main physical interactions are based on PENELOPE as described in [Badal and Badano, 2009], also in that work there is a description of the main methods used as the Woodcock tracking algorithm [Woodcock et al., 1965] or the techniques used to accelerate the code using GPU.

The MCGPU-PET is prepared to read voxelized images of the activity map wanted to simulate. Also, in order to proper determine the interaction of the particles during their path, density map and segmented material images are read. These three images (activity, density and material), need to be generated as vectors in plane text format (ASCII). The code expect to read the images from a single zipped file which should include a header, which must include:

- A line indicating the version of the section opening line.
- A second line indicating number of voxels (in x, y and z directions).
- A third line with the size of each voxel (can be different in each direction).
- Two more lines containing the information of the column where material and density information is located respectively.
- A line to check blank lines.
- A last line to indicate the ending of the source section.

After the header, the information of the images should be included, the first two columns must contain the material and density images in the order specified in the header, the third column contains the activity information.

The information of the sources must be included and referenced into a global input. This input is a text file containing the main information about the simulation parameters.

The input file is divided into 8 different sections, each one describing a part of the simulation as shown in figure 50.

```
# >>>> INPUT FILE FOR MC-GPU v1.3 >>>>>>>>>>>>>>>>>>>>>>>>>>>>>>>>>>>>>>>>>>>>>>>>>>
#
#
#                  @file    MC-GPU_v1.3.in
#                  @author  Andreu Badal (Andreu.Badal-Soler{at}fda.hhs.gov)
#                  @date    2012/12/12
#

#[SECTION SIMULATION CONFIG v.2016-07-05]
12345678                        # RANDOM SEED (ranecu PRNG)
0                               # GPU NUMBER TO USE WHEN MPI IS NOT USED, OR TO BE AVOIDED IN MPI RUNS
32                              # GPU THREADS PER CUDA BLOCK (multiple of 32)
1                               # NO OBJECT (0=OBJECT, 1=No object)


#[SECTION SOURCE PET SCAN v.2017-03-14]
 5000.0     # 300                # TOTAL PET SCAN ACQUISITION TIME  [seconds]
 70000000000.0                         # ISOTOPE MEAN LIFE [s]
   1    0.0  # SUV=9, other brain   # TABLE MATERIAL NUMBER AND VOXEL ACTIVITY [Bq]: 1==1st_material ; 0==end_of_list
   0    0.0


#[SECTION PHASE SPACE FILE v.2016-07-05]
 MCGPU_PET.psf                  # OUTPUT PHASE SPACE FILE FILE NAME
 0.0  0.0  0.0  22.0  -42.78   # CYLINDRIC DETECTOR CENTER, HEIGHT, AND RADIUS: X, Y, Z, H, RADIUS [cm] (IF RADIUS<0: DETECTOR CENTERED AT THE CENTER OF THE VOXELI
ZED GEOMETRY)
 15000000                      # PHASE SPACE FILE SIZE (MAXIMUM NUMBER OF ELEMENTS)
  0                              # REPORT TRUES(1), SCATTER (2) or BOTH (0)
  0                              # REPORT PSF (1), SINOGRAM (2) or BOTH (0)

#[SECTION DOSE DEPOSITION v.2012-12-12]
YES                             # TALLY MATERIAL DOSE? [YES/NO] (electrons not transported, x-ray energy locally deposited at interaction)
NO                              # TALLY 3D VOXEL DOSE? [YES/NO] (dose measured separately for each voxel)
mc-gpu_dose.dat                 # OUTPUT VOXEL DOSE FILE NAME
  1  400                        # VOXEL DOSE ROI: X-index min max (first voxel has index 1)
  1  400                        # VOXEL DOSE ROI: Y-index min max
  1  109                         # VOXEL DOSE ROI: Z-index min max


#[SECTION ENERGY PARAMETERS v.2019-04-25]
0.12      #ENERGY RESOLUTION OF THE CRYSTALS
435000.0      #ENERGY WINDOW LOW (keV)
650000.0      #ENERGY WINDOW HIGH (keV)


#[SECTION SINOGRAM PARAMETERS v.2019-04-25]
22.0 #FOVz (AXIAL FOV) in cm //22.0 16.4
55   #NUMBER OF ROWS
672  #TOTAL NUMBER OF CRYSTALS
336  #NUMBER OF ANGULAR (NCRYSTALS/2)
400  #NUMBER OF RADIAL BINS // 391
109  #NUMBER OF Z SLICES
400  #RES
700  #NE
49   #MRD
11   #SPAN

#[SECTION VOXELIZED GEOMETRY FILE v.2009-11-30]
phantom.vox.gz          # VOXEL GEOMETRY FILE (penEasy 2008 format; .gz accepted)


#[SECTION MATERIAL FILE LIST v.2009-11-30]
/home/mpet/MCGPU/MATERIALS/air_5-515keV.mcgpu.gz
/home/mpet/MCGPU/MATERIALS/water_5-515keV.mcgpu.gz
#/home/petgfn/ALEX/MCGPU/MATERIALS/water_5-515keV.mcgpu.gz
#/home/mpet/MCGPU/MATERIALS/air_5-515keV.mcgpu.gz             # 1
#/home/mpet/MCGPU/MATERIALS/water_5-515keV.mcgpu.gz           # 2 agua

# >>>> END INPUT FILE >>>>>>>>>>>>>>>>>>>>>>>>>>>>>>>>>>>>>>>>>>>>>>>>>>>>>>>>
```

Figure 50: Example of an input file for a simulation of MCGPU-PET.

Additionally, when the code is executed, the user may add a 0 in the command line. In this mode, the two photons simulated are not co-linear, and the direction of one of them is set randomly. This mode is used to estimate the contribution of spurious background due to additional prompt-γ rays.

After the simulation, the code give several outputs. The information about the simulation process is shown in the screen during the process. Furthermore, depending on the inputs selected, some other outputs can be found:

- Trues and scatter sinograms: the format of the sinograms is similar to those described in section 3.2.2. MCGPU generates sinograms for both trues and scatter coincidences as selected in the corresponding input section. Note that the contribution of random coincidences is not simulated in MCGPU-PET, this is because most scanners include tools to estimate the contribution of random coincidences and are assumed to have been corrected before and not considered in the simulation. One of the aims of MCGPU is to provide fast and accurate simulations for scatter coincidences contribution and, for the moment, not including random coincidences accelerate and simplify the simulation process. Other important point about the generated sinograms is that they are produced by the coincidences getting an ideal phase space (not considering scanner geometries nor detectors). Furthermore, notice that, if these sinograms are used for correction and reconstruction, they should be corrected by attenuation and properly normalized. The normalization of the sinograms can be performed obtaining the corresponding normalization factors for the simulated geometry using the simulation of, for example, a uniform cylinder centered in the FOV and covering all the axial FOV. As in this simulation all the ideal detectors are assumed to detect the same number of coincidences, normalization factors can be obtained once and used in every simulation with the same geometry. The sinograms are generated in integer mode as unsigned integers.

- Phase space file (PSF): it is the list-mode file containing all the information about the photons arriving the phase space. Since this file is usually very large, it can be omitted, using instead the sinograms if no further information is needed. Two files are generated, one plain text file with the first coincidences information of the simulation (see figure 51) and another one with the full simulation which is written in binary raw mode to save memory. One important thing about the events of this PSF file is that they are not written ordered in time. This is because of the atomic sums of the GPU acceleration, which are regular GPU sums that ensures that no other threads can perform modifications on the same location until the current sum is complete. However, each one of the coincidences in this file has its own time stamp so they can be ordered using an external tool provided with the code. Having the events ordered in time of arrival to the detector can be useful for example to estimate the random coincidences from the list-mode using delayed time windows but for the most relevant applications of MCGPU-PET as scatter correction it is not needed.

```
#
#     ********************************************************************************
#     ***         MC-GPU-PET, version 0.1 (http://code.google.com/p/mcgpu/)      ***
#     ***                                                                        ***
#     ***                     Andreu Badal (Andreu.Badal-Soler@fda.hhs.gov)      ***
#     ********************************************************************************
#
#  *** SIMULATION IN THE GPU USING CUDA ***
#
#  Phase space file of particles arriving at the ideal cylindrical detector surrounding the object.
#
#        Elements in this PSF   = 15000000
#        Allocated PSF elements = 15000000
#        PET acquistion time    = 5000.000000 s
#        mean life isotope      = 70000001024.000000
#        Material activities:
#        PSF detector center    = (40.00000,40.00000,10.90000) cm
#        PSF detector height and radius = 22.00000, 42.78000 cm
#        Input voxel file       = phantom_T.vox.gz
#
#        PSF includes both True and Scatter coincidences.
#        Reported both PSF and Sinogram.
#
#        Reporting only the 100 first elements below in ASCII. Complete PSF available in binary form in the file MCGPU_PET.psf.raw
#        Binary size for each reported variable:
#               - emission_time (ps): unsigned long long int
#               - travel_time (ps): float
#               - emission voxel: int
#               - energy (eV), z (cm), phi (deg), vx, vy, vz: float
#               - index1 (Flag for scatter: =0 for non-scattered, =1 for Compton, =2 for Rayleigh, and =3 for multiple scatter), index2: short int
#
#  [emission_time (ps)]    [travel_time (ps)]    [emission voxel]  [energy (eV)]  [z (cm)]  [phi (deg)]  [vx]  [vy]  [vz]  [index1]  [index2]
# ==============================================================================================================================================
154112898171597 496.193085 700634 478181.437500 3.242739 -0.910178 0.578586 -0.714130 0.394026 0 0
154112898171597 811.097717 700634 496894.468750 -10.100079 -0.633983 0.871568 -0.490264 -0.003224 0 0
222896456895441 1356.488159 701031 484349.437500 6.068252 -1.712020 -0.320013 -0.850811 0.416788 0 0
```

Figure 51: Initial part of a phase space file generated by MCGPU-PET.

- Background sinogram: when this method is selected, the code will also provide a 3D sinogram of the estimated map of spurious background coincidences due to additional prompt-γ rays. This sinogram has a similar format to the trues and scatter sinograms but it should be considered that some method to estimate the amount of coincidences would be required, for instance, adjusting the coincidences to match the activity outside the image after scatter and other corrections have been made.

- Emissions map: it is the image of the distribution of emitted counts that have arrived to the phase space. One image is generated for the true coincidences and other for scatter coincidences. If the option is selected, the code will also provide the map of emissions for spurious background coincidences.

4.1.1 MCGPU-PET current limitations

MCGPU-PET has currently some limitations: It does not simulate a real detector, as all photons are collected in the phase space, and the interactions between detector and photon are not simulated. For this reasons, geometrical effects as inter detector gaps are not simulated using the code.

The emission, transport and annihilation of the positrons is modelled with a CPU code. It produces very large files if the PSF output is selected. This can be solved by using sinogram outputs.

4.2 MCGPU-PET validation

4.2.1 Methods

In this section we explain how we compared the results of MCGPU-PET with a validated software as GATE. It is important to take into account that, in contrast with MCGPU-PET, GATE does not generate an ideal acquisition, in which all photons are collected, and the scanner does not have gaps. These differences are going to affect the comparison between the two software codes.

In an ideal detector, all photons that arrive at its surface are fully detected. In a real detector we have a volume, because detectors have a considerable length, in the case of the Biograph mCT PET/CT scanner, the scintillating crystal has a length of 2 cm. In the case of photons which are produced far away to the center of the scanner can be detected in the lateral of the detector, not in the main surface. This problem is known as elongation effect [Moses and Derenzo, 1990]. Super-dense Pb has been chosen to simulate an ideal detector where all photons are detected via photoelectric effect, because Pb has a high absorption cross section for these energies. Furthermore, we used a larger density (1135 g/cm^3) for the Pb sections, to increase the number of targets per area and increase the absorption probability.

Therefore, several GATE simulations were performed to evaluate the impact of the phase-space approximation (i.e. using a modified phase-space file as an ideal detector), one with an Inveon PET/CT scanner, another with an Inveon PET/CT scanner where the scintillating crystals are composed by super dense lead (1135 g/cm^3), and finally with an Inveon PET/CT scanner where the scintillating crystals are composed by super-dense lead and the crystals length is 0.05 cm for all crystals (see table 3). These geometries were used to simulate both mouse and rat like phantoms to study the scatter fractions using each approximation and to compare them with experimental results.

	Scintillators	
	Material	Length
Scanner MCGPU	Ideal (Phase-Space)	Ideal (Phase-Space)
Scanner GATE #1	LSO (7.4g/cm^3)	2
Scanner GATE #2	Super-dense Pb (1135 g/cm^3)	2
Scanner GATE #3	Super-dense Pb (1135 g/cm^3)	0.05

Table 3: Scanner scintillators parameters.

For the comparison with GATE, the CPU used corresponds to a Intel(R) Xeon(R) CPU

E5-2640 v4 @ 2.40GHz. x86_64. The GPU used was the GeForce GTX 1080. Compute capability: 6.1, Number multiprocessors: 20. Clock rate: 1.73 GHz. Memory: 8119.188 Mbytes using the same CPU.

Furthermore, we simulated an IQ-NEMA phantom for preclinical scanners using GATE and MCGPU-PET. We use it to compare the sum of the radial profiles of the sinogram for trues and scatter estimated with each one of the codes.

We also tested and validated MCGPU-PET against real acquisitions. For this purpose, we simulated an IQ-NEMA phantom using the geometry of Biograph mCT PET/CT scanner and we compared the output trues and scatter sinograms with the real sinograms acquired with Biograph mCT and with the estimation using SSS in the case of scatter sinogram.

In MCGPU-PET the ideal detector will have the same height and diameter as the Biograph mCT scanner. As we need six thousand times more time for obtaining a GATE estimation than a MCGPU-PET estimation with the same number of counts, we scaled the total counts of MCGPU-PET to the ones obtained with GATE.

The input activity was obtained from an initial reconstructed image without scatter or background corrections. The density and material maps were obtained from the CT images. The voxel size of the simulations was $2 \times 2 \times 2$ mm with a total of $400 \times 400 \times 109$ voxels in the image.

4.2.2 Results

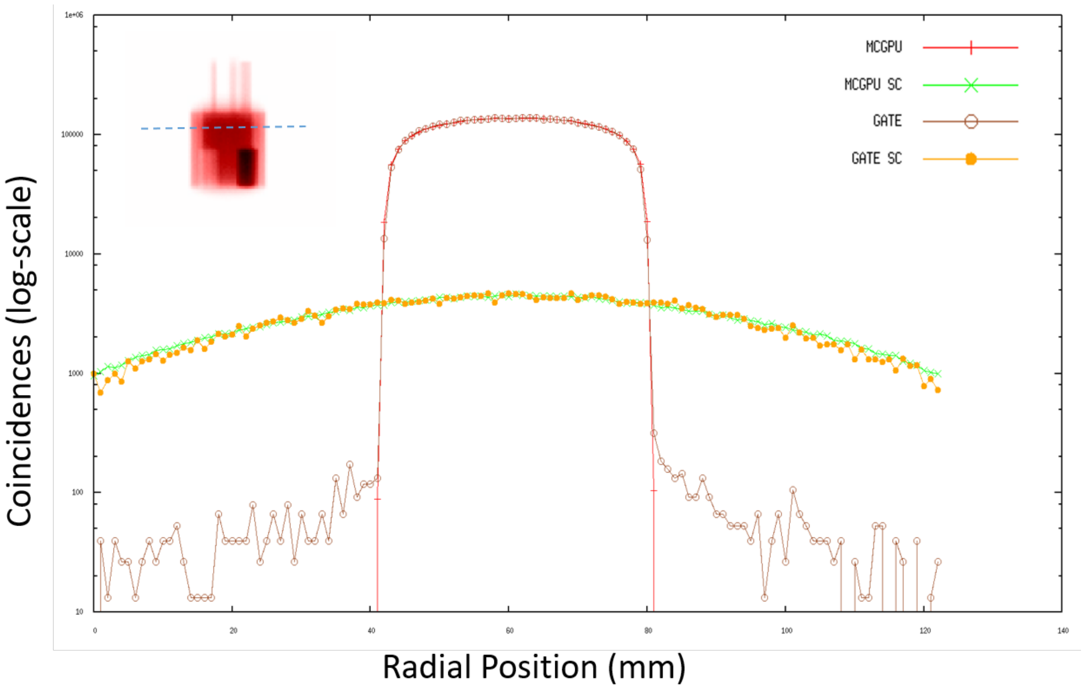

Figure 52: Radial profile of the True and Scatter coincidences of the IQ-NEMA Phantom for preclinical scanners from MCGPU-PET and GATE

Figure 52 shows a radial profile in the sinogram of both the Trues and Scatter obtained from MCGPU-PET and GATE simulations of the preclinical IQ phantom for the Inveon PET/CT scanner. The amount of time required to obtain $1 \cdot 10^6$ coincidences with GATE using 1 CPU was 12 hours, while MCGPU obtained $40 \cdot 10^6$ coincidences in 7.8 s using 1 GPU (see details in the methods section).

The results from the NEMA analysis of these simulations obtained with mouse and rat-size phantoms are shown in table 4, together with the experimental results from [Bao et al., 2009].

	MCGPU-PET (PHSP)	**GATE (PHSP)**	**GATE(LSO)**	**EXP. (*)**
MOUSE-SIZE PHANTOM	6.7 %	6.4 %	7.9 %	7.8 ± 1.0 %
RAT-SIZE PHANTOM	16.0 %	17.3 %	20.8 %	17.2 ± 2.0 %

Table 4: Simulation time for different cases. INVEON SCATTER FRACTION (NEMA NU4-2008) (Bao, 2009) For GATE simulations we used LSO (standard simulation) but also Lead with d=1000.0 g/cm^3 as a surrogate of Phase-Space File ideal detector.

With real acquisitions, we do not have a ground-truth reference for the Scatter estimation, only the SSS algorithm from Siemens, but we compare the results from both methods in figure 53.

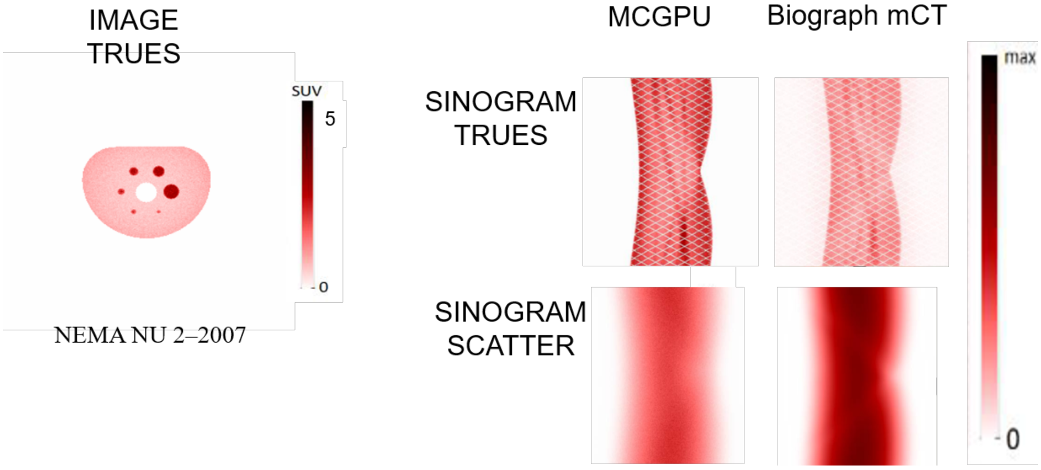

Figure 53: (A) Activity distribution of the IQ Phantom (from reconstructed PET acquisition) (B) True and Scatter coincidences estimated with the MCGPU-PET code and from the scanner SSS algorithm.

The computing times and total number of coincidences of the results presented in figures 52 and 53 are shown in table 5.

SIZE (voxels)	TIME (s)	# Coincidences
256×256 × 128	69.56	60 M
336×336 × 109	433.96	150 M

Table 5: Simulation time for different cases. (Up) IQ-NEMA phantom for Inveon PET/CT scanner. (Down) IQ-NEMA phantom for Biograph mCT PET/CT scanner.

An example of an output of the MCGPU-PET with information about the execution time, total number of simulated histories and sinogram information is shown in table 6.

EXECUTION TIME	
Execution time including initialization, transport and report:	27.050 s.
Time spent in the Monte Carlo transport only:	20.450 s.
Time spent in initialization, reporting and clean up:	6.600 s.
Total number of simulated histories:	861598928 (each positron produces 2 histories)
Total speed (including transport, initialization and report times) [γ-rays/s]:	31,852,086.06
Total speed Monte Carlo transport only (using 1 thread) [γ-rays/s]:	42,131,976.92
SINOGRAM INFORMATION (AFTER ENERGY WINDOW APPLIED)	
Number of true coincidences in the sinogram	16,103,927
Number of scatter coincidences in the sinogram	11,059,791
Scatter Fraction	0.407
Size of the 3D sinogram	255 $\times$336 $\times$ 159

Table 6: Example of output produced in a simulation of MCGPU-PET.

4.3 Applications for Fast Scatter and Prompt-Gamma Corrections of MCGPU-PET

4.3.1 Motivation.

Scatter coincidences are an important source of inaccuracy in PET imaging, as they introduce a non-uniform background in the reconstructed images that affect the image contrast and quantification. This effect becomes even more pronounced in modern PET scanners with long axial field-of-view (FOV) and larger acceptance angle. Scatter coincidences are usually estimated using fast analytical techniques such as single-scatter simulation (SSS) [Watson et al., 1996], which provide accurate enough results in most cases. Nevertheless, in some cases, their simplifications and assumptions, such as considering only single-scattered events, may not be realistic enough and images may show strong artifacts, due to the under- or over- estimation, which limits their quantitative accuracy.

Another background affecting the quality in the images may be present when using PET radionuclides such as ^{124}I, ^{86}Y, ^{52}Mn, ^{82}Rb, and ^{44}Sc, that emit one or more prompt-γ

photons together with the β^+ emission [Conti and Eriksson, 2016] [Cal González, 2015]. In that case, spurious coincidences may be produced between one of the annihilation photons and one of the additional prompt-γ rays emitted in a random direction with no correlation with the annihilation process. Several correction models have been proposed using analytical kernels [Beattie et al., 2003] or just even assuming a background similar to random coincidences [Watson et al., 2008] and adjusting the tail of the radial sinogram profiles to match random, scatter and spurious background coincidences. These methods, although useful in some cases, introduce some inaccuracies as using 2D kernels instead of 3D that would increase the computational time or assuming simple models that are not physically correct.

For that reason, Monte Carlo (MC) simulations have been proposed to obtain realistic and accurate estimations of the contribution of scattered and prompt- events. However, they typically require large computational times, which are not compatible for its routine use in the clinical practice. We propose the use of MCGPU-PET to obtain fast and realistic simulations to estimate the contribution of scattered events and spurious background due to non-standard β^+ emitters.

4.3.2 Methods.

We have used data from the Siemens Biograph Vision PET/CT scanner [Van Sluis et al., 2019]. To validate the simulator, we first used data from a 30 mins acquisition of an IQ phantom filled with 95.9 MBq of ^{18}F-FDG, with 4:1 activity ratio between the spheres and background in one study, and with 27.2 MBq of ^{124}I in another study. A challenging situation was evaluated using a phantom with a cylinder inside a larger phantom containing 73.2 MBq of ^{18}F-FDG (which replicates a scan of a bed position centered on a hot bladder), with a $\approx$200:1 activity ratio in the cylinder (bladder) with respect to the background. Finally, the proposed method was evaluated with patient data from an ^{18}F-FDG brain PET scan with 140.0 MBq at scan time and 300 secs scan duration.

We would like to thank Walter Jensen from Essen (Germany) for the ^{124}I IQ phantom dataset, and John Prior from Lausanne (Switzerland) for the PET brain scan dataset, also, we acknowledge Maurizio Conti and Jorge Cabello from Siemens Medical Solutions USA, Inc. Knoxville, TN, USA for their contribution providing some of the acquisitions and images presented in the results of this section.

We also show and extreme case acquired in the BrainPET insert PET/MRI scanner in Jülich, Germany. This is a phantom composed of several cylinders filled with a mixture of two different radionuclides, ^{18}F and ^{52}Mn, which emits a cascade of prompt-γ rays introducing and important background of spurious coincidences. The “Background” compartment contained ^{18}F with an activity concentration of 16 kBq/ml, ^{52}Mn activity concentration in “Hot 1” compartment was 59 kBq/ml. The “Hot 2” compartment was filled with a solution of both 44kBq/ml of 52Mn and 63kBq/ml of ^{18}F. Another compartment was made of teflon and was left empty, in it we can appreciate the effect of scattered coincidences.

We acknowledge Kai Giesen, Lutz Tellmann, Stefan Spellerberg, Ingo Spahn and Christoph Lerche (Institute of Neuroscience and Medicine, Forschungszentrum Jülich GmbH, Germany) for providing the acquisitions of the BrainPET used in this section.

In all cases, the MCGPU-PET was used to estimate the scatter (and spurious background in the case of ^{124}I acquisitions). The input activity was obtained from an initial reconstructed image without scatter or background corrections, this activity was normalized to the mean activity of the initial reconstructed image and the simulation time was 5000 seconds to get enough statistics. The density and material maps were obtained from the CT images (in the case of the BrainPET PET/MRI from a μ-map obtained from the MR image). The voxel size of the simulations was $1.65 \times 1.65 \times 1.65$ mm for the Biograph Vision PET/CT scanner and $1.25 \times 1.25 \times 1.25$ mm in the case of BrainPET.

As scatter and background contributions are usually smooth, we used Gaussian filters to reduce the variability on the output sinograms for scatter and spurious background coincidences. Standard scatter and spurious background estimation requires also a scale factor to match the estimated distribution with the measured data. This factor provides an effective way to take into account the sensitivity of the specific scanner. The factor is obtained by minimizing the likelihood as described in [Reddin et al., 2018]. The sum of Trues, scatter and spurious background should match the data. The initial estimations are then used to obtain an image reconstruction with significantly reduced background. In normal scenarios, the scatter estimation needs to be performed only once. However, in challenging cases, the scatter simulation may need to be repeated to refine the scatter estimation. These calculations may be incorporated within image updates in an iterative algorithm to speed-up the whole reconstruction process.

4.3.3 Results.

Figure 54 shows the resulting reconstructed ^{18}F-FDG IQ phantom using MCGPU-PET-based scatter correction, and profiles across radial bins of the sinogram of prompts and randoms of the measured data, and trues and scatter with MCGPU-PET.

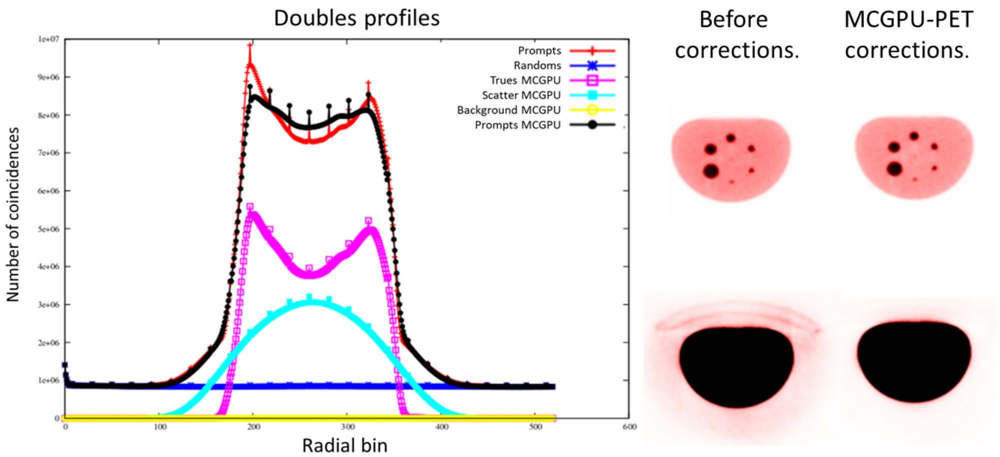

Figure 54: (Left) Radial profiles for the different contributions given by MCGPU-PET. (Right) Reconstructed images before and after MCGPU-PET corrections. Images using a 1% threshold of the maximum intensity pixel are also shown where scatter correction can be better appreciated.

Figure 55 shows a brain dataset reconstructed using SSS and MCGPU-PET scatter correction, showing comparable results, with differences 5%. Figure 56 shows the reconstructed bladder phantom using SSS and MCGPU-PET for scatter correction, a profile across the central axial slices, and their relative differences. It can be observed how using SSS the typical halo effect is present, while using MCGPU-PET the artifact is greatly corrected. It can be more clearly observed in the profiles, where there is up to a 100% difference between the images with SSS and MCGPU-PET around the hot cylinder, where the artifact is observed. These images were provided by Jorge Cabello from Siemens Medical Solutions (USA).

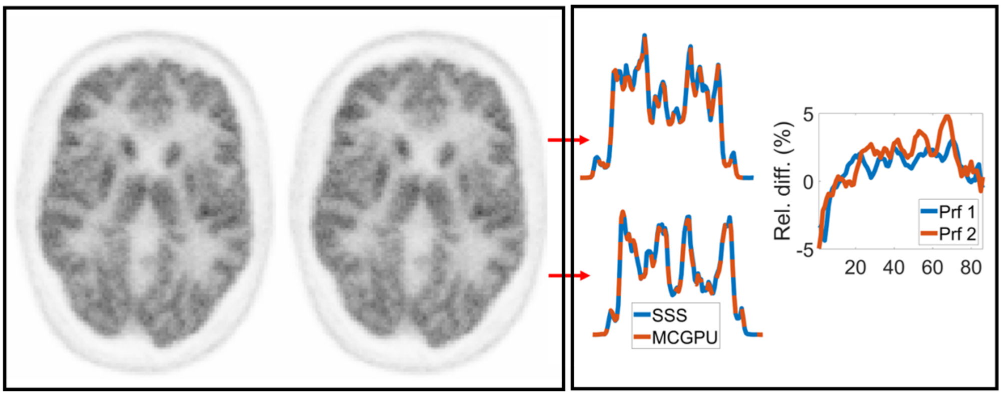

Figure 55: Patient study with scatter correction obtained with SSS (left) and with MCGPU-PET (right), together with profiles across both images, and relative difference between profiles obtained with SSS and MCGPU. (Provided by Jorge Cabello, Siemens Medical Solutions USA).

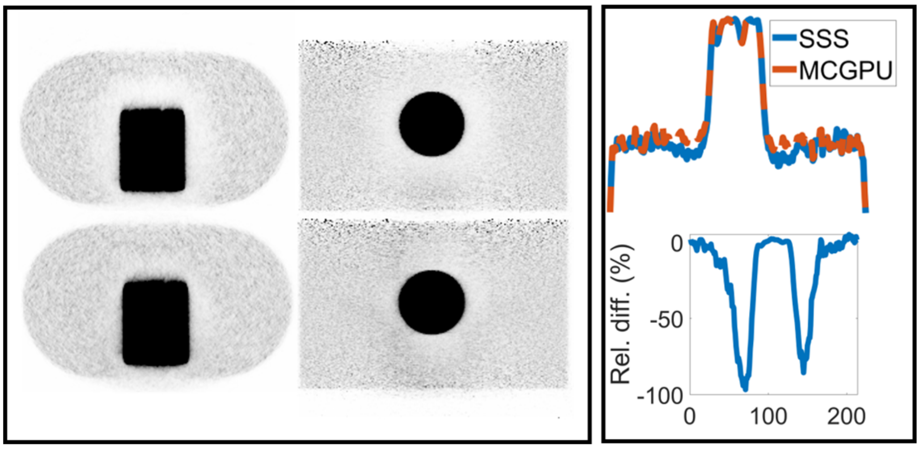

Figure 56: Axial and coronal slices of the bladder phantom with scatter correction using SSS (top) and MCGPU (bottom), together with horizontal profiles across the axial slices and relative differences. (Provided by Jorge Cabello, Siemens Medical Solutions USA).

In figure 57, we show the resulting reconstructed ^{124}I IQ phantom obtained without scatter correction and with MCGPU-PET based scatter correction, and the same profiles across the sinograms as in figure 54. In this case, also background correction for spurious prompt-γ coincidences is performed using MCGPU-PET. The background contribution can be clearly appreciated in the profiles as well as in the image using a threshold to better appreciate the background in the images.

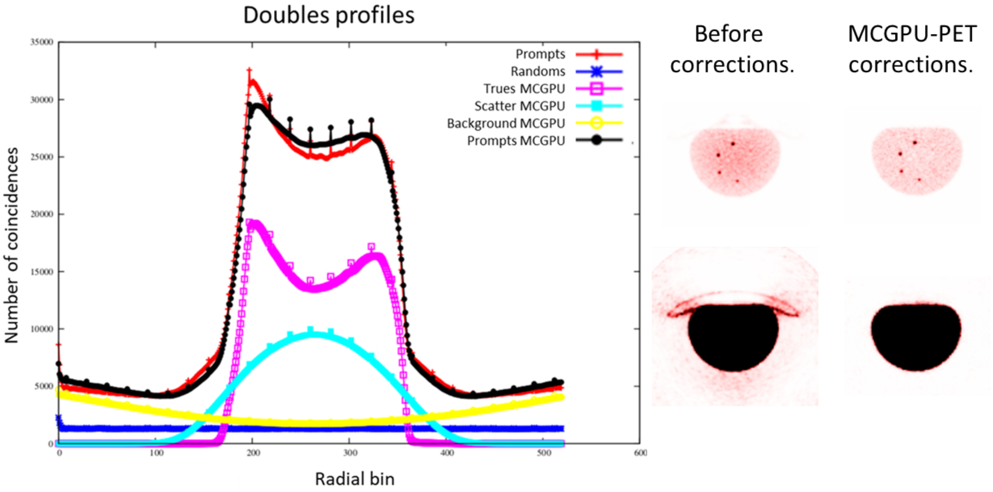

Figure 57: (Left) Radial profiles of the IQ phantom filled with ^{124}I, showing the different contributions estimated by the MCGPU-PET. (Right), reconstructed images with and without the corrections. Images using a 1% threshold of the maximum intensity pixel are also shown where corrections can be better appreciated.

Similar results of corrections using MCGPU-PET for scatter and spurious background contributions is shown in figure 58 for the acquisition of the cylinders phantom at the BrainPET scanner. In this case, due to the decay cascade of the ^{52}Mn, a higher contribution of spurious background can be clearly seen. Moreover, one of the cylinders was a teflon rod, and no activity was placed inside. However, due to scattered coincidences, in the non-corrected image, part of the activity is reconstructed inside that empty rod, this effect is clearly improved using MCGPU-PET corrections.

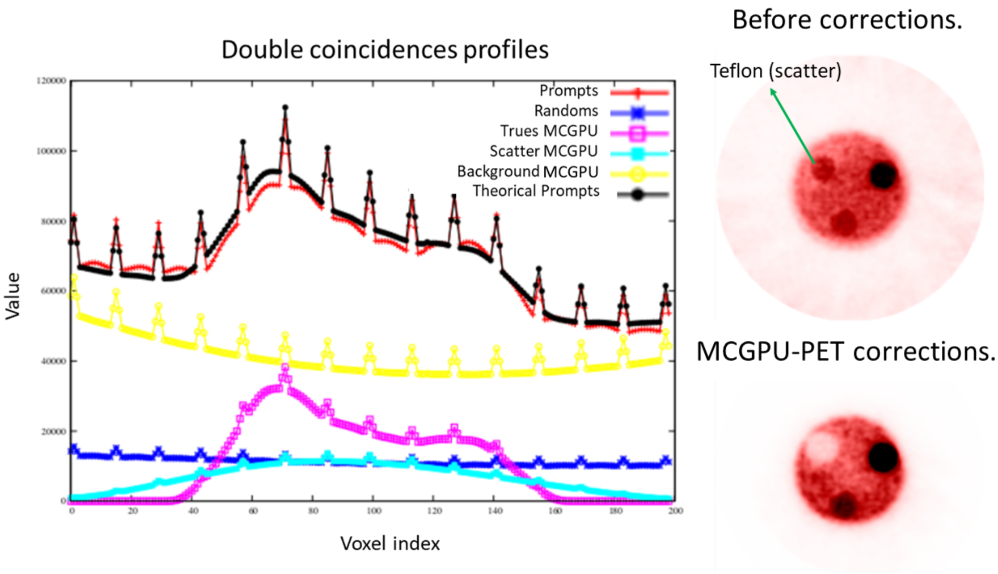

Figure 58: (Left) Radial profiles for the different contributions given by MCGPU-PET. (Right) Reconstructed images before corrections (up) and after MCGPU-PET scatter and background corrections (down).

4.4 Discussion

The main advantages of MCGPU-PET is that it allows the use of voxelized images (for both the source and the object) and that it is three orders of magnitude faster than GATE. In any case, it is important to note that MC methods require the reconstruction of the PET and μ-map images before they can be used to estimate the scatter distribution. The SSS method does not require any reconstruction for that, making it intrinsically faster than MC methods.

In this work we have shown an initial validation of MCGPU-PET. We can see from the results that there are some differences in the profile of the sinogram, it may be due in part to how the detectors response can be simulated by GATE. Although the ratios of trues and ratios of Scatter are very near to the unity, it is shown that there are differences in the profiles. These differences are reduced when a more ideal detector (thin Pb) is used in GATE (see table 4).

The possibility of incorporating the model of the interaction of the photons in the detector in the MCGPU-PET code is under study. It could be done by combining its phase-space file with PeneloPET or GATE.

MCGPU-PET is a fast open-source simulation tool which could be a very useful resource to the medical imaging community. In this work, we evaluated its application for PET scatter estimation, and spurious background. Our results show that it might be fast enough to be used within an iterative image reconstruction process.

4.5 Conclusions

MCGPU-PET has shown to improve by several orders of magnitude the speed of not GPU-based current MC codes such as GATE. Although some improvements and additional features can be included into the code, it has been shown to be a powerful tool to obtain realistic and fast simulations.

State-of-the-art MC methods such as the MCGPU-PET may be now fast enough for some clinical applications. Simulating several million coincidences per second, their estimations of scatter and spurious background can be applied within the image reconstruction process. Their improved accuracy may be negligible in typical scans compared to SSS. However, in the case of challenging scenarios such as extremely hot regions on warm background, MCGPU-PET based scatter may provide improved scatter estimation compared to SSS, in clinically acceptable computational times.

5 Pseudo-inverse Reconstruction

Some of these results were published at the journal ”Applied Sciences” in 2020 [López-Montes et al., 2020], they have been also presented in several international conferences [Lopez-Montes et al., 2017] [López-Montes et al., 2019].

5.1 Motivation and objectives

In many applications of PET, such as first-shot tests for chemicals [Shimizu et al., 2014], or PET image-guided surgery or biopsy [Venkatesan et al., 2011], it is crucial to be able to obtain images at the fastest rate possible. The time required to obtain PET images depends on the sensitivity of the acquisition system and the software used for data processing and image reconstruction [Selivanov et al., 2006]. State-of-the-art PET systems [MacDonald et al., 2008] [MacDonald et al., 2011] [Udias et al., 2018] are able to acquire in excess of 10 million coincidences per second, providing useful images with very short time frames. These data can be reconstructed with SSRB+FBP in modern multicore computers and obtain quasi real-time images with a delay of less than a second from the moment of acquisition and at a rate of a few frames per second [Udias et al., 2018]. However, SSRB+FBP images are of relatively low quality and better methods should be considered.

As we said in previous sections, in a linearized model of the reconstruction problem, the PET data (Y) are related to the image (X) of the radiotracer via the System Response Matrix (SRM), which we denote in this thesis as A. Tomographic PET image reconstruction methods are usually classified into analytical [Alessio et al., 2006a] [van Velden et al., 2008], and iterative methods [Herraiz et al., 2006] [Brahme, 2014] [Vicente Torrico, 2013] [Cal González, 2015]. Analytical methods generally use a set of assumptions on the SRM such as ideal detection, uniform sampling, and data completeness, to derive the expression of the response of the system in a compact and convenient form [Reader and Zaidi, 2007]. Nevertheless, although these assumptions are quite reasonable for CT imaging [Cherry and Dahlbom, 2006], they are not realistic in PET, which makes the reconstruction sub-optimal [Brahme, 2014] [Qi and Leahy, 2006]. Furthermore, analytical methods usually assume Gaussian noise in the data, while noise of PET real data is predominantly Poisson, which some iterative methods can consider [Tsui et al., 1981] [Vardi et al., 1985]. Another disadvantage of analytical methods is that the resolution of the images is not uniform across the FOV, which may create significant problems in the quantification of the images [Goertzen et al., 2012].

Iterative methods have proved to provide better results than analytical methods [Iriarte, 2017] [Herraiz et al., 2006] (see figure 59). They can take into account the most important physical effects included in the emission, transport and detection of PET radiation [Qi and Leahy, 2006]. These include positron range [Cal-González et al., 2013] [Cal González, 2015], non-collinearity, Depth-Of-Interaction (DOI) in the crystals [Cherry and Dahlbom, 2006], and geometrical considerations of the scanner as inter-detector gap [Cabello and Rafecas, 2012] [Iriarte, 2017]. Nevertheless, iterative methods with realistic SRM are slow and therefore, their application to real-time fully 3D PET imaging is still challenging [Alessio et al., 2006a] [Selivanov et al., 2006].

One of the most common approaches to speed-up the reconstruction process is performing axial rebinning of the data [Alessio et al., 2006a]. Rebinning 3D data into 2D slices makes the reconstruction much faster and easier [Liu et al., 1999], as rebinned 2D slices can be reconstructed with analytical methods such as Filtered Back Projection (FBP) or iterative ones [Herraiz et al., 2011] [Brahme, 2014].

The simplest method for axial rebinning of PET data is SSRB [Daube-Witherspoon and Muehllehner, 1987]. This method is fast but it is only accurate when the object is at the center of the transaxial plane. FORE [Defrise et al., 1997] is a more accurate alternative to SSRB rebinning but it is much slower.

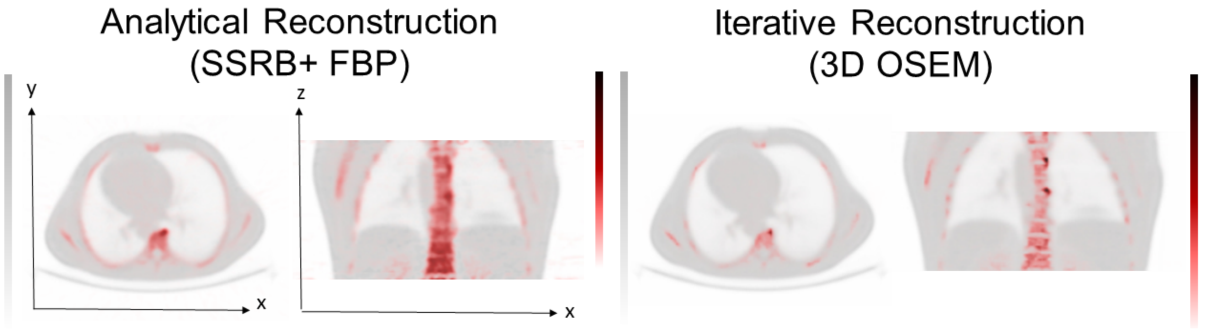

Figure 59: Analytical and iterative reconstructions of a human torso acquisitions injected with ^{18}F-NaF acquired in a Biograph TPTV scanner.

In this thesis, we propose to use the pseudo-inverse (PINV) of the SRM [López-Montes et al., 2020] [Selivanov and Lecomte, 2001] [Selivanov et al., 2001] [Selivanov et al., 2006] in both the axial [Lopez-Montes et al., 2017] and transaxial directions to achieve real-time reconstructions with a good uniform resolution [López-Montes et al., 2019] [López-Montes et al., 2020]. The goal is to achieve some of the features of iterative methods, with computational times compatible with analytical reconstructions, providing faster images than with iterative methods and more accurately than analytical methods.

5.2 Theory

Using a matrix representation of the reconstruction problem, if we assume that we can relate the data and the image through equation (21), we may think that a possible approach to find the solution of the image (X) through the data (Y) is through the computation of the inverse of the SRM (A^{-1}). This is a naive idea since the reconstruction problem is not well posed and, thus, the system of equations is not determined, being also very sensitive to small perturbations that we denote as noise (n) as we did in equation (51). And, thus, if we could find an inverse matrix A^{-1}, we would not obtain the solution X but a perturbed version of if:

$$\hat{X} = A^{-1} \cdot Y \tag{54}$$

However, this inverse matrix is not achievable for several reasons. First of all, A is not necessarily a square matrix, moreover, the SRM has some linear dependencies that make that the matrix is not invertible even though it were squared. Nevertheless, although we cannot find the exact solution of the reconstruction problem via the inverse of the matrix, a well known tool in mathematics, the pseudo-inverse of a matrix ($A^{\dagger}$) , or Moore-Penrose pseudo-inverse [Golub and Kahan, 1965] [Gene H. Golub, 2012] [Ben-Israel, 2002], can be found for every matrix A.

The pseudo-inverse $A^{\dagger}$ of a matrix A [Barata and Hussein, 2012] [Ben-Israel, 2002] [Golub and Kahan, 1965] can provide the solution of the linear least-squares (LLS) problem [Merriman, 1877] for a system of equations such that:

$$\frac{||Y - AX||^2}{2} \geq \frac{||Y - AA^{\dagger}Y||^2}{2} \rightarrow X(argmin(||Y - AX||^2/2)) = A^{\dagger} \cdot Y \tag{55}$$

Several approaches can be used to compute the pseudo-inverse of a matrix [Gower and Richtárik, 2016] [Katsikis et al., 2011], although one of the most commonly used, and the one that we will describe and use in this thesis is via the Singular Value Decomposition (SVD) [Gullberg et al., 1996] [Kalman, 1996] [Cebeiro and Morvidone, 2013] of the SRM. The SVD is based on the decomposition of any matrix (A) into the matrix product of two orthonormal matrices, which we will refer to as U and V and a diagonal matrix S which contains the singular values (σ) of the matrix. These singular values are the square roots of the eigenvalues of the matrix ($A^T \cdot A$), since the SVD is based into the diagonalization of the symmetric, and thus, diagonalizable matrices ($A^T \cdot A$) and ($A \cdot A^T$):

$$A = USV^T \tag{56}$$

Where:

$$S(i,j) = \begin{cases} \sigma_i & if \quad i = j \\ \\ 0 & if \quad i \neq j \end{cases} \tag{57}$$

In general, the singular values are ordered from the mayor singular value (σ_{max}) to the minor one (σ_{min}), being then $\sigma_1 = \sigma_{max}$.

From this decomposition, the inverse of A (if it exists) can be computed as:

$$A^{-1} = (USV^T)^{-1} = (V^T)^{-1}S^{-1}U^{-1} = VS^{-1}U^T \tag{58}$$

Since U and V are orthonormal matrices and, thus, their inverse is their transpose. We can remark here the importance of the singular values. Note that, since S is a diagonal matrix containing the singular values σ, its inverse could be computed from the reciprocals of the singular values $\sigma^{-1} = 1/\sigma$. Thus:

$$S^{-1}(i,j) = \begin{cases} 1/\sigma_i & if \quad i = j \\ \\ 0 & if \quad i \neq j \end{cases} \tag{59}$$

If A were a invertible squared matrix, then we could obtain the inverse of that matrix using (58). However, this expression can be used even for non-squared matrix, being able to find the left-inverse (A_L^{-1}) or the right-inverse (A_R^{-1}) of non-squared matrices that satisfy $A_L^{-1}A = \mathbb{1}$ and $AA_R^{-1} = \mathbb{1}$ respectively. Thus, this is a expression for the generalized inverse of a matrix [Golub and Kahan, 1965]. Note that if any of the singular values of the matrix were exactly 0, then, the inverse of the matrix could not be achieved, since the computation of 1/0 would not be possible. Using the pseudo-inverse of the matrix let us to compute an alternative modified inverse that can deal with the problem of 0 or very small singular values. We can express that pseudo-inverse as:

$$A^{\dagger} = VS^{\dagger}U^T \tag{60}$$

Now, the key point is to find an appropriate expression for the reciprocals of the singular values, that is, for the elements of the $S^{\dagger}$ matrix.

As we said before, when singular values are very small or null, its reciprocals are not well defined. In the case of the image reconstruction, these small singular values correspond to high frequency elements of the Fourier spectrum of the image, containing the finer details of it. This connects the pseudo-inverse method again with other reconstruction algorithms like FBP [Todorov et al., 2008] or even iterative methods, where the number of iterations play a regularization role on the high frequency elements. However, with noisy data [Vardi et al., 1985] [Teymurazyan et al., 2013] [Tsui et al., 1981], noise becomes dominant in the high frequency region, where the signal is weak, and thus the presence of very small singular values in the SRM amplifies the noise in the reconstructed image. This problem can be dealt with a proper regularization when computing the reciprocals of a matrix [Benning and Burger, 2018].

There are many different regularization methods for the pseudo-inverse of a matrix. One common method is called Truncated SVD (TSVD), which is obtained setting to 0 every reciprocal singular value larger than a fixed threshold ε [Todorov et al., 2008]. This regularization is very similar to the use of a ramp-filter for FBP, removing frequencies higher than a certain threshold.

$$\sigma_i^\dagger = \begin{cases} 1/\sigma_i \quad if \quad \sigma_i > \varepsilon \\ \\ 0 \qquad else \end{cases} \tag{61}$$

A smoother and sometimes more recommendable approach is the well known Tikhonov regularization [Benning and Burger, 2018], which replaces the reciprocal singular values by:

$$\sigma_i^\dagger(k) = \frac{\sigma_i}{(\sigma_i + k)^2} \tag{62}$$

where k is a regularization parameter [Press et al., 2007] [Guo and Renaut, 2011].

As discussed before, in the case of iterative reconstruction, the number of iterations plays a regularization role, thus, we could look for regularization techniques for pseudo-inverse via SVD with a similar performance to iterative methods. In fact, it can be found a pseudo-inverse regularization mathematically equivalent to Landweber method [Landweber, 1951] if not introducing non-linear conditions (as positive constraints) [Latham, 1999]. Note that a classical pseudo-inverse method entails pure linear approaches.

The equivalence between pseudo-inverse regularization and Landweber iterations can be deduced from equation (35). For simplicity, we will assume normalized matrices such that $\sigma_1 = 1$ (Euclidean norm) and thus, we will ignore the relaxation parameter in Landweber method. Thus, to obtain the Landweber like regularization, we could perform the first iterations of the Landweber method starting with an initial zeroes image [López-Montes et al., 2020]:

$$X^0 = (0) \tag{63}$$

$$X^{n+1} = X^n - A^T(AX - Y) \tag{64}$$

$$X^1 = A^T Y \tag{65}$$

$$X^2 = (2\mathbb{I} - A^T A) \cdot A^T Y = (\mathbb{I} - (\mathbb{I} - A^T A)^2) \cdot (A^T A)^{-1} \tag{66}$$

$$X^3 = (3\mathbb{I} - 3A^T A + A^T A A^T A) \cdot A^T Y = (\mathbb{I} - (\mathbb{I} - A^T A)^3) \cdot (A^T A)^{-1} \tag{67}$$

Thus, in general, assuming that we can compute $(A^T A)^{-1}$, we can write a generic result as:

$$X^n = (\mathbb{I} - (\mathbb{I} - A^T A)^n) \cdot (A^T A)^{-1} \tag{68}$$

Now, using a SVD of A ($A = U \cdot S \cdot V^T$), this last equation can be rewriten as [López-Montes et al., 2020]:

$$X^n = V \cdot (\mathbb{I} - (\mathbb{I} - S^2)^n) \cdot (S)^{-1} \cdot U^T \cdot Y = V S_n^\dagger U^T Y = A_n^\dagger Y \tag{69}$$

And, since S is a diagonal matrix, the diagonal elements of $S_n^\dagger$ can be written as:

$$\sigma_i^\dagger(n) = \frac{1-(1-\sigma_i^2)^n}{\sigma_i} \tag{70}$$

Where n is the number of Landweber iterations. This implies that by means of the pseudo-inverse, an iterative Landweber reconstruction, which despites being iterative, is linear, can be performed in one single step.

Also, a connection can be established between the number of iterations in a Landweber regularization and the regularization parameter k in Tikhonov regularization expressed as:

$$Tikh(k = 1/n) \approx Landweber(n) \tag{71}$$

This allows to study resolution recovery and noise in the image in terms of the number of equivalent iterations, as it is usually done with iterative methods.

Note that, an equivalent SRM to the Radon transform can be obtained [Todorov et al., 2008], and, using the pseudo-inverse of this matrix would provide the exact same result that using a FBP approach (using a filter that match the regularization of the pseudo-inverse). Then, the advantages of using pseudo-inverse instead of FBP are similar to the advantages of using liner iterative methods: inclusion of geometrical and physical effects into the SRM making it more realistic than Radon transform.

Some works propose the use of pseudo-inverse methods for PET image reconstruction [Selivanov and Lecomte, 2001] [Selivanov et al., 2001] [Selivanov, 2002], exploiting the possibilities of using TSVD for ultra-fast or even real time PET image reconstruction, although due to the high computational requirements to compute the pseudo-inverse of the SRM, only small matrices had been used.In this thesis, we include a section dedicated to pseudo-inverse reconstruction and its potential use for real-time PET reconstruction for different current scanners, both clinical and preclinical [López-Montes et al., 2020] [Lopez-Montes et al., 2017] [López-Montes et al., 2019].

5.3 Materials and methods

5.3.1 Pseudo-inverse reconstruction algorithm

For PINV reconstruction, the computation of the PINV of the SRM does require the use of the whole matrix, because even when the SRM can be sparse, the pseudo-inverse is not [Dokmanić et al., 2013] [López-Montes et al., 2020]. To remedy this, in this work, we propose to decompose the SRM into axial A_z and transaxial $A_{x,y}$ components (see figure 60):

$$A_{x,y,z}(\rho,\theta,z_1,z_2,x,y,z) \approx [A_{x,y}(\rho,\theta,x,y); A_z(z_1,z_2,z)] \tag{72}$$

The axial matrix can be used for data rebinning and the transaxial one for 2D reconstruction of rebinned 2D slices.

To generate the SRMs used for PINV reconstruction, we used analytic SRMs. To consider more realistic effects, instead of LORs, we consider Tubes of Response, (TORs), [Popescu and Lewitt, 2004] with a width due to physical and geometrical effects as the crystal size, non-collinearity, positron range, depth of interaction, etc. We considered TORs to have a Gaussian cross section [Lougovski et al., 2015] [Iriarte, 2017] [Pratx et al., 2008]. The width of the Gaussian $(\sigma_(x,y),\sigma_z)$ is obtained empirically for each scanner considered in this work from the simulation with PenloPET of ^{18}F point sources (placed at the center of the FOV) and assuming the same for all LORs of the same scanner.

In the axial part of the SRM, we consider an image space discretized in axial (z) and length coordinates (t) along the LOR. The probability for each voxel to be connected to each LOR is obtained from the distance of the voxel to the LOR:

$$A_z(z,t,z_1,z_2) = e^{\frac{(-1/2)\cdot d(z,t,z_1,z_2)^2}{\sigma_z^2}}, \tag{73}$$

where $d(z,t,z_1,z_2)$ is the minimum distance between the voxel at (z,t) and the LOR given by (z_1,z_2). In a similar way to the axial SRM, each element of the transaxial part of the SRM can be modelled as:

$$A_{xy}(x,y,\rho,\theta) = Ne^{\frac{(-1/2)\cdot d(x,y,\rho,\theta^2)}{\sigma_(x,y)^2}} \tag{74}$$

where $d(z,y,\rho,\theta)$ is the distance from the voxel (x,y) to the line of response given by (ρ,θ). [Pratx et al., 2008]

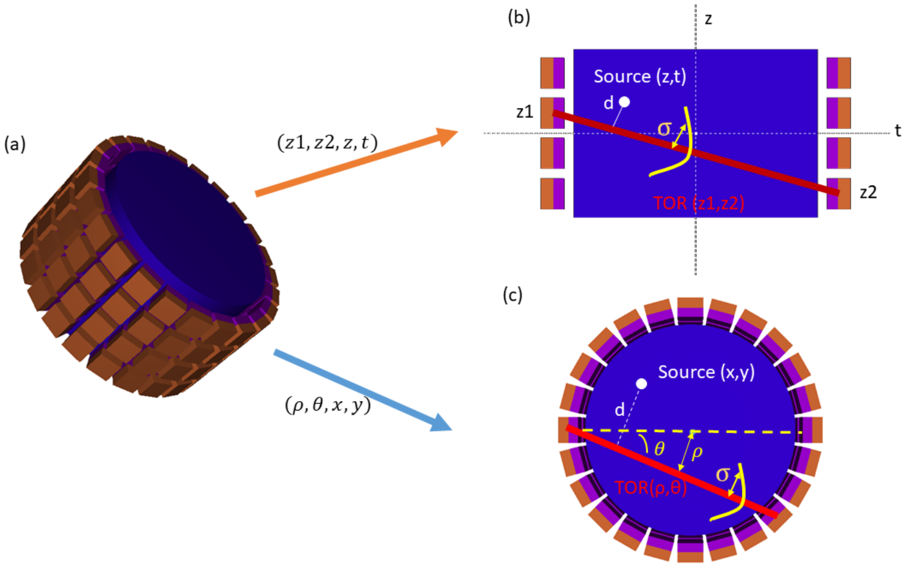

Figure 60: Representation of the separtion of axial and transaxial components of the SRM.

As we have modeled the SRM using two independent components, the reconstruction process can be split into two smaller and separated problems: axial rebinning (PINVz), and 2D reconstruction of the rebinned slices (2D-PINV).

$$Y_{reb}^T(z,\rho\theta) = A_z^\dagger(z,z_1z_2)Y^T(z_1z_2,\rho\theta); Y_{reb}(\rho\theta,z) = (Y_{reb}^T(z,\rho\theta))^T \tag{75}$$

$A_z^\dagger(z,z_1z_2)$ was obtained as the pseudo-inverse of $A_z(zt,z_1z_2)$ and then collapsing in the t direction (sum over t).

On the other hand,

$$X(xy,z) = A_{xy}^\dagger(xy,\rho\theta)Y_{reb}(\rho\theta,z) \tag{76}$$

Where $A_{xy}^\dagger(xy,\rho\theta)$ is the pseudo-inverse of $A_{xy}(xy,\rho\theta)$.

Since both processes are considered independent and only involve matrix products, the reconstruction can be done in a single step in which the 3D data are multiplied by each matrix from the left and right:

$$X(xy,z) = A_{xy}^\dagger(xy,\rho\theta)Y(\rho\theta,z_1z_2)A_z^\dagger(z_1z_2,z) \tag{77}$$

5.3.2 List mode event by event reconstruction

As it has been shown in previous works [Selivanov et al., 2006], the pseudo-inverse of the SRM can be used for list-mode data reconstruction. In a 3D problem, each column of the PINV of the SRM, $A^{\dagger}(:,i)$, contains the region of the image that would produce a coincidence in the given LOR i. Taking this into account, the image could be refreshed after every event. A similar approach is also feasible in the proposed scheme. Each coincidence with coordinates (ρ, θ, z_1, z_2) can be separated into transaxial and axial coordinates. Using $A_z^{\dagger}$, for every coincidence with $z_1 z_2$ axial coordinates, each z slice (z) of the image is weighted by the corresponding element of the pseudo-inverse of the axial SRM $A_z^{\dagger}(z_1 z_2, z)$. Then, for each axial slice, coordinates (x, y) of the image are updated event by event using each row of the transaxial SRM pseudo-inverse $A_{xy}^{\dagger}(xy, \rho\theta)$. Although this is fast and feasible for a 2D case as presented by Selivanov and Lecompte [Selivanov et al., 2006], it takes longer than reconstructing using the whole sinogram for except when the number of coincidences is very small. In our case, reading the list-mode coincidences and histograming them in a sinogram is faster than event by event reconstruction, even for frames as small as 0.1 seconds for the preclinical SuperArgus PET-CT scanner.

5.3.3 Projections over planes

In many cases, real-time images are used to follow radiotracer distribution along the body of the patient for which the sum of the image collapsed in specific directions instead of a 3D presentation of the full image may be enough. This way of presenting real-time PET images is also convenient as short frame images would typically contain a very low number of counts, and 2D projections will be less noisy in this case.

In general, to obtain images collapsed over planes, it is needed a 3D image which is later projected. But using the pseudo-inverse, this process can be reduced to one single step, if the pseudo-inverse, instead of the image, is collapsed once and for all. This leads to much smaller PINV matrices and thus, much faster matrix products.

In this work, we used 2D-PINV matrices collapsed over X and Y directions. These matrices, combined with PINV_z, produces projections in the XZ and YZ planes respectively. Note that if we sum over all the slices obtained from the rebinning step, and then we reconstruct the resulting slice, we obtain the equivalent of the 3D image collapsed into the XY plane.

5.3.4 Simulated data

PeneloPET 3.3.1 [España et al., 2009] [Lopez-Montes et al., 2019] was used for the simulations presented in this work.

^{18}F point sources (radius 0.5 mm) were simulated for a geometry similar to the Biograph TPTV (Siemens) (see section 3.1.3) scanner to evaluate the axial resolution of the different rebinning strategies discussed. The point sources were distributed each 5 cm both in the axial and transaxial direction. The activity of each point source was 1000 Bq and the simulation time was 5 minutes. The image noise was evaluated with another simulation of two homogeneous cylinders with a concentration of activity of 5 kBq/ml and a simulation time of 5 minutes. One of the cylinders was centered in the FOV while the other one was displaced 10 cm radially from the center of the scanner, both cylinders had a radius of 5 cm and covered the whole axial FOV. The axial resolution was obtained from the Full Width at Half Maximum (FWHM) of the 1D-Gaussian fit to the axial profile obtained in the center of each source. The noise level was obtained as the ratio of the standard deviation to the average value in spherical ROI's with a radius of 5 cm located inside the simulated cylinders.

We used the same sinogram dimensions as the actual clinical scanner data described below. The rebinned 2D slices were reconstructed using FBP with a Hamming filter (cut-off 0.5).

A thin slice Defrise phantom [Erlandsson et al., 1994] was simulated to study axial rebinning with different methods. In this case the simulated geometry was the one corresponding to the preclinical SuperArgus PET-CT scanner (SEDECAL). The simulated phantom was composed of several disks of 8 cm diameter and 3 mm thickness. The gap between disks was 3 mm.

5.3.5 Real data

- Preclinical PET/CT scanner: we used the 6 ring version of the SuperArgus PET/CT scanner. The used axial pseudo-inverse matrices for this scanner $A_z^{\dagger}(z_1 z_2, z)$ had a size of 1185 × 195. For the 2D matrices, 175 voxels were chosen for the image FOV. The size of 2D matrices for the SuperArgus PET/CT was around 2.6 Gb. Both σ_z and σ_{xy} of the Gaussian distributions of the TOR were 0.6 mm.

  For the evaluation of the image quality we used the IQ NEMA and a Derenzo phantoms. The rod diameters (Derenzo phantom) were 1.2, 1.6, 2.4, 3.2, 4 and 4.8 mm.

  Two animal acquisitions injected with fluorodeoxyglucose (^{18}F-FDG) were also used to evaluate the performance of the PINV (PINVz+2D-PINV) methodology: a 200 grams' rat and a cardiac acquisition of a 15 grams' mouse. Over the cardiac mouse acquisition, a quantitative comparison of 2D-PINV and FBP in real preclinical acquisitions was made. A profile over the heart was fit to two gaussians (one to each side of the heart). The average of the standard deviation of both gaussians is shown and the relative improvement of 2D-PINV over FBP is calculated as $|\sigma_{2D-PINV} - \sigma_{FBP}|/\sigma_{FBP}$. Moreover, we used a first pass acquisition of a mouse injected with ^{18}F-FDG to demonstrate the real-time capabilities of PINV reconstructions.

Acquisitions were performed at the Instituto de Investigacion Sanitaria Gregorio Maranon (Madrid, Spain). All experimental procedures have been done in compliance with the European Communities Council Directive 2010/63/EU and submitted for approval to the Institutional Animal Care and Use and Ethics Committee of the Hospital General Universitario Gregorio Marañón (HGUGM), supervised by the Comunidad de Madrid according to the Annex X of the RD 53/2013. The subjects were kept at the animal housing facilities of the Unidad de Medicina y Cirugía Experimental (UMCE-HGUGM) in Madrid, Spain.

We acknowledge Dr. Manuel Desco and Dr. Juan José Vaquero for kindly sharing the acquisitions described in this section.

- Clinical PET/CT scanner: for the clinical data, we used ^{18}F acquisitions of an IQ-NEMA phantom obtained with a Biograph TPTV scanner, at the Medical University of Vienna (Austria). The axial matrices $A_z^{\dagger}(z_1 z_2, z)$ had a size of 559 × 109 (238 kBytes). For the 2D matrices, 225 voxels were chosen, providing a FOV of 45.54 cm. The size of 2D matrices was around 21 Gb. The σ_{xy} and σ_z for the TORs in the matrices were 2 mm.

  Also for Biograph TPTV, we performed a qualitative study of the reconstruction of a 20 minutes' acquisition of a male patient in one bed position, belonging to a study on atherosclerosis plaque ^{18}F-NaF uptake in patients with cardiovascular events, performed in the Medical University of Vienna. This study was approved by the ethical commission of the Medical University of Vienna (EK-Nr 1322-2014) and was conducted in accordance with the 1964 Helsinki declaration and its later amendments or comparable ethical standards. The tracer activity at time of injection was 366 MBq.

  We acknowledge Dr. Jacobo Cal-González and Dr. Ivo Rausch who acquired the acquisitions of the IQ-NEMA phantom. We also acknowledge Dr. Marcus Hacker for providing the acquisitions of the atherosclerotic plaques.

- Image Quality Evaluation: we evaluate the reconstructed images of the phantoms following the National Electrical Manufacturers Association (NEMA) NU 2-2007 and NU 4-2008 protocols, respectively for clinical and preclinical phantoms. The noise level in the image (%) was evaluated as the standard deviation of the activity in a uniform region divided by the average activity in that region. The resolution recovery (%), following the NEMA standards. For the preclinical scanner, the mouse-size IQ phantom was used. Sinograms were corrected by attenuation and random coincidences. In the case of the clinical NEMA, scatter corrections were also included. We present a comparison of SSRB+FBP or FORE+FBP with the proposed method (PINVz+2D-PINV). Unless otherwise noted, execution times correspond to one thread of a CPU E5-2640 v4 @ 2.40 GHz in a Linux computer with Centos 7 OS.

5.4 Results

5.4.1 Pseudo-inverse regularization

We studied the effects of different regularization algorithms for the pseudo-inverse method. We compared TSVD, Tikhonov regularization and Landweber regularization. In general, we observed that TSVD provide noisier images and with more negative bounces while Tikhonov and Landweber regularization provide smoother solutions as it can be appreciated in figure 61. Comparing Landweber and Tikhonov, the first yielded slightly better results in terms of resolution recovery although the results were quite similar when the number of equivalent iterations of Landweber regularization (n) matches to the inverse of the regularization parameter of Tikhonov (k). These effects can be explained attending to the reciprocal singular values given by each method, which can be observed in figure 62.

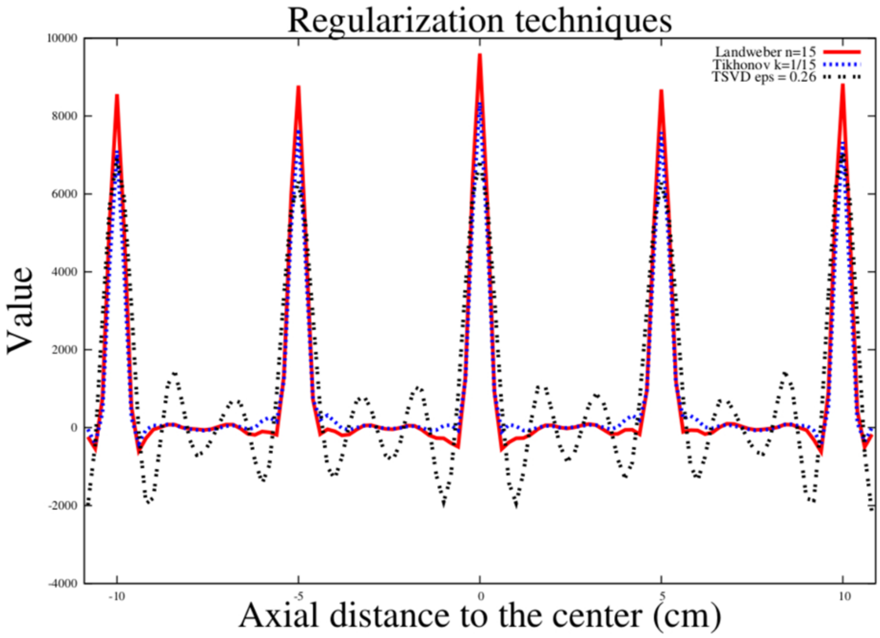

Figure 61: Axial profiles over five point sources placed at different axial positions and at a radial distance of 5 cm to the center of the scanner using PINV rebinning with different regularization strategies. The in-plane reconstruction was performed using FBP.

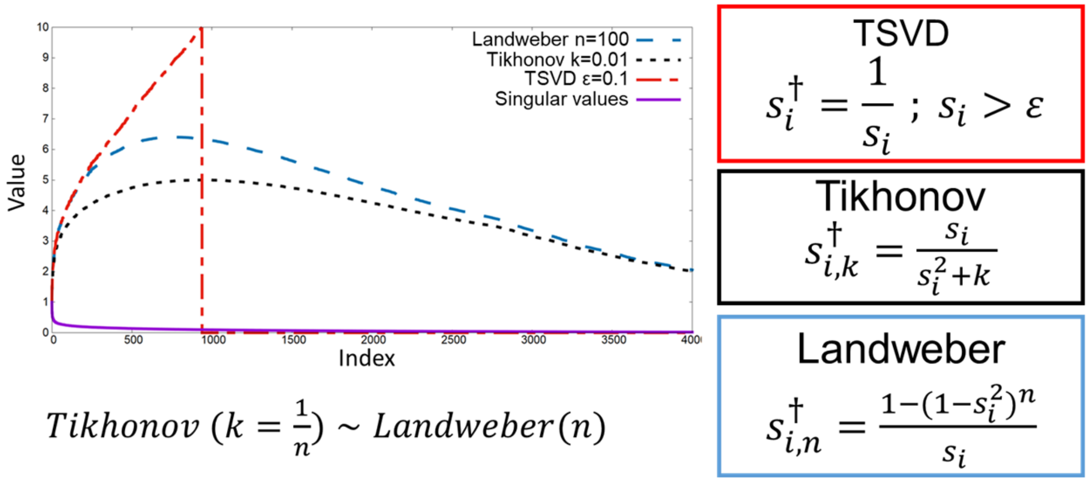

$$s_i^{\dagger} = \frac{1}{s_i}\ ;\ s_i > \varepsilon$$

$$s_{i,k}^{\dagger} = \frac{s_i}{s_i^2 + k}$$

$$s_{i,n}^{\dagger} = \frac{1-(1-s_i^2)^n}{s_i}$$

$$Tikhonov\ (k = \tfrac{1}{n}) \sim Landweber(n)$$

Figure 62: Singular values of a small matrix (solid line) and its reciprocals using different regularization methods. Tikhonov (k=0.01) and Landweber (n=100) regularization for equivalent iterations. Truncated Singular Values (TSVD) with a threshold of 0.1 and original singular values (SV) are also shown.

5.4.2 Axial Rebining PINV: simulated data

Figure 63 shows resolution recovery and noise of four point sources located at different radial and axial positions. Off-axis sources in SSRB reconstructions exhibit much worse resolution than the other two rebinning methods studied. FORE does provide the best axial resolution and less noise. PINV on the other hand provides a more uniform resolution and noise level across the FOV, clearly improving SSRB for off-axis values, where it approaches the best results of FORE. Indeed, with a proper regularization parameter (around the equivalent to 8 Landweber iterations), similar results in terms of resolution and noise were obtained for the sources placed at 10 cm radially from the center of the scanner, using PINV and FORE.

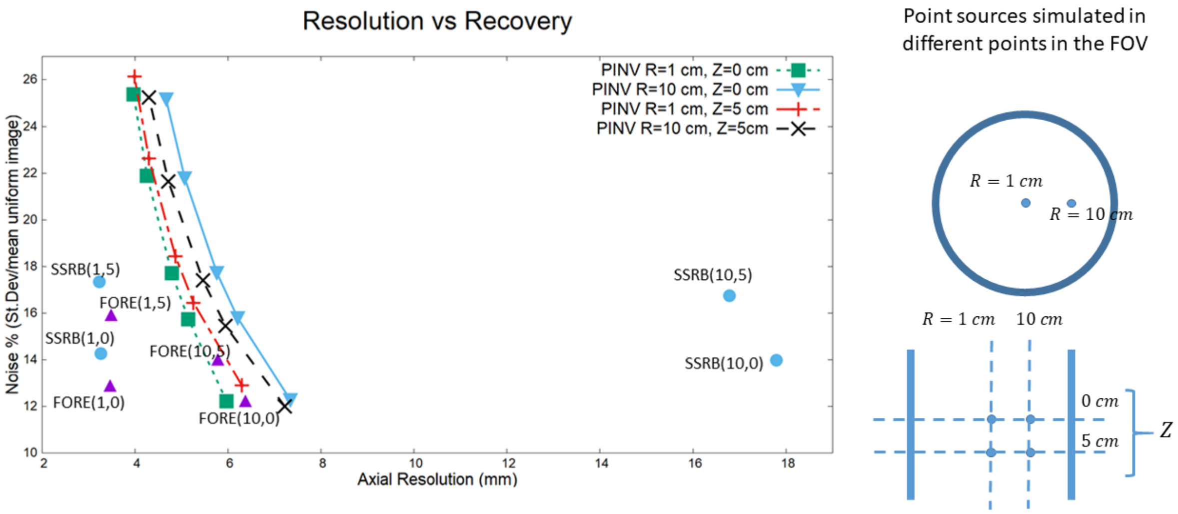

Figure 63: Noise vs resolution recovery for different rebinning methods (SSRB, FORE and PINVz). Point sources simulated in a scanner with a geometry similar to Biograph TPTV with MRD 38 and SPAN 11. Numbers in brackets in FORE and SSRB points determine the distance (R,Z) to the center of the scanner in cm, for example (10,0) represents a source at a radial distance of 10 cm from the center of the scanner and centered in the axial FOV . The curves for PINVz represent the axial resolution vs recovery for a different number of equivalent Landweber iterations (i.e. different regularization parameters), from right to left 5, 8, 10, 15 and 20 iterations. Far from the axis of the scanner SSRB is not accurate, while FORE is still good enough. PINVz keeps resolution recovery across the whole FOV.

In figure 64 we can see a coronal view of the reconstruction of a Defrise disk phantom where we can appreciate the improvement of pseudo-inverse rebinning compared to SSRB. We can see that FORE and PINVz provide similar detail. In terms of computational time, as shown in figure 65, we can appreciate that $PINV_z$ is approximately as fast as SSRB and both of them are much faster than FORE.

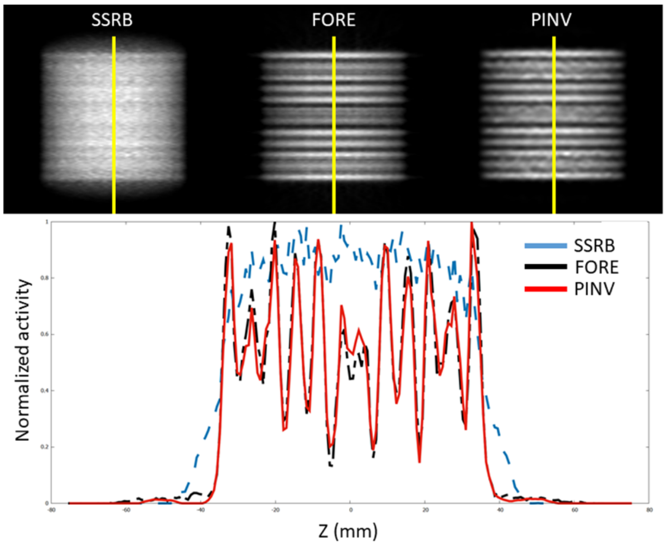

Figure 64: Axial profile of the reconstructed images of a PeneloPET simulation of a Defrise phantom (8 cm diameter 3 mm thickness) for the SuperArgus scanner geometry. Reconstructions for the three rebinning methods are presented (top) together with a profile along the axis of the scanner (bottom) as indicated with the yellow line in the images. Equivalent Landweber iterations for PINVz rebinnig was 20.

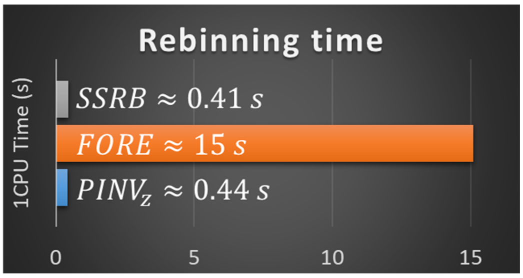

Figure 65: Rebinning computational times for each one of the studied methods using 1 core Intel E5-2640 v4 @ 2.40 GHz processor.

5.4.3 Preclinical data

In this section we present results of a fully PINV reconstruction (PINVz+2D-PINV) compared with common analytical method FORE+FBP. We compare also only 2D reconstruction with FBP and PINV from a FORE rebinned sinogram for the IQ-NEMA phantom mouse like. These results are presented in figure 66 and table 7.

	% Recovery (rods)					% Uniformity
Method	1 mm	2 mm	3 mm	4 mm	5 mm	
FORE+FBP	23.3	55.2	85.0	92.2	101.2	12.2
FORE+2DPINV	24.4	62.0	96.9	104.0	105.3	11.7
PINVz+FBP	20.8	57.1	85.9	96.8	101.7	12.2
PINVz+2DPINV	22.8	62.7	95.7	105.6	101.4	12.9

Table 7: Recovery coefficients and uniformity according to NEMA 4-2008.

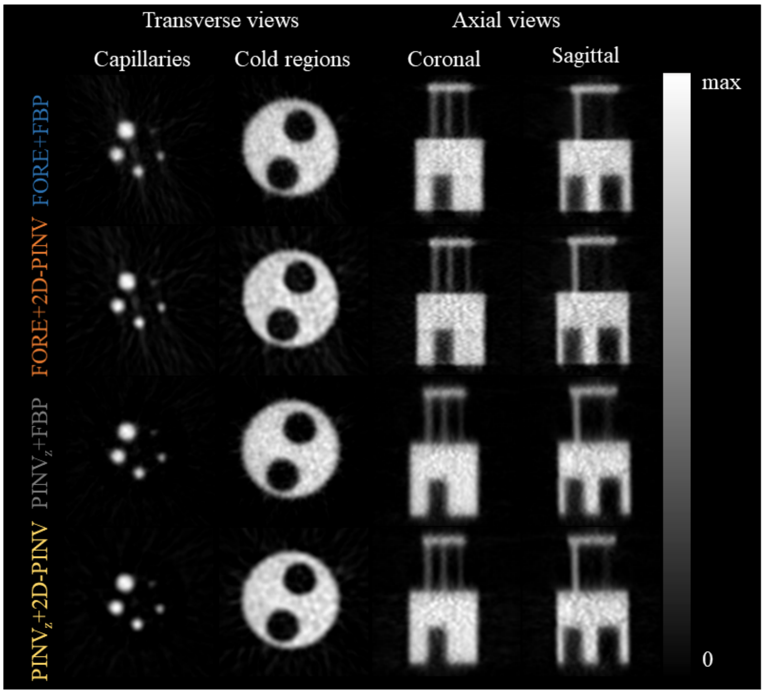

Figure 66: FORE and PINVz rebinned data, coupled with different 2D reconstruction (FBP and 2D-PINV) for the IQ NEMA phantom.

In table 7, we compare the recovery coefficients for the IQ-NEMA phantom, at approximately the same level of uniformity for every rebinning+2D reconstruction combination.2D-PINV slice reconstruction systematically outperforms (around 5-10% better for the smallest capillary and up to 15% in the 2 mm capillary). As expected, FORE rebinning provides the best recovery, improving marginally on the pseudo-inverse rebinning results.

Furthermore, in figure 67 we present results for a Derenzo filled with 250 μCi of ^{18}F-FDG measured with a well-counter with an accuracy of ±5%. It can be seen an improvement in resolution for 2D-PINV reconstruction compared to FBP. A relative improvement of 15% in spatial resolution using 2D-PINV respect to FBP. This result is consistent with table 7.

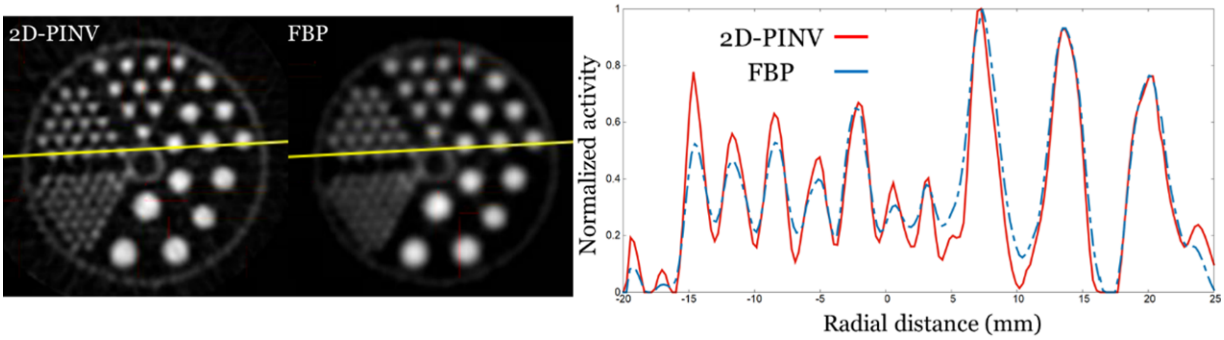

Figure 67: 8. 5 cm diameter Derenzo phantom. Rods are 1.2, 1.6, 2.4 3.2, 4 and 4.8 mm in diameter. (Left) reconstructed with 2D-PINV and FBP respectively from same sinogram rebinned with FORE. We show 10 axial slices summed up. (Right) Profile along the yellow line showing the 1.6 and 3.2 mm rods.

Figure 68 shows the cardiac region of a 15g mouse injected with 170 μCi of ^{18}F-FDG, with slices reconstructed with FBP and 2D-PINV from a PINV rebinned sinogram. Improvement in spatial resolution (a relative 15%)for 2D-PINV reconstructions is clearly seen.

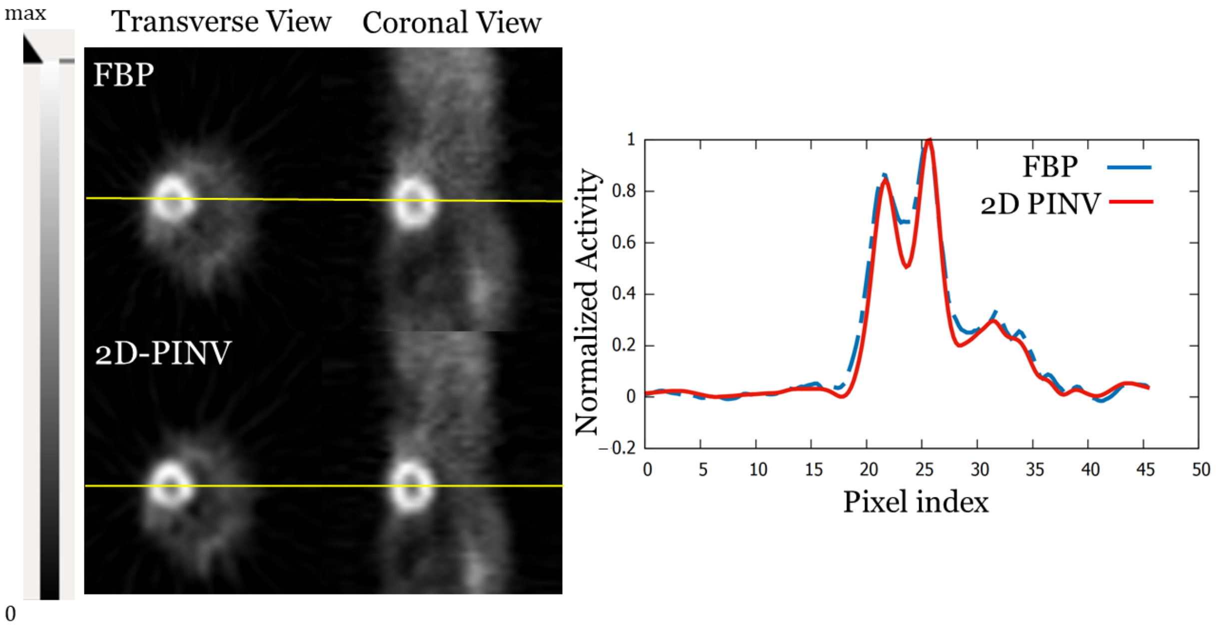

Figure 68: FBP and 2D-PINV reconstruction of a15 g mouse injected with 170 μCi of ^{18}F-FDG. from data rebinned using PINV. A profile along the heart is also shown.

In figure 69 shows PINV$_z$+2D-PINV versus SSRB+FBP reconstructions, of a 200g rat injected with 300 μCi of ^{18}F-FDG. The improvement using PINV is evident. Images from both 30 minutes (bottom) and 5s (top) acquisitions are shown, the second demonstrating the capabilities for near real time imaging.

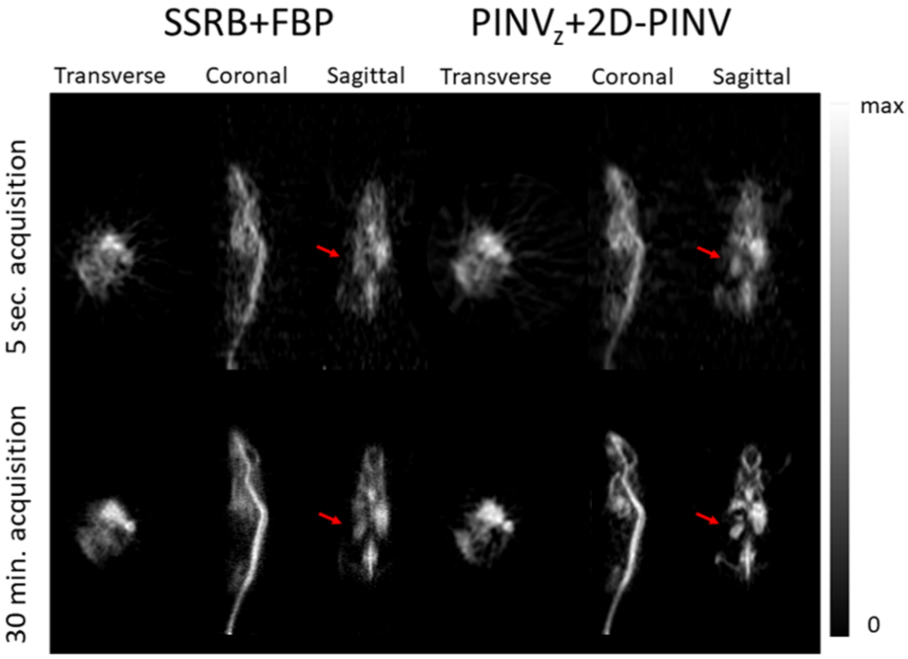

Figure 69: (Left) SSRB+FBP and (Right) PINV_z+2D-PINV image reconstruction of a rat injected with 300 μCi ^{18}F-FDG. The transverse, coronal and sagittal views are shown for a slice of the image. Top (Bottom) panel shows 5s (1800s)acquisition.

Reconstruction times for the methods studied in this section are shown in figure 70. These times do not consider the time needed to generate the PINV of the SRM and pre-load it to RAM memory as both processes are performed before the reconstruction. Times required for the recovery of missing data in FBP are not included neither, only the reconstruction time of the processed data.

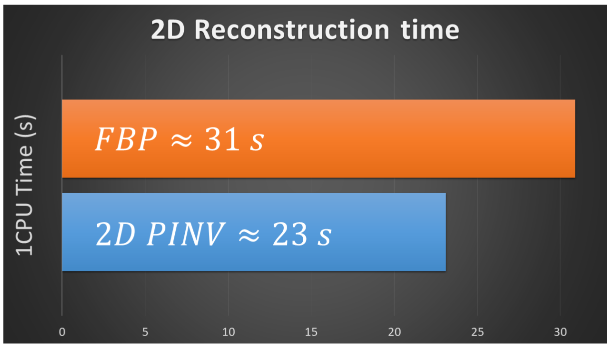

Figure 70: Computational times for the different in-plane reconstruction methods using a single core of an Intel E5-2640 v4 @ 2.40 GHz processor. Sinogram size was $175 \times 128 \times 195$ and the final images was $175 \times 175 \times 195$ voxels.

5.4.4 Clinical data

While in the phantoms studied in the previous section there was an axial symmetry, in the case of IQ NEMA phantoms for humans, instead of capillaries there are spheres placed over a homogeneous background. This phantom is accurate to show the effect of different rebinning in the axial direction. So in this section we will study the effect on the recovery coefficients for a IQ NEMA phantom for humans in images rebinned with SSRB, FORE and PINV and reconstructed with the same parameters of a 2D FBP + Hamming filter, just like we did in the previous section.

In table 8 we can see the parameters obtained for the recovery coefficients over the 6 spheres in the phantom and the standard deviation over the mean for the different spheres following criteria of NEMA 2- 2007. The reconstructed images are shown in figure 71.

Method	Sphere	3.7 cm	2.7 cm	2.2 cm	1.7 cm	1.3 cm	1.1 cm
SSRB+FBP	% RC	72.0	63.1	54.2	42.4	27.4	18.1
	%Stdv	1.5	1.9	2.3	3.1	4.1	5.2
FORE+FBP	% RC	75.6	67.5	60.2	49.6	35.5	25.3
	%Stdv	1.6	1.8	2.2	2.9	3.9	4.8
$PINV_z$+FBP	% RC	78.7	70.8	63.0	52.2	37.4	26.8
	%Stdv	1.5	2.0	2.5	3.5	4.9	6.5
$PINV_z$+2D-PINV	% RC	78.9	70.7	65.0	53.0	37.9	26.7
	%Stdv	2.7	2.9	3.5	4.3	6.0	8.0

Table 8: RC and noise for the clinical IQ NEMA phantom (NEMA NU 2-2017).

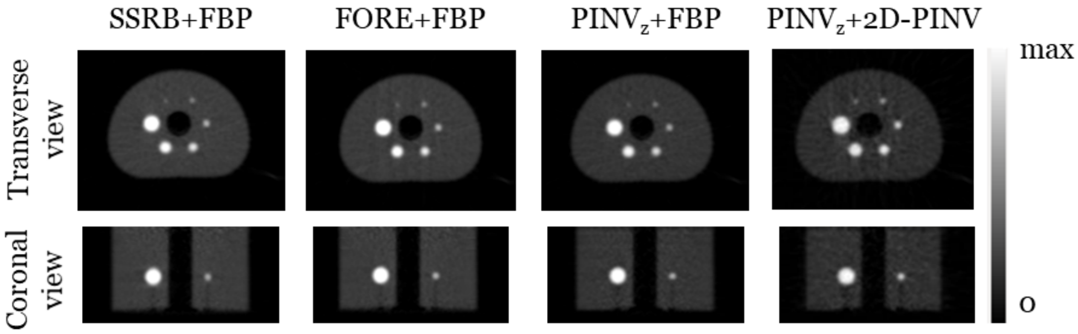

Figure 71: FBP and 2D-PINV images from of data rebinned with PINV, FORE and SSRB of the clinical IQ NEMA phantom.

In figure 72 we show the results of the different methods evaluated in this section for an acquisition of ^{18}F-NaF in a human.

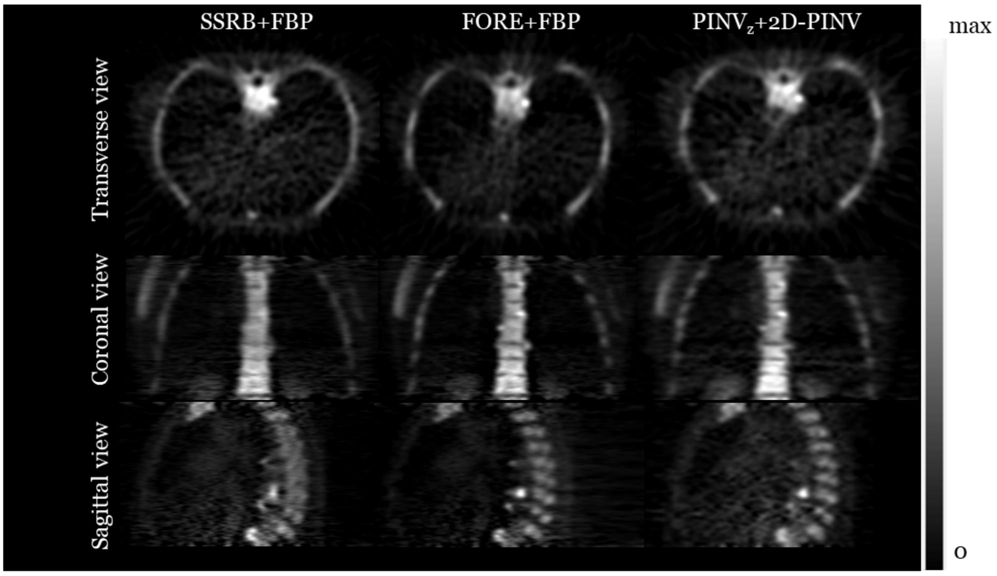

Figure 72: Reconstruction using standard methods SSRB + FBP FORE + FBP and using PINV rebinning + 2D PINV of a man injected with ^{18}F. In the image, it can be seen the uptake of ^{18}F-NaF of a human male. Images are corrected for attenuation and scatter.

The reconstruction and rebinning computational times for each one of the methods for clinical images are shown in figure 73.

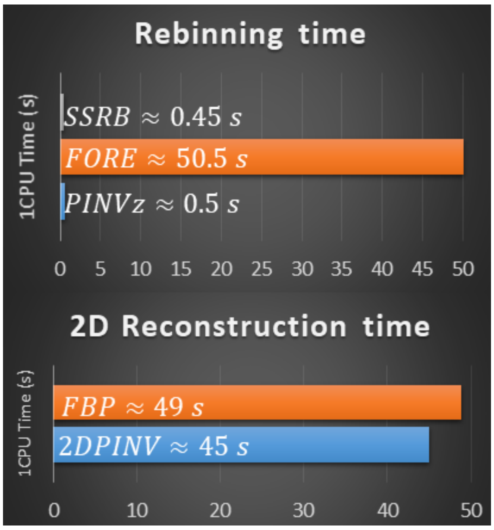

Figure 73: Computational times for the different methods for clinical data acquired in a Biograph TPTV scanner. Input sinograms were 336 × 336 × 559 bins. Reconstructed images were 255 × 255 × 109 voxels.

5.4.5 Real-time PINV reconstruction. Projections over planes

Figure 74 shows the results of a reconstruction collapsed over YZ plane for a first shot acquisition for a 13g mouse injected with ^{18}F-FDG. Frames of 1 second each are presented. In them the uptake is clearly seen distributing along the body of the mouse. The reconstruction over the 6 first seconds is also included as a reference. The computational times using multi-CPU parallelization are shown if table 9.

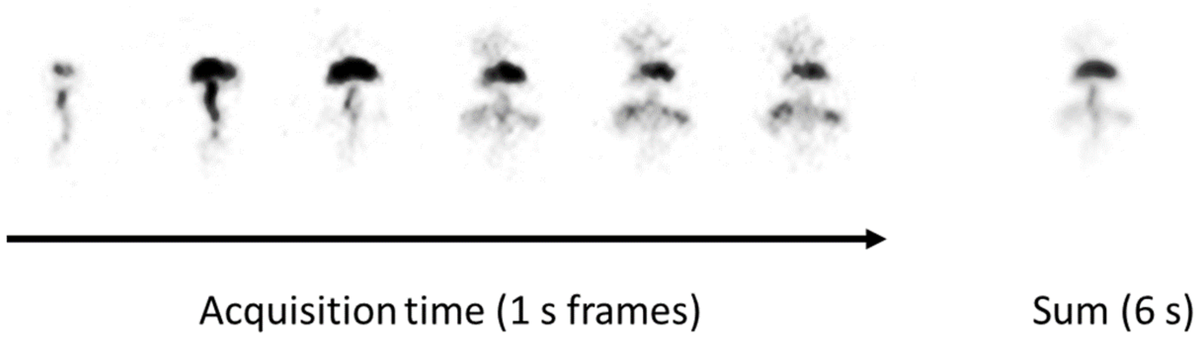

Figure 74: YZ plane reconstructed with PINVz+2D-PINV (collapsed over the x coordinates) of a 13g mouse injected with ^{18}F-FDG.

Plane	XY	XZ	YZ	3D Image
Time (s)	0.08	0.11	0.11	1.6

Table 9: Computational times for the plane projected images using 2D PINV+PINVz with 8 cores of an Intel E5-2640 v4 @ 2.40 GHz processor. 175x128x1187 sinograms.

5.5 Discussion

In this work, we showed that pseudo-inverse reconstruction of 3D PET data using PINVz + 2D-PINV provided better and faster reconstructions than SSRB + FBP.

It is worth noting that in FBP, it is further needed to estimate the missing data (filling in the gaps in between detectors), and this time was left out from results. On the other hand, pseudo-inverse reconstruction only requires knowing the position of the missing data in order to skip those, further speeding the process.

Pseudo-inverse axial rebinning was much faster than FORE, with just a moderately worse performance in terms of noise/resolution. Furthermore, pseudo-inverse axial rebinning involves resolution recovery, while FORE does not, this can be exploited selecting an appropriate regularization level depending on the acquisition, being able to use a low number of equivalent Landweber iterations in the case of noisy acquisitions (low signal to noise ratio) and a higher number in the case of acquisitions with more statistics.

As has been noted in previous works [Selivanov et al., 2006], there is a 2D-PINV matrix that would be fully equivalent to FBP. However, in the construction of the 2D-PINV, it is also possible to add geometrical information and physics effects, which introduce blurring to the TORs. This is the main reason for the improved resolution of in-slice PINV images compared to FBP ones. The matrices for PINV rebinning and slice reconstruction can be pre-computed and stored once and for all for a given scanner, making it easy for the user to produce their own reconstructions.

Although it would be desirable to apply PINV methods in 3D altogether instead of the division into axial and transaxial components employed in this work, building a 3D PINV matrix currently seems impractical as 3D PINV arrays for modern complex scanners will not fit in the memory of common computers. Furthermore, as we have presented here, the noise exhibited by PINV rebinning methods is slightly larger than that of FORE. Better regularization techniques or improvements in the SRM could remedy this.

New regularization techniques could involve filtering of the reconstructed image or even the data before reconstruction. Any linear filter (F) can be applied during PINV reconstruction from its matrix representation:

$$X \approx A^{\dagger} \cdot Y \rightarrow X_F = F \cdot X = F \cdot A^{\dagger} Y = (F \cdot A^{\dagger}) \cdot Y \tag{78}$$

Therefore, applying the filter in the pseudo-inverse before the reconstruction would result in the same image as using the filter over the reconstructed image. The same applies to any linear filter applied in the data domain:

$$X \approx A^{\dagger} Y_F = A^{\dagger} \cdot F \cdot Y = A_F^{\dagger} \cdot Y \tag{79}$$

Matrices to represent the SRM in this work were obtained analytically for convenience, but they can also be obtained from Monte Carlo simulations, with likely improvement in image quality without affecting the speed of the method.

Reconstruction times presented in the results section corresponded to only one CPU core. Multi-CPU or Graphics Processing Unit (GPU) strategies can be used to further accelerate the reconstructions. For instance, we have verified a very straightforward method to use multicore 2D by assigning each slice to a CPU-thread, reducing the total time almost linearly within the number of threads employed.

Notice also that smaller sinograms with a radial bins reduction can be used. Although some resolution will be lost with these smaller sinograms, their very short reconstruction times make them suitable for real time imaging. Moreover, for real time applications, most often, only projection images into predefined planes will be needed. This projection operation can be incorporated into the pseudo-inverse array before reconstruction, drastically reducing the size of the matrices needed as well as the reconstruction time as shown in figure 74 and table 9.

5.6 Conclusions

We show that PINVz outperforms SSRB in terms of resolution for non-centered sources and provide a more homogeneous resolution recovery in the whole FOV than SSRB or FORE. Furthermore, pseudo-inverse methods are fast and can be implemented for real time applications, while other methods such as FORE are not currently fast enough.

Besides, 2D-PINV reconstruction can take into account physical and geometrical information in the SRM which may result in improved resolution recovery compared to analytical reconstructions, while keeping or even improve reconstruction times.

Furthermore, PINV reconstruction make possible a direct reconstruction over planes in fractions of seconds, making the method suitable for real-time imaging and faster that any other tested method which require a total 3D reconstruction before the projection over planes.

6 Deep PRC

In this section of the thesis, we propose the use of DL techniques for fast and accurate PR correction. These results have been published in 2021 in the journal ”Applied Sciences” [Herraiz et al., 2021] and presented in the III Jornadas RSEF/IFIMED de Física Médica. Part of them have been also sent to the 16^{th} International Meeting on Fully Three-Dimensional Image Reconstruction in Radiology and Nuclear Medicine (Fully3D 2021), where they have been accepted as a talk contribution.

6.1 Motivation and objectives.

Many correction approaches have been proposed to remove the blurring caused by the PR on PET reconstructed images. They differ, not only on the PR model they are based on, but also on how they are applied. Two main approaches to perform PRC in PET can be identified. [Herraiz et al., 2021]

- PRC applied as a post-processing step to the reconstructed images. In this approach, the reconstructed images before PRC are considered to represent the distribution of the positron annihilation events, instead of the distribution of the positron emissions. Therefore, the goal of the post-processing PRC procedure is to convert the annihilation distribution into the positron emission distribution (the one expected to be seen with PET). Post-processing PRC has the advantage of being fast, simple, and to some extent independent of the procedures, algorithms and codes used in the image reconstruction. On the other hand, it has the risk of increasing the noise in the final corrected images [Cal González, 2015] [Carter et al., 2020] [Bertolli et al., 2016]. This approach has been applied using Fourier-deconvolution techniques [Derenzo, 1986], with isotropic and tissue-independent kernels, as well as iterative deconvolution methods, such as Richardson-Lucy [Rukiah et al., 2018] which enables the use of more realistic PR models.
- PRC applied within the tomographic iterative image reconstruction process. PR models can be included into a Point-Spread-Function (PSF) or resolution kernel [Cal-González et al., 2015] [Cal-Gonzalez et al., 2018] [Bertolli et al., 2016], or within the System Response Matrix (SRM) used in the iterative reconstruction. This can be argued to be the most common approach for PRC with ^{18}F, as in fact, many image reconstruction methods use SRM from point source measurements [Panin et al., 2006] obtained from ^{18}F in water, or ^{22}Na in plastic, or realistic simulations [Herraiz et al., 2006] that incorporate PR effects. This approach has some important limitations: on one hand, adapting an existing SRM to other radionuclides could be difficult, unless a SRM where PR is factored out is used [Zhou and Qi, 2011]. Furthermore, fully realistic PR models would require evaluating the SRM in each particular acquisition. In some works, a miss-matched projector / backprojector pair has been proposed, with PR blurring only applied right before the forward projection operation. It has been shown that using a PR blurring kernel in the backprojector has only the effect of reducing the convergence speed of the iterative algorithm [8]. In this case, the

> SRM used should not incorporate any PR effects. In many cases it is difficult to separate the PR from other blurring effects considered in the SRM, and including an radionuclide-dependent PRC into a reconstruction procedure has the risk of overcorrecting the PRC, yielding overshooting and Gibbs artifacts [Rahmim et al., 2013].

We propose a deep-learning based PRC method (Deep-PRC) [Herraiz et al., 2021] applied as a post-processing step to the reconstructed PET images. Our goal was to develop a fast PRC method for 3D PET imaging, that provides PET images for medium and large range radionuclides rivaling in spatial resolution to the ones reconstructed with the standard short-range ^{18}F radionuclide. We trained a Convolutional Neural Network (CNN) with realistic simulated cases of preclinical studies of reconstructed images of ^{68}Ga and ^{18}F. It is able to produce accurate ^{68}Ga PR-corrected images similar to the ^{18}F ones. Our image reconstruction method already incorporated the ^{18}F PRC, and therefore, the purpose of this work is to obtain a PRC for ^{68}Ga that makes it look similar to the corresponding ^{18}F counterpart.

6.2 Materials and methods

Supervised Machine Learning (ML) requires a set of reference cases to train the CNN. In this work, we generated simulated cases with realistic activity, material and density distribution. The complete workflow is depicted in figure 75.

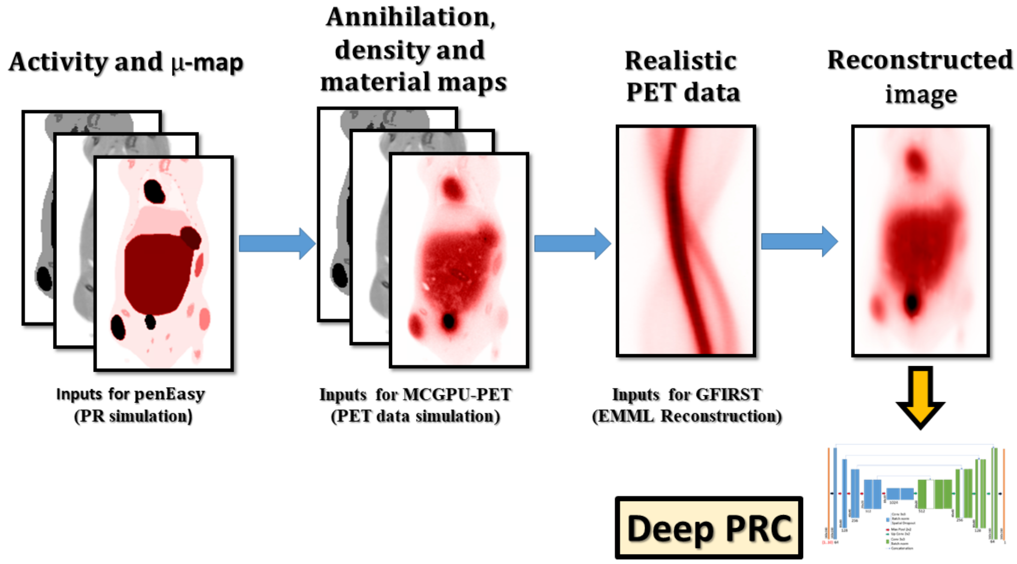

Figure 75: Workflow to produce the realistic simulated cases with different radionuclides.

6.2.1 MC simulations for PR:

The MC tool penEasy (v2020) [Sempau et al., 2011] based on PENELOPE [Sempau et al., 2003] [Sempau and Andreo, 2006] was used to simulate the PR for different radionuclides in several heterogeneous biological tissues. In this work, penEasy was adapted to generate 3D images of the spatial distribution of the positron annihilation points using as an input the 3D images of the positron emissions and CT (see figure 75). PenEasy takes into account the path traveled by each positron until its annihilation taking into account their energy distribution and all the materials in the field-of-view.

The energy distribution of the positrons emitted by ^{68}Ga and ^{18}F was obtained with PenNuc [García-Toraño et al., 2019] which considers all possible decay branches and nuclear properties for a large set of tabulated radionuclides (see figure 76).

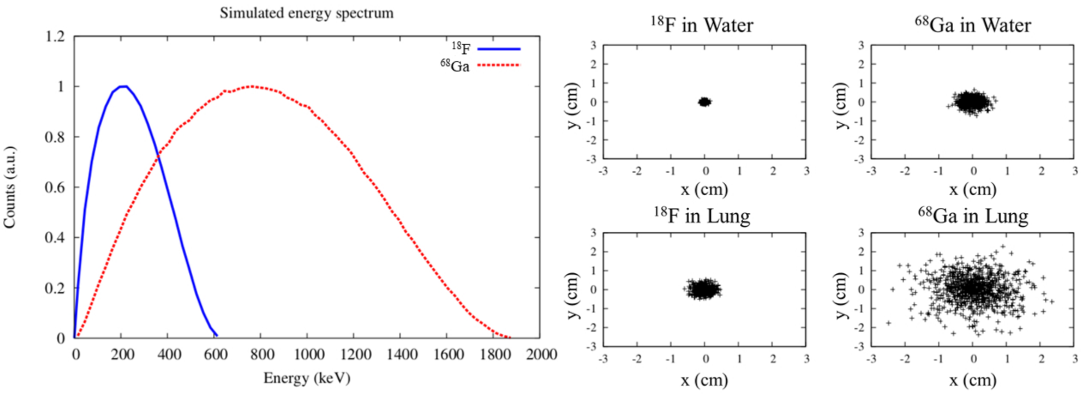

Figure 76: Simulated energy spectra of the positrons emitted by ^{18}F and ^{68}Ga obtained with PenNuc [García-Toraño et al., 2019], and distribution of annihilation points for ^{18}F and ^{68}Ga in water and lung tissue.

6.2.2 Simulated cases:

Numerical mice models from a repository [Rosenhain et al., 2018] were used to simulate the different cases of activity, material, and density distributions needed for training, testing and validating the CNN. The material composition and density of each tissue in the models were directly obtained from the repository, while different activities were assigned to each tissue type such as heart, liver, kidneys, and tumors using a range of typical values found in ^{18}F-FDG acquisitions. The numerical models consisted of 154 × 154 × 242 cubic voxels of 0.28 × 0.28 × 0.28 mm.

Each model was simulated twice, once for ^{18}F and once for ^{68}Ga (see figure 77). Each simulation consisted of around $3 \cdot 10^8$ positron emissions simulated at a rate of $3.4 \cdot 10^4$ histories per second for the ^{18}F simulations and $2.2 \cdot 10^4$ histories per second for the ^{68}Ga simulations in an Intel(R) Xeon(R) CPU @ 2.30GHz computer.

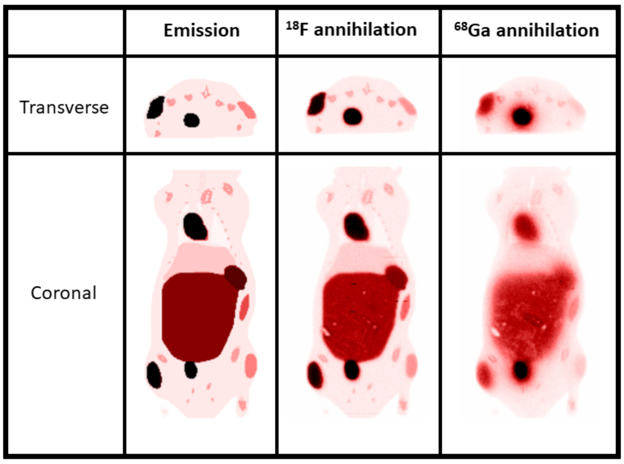

Figure 77: Example of the simulated cases with penEasy. The effects of PR on the images can be clearly appreciated.

6.2.3 PET Acquisition Simulation and Reconstruction:

In order to generate images more similar to actual PET reconstructed images, the positron annihilation distributions obtained from penEasy were used to simulate a realistic PET acquisition in a generic preclinical scanner similar to Inveon PET/CT scanner [Constantinescu and Mukherjee, 2009] using the MC simulator MCGPU-PET [Badal et al., 2018]. MCGPU-PET is an adapted version for PET of the MC-GPU software, which was developed for X-ray imaging [Badal and Badano, 2009]. MCGPU-PET allows simulating in a very fast and realistic way PET acquisitions from voxelized activity, material and density distribution. MCGPU-PET can generate data which can be histogrammed into 3D sinograms, in our case with 147 × 168 × 1293 bins considering a maximum ring difference of 79, an axial compression factor of 11 and a radial bin size of 0.795 mm. MCGPU-PET simulations contain around $1.2 \cdot 10^9$ coincidences including scatter and non-scattered true coincidences in a minute ($2 \cdot 10^7$ coincidences/second) in a computer with a GeForce GTX 1080 8Gb GPU.

For the reconstruction of the sinograms, we used GFIRST (see section 3.4) [Herraiz et al., 2006]. In this case, the SRM used was the standard one created based on ^{18}F in water. We used 1 subset and 40 iterations. The final images consisted of 154 ×154 × 80 voxels with a size of 0.28 × 0.28 × 0.795 mm, as this is the typical size of the images reconstructed in the Inveon scanner [Constantinescu and Mukherjee, 2009]. The total reconstruction time was 50 seconds in a GTX 1080 8Gb GPU. The values of the reconstructed images were converted into standardized uptake value units (SUV) to make it more easy to evaluate the performance of the method. Using SUV units, a radiotracer with uniform distribution in the body would have a SUV of 1.

At the end of the whole simulation workflow (see figure 75), 8 mice were simulated with ^{18}F and ^{68}Ga, with a total of 640 slices. In order to make the size of the slices more tractable to the neural network, each image of 154 × 154 pixels were padded with zeros to reach a size of 160 × 160 pixels.

6.2.4 Neural Network:

The CNN was implemented in Python within the Tensorflow framework [Abadi et al., 2016] (v 2.3.0) with Keras [Chollet, 2015]. It is based on the U-NET network [Ronneberger et al., 2015] which has demonstrated to be useful in many medical imaging applications [Berker et al., 2018] [Leung et al., 2020]. We directly used the U-NET model available in Keras with 4 levels, 64 filters and dropout factor of 0.2.

Inputs to the model were slices of the ^{68}Ga (PET) and μ-maps (CT) volumes. In this work, we considered different cases (see table 10), in each of them, we evaluated the performance of the method when using 1, 3 and 5 input slices and also using 3D patches of the image instead of complete slices. The different slices were used as channels in the input layer. In all cases, the output was the corresponding central slice from the ^{18}F-PET image with 160 × 160 × (1 channel). In the case of the 3D patches, each input patch had 32 × 32 × 9 voxels, and the output was the central 16 × 16 × 1 voxel. The use of 3D patches approach showed to improve the results, and reduce the risk of over-fitting since using 3D patches let us to increase the number of trained images in two orders of magnitude compared to the use of whole 2D slices. Moreover it also makes it easier to fit the training data into the GPU memory. This can be explained since we know that the PR is a local effect and, for an emission point, its PR kernel involves a certain volume around this point. Thus, using only one or a few slices results into the loss of relevant information in the axial direction, but using the whole 3D image is not necessary since PR effect at large distances from the emission point is negligible. The input patches were normalized to make their values to be between 0 and 1. This normalization is restored in the output, so that the PRC preserves the appropriate units.

INPUT	^{68}Ga (PET)
1 slice	$160 \times 160 \times 1$
3 slices	$160 \times 160 \times 3$
5 slices	$160 \times 160 \times 5$
3D patches	$32 \times 32 \times 9$

Table 10: Size of the Input Layer for the different evaluated cases of the Deep PRC network. Only the size of the PET images are specified, the size of the μ-norm images is the same that the PET one.

In this work, the Swish activation function [Ramachandran et al., 2017] was used instead of Relu. Swish is a new, self-gated activation function which performs better than ReLU with a similar level of computational efficiency.

6.2.5 Model Training:

The simulated cases were separated as follows: one volume was set aside and not used in the training/validation process, while the other 7 volumes were processed and data augmentation was used with flip and shifts in horizontal and vertical directions and in-plane rotations. This enabled training the network with a much larger variety of cases than the initially simulated ones.

Model training was performed with the recently proposed Rectified Adam optimizer [Liu et al., 2019] (learning rate of $1 \cdot 10^{-3}$) and with the Lookahead technique [Zhang et al., 2019]. The combination of these techniques provides a much faster convergence of the training process compared to the most commonly used Adam optimizer. The loss function used was the L1-norm between each patch or slice of the ground-truth of the ^{18}F image , and the output patch or slice of the Deep-PRC network.

We used for training, an NVIDIA T4 (NVIDIA Corporation, Santa Clara, CA, USA) graphics processing unit (GPU) with 16GB of memory from Google Cloud (AI notebook running Jupyter Lab, with CUDA 10.1). The models were trained for 50 epochs with 100 iterations each. It took around 1 hour to train each considered case. In the case of 3D patches the model was trained for 200 epochs with 100 iterations each, taking also around 1 hour to train (see figure 78).

One simulated case was set aside and not used in the training/validation process, to perform the final test.

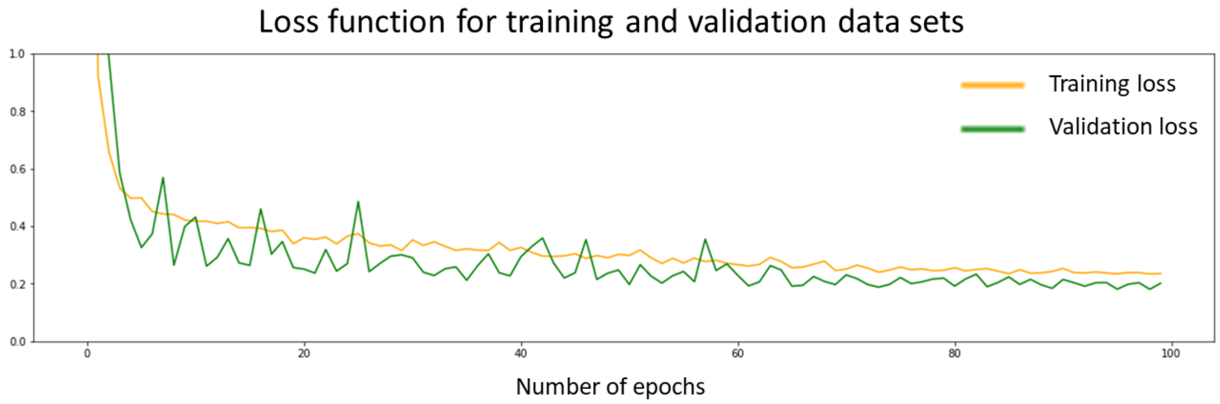

Figure 78: Evolution of the loss function over the epochs during the training using the train and the test data-sets for the 3D patch model.

6.2.6 Application and Quantitative Analysis:

The trained models were saved as Keras models in hdf5 format. The models were then loaded and applied to a simulated study not included in the training nor the validation datasets. In the case of the models with 3 and 5 input slices, the slices closer to the edges of the axial FOV were extended to avoid truncation. A quantitative analysis of the resulting image was performed obtaining the mean (μ) and standard deviation (σ) in different organs. The noise was defined as the ratio σ/μ in uniform regions away from any boundary and edges. The recovery coefficients were obtained defining regions over the whole organs, and their values were then normalized with respect to the reference reconstruction with ^{18}F. The differences between the ^{68}Ga images before and after the proposed PRC can be easily evaluated from the obtained coefficients.

6.3 Results

The trained models were applied to a simulated case not considered in the training nor the validation process. The input was adapted to the specific characteristics of each trained network (selecting the corresponding input slices, zero-padding the images to obtain 160x160 pixels in each slice, normalizing the values to be between -1 and 1). The time required for obtaining the PRC on the 80 slices of the whole volume was: 5.14s in a T4 GPU and 2.85s in a V100 GPU. Although these results can be speeded-up by using multiple GPUs, they are already fast enough to be used in preclinical and clinical applications.

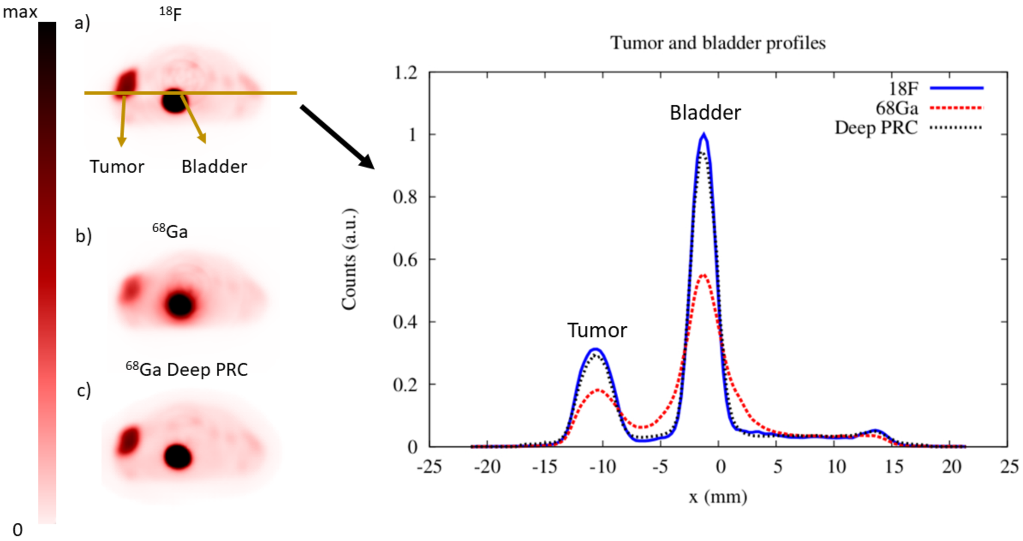

Figure 79: Profiles across different organs in the 18F, 68Ga and 68Ga with Deep-PRC images.

The differences in SUV units between the estimated images (^{68}Ga with Deep-PRC) and the reference one (^{18}F) are shown in figures 79 and 80.

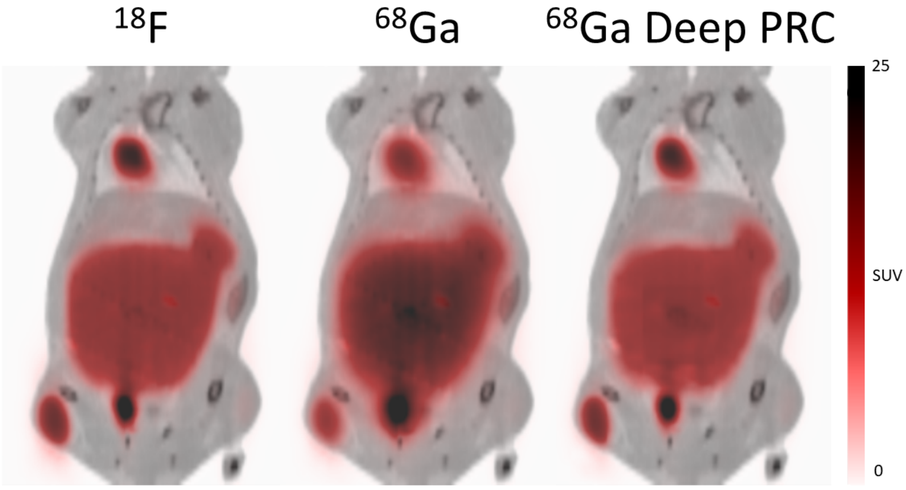

Figure 80: Images of the difference between the estimated images (68Ga with Deep-PRC) and the reference one (^{18}F) for each of the cases considered.

The results of the quantitative analysis are shown in table 11. From the table, it is clear that the ^{68}Ga images corrected by PR images are very similar to the ^{18}F images (with recoveries greater than 95 % of the reference values). Additionally, the noise level of the estimated images is comparable to the reference one, which indicates that the proposed method does not trade noise for resolution, as it is the case in many deconvolution-based approaches for PRC.

	Recovery (%)			Noise (%)		
	Heart	Bladder	Tumor	Heart	Bladder	Tumor
^{18}F	100.00	100.00	100.00	2.00	3.75	3.39
^{68}Ga	67.41	53.49	60.50	4.03	4.96	4.08
^{68}Ga Deep PRC	95.19	96.16	97.46	2.52	3.96	3.02

Table 11: Quantitative analysis of the results over different regions.

6.4 Discussion

This section presents the use of a deep convolutional neural network to provide an accurate positron range correction in PET. The method has been evaluated in simulations in preclinical studies and its performance characterized.

Our results indicate that overall the image quality produced by the learned model is comparable to that of the reference images, with recoveries going up from around 60% to more than 95%, while keeping low noise levels.

One interesting question that we wanted to address in this work is the amount of input data required for these types of algorithms. Being the PR a 3-dimensional effect (i.e. it affects not only a particular single slice) and being dependent on both the PET activity and the material distribution (CT), it may be reasonable to expect that many PET and CT input slices are needed to generate an accurate output slice. On the other hand, many works have shown that the information in PET and CT images is not independent, and that a deep neural network may be able to estimate to some extent images of one modality from the other. This fact may indicate that using only the PET image as input may be enough.

The results obtained with all methods considered were good, as shown by the L1-loss function in the validation cases. Nevertheless, it seems that the training with just the PET images as input, and with large enough axial slices is the best option. It is important to note that in our case, each slice is two times larger than the voxel size in the transverse direction. Therefore, considering 5 slices corresponds to 4mm in the axial direction, which seems enough to consider the effects of surrounding slices for a specific slice. In this work the number of slices were limited by the amount of memory available in the GPU. Nevertheless, this is something that will be easily solved with new GPU models.

It is important to note that although we proposed the method as a post-processing step, the same neural network architecture could be used to generate the PR model that can be applied in the forward projection within an image reconstruction reconstruction (simply by inverting the input and outputs of the NN). This line of research will be explored in future works.

In this work, the axial FOV of the scanner was large enough for mice, so no significant axial truncation of the PET activity was present. If there is significant truncation (as it usually happens in whole-body PET acquisitions in which only a section of the body is examined in each bed axial position), it may be advisable to perform this PRC on the final 3D whole-body volume, to avoid possible truncation artifacts (from activity out of the axial FOV in each particular bed position). This can be argued to be an advantage of the post-processing PRC approach, as it may be easily applied to multi-bed studies in which the activity from other bed positions may have a non-negligible effect.

In this work, the effect of positronium formation in the positron range has not been considered. This may occur when after losing its kinetic energy, the positron reaches thermal velocities (a few eV), and instead of annihilating directly with an electron into two gammas, forms an intermediate state called positronium which may extend its life-time. Its effect on the PR is not well established but it may have a non-negligible effect in porous materials or low-density ones such as the lungs.

The cases developed in this work are not exclusive of any scanner or radionuclide in particular. In this work we have used the preclinical scanner Inveon and 68Ga as a reference, but the proposed approach is flexible and suitable for any preclinical and clinical PET systems and with any other radionuclide.

Furthermore, for the moment, the number of cases used in the training of the model is limited and only from simulated cases, not including many of the effects present in real acquisitions that may affect to the images. This may have an effect on the performance of the method in real PET acquisitions. However the proposed method present an interesting starting point to further include real cases and more variability in the training of the network in future works.

6.5 Conclusions

We have developed and evaluated a deep Convolutional Neural Network (CNN), DeepPRC, that provides a fast and accurate PRC method to recover the resolution loss present in PET studies with radionuclides that emit positrons with large PR. We demonstrated its quantitative accuracy in realistic simulations of preclinical PET/CT studies with 68Ga.

Our results suggest that it is sufficient to use PET images as input for the neural network (i.e. without the corresponding CT or the u-map extracted from it), but it it important to include not only the reference slice (i.e. 2D case), but also some additional neighbour slices.

The correction of PR effects in PET image reconstruction is becoming mandatory in the light of the increasing use of high-energy positron emitters in preclinical and clinical PET imaging and their improved spatial resolution. CNNs seem to be very well suited for this type of correction.

7 Multiplexed PET. Radionuclides Separation

Some of the results of this section were presented at the 2020 IEEE Nuclear Science Symposium and Medical Imaging Conference (NSS/MIC). Some other results will be published in next months since scientific papers are currently being written.

7.1 Motivation and objectives.

In this chapter, we evaluated the simultaneous use of a variety of non-standard radionuclides, emitting additional prompt-γ rays together with a standard β^+ emitter as ^{18}F. Multiplexed PET (mPET) allows us to the separate the images of two different radionuclides used in the same acquisition. The method is based on the identification and reconstruction of triple coincidences created by non-standard β^+ emitters. While standard PET radionuclides generate only two photons, both coming from the annihilation of the positron emitted, some non-standard radionuclides emit additional prompt-γ rays. Thus, we can identify double coincidences, produced by emitted positrons, coming from both radionuclides, and triple coincidences, where one of the additional γ rays emitted by the non-standard nuclide, is detected in coincidence with the photons from the annihilation.

7.2 Materials and methods.

7.2.1 Description of the proposed method

There are several steps to follow for mPET reconstruction as shown in figure 81 [Herraiz et al., 2013] [Herraiz et al., 2014b].

- **Step 1:** In this thesis, we developed a list-mode reader able to process coincidences from a good number of PET scanners (see section 3.2). This reader provides double and triple coincidences sinograms separately. Using delayed time windows, random events for double and triple coincidences are estimated.

- **Step 2:** Then, we perform an initial reconstruction of the double and triple coincidences using the adapted version of GFIRST as described in section 3.4.

- **Step 3:** We used the reconstructed images as input activity for the MCGPU-PET together with the information about density and segmented materials from the μ-map, we estimate the contribution of scatter spurious coincidences estimation.

- **Step 4:** With all the required corrections, we make a final reconstruction using again the adapted version of GFIRST.

- **Step 5:** Using those images, and the triple/double rate of each radionuclide, we perform the radionuclides separation to finally obtain the images of each radionuclide. This separations is performed using an iterative EM approach assuming that the reconstructed image of the double coincidences (D) is produced by a combination of both radionuclides (A+B), while the reconstructed image of the triple coincidences (T) is just produced by non-standard β^+ emitters (B) [Fukuchi et al., 2021] [Herraiz et al., 2014b].

$$\begin{aligned} D &= A + B \\ T &= \alpha \cdot B \end{aligned} \tag{80}$$

Where α is a sensitivity factor for triple coincidences. Note that, in general, this sensitivity factor depends on the position, since not every point of the image has the same sensitivity for triple coincidences.

Besides the scatter produced into the object and which we have discussed previously, it is also non-negligible the effect that Inter Detector Scatter (IDS) may have for the mPET process. It is important since we could find triple coincidences that are actually produced by two interactions with different detectors from the same annihilation photon. This is possible if the incident photon is not absorbed in the first interaction with the detector, but instead it suffers a Compton scattering process and change its direction, being later absorbed by another detector. That way, we would find a first coincidence between the two photons of the annihilation (one absorbed and the other scattered) and another one produced by the scattered photon. In our case, we take this effect into account during the separation code, considering that the IDS produces a small presence of the double coincidences contribution into the triple coincidences image. We can estimate the IDS factor (f_{IDS}) from acquisitions that only contains the standard β^+ emitter. Thus, we slightly modify equation 80 to:

$$\begin{aligned} D &= A + B \\ T &= f_{IDS} \cdot D + \alpha \cdot B \end{aligned} \tag{81}$$

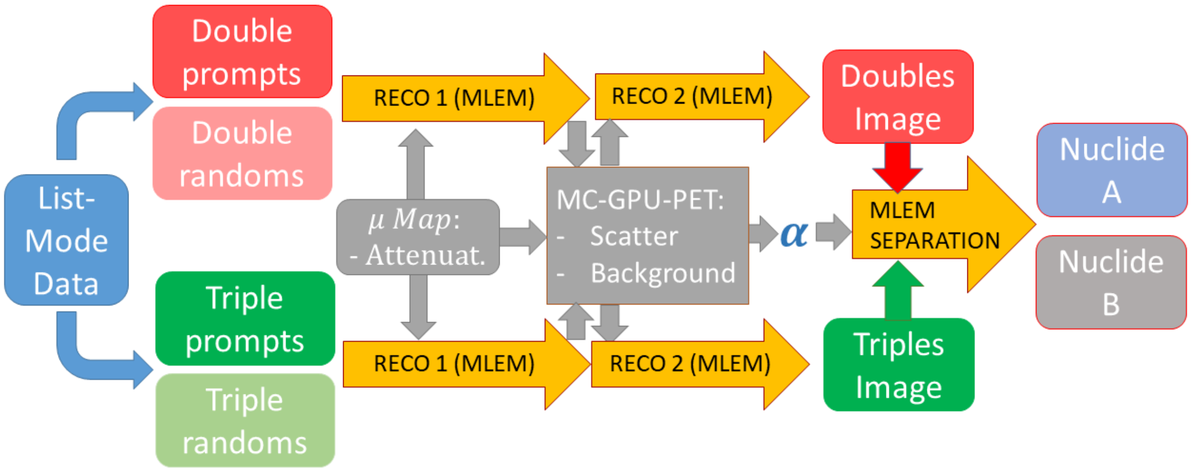

Figure 81: Schematic representation of the workflow for mPET reconstruction. We obtain the double and triple coincidences sinograms from the list-mode file. These sinograms are reconstructed to obtain an initial estimation of the activity map. Then, using these activiy maps and the material and density information provided by the CT images, corrections for scatter and spurious background coincidences are obtained with MCGPU-PET. Finally, the reconstructed images considering all corrections are used for the mPET separation.

7.2.2 Triple coincidences reconstruction

There are several approaches to reconstruct triple coincidences. In this thesis, we will consider that every triple coincidence consists on one line of response coming from the annihilation of the positron, and another line coming from the coincidence produced by one of the photons of the annihilation and one of the additional gamma rays. We can gather both coincidences and reconstruct the image considering that only one of the lines is a real coincidence. The other line of response will introduce a spurious background which should be considered and corrected during the reconstruction. In this thesis, we present two different methods for correcting the background introduced in the triple coincidences reconstruction.

A simple approach consists on reconstructing all the LORs as if they were double coincidences. Then, the background contribution can be estimated (for instance using MCGPU-PET). This approach is very easy to implement although, in some cases, especially when using radionuclides emitting multiple prompt-γ rays in the decay cascade, the estimation of the background in the triple images can be more difficult and it provide images with worse signal to noise ratio.

Another, and more accurate way of dealing with triple coincidences is to use what we refer to as VLOR reconstruction [Lage et al., 2015]. In this approach, we use a maximum likelihood algorithm to determine the probability that each one of the LORs, the actual coincidence coming from the annihilation and the one formed by the additional γ ray, is the one coming from the annihilation. These weights are updated during the reconstruction workflow until convergence. The process is performed modifying the forward projector operator for triple coincidences in the 3D-OSEM algorithm. Instead of projecting the voxels to the LORs of the data, we project them to the VLORs using the list-mode file information during the reconstruction workflow (see figure 82).

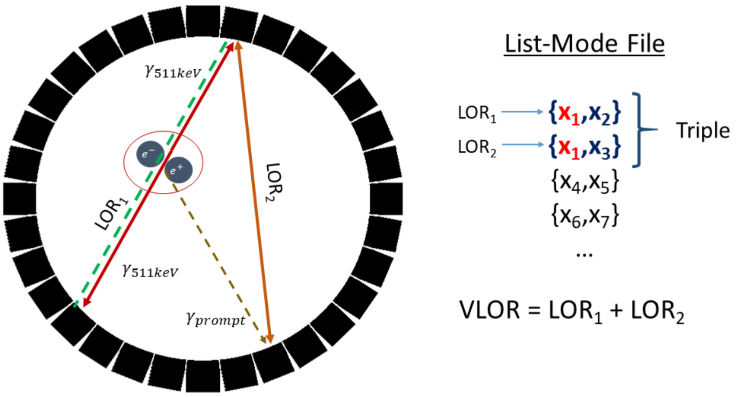

Figure 82: Schematic representation of the triple coincidences identification and the VLOR assignment.

Both approaches have been shown to be good enough to obtain triple coincidence images.

Besides, in general, the amount of coincidences in the triples sinogram is very low compared to the doubles sinogram. This can be a problem since it leads to noisy triple images, which noise level could make the separation process inaccurate. To avoid this, a guided filter [He et al., 2012] is included into the reconstruction algorithm using the double images to guide the noise filtering for the triple reconstruction which contributes to considerably reduce the noise in the triple coincidences image.

7.2.3 Phantom experiments ^{44}Sc + ^{18}F

In a set of experiments, we used two different acquisitions using ^{18}F and ^{44}Sc simultaneously, both of them using acquisitions of a NEMA IQ phantom [National Electrical

Manufacturers Association, 2008] in an Inveon PET/CT scanner [Constantinescu and Mukherjee, 2009]. The measurements were acquired at the Medical University of Vienna in September 2019. In the first measurement, only the cylinders of the IQ phantom were filled, each one with a different radionuclide. In the other acquisition, the cylinders were filled as well with a different radionuclide in each one, and the rest of the phantom were filled with a mix of both radionuclides.

We ackwnowledge these data to Dr. Thomas Mindt, Dr. Theresa Balber, Dr. Jens Cardinale (all LBIAD, Vienna, AT), Dr. Nick van der Meulen (Paul Scherrer Institute, Switzerland) and Dr. Ivo Rausch (Center for Medical Physics and Biomedical Engineering, Medical University Vienna, AT).

For the reconstructions, we used GFIRST, using 60 iterations without subsets. Sinograms of 147×168 radial and angular bins were used with an axial compression (span) of 11 and a maximum ring difference of 79, resulting in a total of 1293 sinograms. Reconstructed images were 128×128×159 (x,y,z voxels) with a voxel size of 0.815×0.815×0.795 mm. Attenuation correction was made using a CT acquisition of the phantom. Random correction was considered as provided in the acquired data, using a delayed window of coincidences. Scatter and the spurious background due to additional gamma rays was estimated using MCGPU-PET, simulating a total of $2.6 \cdot 10^9$ emissions in less than 30 seconds of simulation.

7.2.4 Phantom experiments ^{52}Mn + ^{18}F

Two different acquisitions using ^{18}F and ^{52}Mn simultaneously, in the BrainPET insert PET/MRI scanner were reconstructed. We used the standard acquisition process with a standard configuration (400-650 keV Energy window).

In the first measurement, two syringes were filled, one of them filled with 17MBq of ^{18}F and the other with 24.5MBq of ^{52}Mn. In the other acquisition, a phantom composed of several cylinders was acquired. The “Background” compartment contained ^{18}F with an activity concentration of 16 kBq/ml, ^{52}Mn activity concentration in “Hot 1” compartment was 59kBq/ml. The “Hot 2” compartment was filled with a solution of both 44kBq/ml of ^{52}Mn and 63kBq/ml of ^{18}F.

We acknowledge Kai Giesen, Lutz Tellmann, Stefan Spellerberg, Ingo Spahn and Christoph Lerche (Institute of Neuroscience and Medicine, Forschungszentrum Jülich GmbH, Germany) for providing the acquisitions used in this section.

Sinograms of 199×224 radial and angular bins were used with an axial compression (span) of 11 and a maximum ring difference of 79, resulting in a total of 1203 sinograms. Reconstructed images were 256×256×153 (x,y,z voxels) with a voxel size of 1.25×1.25×1.25 mm. Attenuation correction was made using a model of the phantom. Randoms correction were performed using delayed coincidences. Scatter and the spurious background due to additional gamma rays were estimated using a fast MCGPU-PET, simulating $5 \cdot 10^9$ emissions in less than 90 seconds for each simulation.

7.2.5 Mice experiments

In the context of a collaboration between our research group at UCM and The Jan Grimm Lab at Sloan Kettering Institute of New York, funded by **NIH Project 5 R01 CA215700-05**: *Smart and self-reporting clinical nano-carriers for drug delivery*, we performed mPET studies on several mice in-vivo experiments for antibodies studies. In this thesis, we present the results of some of these acquisitions where the radionuclides separation can be observed. We show results of different radionuclides combinations. All the acquisitions were made at the Sloan Kettering Institute in collaboration with the Weill Cornell Medical College, both in New York. We acknowledge Jan Grimm and Edwin C. Pratt from the Sloan Kettering Institute and Vivek Mittal and Michale J. Crowley from the Weill Cornell Medical College.

7.3 Results

7.3.1 Phantom experiments ^{44}Sc + ^{18}F

In figure 83, we show the results of the radionuclides separation in an IQ-NEMA phantom without background activity. Each one of the rods contains only one of the radionuclides. The results show a perfect separation between both radionuclides. Although this acquisition is less challenging since each radionuclide is delimited in a certain region, it is accurate to calibrate the method and to validate it into simple cases.

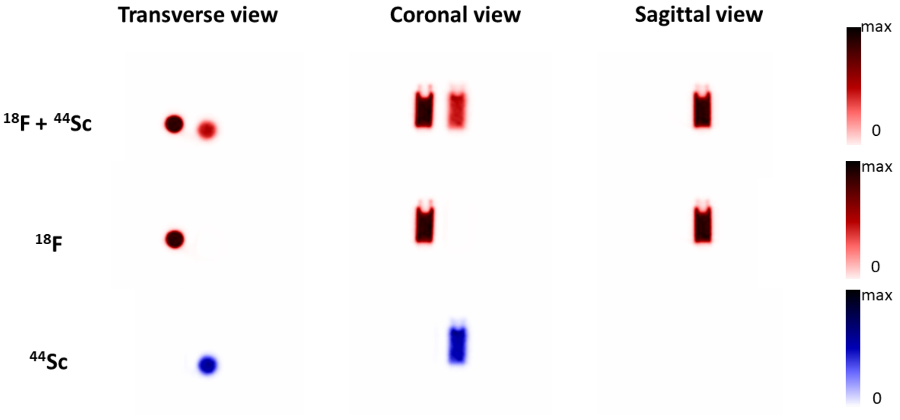

Figure 83: Radionuclides separation for ^{18}F and ^{44}Sc for an IQ-NEMA acquisition without background region.

In figure 84, we present the results for the same IQ-NEMA phantom. In addition to the last case, we filled the background region with a mixture of both radionuclides. We also present a quantitative study of this case in table 12. The results are very promising as both radionuclides could be properly separated even when they were mixed. Due to positron range, which has not been considered in this case, the part of the image corresponding to ^{44}Sc is slightly blurred compared with the image of ^{18}F.

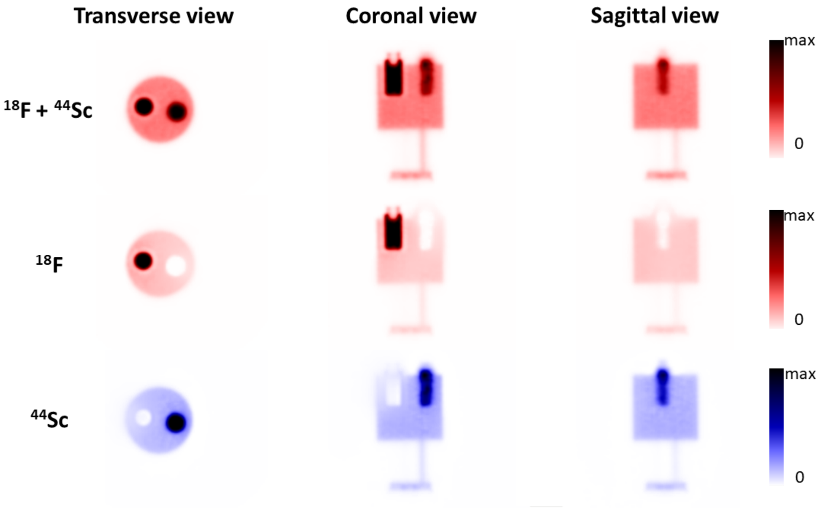

Figure 84: Radionuclides separation for ^{18}F and ^{44}Sc for an IQ-NEMA acquisition.

	Measured MBq	
Region	^{18}F	^{44}Sc
Background	0.85	1.00
Rod 1	0.28	0.01
Rod 2	0.85	0.43

Table 12: Quantitative analysis of the results over different regions for ^{18}F and ^{44}Sc in an IQ-NEMA phantom.

It should be considered that, in this case, reference values for the expected activities were not reliable due to the presence of impurities in the ^{44}Sc sample. However, we know that each one of the rods were filled with different radionuclides while the background was filled with a mixture of both radionuclides which is in concordance to the measured values of the activity in the separation (see table 12).

7.3.2 Phantom experiments ^{52}Mn + ^{18}F

The results in figures 85 showed a good result in the radionuclides separation, a more challenging phantom, with regions with mixed activity is shown in figure 86, where we still see a good result, as we can see in table 13 the results are in agreement with the expected values. In the case of the cylinders, there is still a low amount of ^{52}Mn that should not appear in the background region. These discrepancies could be an effect of non-corrected multiple events which introduce a background that became relevant for the triples image. However,the results are still good enough as we can see in the quantification.

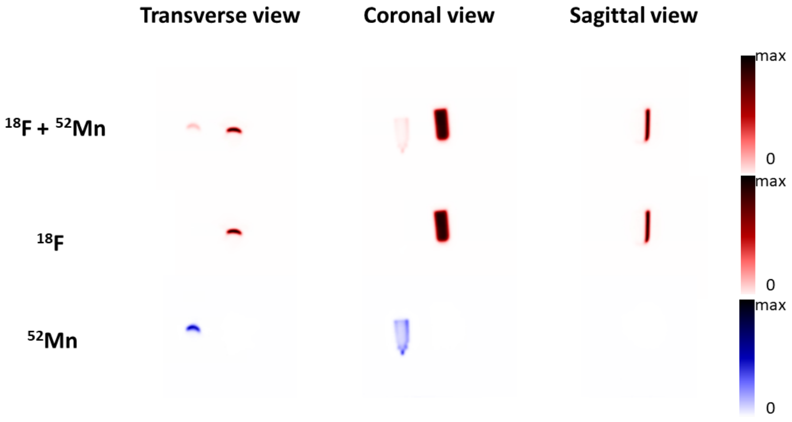

Figure 85: Radionuclides separation for ^{18}F and ^{52}Mn in separated syringes.

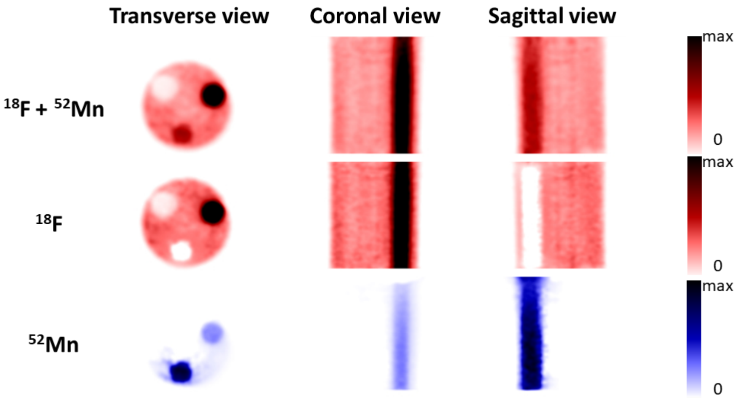

Figure 86: Radionuclides separation for ^{18}F and ^{52}Mn in a cylinder phantom.

	Reference kBq/ml		Measured kBq/ml	
Region	^{18}F	^{52}Mn	^{18}F	^{52}Mn
Background	15.36	0	15.34	1.5
Rod 1	0	17.11	2.3	20.74
Rod 2	60.48	12.76	62.83	11.31

Table 13: Quantitative analysis of the results over different regions for ^{18}F and ^{52}Mn in a cylinders phantom.

7.3.3 Mice experiments

In this section we present the results of some experiments selected among a variety of acquisitions with a combination of different radionuclides that were performed along the last year. In particular, we show the results of a four-bed mice experiments where ^{68}Ga was used as standard β^+ emitter and ^{124}I as non-standard one. As a proof of concept, we reconstructed and performed radionuclides separation on an acquisition with only ^{68}Ga and other one where only ^{124}I was injected. This experiments, although trivial, are useful to calibrate the method. Indeed, one of the most important steps was to calibrate the method for each one of the scanners and configurations (energy window and used radionuclides for example). These results are shown in figure 87.

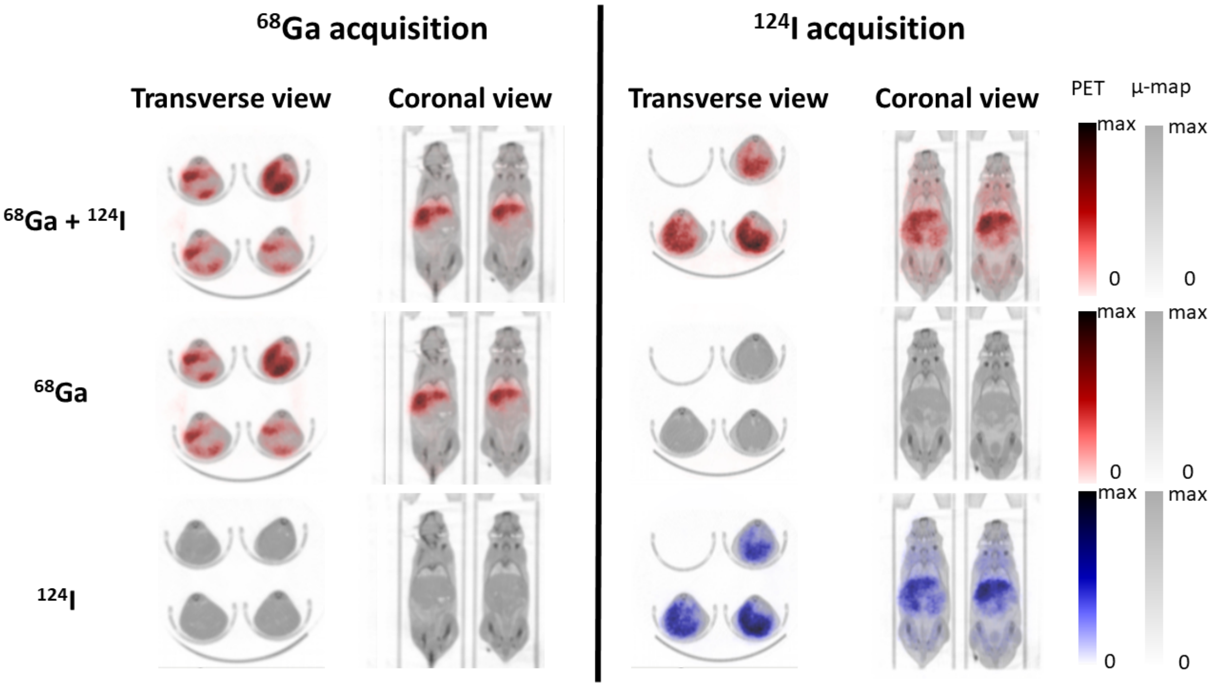

Figure 87: Nuclides separation with 68Ga only (left) and 124I only (right). We can see that no activity is observed in the empty channels.

Then, we performed the mPET separation in acquisitions were both nuclides are mixed. As we can appreciate in figures 88 and 89, the separation was made successfully. The regions with uptake of each isotope are in concordance with the expected values with only one isotope experiments for both radionuclides.

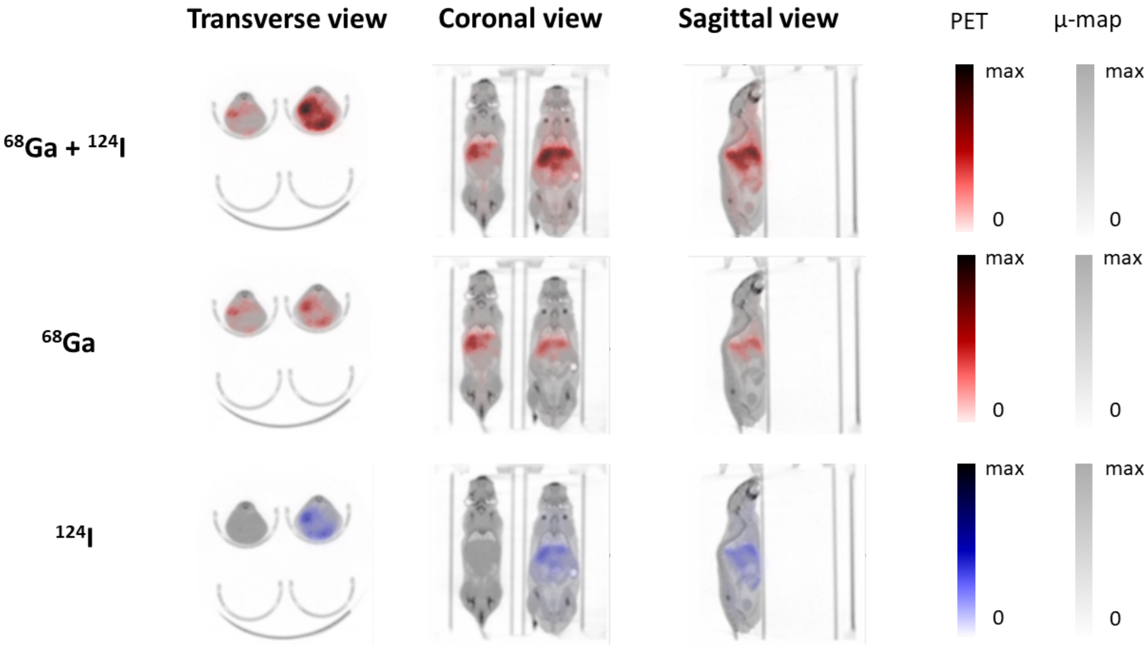

Figure 88: Radionuclides separation for ^{68}Ga and ^{124}I in a four bed mice experiment. In this acquisition, one mouse was injected with only ^{68}Ga and the other one with a mixture of ^{68}Ga and ^{124}I

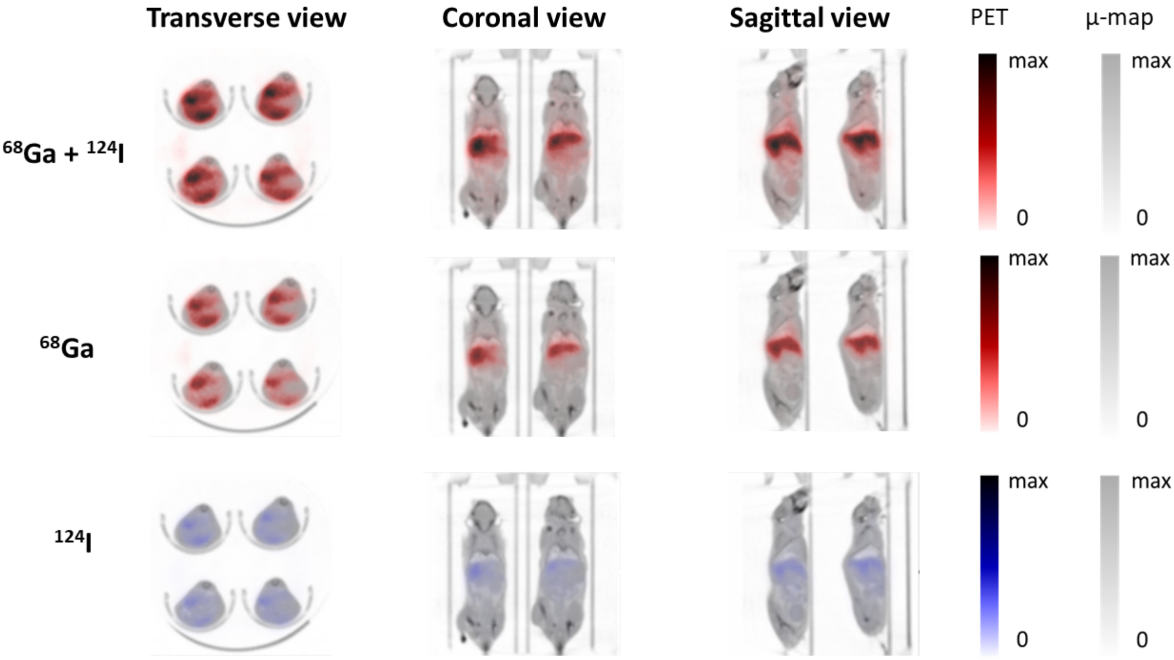

Figure 89: Radionuclides separation for ^{68}Ga and ^{124}I in a four bed mice experiment. In this acquisition, each mouse was injected with a mixture of ^{68}Ga and ^{124}I

We also present a detailed study of ^{89}Zr and ^{124}I acquisitions. In these experiments, ^{89}Zr acts as the pure β^+ emitter. Although it may emit additional γ-rays they are delayed and not prompt-γ, so we can consider it as a pure β^+ emitter for mPET purposes. For these experiments, an initial phantom acquisition with different activity concentrations of both radionuclides was considered. This first experiment is important to show the feasibility of the separation and, more important, to calibrate the separation parameters for this performance. In table 14, we present the quantitative results of the phantom. We also show the radionuclides separation image in figure 90.

	Reference μCi		Measured μCi	
Region	^{89}Zr	^{124}I	^{89}Zr	^{124}I
Background	250	0	237.81	11.92
Sph. 1	64	0	63.09	0
Sph. 2	41.6	10	41.44	9.76
Sph. 3	21.6	20.35	18.80	21.78
Sph. 4	0	30.5	1.35	32.10

Table 14: Quantitative analysis of the results over different regions for a mouse size phantom with different fillable spheres.

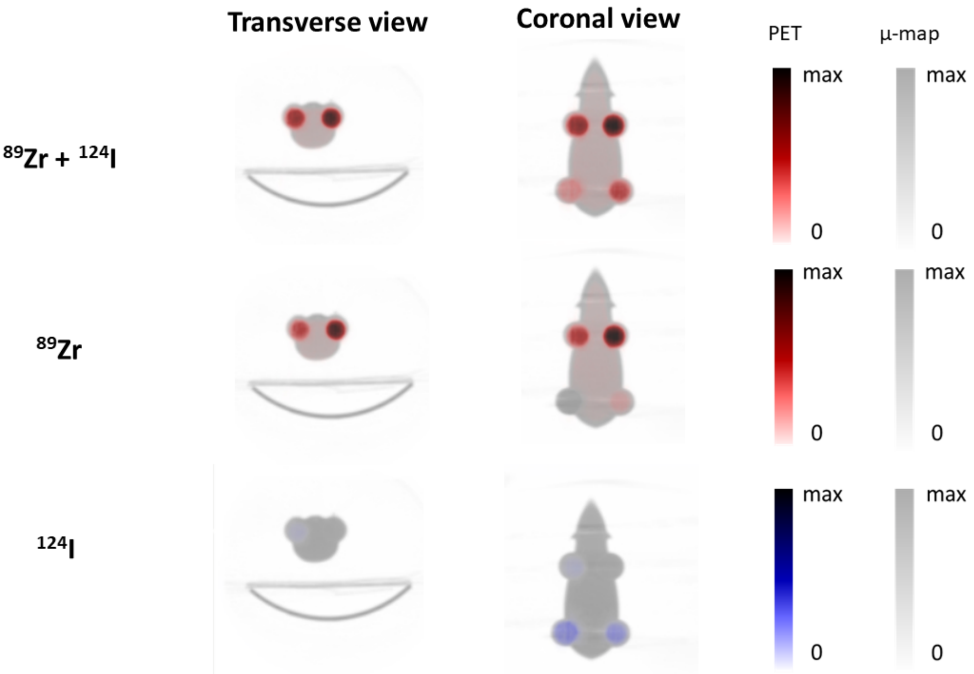

Figure 90: Radionuclides separation for ^{89}Zr and ^{124}I in a mouse phantom. Each one of the spheres of the mouse was filled with different amounts of each radionuclide

As we can appreciate, the results of the radionuclides separation are in concordance with the expected values, we saw an average deviation of 2.85% considering the proportions of each radionuclides expected compared with the measured ones. Also, the maximum deviation was 5.16%.

Using the parameters obtained from the phantom experiment, we proceed to study the method in real mice acquisitions. In this case, we show a two days study. We show the reconstructed and separated images of three different mice injected with ^{89}Zr and ^{124}I one day and two days after the injection of the nuclides. Both radionuclides were labelling antibody molecules. These results are presented in figure 91, also a quantification is shown in table 15.

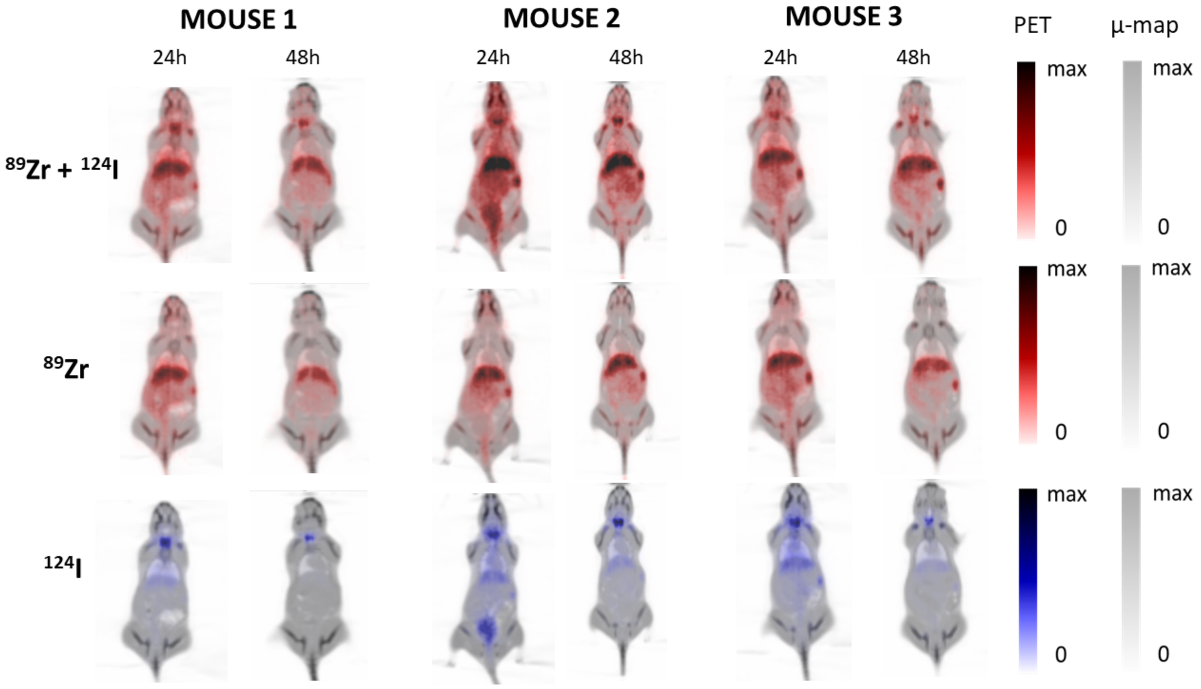

Figure 91: Radionuclides separation for ^{89}Zr and ^{124}I in mice. Both molecules were labelling antibodies although the iodine went progressively away from the molecule as we can clearly appreciate iodine uptake in the thyroids of the mice. This leads to a biological elimination of the radionuclide. We present the results one day and two days after the injection. Only coronal view is shown.

	Reference μCi		Measured μCi		Error (%)	
Region	^{89}Zr	^{124}I	^{89}Zr	^{124}I	^{89}Zr	^{124}I
Mouse 1 24h	452.31	181.76	467.08	175.70	3.27	3.34
Mouse 1 48h	366.80	154.28	373.54	90.89	1.84	41.09
Mouse 2 24h	448.94	180.60	465.81	189.58	3.76	4.97
Mouse 2 48h	363.35	153.05	367.92	90.59	1.26	40.81
Mouse 3 24h	365.87	147.31	381.97	135.16	4.40	8.25
Mouse 3 48h	295.62	124.68	301.46	72.19	1.97	42.10

Table 15: Quantitative analysis of the results over different mice experiments. The total activity inside each mouse was considered for this quantification analysis.

According to the results shown in table 15 we see very good agreement between the observed values and the expected ones. It is remarkable that, in the case of ^{124}I 48h after the injection, we see a much lower activity concentration than expected. This is due to the separation of the nuclide from the labelled molecule. This cause the uptake of ^{124}I in the thyroids which can be appreciated in figure 91, moreover, a good part of the tracer after 24h can be appreciated inside the bladder in mouse 2, which gives us the idea that the radionuclide is being eliminated from the body of the mice. On the other hand, the amount of iodine lost is proportional and more or less the same in each mouse which strengthen the idea of the biological elimination of the radionuclide.

7.4 Discussion

In this chapter, we have implemented the mPET technique for nuclides separation. In all the cases, the technique successfully separated the contribution of two different tracers injected during the same acquisition.. Although the results are very satisfactory, the method also has some limitations that should be considered.

- **Scatter and background estimation:** it is essential to properly correct images to obtain accurate results for the separated images. In the case of mPET, the main factors affecting the images are scattering effect and the spurious background introduced by the additional prompt-γ rays emitted by non standard β^+ emitters. Moreover, for mPET, these corrections should be done not only in the standard double coincidences reconstruction but also for triple coincidences, which makes the process even more challenging. In our case, scatter and background corrections were done using MCGPU-PET, although other approaches can be used.
- **Positron Range (PR) effect:** PR is always a limiting factor for image resolution in PET, in the case of mPET, it is even more challenging since the effects of the different PET emitters, with different PR, are mixed. This may lead to undesirable effects, as

contamination of the large PR radionulcide activity in some regions of the low PR emitter image. We saw this effect for example using ^{18}F with a small PR together with ^{44}Sc with a large PR (see figure 84). The use of PR correction techniques is really challenging for mPET, since as we have two different radionuclides with two different contributions to PR blurring, the correction cannot be done assuming only the PR of one of them. For the future, Deep PRC based on DL techniques can be proposed to correct PR in mPET. Also, it could be included during the iterative images separation process, considering a blurring of each one of the images according to the PR of the nulcides. For the moment, and in the results presented in this thesis, PR effect was not corrected.

- **Inter Detector Scatter (IDS):** the approach we used for IDS effect could be improved correcting it during the reconstruction process instead of after the reconstruction using, for example, MC simulations to estimate the contribution of IDS into the triple coincidences image. However, as in the current version of MCGPU-PET the effect of the interactions with the detectors of the scanner is not considered we could not use it to estimate IDS and instead we opted for the method explained above. It should be noticed that the IDS can be neglected in some cases, specially for clinical large scanners, where the probability of finding this kind of events is really low.

- **Triple coincidences sensitivity:** to obtain an accurate separation for mPET we need good statistics of triple coincidences.

$$TDR(\%) = 100 \cdot T/D \tag{82}$$

This TDR defined in equation 82, where T is the number of triple coincidences and D the number of standard double coincidences, depends mainly on the scanner geometry, the radionuclides used (and the probability of emission of prompt-γ rays), and the relationship between the emission energy of the prompt-γ rays and the energy window used in the scanner. For example using pure ^{124}I acquisitions, we saw TDRs around 10% for Inveon PET/CT scanner, while for clinical scanners as mCT, this rate was reduced to around 3%. This was also a consequence of the energy window, because for most of Inveon PET/CT acquisitions, an energy window of 350-815 keV or 350-750 keV was used while for mCT it was reduced to around 435-650 keV. In the case of ^{124}I, the energy of the most probable prompt-γ ray is around 602 keV, this may produce that some of the additional photons are not detected due to the energy resolution of the detectors. However, using the same narrow energy window for preclinnical scanners as Inveon PET/CT still provides better TDR than for clinical scanners which makes mPET more challenging although still possible for clinical PET.

- **Very hot regions:** other important limitation of the mPET technique is related to the fact that the radionuclides separation may presents some inaccuracies around 5 to 10%. This is fine for most cases but, if the activity concentration in certain regions of the image of one of the nuclides is much higher than for the other one, this discrepancies can be enough to obtain inconsistent results, as the appearance of empty regions where there should be the low concentration radionuclide. We have seen this effect, specially with the combination of high activities of ^{18}F-FDG with antibodies labelled with ^{124}I in the regions of the heart and the bladder where the expected activity of ^{18}F was several orders of magnitude higher that the expected for ^{124}I.

7.5 Conclusions

We have shown a wide number of results of the mPET method for radionuclides separation. In general, we have proven the feasibility of the method for many nuclides combination and for several scanners. Although there is still room for improvement in the method, it can successfully provide the separated images of two different nuclides in the same acquisition. This method has an important potential for many different applications, as different molecules uptake inside a tumor presenting some interesting uses for immuno-PET.

8 Conclusions of this thesis

Looking back to the PET scanners mentioned in this thesis, one can see that many of them are quite old, such as the Inveon PET/CT scanner, and that, however, hardware-wise, newest scanners are not that different from the ones developed one decade ago. There have been incremental improvements for instance in the time of flight capability, number of detectors and sensitivity, size of crystal or technology of the detectors (continuous scintillator blocks are being introduced in some new scanners), compatibility with magnetic fields to make it possible MRI/PET combined scanners, yet a real revolution in the hardware section of PET imaging is just only arriving. However, even if at the hardware level the evolution experienced during the last decade does not seem very dramatic, PET data processing and quality and information we obtain from the images these days is however hugely superior to what we even though possible ten years ago. This has been driven by the exponential increase in the computational capabilities at hand, which allowed for faster, more powerful image reconstructions, more realistic and detailed simulations of the scanner, and improved data processing and filtering.

Indeed, in this thesis, we describe how the technological advances in computer sciences have been used to improve image quality in tomographic image reconstruction and to propose new algorithms that may be used for cutting edge PET applications as real-time PET or mPET. Some years ago, most of the techniques used in this thesis were not feasible or they were assumed computationally too expensive to be considered as an alternative to the state of the art methods.

Specifically, the use of the pseudo-inverse approach shown in this thesis had been presented as a possible method by many authors but it had been only vaguely used before [Selivanov et al., 2006] for 2D PET acquisitions and only for small sinograms. In this thesis, we exploited the increased speed, larger memory of modern computers to yield ultra-fast, even real time, 3D image reconstructions using pseudo-inverse techniques, becoming a brand-name of GFN and presenting a new approach for tomographic image reconstruction. It has been shown to be better than many analytical methods in terms of resolution recovery and noise, and faster than them, making the method feasible for real-time applications, specially through the use of the projections over planes in the pseudo-inverse which may produce several updates of the images each second. Due to the size of a fully 3D SRM, a fully 3D approach is not possible right now using pseudo-inverse reconstruction, although, regarding the evolution of computational resources, maybe in some years that become a real possibility.

On the other hand, MC methods, one of the strongholds of the GFN, have been widely used in PET since many years ago as they are a powerful and realistic tool for PET applications and corrections. However, due to their computational cost, they were too slow to provide real tools that can be used during the reconstruction workflow. The development of GPUs have open a new window to fast MC methods that can be used to apply important corrections in current iterative reconstruction process. In this work we have contributed to the development of MCGPU-PET, a powerful tool, able to provide really fast simulations much faster than usual MC simulator codes. Furthermore, MCGPU-PET is an open-source code which suppose an important advantage for the users. MCGPU-PET can be used to include corrections of scatter and spurious background coincidences for non-standard PET emitters.

The combination of powerful reconstruction algorithms, realistic simulations and a clever interpretation of data from common scanners, looking for triple coincidence events, allowed for multi-nuclide simultaneous acquisitions or mPET. This technique is a cutting-edge approach that allows to obtain the separate images of two different radionuclides, one of them a standard β^+ emitter and the other one emitting also additional prompt-γ rays, used together in the same acquisition without needing hardware modifications. In this thesis, we developed a list mode reader code, able to obtain double and triple coincidences sinograms from a wide number of commercial scanners, clinical and preclinical. The differentiation between triple coincidences, just produced by the additional prompt-γ rays emitter, and double coincidences, produced as a combination of both radionuclides, are further used in the mPET technique to achieve the nuclides separation. Good quality images are required to obtain satisfactory results using this technique, thus, we used the MCGPU-PET tool to perform some of the main important corrections to the images.

Moreover, the use of Artificial Intelligence (AI) techniques such as Deep Learning (DL) has supposed a revolution in the field of medical imaging, being a completely different approach and a change of paradigms, not only in this field but also in science in general. DL algorithms begin to shape the way we introduce corrections in PET, given rise to ultra-fast correction algorithms. In this thesis, we have studied a possible application of DL techniques for Positron Range Correction (PRC), which is one of the main limiting factors in PET imaging. The use of the proposed Deep-PRC algorithm has been shown to be an interesting approach able to recover the resolution lost due to PR without increasing the noise in the image. The method has been tested with simulations and, thus, it should be tested with real data to determine if this approach is as good in real cases as it is for simulations. Moreover, in this thesis we only present results for a specific radionuclide, ^{68}Ga, being necessary the training of a model for each radionuclide used.

The results presented in this thesis exemplify some new lines of research which the advances in computation combined with a deep understanding of the physical processes involved in PET imaging, made possible, even when dealing to conventional PET hardware. We are, however, just starting to glimpse what these advances will provide when incorporated deep down, at the hardware level, with PET devices which are fully ready to deal with mPET, real time imaging, deep learning algorithms to analyze events and to apply corrections to them. A giant, non-incremental revolution in PET imaging awaits around the corner. The work we did in this thesis has contributed to it.

9 Bibliography

References

[Abadi et al., 2016] Abadi, M., Agarwal, A., Barham, P., Brevdo, E., Chen, Z., Citro, C., Corrado, G. S., Davis, A., Dean, J., Devin, M., et al. (2016). Tensorflow: Large-scale machine learning on heterogeneous distributed systems. *arXiv preprint arXiv:1603.04467*.

[Abushab, 2013] Abushab, K. (2013). *Simulation and image reconstruction of clinical TOF-PET scanners*. PhD thesis, Universidad Complutense de Madrid.

[Abushab et al., 2016] Abushab, K. M., Herraiz, J. L., Vicente, E., Cal-Gonzalez, J., Espana, S., Vaquero, J. J., Jakoby, B. W., and Udias, J. M. (2016). Evaluation of PeneloPET Simulations of Biograph PET/CT Scanners. *IEEE Transactions on Nuclear Science*, 63(3):1367–1374.

[Adam et al., 1997] Adam, L.-E., Zaers, J., Ostertag, H., Trojan, H., Bellemann, M., and Brix, G. (1997). Performance evaluation of the whole-body pet scanner ecat exact hr/sup+/following the iec standard. *IEEE Transactions on Nuclear Science*, 44(3):1172–1179.

[Afshar-Oromieh et al., 2014] Afshar-Oromieh, A., Zechmann, C. M., Malcher, A., Eder, M., Eisenhut, M., Linhart, H. G., Holland-Letz, T., Hadaschik, B. A., Giesel, F. L., Debus, J., et al. (2014). Comparison of pet imaging with a 68 ga-labelled psma ligand and 18 f-choline-based pet/ct for the diagnosis of recurrent prostate cancer. *European journal of nuclear medicine and molecular imaging*, 41(1):11–20.

[Agostinelli et al., 2003] Agostinelli, S., Allison, J., Amako, K. a., Apostolakis, J., Araujo, H., Arce, P., Asai, M., Axen, D., Banerjee, S., Barrand, G. ., et al. (2003). Geant4—a simulation toolkit. *Nuclear instruments and methods in physics research section A: Accelerators, Spectrometers, Detectors and Associated Equipment*, 506(3):250–303.

[Aguiar et al., 2010] Aguiar, P., Rafecas, M., Ortuño, J. E., Kontaxakis, G., Santos, A., Pavía, J., and Ros, D. (2010). Geometrical and monte carlo projectors in 3d pet reconstruction. *Medical physics*, 37(11):5691–5702.

[Alessio et al., 2006a] Alessio, A., Kinahan, P., et al. (2006a). Pet image reconstruction. *Nuclear medicine*, 1(1):1–22.

[Alessio et al., 2006b] Alessio, A. M., Ieee, M., Kinahan, P. E., Ieee, S. M., Lewellen, T. K., and Ieee, S. M. (2006b). Modeling and Incorporation of System Response Functions in 3D Whole Body PET. *IEEE Transactions on Medical Imaging*, 25(7):828–837.

[Alliot et al., 2015] Alliot, C., Kerdjoudj, R., Michel, N., Haddad, F., and Huclier-Markai, S. (2015). Cyclotron production of high purity 44m, 44sc with deuterons from 44caco3 targets. *Nuclear Medicine and Biology*, 42(6):524–529.

[Andersen and Kak, 1984] Andersen, A. H. and Kak, A. C. (1984). Simultaneous algebraic reconstruction technique (sart): a superior implementation of the art algorithm. *Ultrasonic imaging*, 6(1):81–94.

[Anderson et al., 1997] Anderson, J. M., Mair, B. A., Rao, M., and Wu, C. H. (1997). Weighted least-squares reconstruction methods for positron emission tomography. *IEEE Transactions on Medical Imaging*, 16(2):159–165.

[Andreo, 1991] Andreo, P. (1991). Monte carlo techniques in medical radiation physics. *Physics in Medicine & Biology*, 36(7):861.

[Andreyev and Celler, 2011] Andreyev, A. and Celler, A. (2011). Dual-isotope pet using positron-gamma emitters. *Physics in Medicine & Biology*, 56(14):4539.

[Andreyev et al., 2014] Andreyev, A., Sitek, A., and Celler, A. (2014). Em reconstruction of dual isotope pet using staggered injections and prompt gamma positron emitters. *Medical physics*, 41(2):022501.

[Anger, 1969] Anger, H. (1969). Scintillation camera and multiplane tomographic scanner.

[Archer and Titterington, 1995] Archer, G. and Titterington, D. (1995). The iterative image space reconstruction algorithm (isra) as an alternative to the em algorithm for solving positive linear inverse problems. *Statistica Sinica*, pages 77–96.

[Badal and Badano, 2009] Badal, A. and Badano, A. (2009). Accelerating Monte Carlo simulations of photon transport in a voxelized geometry using a massively parallel Graphics Processing Unit. *Med. Phys.*, 36:4878–4880.

[Badal et al., 2018] Badal, A., Domarco, J., Udias, J., and Herraiz, J. (2018). Mcgpu-pet: a real-time monte carlo pet simulator. In *International Symposium on Biomedical Imaging*.

[Badal and Sempau, 2006] Badal, A. and Sempau, J. (2006). A package of Linux scripts for the parallelization of Monte Carlo simulations. *Comput. Phys. Commun.*, 175:440–450.

[Badawi and Marsden, 1999] Badawi, R. D. and Marsden, P. (1999). Developments in component-based normalization for 3d pet. *Physics in Medicine & Biology*, 44(2):571.

[Badawi et al., 2019] Badawi, R. D., Shi, H., Hu, P., Chen, S., Xu, T., Price, P. M., Ding, Y., Spencer, B. A., Nardo, L., Liu, W., et al. (2019). First human imaging studies with the explorer total-body pet scanner. *Journal of Nuclear Medicine*, 60(3):299–303.

[Bai et al., 2002] Bai, B., Li, Q., Holdsworth, C., Asma, E., Tai, Y.-C., Chatziioannou, A., and Leahy, R. M. (2002). Model-based normalization for iterative 3d pet image reconstruction. *Physics in medicine & biology*, 47(15):2773.

[Bao et al., 2009] Bao, Q., Newport, D., Chen, M., Stout, D. B., and Chatziioannou, A. F. (2009). Performance evaluation of the inveon dedicated pet preclinical tomograph based on the nema nu-4 standards. *Journal of Nuclear Medicine*, 50(3):401–408.

[Barata and Hussein, 2012] Barata, J. C. A. and Hussein, M. S. (2012). The Moore-Penrose Pseudoinverse: A Tutorial Review of the Theory. *Brazilian Journal of Physics*, 42(1-2):146–165.

[Barret et al., 2005] Barret, O., Carpenter, T. A., Clark, J. C., Ansorge, R. E., and Fryer, T. D. (2005). Monte carlo simulation and scatter correction of the ge advance pet scanner with simset and geant4. *Physics in Medicine & Biology*, 50(20):4823.

[Barrett, 1984] Barrett, H. H. (1984). Iii the radon transform and its applications. *Progress in optics*, 21:217–286.

[Bastianello et al., 2017] Bastianello, M., Hernández Pinzon, J., and Pérez, A. (2017). 18f-dopa pet/tc para el diagnóstico del hiperinsulinismo congénito. *Rev. argent. radiol*, pages 226–228.

[Basu et al., 2011] Basu, S., Kwee, T. C., Surti, S., Akin, E. A., Yoo, D., and Alavi, A. (2011). Fundamentals of pet and pet/ct imaging. *Annals of the New York Academy of Sciences*, 1228(1):1–18.

[Bazaraa et al., 2013] Bazaraa, M. S., Sherali, H. D., and Shetty, C. M. (2013). *Nonlinear programming: theory and algorithms*. John Wiley & Sons.

[Beattie et al., 2003] Beattie, B. J., Finn, R. D., Rowland, D. J., and Pentlow, K. S. (2003). Quantitative imaging of bromine-76 and yttrium-86 with pet: A method for the removal of spurious activity introduced by cascade gamma rays. *Medical physics*, 30(9):2410–2423.

[Ben-Israel, 2002] Ben-Israel, A. (2002). The moore of the moore-penrose inverse. *The Electronic Journal of Linear Algebra*, 9.

[Bendriem and Townsend, 2003] Bendriem, B. and Townsend, D. W. (2003). *The Theory and Practice of 3D PET*. Springer, springer edition.

[Benning and Burger, 2018] Benning, M. and Burger, M. (2018). Modern Regularization Methods for Inverse Problems. *Acta Numerica*, 27(January):1–111.

[Berker et al., 2018] Berker, Y., Maier, J., and Kachelrieß, M. (2018). Deep scatter estimation in pet: fast scatter correction using a convolutional neural network. In *2018 IEEE Nuclear Science Symposium and Medical Imaging Conference Proceedings (NSS/MIC)*, pages 1–5. IEEE.

[Bert et al., 2012] Bert, J., Perez-Ponce, H., Jan, S., El Bitar, Z., Gueth, P., Cuplov, V., Chekatt, H., Benoit, D., Sarrut, D., Boursier, Y., et al. (2012). Hybrid gate: A gpu/cpu implementation for imaging and therapy applications. In *2012 IEEE Nuclear*

Science Symposium and Medical Imaging Conference Record (NSS/MIC), pages 2247–2250. IEEE.

[Bertolli et al., 2016] Bertolli, O., Eleftheriou, A., Cecchetti, M., Camarlinghi, N., Belcari, N., and Tsoumpas, C. (2016). Pet iterative reconstruction incorporating an efficient positron range correction method. *Physica medica*, 32(2):323–330.

[Bezrukov et al., 2013] Bezrukov, I., Mantlik, F., Schmidt, H., Schölkopf, B., and Pichler, B. J. (2013). Mr-based pet attenuation correction for pet/mr imaging. In *Seminars in nuclear medicine*, volume 43, pages 45–59. Elsevier.

[Bindseil, 2013] Bindseil, G. A. (2013). Approaches toward combining positron emission tomography with magnetic resonance imaging.

[Boecker et al., 1998] Boecker, H., Dagher, A., Ceballos-Baumann, A., Passingham, R., Samuel, M., Friston, K., Poline, J.-B., Dettmers, C., Conrad, B., and Brooks, D. (1998). Role of the human rostral supplementary motor area and the basal ganglia in motor sequence control: investigations with h2 15o pet. *Journal of Neurophysiology*, 79(2):1070–1080.

[Bolwin et al., 2017] Bolwin, K., Vernekohl, D., Lühder, J., Czekalla, B., Wessels, J., and Schäfers, K. (2017). Development of a clear sub-millimeter small animal pet scanner by reducing the influence of the non-collinearity effect. *Journal of Instrumentation*, 12(03):C03006.

[Bosman et al., 2021] Bosman, D. F., Balcaza, V. G., Delgado, C., Principi, S., Duch, M. A., and Ginjaume, M. (2021). Validation of the mc-gpu monte carlo code against the penelope/peneasy code system and benchmarking against experimental conditions for typical radiation qualities and setups in interventional radiology and cardiology. *Physica Medica*, 82:64–71.

[Bower et al., 2019] Bower, D. V., Richter, J. K., von Tengg-Kobligk, H., Heverhagen, J. T., and Runge, V. M. (2019). Gadolinium-based mri contrast agents induce mitochondrial toxicity and cell death in human neurons, and toxicity increases with reduced kinetic stability of the agent. *Investigative radiology*, 54(8):453–463.

[Braad et al., 2015] Braad, P., Hansen, S., Thisgaard, H., and Høilund-Carlsen, P. (2015). Pet imaging with the non-pure positron emitters: 55co, 86y and 124i. *Physics in Medicine & Biology*, 60(9):3479.

[Bradley, 2008] Bradley, W. G. (2008). History of Medical Imaging. *Proceedings of the American Philosophical Society*, 152(3):349–361.

[Brahme, 2014] Brahme, A. (2014). *Comprehensive biomedical physics.* Newnes.

[Brandt et al., 2019] Brandt, M., Cardinale, J., Rausch, I., and Mindt, T. L. (2019). Manganese in pet imaging: Opportunities and challenges. *Journal of Labelled Compounds and Radiopharmaceuticals*, 62(8):541–551.

[Brasse et al., 2005] Brasse, D., Kinahan, P. E., Lartizien, C., Comtat, C., Casey, M., and Michel, C. (2005). Correction methods for random coincidences in fully 3d whole-body pet: impact on data and image quality. *Journal of nuclear medicine*, 46(5):859–867.

[Bruehlmeier et al., 2003] Bruehlmeier, M., Roelcke, U., Bläuenstein, P., Missimer, J., Schubiger, P. A., Locher, J. T., Pellikka, R., and Ametamey, S. M. (2003). Measurement of the extracellular space in brain tumors using 76br-bromide and pet. *Journal of Nuclear Medicine*, 44(8):1210–1218.

[Buchholz et al., 2015] Buchholz, M., Spahn, I., and Coenen, H. H. (2015). Optimized separation procedure for production of no-carrier-added radiomanganese for positron emission tomography. *Radiochimica Acta*, 103(12):893–899.

[Buchholz et al., 2013] Buchholz, M., Spahn, I., Scholten, B., and Coenen, H. (2013). Cross-section measurements for the formation of manganese-52 and its isolation with a non-hazardous eluent. *Radiochimica Acta*, 101(8):491–499.

[Burger et al., 2002] Burger, C., Goerres, G., Schoenes, S., Buck, A., Lonn, A., and Von Schulthess, G. (2002). Pet attenuation coefficients from ct images: experimental evaluation of the transformation of ct into pet 511-kev attenuation coefficients. *European journal of nuclear medicine and molecular imaging*, 29(7):922–927.

[Buvat et al., 2002] Buvat, I., Castiglioni, I., et al. (2002). Monte carlo simulations in spet and pet. *QJ Nucl Med*, 46(1):48–61.

[Cabello and Rafecas, 2012] Cabello, J. and Rafecas, M. (2012). Comparison of basis functions for 3d pet reconstruction using a monte carlo system matrix. *Physics in Medicine & Biology*, 57(7):1759.

[Cal González, 2015] Cal González, J. (2015). *Positron range and prompt gamma modeling in PET imaging*. PhD thesis, Universidad Complutense de Madrid.

[Cal-González et al., 2013] Cal-González, J., Herraiz, J. L., España, S., Corzo, P. M., Vaquero, J. J., Desco, M., and Udias, J. M. (2013). Positron range estimations with PeneloPET. *Physics in Medicine and Biology*, 58(15).

[Cal-González et al., 2014] Cal-González, J., Lage, E., Herranz, E., Vicente, E., Udías, J. M., Moore, S. C., Park, M., Dave, S. R., Parot, V., and Herraiz, J. L. (2014). Simulation of triple coincidences in pet. *Physics in Medicine & Biology*, 60(1):117.

[Cal-González et al., 2015] Cal-González, J., Pérez-Liva, M., Herraiz, J. L., Vaquero, J. J., Desco, M., and Udías, J. M. (2015). Tissue-dependent and spatially-variant positron range correction in 3d pet. *IEEE transactions on medical imaging*, 34(11):2394–2403.

[Cal-Gonzalez et al., 2018] Cal-Gonzalez, J., Vaquero, J. J., Herraiz, J. L., Pérez-Liva, M., Soto-Montenegro, M. L., Peña-Zalbidea, S., Desco, M., and Udías, J. M. (2018). Improving pet quantification of small animal [68 ga] dota-labeled pet/ct studies by using a ct-based positron range correction. *Molecular Imaging and Biology*, 20(4):584–593.

[Caldeira et al., 2018] Caldeira, L., Kops, E. R., Yun, S. D., da Silva, N., Mauler, J., Weirich, C., Scheins, J., Herzog, H., Tellmann, L., Lohmann, P., et al. (2018). The jülich experience with simultaneous 3t mr-brainpet: Methods and technology. *IEEE transactions on radiation and plasma medical sciences*, 3(3):352–362.

[Carrasquillo et al., 2011] Carrasquillo, J. A., Pandit-Taskar, N., O'Donoghue, J. A., Humm, J. L., Zanzonico, P., Smith-Jones, P. M., Divgi, C. R., Pryma, D. A., Ruan, S., Kemeny, N. E., et al. (2011). 124i-hua33 antibody pet of colorectal cancer. *Journal of Nuclear Medicine*, 52(8):1173–1180.

[Carter et al., 2020] Carter, L. M., Kesner, A. L., Pratt, E., Sanders, V., Massicano, A., Cutler, C., Lapi, S., and Lewis, J. S. (2020). The impact of positron range on pet resolution, evaluated with phantoms and phits monte carlo simulations for conventional and non-conventional radionuclides. *Molecular imaging and biology*, 22(1):73–84.

[Cassidy, 2018] Cassidy, D. B. (2018). Experimental progress in positronium laser physics. *The European Physical Journal D*, 72(3):1–72.

[Castiglioni et al., 1999] Castiglioni, I., Cremonesi, O., Gilardi, M., Bettinardi, V., Rizzo, G., Savi, A., Bellotti, E., and Fazio, F. (1999). Scatter correction techniques in 3d pet: a monte carlo evaluation. *IEEE Transactions on Nuclear Science*, 46(6):2053–2058.

[Cebeiro and Morvidone, 2013] Cebeiro, J. and Morvidone, M. (2013). SVD inversion for the bi-dimensional Conical Radon Transform. *Journal of Physics: Conference Series*, 477(1).

[Chatziioannou et al., 1999] Chatziioannou, A. F., Cherry, S. R., Shao, Y., Silverman, R. W., Meadors, K., Farquhar, T. H., Pedarsani, M., and Phelps, M. E. (1999). Performance evaluation of micropet: a high-resolution lutetium oxyorthosilicate pet scanner for animal imaging. *Journal of Nuclear Medicine*, 40(7):1164.

[Cheng et al., 2012] Cheng, J.-C., Shoghi, K., and Laforest, R. (2012). Quantitative accuracy of map reconstruction for dynamic pet imaging in small animals. *Medical physics*, 39(2):1029–1041.

[Cherry and Dahlbom, 2006] Cherry, S. R. and Dahlbom, M. (2006). Pet: physics, instrumentation, and scanners. In *PET*, pages 1–117. Springer.

[Cherry et al., 2018] Cherry, S. R., Jones, T., Karp, J. S., Qi, J., Moses, W. W., and Badawi, R. D. (2018). Total-body pet: maximizing sensitivity to create new opportunities for clinical research and patient care. *Journal of Nuclear Medicine*, 59(1):3–12.

[Choi et al., 1999] Choi, Y., Huang, S.-C., Hawkins, R. A., Kim, J. Y., Kim, B.-T., Hoh, C. K., Chen, K., Phelps, M. E., and Schelbert, H. R. (1999). Quantification of myocardial blood flow using 13n-ammonia and pet: comparison of tracer models. *Journal of Nuclear Medicine*, 40(6):1045–1055.

[Chollet, 2015] Chollet, F. (2015). others,“keras”, github.

[Christian et al., 1995] Christian, B. T., Nickles, R. J., Stone, C. K., Mulnix, T. L., and Clark, J. (1995). Improving the radionuclidic purity of 94mtc for pet imaging. *Applied radiation and isotopes*, 46(2):69–73.

[Coles et al., 2006] Coles, J. P., Fryer, T. D., Bradley, P. G., Nortje, J., Smielewski, P., Rice, K., Clark, J. C., Pickard, J. D., and Menon, D. K. (2006). Intersubject variability and reproducibility of 15o pet studies. *Journal of Cerebral Blood Flow & Metabolism*, 26(1):48–57.

[Constantinescu and Mukherjee, 2009] Constantinescu, C. C. and Mukherjee, J. (2009). Performance evaluation of an inveon pet preclinical scanner. *Physics in Medicine & Biology*, 54(9):2885.

[Conti, 2009] Conti, M. (2009). State of the art and challenges of time-of-flight pet. *Physica Medica*, 25(1):1–11.

[Conti, 2010] Conti, M. (2010). Why is tof pet reconstruction a more robust method in the presence of inconsistent data? *Physics in Medicine & Biology*, 56(1):155.

[Conti and Bendriem, 2019] Conti, M. and Bendriem, B. (2019). The new opportunities for high time resolution clinical tof pet. *Clinical and Translational Imaging*, 7(2):139–147.

[Conti and Eriksson, 2016] Conti, M. and Eriksson, L. (2016). Physics of pure and non-pure positron emitters for pet: a review and a discussion. *EJNMMI physics*, 3(1):8.

[Conti et al., 2017] Conti, M., Eriksson, L., Rothfuss, H., Sjoeholm, T., Townsend, D., Rosenqvist, G., and Carlier, T. (2017). Characterization of 176lu background in lso-based pet scanners. *Physics in Medicine & Biology*, 62(9):3700.

[Daube-Witherspoon and Muehllehner, 1986] Daube-Witherspoon, M. E. and Muehllehner, G. (1986). An iterative image space reconstruction algorthm suitable for volume ect. *IEEE transactions on medical imaging*, 5(2):61–66.

[Daube-Witherspoon and Muehllehner, 1987] Daube-Witherspoon, M. E. and Muehllehner, G. (1987). Treatment of axial data in three-dimensional pet. *Journal of nuclear medicine*, 28(11):1717–1724.

[Davis et al., 2020] Davis, K. M., Ryan, J. L., Aaron, V. D., and Sims, J. B. (2020). Pet and spect imaging of the brain: History, technical considerations, applications, and radiotracers. In *Seminars in Ultrasound, CT and MRI*. Elsevier.

[De Beenhouwer et al., 2009] De Beenhouwer, J., Staelens, S., Vandenberghe, S., Verhaeghe, J., Van Holen, R., Rault, E., and Lemahieu, I. (2009). Physics process level discrimination of detections for gate: assessment of contamination in spect and spurious activity in pet. *Medical physics*, 36(4):1053–1060.

[De Pierro, 1993] De Pierro, A. R. (1993). On the relation between the isra and the em algorithm for positron emission tomography. *IEEE transactions on Medical Imaging*, 12(2):328–333.

[Deans, 1985] Deans, S. R. (1985). The Radon Transform and Some of Its Applications.

[DeBenedetti et al., 1950] DeBenedetti, S., Cowan, C., Konneker, W. R., and Primakoff, H. (1950). On the angular distribution of two-photon annihilation radiation. *Physical Review*, 77(2):205.

[Defrise and Kinahan, 1998] Defrise, M. and Kinahan, P. (1998). Data Acquisition and Image Reconstruction for 3D PET. In *The Theory and Practice of 3D PET*, pages 11–53.

[Defrise et al., 2005] Defrise, M., Kinahan, P. E., and Michel, C. J. (2005). Image reconstruction algorithms in pet. In *Positron Emission Tomography*, pages 63–91. Springer.

[Defrise et al., 1997] Defrise, M., Kinahan, P. E., Townsend, D. W., Michel, C., Sibomana, M., and Newport, D. F. (1997). Exact and Approximate Rebinning. *IEEE Transactions on Medical Imaging*, 16(2):145–157.

[Defrise et al., 1991] Defrise, M., Townsend, D., Bailey, D., Geissbuhler, A., and Jones, T. (1991). A normalization technique for 3d pet data. *Physics in Medicine & Biology*, 36(7):939.

[Delso et al., 2011] Delso, G., Fürst, S., Jakoby, B., Ladebeck, R., Ganter, C., Nekolla, S. G., Schwaiger, M., and Ziegler, S. I. (2011). Performance measurements of the siemens mmr integrated whole-body pet/mr scanner. *Journal of nuclear medicine*, 52(12):1914–1922.

[Dempster et al., 1977] Dempster, A. P., Laird, N. M., and Rubin, D. B. (1977). Maximum likelihood from incomplete data via the em algorithm. *Journal of the Royal Statistical Society: Series B (Methodological)*, 39(1):1–22.

[Derenzo, 1986] Derenzo, S. E. (1986). Mathematical removal of positron range blurring in high resolution tomography. *IEEE Transactions on Nuclear Science*, 33(1):565–569.

[Deri et al., 2013] Deri, M. A., Zeglis, B. M., Francesconi, L. C., and Lewis, J. S. (2013). Pet imaging with 89zr: from radiochemistry to the clinic. *Nuclear medicine and biology*, 40(1):3–14.

[Dick, 2019] Dick, S. (2019). Artificial intelligence.

[Dokmanić et al., 2013] Dokmanić, I., Kolundžija, M., and Vetterli, M. (2013). Beyond moore-penrose: Sparse pseudoinverse. In *2013 IEEE International Conference on Acoustics, Speech and Signal Processing*, pages 6526–6530. IEEE.

[Domnanich et al., 2017a] Domnanich, K. A., Müller, C., Benešová, M., Dressler, R., Haller, S., Köster, U., Ponsard, B., Schibli, R., Türler, A., and van der Meulen, N. P. (2017a). 47 sc as useful β—emitter for the radiotheragnostic paradigm: a comparative study of feasible production routes. *EJNMMI Radiopharmacy and Chemistry*, 2(1):1–17.

[Domnanich et al., 2017b] Domnanich, K. A., Müller, C., Farkas, R., Schmid, R. M., Ponsard, B., Schibli, R., Türler, A., and van der Meulen, N. P. (2017b). 44 sc for labeling of dota-and nodaga-functionalized peptides: preclinical in vitro and in vivo investigations. *EJNMMI Radiopharmacy and Chemistry*, 1(1):1–19.

[Easton Jr, 2010] Easton Jr, R. L. (2010). *Fourier methods in imaging.* John Wiley & Sons.

[Edison et al., 2008] Edison, P., Archer, H. A., Gerhard, A., Hinz, R., Pavese, N., Turkheimer, F. E., Hammers, A., Tai, Y. F., Fox, N., Kennedy, A., et al. (2008). Microglia, amyloid, and cognition in alzheimer's disease: An [11c](r) pk11195-pet and [11c] pib-pet study. *Neurobiology of disease*, 32(3):412–419.

[Eiber et al., 2015] Eiber, M., Maurer, T., Souvatzoglou, M., Beer, A. J., Ruffani, A., Haller, B., Graner, F.-P., Kübler, H., Haberhorn, U., Eisenhut, M., Wester, H.-J., Gschwend, J. E., and Schwaiger, M. (2015). Evaluation of hybrid 68ga-psma ligand pet/ct in 248 patients with biochemical recurrence after radical prostatectomy. *Journal of Nuclear Medicine*, 56(5):668–674.

[Eiber et al., 2016] Eiber, M., Weirich, G., Holzapfel, K., Souvatzoglou, M., Haller, B., Rauscher, I., Beer, A. J., Wester, H.-J., Gschwend, J., Schwaiger, M., and Maurer, T. (2016). Simultaneous 68ga-psma hbed-cc pet/mri improves the localization of primary prostate cancer. *European Urology*, 70(5):829 – 836.

[El Fakhri et al., 2009] El Fakhri, G., Kardan, A., Sitek, A., Dorbala, S., Abi-Hatem, N., Lahoud, Y., Fischman, A., Coughlan, M., Yasuda, T., and Di Carli, M. F. (2009). Reproducibility and accuracy of quantitative myocardial blood flow assessment with 82rb pet: comparison with 13n-ammonia pet. *Journal of Nuclear Medicine*, 50(7):1062–1071.

[El Fakhri et al., 2005] El Fakhri, G., Sitek, A., Guérin, B., Kijewski, M. F., Di Carli, M. F., and Moore, S. C. (2005). Quantitative dynamic cardiac 82rb pet using generalized factor and compartment analyses. *Journal of nuclear medicine*, 46(8):1264–1271.

[El Sayed et al., 2019] El Sayed, R., Massicano, A. V., Queern, S. L., Loveless, C. S., and Lapi, S. E. (2019). Manganese-52 production cross-section measurements via irradiation of natural chromium targets up to 20 mev. *Applied Radiation and Isotopes*, 147:165–170.

[Erlandsson et al., 1994] Erlandsson, K., Esser, P., Strand, S.-E., and Van Heertum, R. (1994). 3d reconstruction for a multi-ring pet scanner by single-slice rebinning and axial deconvolution. *Physics in Medicine & Biology*, 39(3):619.

[España et al., 2007] España, S., Herraiz, J., Vicente, E., Herranz, E., Vaquero, J., Desco, M., and Udías, J. M. (2007). Validation of penelopet against two small animal pet scanners. In *2007 IEEE Nuclear Science Symposium Conference Record*, volume 5, pages 3640–3643. IEEE.

[España et al., 2009] España, S., Herraiz, J., Vicente, E., Vaquero, J. J., Desco, M., and Udías, J. M. (2009). Penelopet, a monte carlo pet simulation tool based on penelope: features and validation. *Physics in Medicine & Biology*, 54(6):1723.

[Evans and Evans, 1955] Evans, R. D. and Evans, R. (1955). The atomic nucleus.

[Fahey, 2002] Fahey, F. H. (2002). Data Acquisition in PET Imaging. *Journal of nuclear medicine technology*, 30(2):39–49.

[Fani et al., 2008] Fani, M., AndrÃ©, J. P., and Maecke, H. R. (2008). 68ga-pet: a powerful generator-based alternative to cyclotron-based pet radiopharmaceuticals. *Contrast Media & Molecular Imaging*, 3(2):53–63.

[Fiechter et al., 2012] Fiechter, M., Ghadri, J. R., Gebhard, C., Fuchs, T. A., Pazhenkottil, A. P., Nkoulou, R. N., Herzog, B. A., Wyss, C. A., Gaemperli, O., and Kaufmann, P. A. (2012). Diagnostic value of 13n-ammonia myocardial perfusion pet: added value of myocardial flow reserve. *Journal of Nuclear Medicine*, 53(8):1230–1234.

[Filosofov et al., 2010] Filosofov, D., Loktionova, N., and Rösch, F. (2010). A 44ti/44sc radionuclide generator for potential application of 44sc-based pet-radiopharmaceuticals. *Radiochimica Acta International journal for chemical aspects of nuclear science and technology*, 98(3):149–156.

[Ford et al., 2006] Ford, R. L., Nelson, W. R., et al. (2006). The egs code system: Computer programs for the monte carlo simulation of electromagnetic cascade showers (version 3). Technical report, SLAC National Accelerator Lab., Menlo Park, CA (United States).

[Frese et al., 2003] Frese, T., Rouze, N. C., Bouman, C. A., Sauer, K., and Hutchins, G. D. (2003). Quantitative comparison of FBP, EM, and Bayesian reconstruction algorithms for the IndyPET scanner. *IEEE Transactions on Medical Imaging*, 22(2):258–276.

[Freudenberg et al., 2004] Freudenberg, L., Antoch, G., Jentzen, W., Pink, R., Knust, J., Görges, R., Müller, S., Bockisch, A., Debatin, J., and Brandau, W. (2004). Value of 124 i-pet/ct in staging of patients with differentiated thyroid cancer. *European radiology*, 14(11):2092–2098.

[Freudenberg et al., 2007] Freudenberg, L., Jentzen, W., Görges, R., Petrich, T., Marlowe, R., Knust, J., and Bockisch, A. (2007). 124i-pet dosimetry in advanced differentiated thyroid cancer: therapeutic impact. *Nuklearmedizin*, 46(04):121–128.

[Freudenberg et al., 2011] Freudenberg, L. S., Jentzen, W., Stahl, A., Bockisch, A., and Rosenbaum-Krumme, S. J. (2011). Clinical applications of 124 i-pet/ct in patients with differentiated thyroid cancer. *European journal of nuclear medicine and molecular imaging*, 38(1):48–56.

[Fukuchi et al., 2021] Fukuchi, T., Shigeta, M., Haba, H., Mori, D., Yokokita, T., Komori, Y., Yamamoto, S., and Watanabe, Y. (2021). Image reconstruction method for dual-isotope positron emission tomography. *Journal of Instrumentation*, 16(01):P01035.

[Gabriel et al., 2007] Gabriel, M., Decristoforo, C., Kendler, D., Dobrozemsky, G., Heute, D., Uprimny, C., Kovacs, P., Von Guggenberg, E., Bale, R., and Virgolini, I. J. (2007). 68ga-dota-tyr3-octreotide pet in neuroendocrine tumors: comparison with somatostatin receptor scintigraphy and ct. *Journal of Nuclear Medicine*, 48(4):508–518.

[Gagnon et al., 2011] Gagnon, K., McQuarrie, S., Abrams, D., J McEwan, A., and Wuest, F. (2011). Radiotracers based on technetium-94m. *Current Radiopharmaceuticals*, 4(2):90–101.

[Galve, 2016] Galve, P. (2016). Depth of interaction correction strategies in high sensitivity pet preclinical scanners. Master's thesis.

[Gambhir et al., 2001] Gambhir, S. S., Czernin, J., Schwimmer, J., Silverman, D. H., Coleman, R. E., and Phelps, M. E. (2001). A tabulated summary of the fdg pet literature. *Journal of nuclear medicine*, 42(5 suppl):1S–93S.

[García-Toraño et al., 2019] García-Toraño, E., Peyres, V., and Salvat, F. (2019). Pennuc: Monte carlo simulation of the decay of radionuclides. *Computer Physics Communications*, 245:106849.

[Gardelle et al., 2001] Gardelle, O., Roelcke, U., Vontobel, P., Crompton, N. E., Guenther, I., Bläuenstein, P., Schubiger, A. P., Blattmann, H., Ryser, J. E., Leenders, K. L., et al. (2001). [76br] bromodeoxyuridine pet in tumor-bearing animals. *Nuclear medicine and biology*, 28(1):51–57.

[Gawne et al., 2018] Gawne, P., Man, F., Fonslet, J., Radia, R., Bordoloi, J., Cleveland, M., Jimenez-Royo, P., Gabizon, A., Blower, P. J., Long, N., et al. (2018). Manganese-52: applications in cell radiolabelling and liposomal nanomedicine pet imaging using oxine (8-hydroxyquinoline) as an ionophore. *Dalton Transactions*, 47(28):9283–9293.

[Gaykema et al., 2013] Gaykema, S. B., Brouwers, A. H., Lub-de Hooge, M. N., Pleijhuis, R. G., Timmer-Bosscha, H., Pot, L., van Dam, G. M., van der Meulen, S. B., de Jong, J. R., Bart, J., et al. (2013). 89zr-bevacizumab pet imaging in primary breast cancer. *Journal of nuclear medicine*, 54(7):1014–1018.

[Gene H. Golub, 2012] Gene H. Golub, C. F. V. L. (2012). *Matrix Computations*. JHU Press.

[Ghammraoui et al., 2014] Ghammraoui, B., Peng, R., Suarez, I., Bettolo, C., and Badal, A. (2014). Including the effect of molecular interference in the coherent x-ray scattering modeling in mc-gpu and penelope for the study of novel breast imaging modalities. In *Medical Imaging 2014: Physics of Medical Imaging*, volume 9033, page 90334N. International Society for Optics and Photonics.

[Glaus et al., 2010] Glaus, C., Rossin, R., Welch, M. J., and Bao, G. (2010). In vivo evaluation of 64cu-labeled magnetic nanoparticles as a dual-modality pet/mr imaging agent. *Bioconjugate chemistry*, 21(4):715–722.

[Goertzen et al., 2012] Goertzen, A. L., Bao, Q., Bergeron, M., Blankemeyer, E., Blinder, S., Canadas, M., Chatziioannou, A. F., Dinelle, K., Elhami, E., Jans, H.-S., Lage, E., Lecomte, R., Sossi, V., Surti, S., Tai, Y.-C., Vaquero, J. J., Vicente, E., Williams, D. A., and Laforest, R. (2012). NEMA NU 4-2008 Comparison of Preclinical PET Imaging Systems. *Journal of Nuclear Medicine*, 53(8):1300–1309.

[Golub and Kahan, 1965] Golub, G. and Kahan, W. (1965). Calculating the singular values and pseudo-inverse of a matrix. *Journal of the Society for Industrial and Applied Mathematics, Series B: Numerical Analysis*, 2(2):205–224.

[Gong et al., 2019] Gong, K., Berg, E., Cherry, S. R., and Qi, J. (2019). Machine learning in pet: from photon detection to quantitative image reconstruction. *Proceedings of the IEEE*, 108(1):51–68.

[Goodfellow et al., 2016] Goodfellow, I., Bengio, Y., Courville, A., and Bengio, Y. (2016). *Deep learning*, volume 1. MIT press Cambridge.

[Gordon et al., 1970] Gordon, R., Bender, R., and Herman, G. T. (1970). Algebraic reconstruction techniques (art) for three-dimensional electron microscopy and x-ray photography. *Journal of theoretical Biology*, 29(3):471–481.

[Gower and Richtárik, 2016] Gower, R. M. and Richtárik, P. (2016). Linearly Convergent Randomized Iterative Methods for Computing the Pseudoinverse. *arXiv preprint*, (arXiv:1612.06255):1–30.

[Grassi et al., 2012] Grassi, I., Nanni, C., Allegri, V., Morigi, J. J., Montini, G. C., Castellucci, P., and Fanti, S. (2012). The clinical use of pet with 11c-acetate. *American journal of nuclear medicine and molecular imaging*, 2(1):33.

[Griffiths, 2008] Griffiths, D. (2008). *Introduction to elementary particles.* John Wiley & Sons.

[Gullberg et al., 1996] Gullberg, G. T., Hsieh, Y.-l., and Zeng, G. I. L. (1996). An SVD Reconstruction Algorithm Using a Natural Pixel Represen tation of the Attenuated Radon Transform. *IEEE Transactions on Nuclear Science*, 43(1):295–303.

[Guo and Renaut, 2011] Guo, H. and Renaut, R. A. (2011). Revisiting stopping rules for iterative methods used in emission tomography. *Computerized Medical Imaging and Graphics*, 35(5):398–406.

[Hamdy et al., 1999] Hamdy, S., Rothwell, J. C., Brooks, D. J., Bailey, D., Aziz, Q., and Thompson, D. G. (1999). Identification of the cerebral loci processing human swallowing with h2 15o pet activation. *Journal of Neurophysiology*, 81(4):1917–1926.

[Hanaoka et al., 2015] Hanaoka, H., Ohshima, Y., Suzuki, Y., Yamaguchi, A., Watanabe, S., Uehara, T., Nagamori, S., Kanai, Y., Ishioka, N. S., Tsushima, Y., et al. (2015). Development of a widely usable amino acid tracer: 76br-α-methyl-phenylalanine for tumor pet imaging. *Journal of Nuclear Medicine*, 56(5):791–797.

[Hao et al., 2010] Hao, G., N Singh, A., Liu, W., and Sun, X. (2010). Pet with non-standard nuclides. *Current topics in medicinal chemistry*, 10(11):1096–1112.

[Hara et al., 1997] Hara, T., Kosaka, N., Shinoura, N., and Kondo, T. (1997). Pet imaging of brain tumor with [methyl-11c] choline. *Journal of Nuclear Medicine*, 38(6):842–847.

[Hasebroock and Serkova, 2009] Hasebroock, K. M. and Serkova, N. J. (2009). Toxicity of mri and ct contrast agents. *Expert opinion on drug metabolism & toxicology*, 5(4):403–416.

[He et al., 2012] He, K., Sun, J., and Tang, X. (2012). Guided image filtering. *IEEE transactions on pattern analysis and machine intelligence*, 35(6):1397–1409.

[Henning, 2012] Henning, G. (2012). *Stability of transfermium elements at high spin: measuring the fission barrier of 254No*. PhD thesis, Paris 11.

[Herholz et al., 1998] Herholz, K., Hölzer, T., Bauer, B., Schröder, R., Voges, J., Ernestus, R., Mendoza, G., Weber-Luxenburger, G., Löttgen, J., Thiel, A., et al. (1998). 11c-methionine pet for differential diagnosis of low-grade gliomas. *Neurology*, 50(5):1316–1322.

[Herman, 1995] Herman, G. T. (1995). Image reconstruction from projections. *Real-Time Imaging*, 1(1):3–18.

[Herman, 2009] Herman, G. T. (2009). *Fundamentals of computerized tomography: image reconstruction from projections*. Springer Science & Business Media.

[Hernandez et al., 2014] Hernandez, R., Valdovinos, H. F., Yang, Y., Chakravarty, R., Hong, H., Barnhart, T. E., and Cai, W. (2014). 44sc: an attractive isotope for peptide-based pet imaging. *Molecular pharmaceutics*, 11(8):2954–2961.

[Herraiz et al., 2014a] Herraiz, J., Moore, S., Parot, V., Dave, S., Park, M., Yoo, S., Lee, W., Kim, H., and Lage, E. (2014a). A prompt-gamma correction method for non-standard pet radionuclides base on the detection of triple coincidences. In *IEEE Nuclear Science Symposium & Medical Imaging Conference (NSS/MIC), Oral Presentation M22-3*.

[Herraiz et al., 2021] Herraiz, J. L., Bembibre, A., and López-Montes, A. (2021). Deep-learning based positron range correction of pet images. *Applied Sciences*, 11(1):266.

[Herraiz et al., 2006] Herraiz, J. L., España, S., Vaquero, J. J., Desco, M., and Udías, J. M. (2006). FIRST: Fast Iterative Reconstruction Software for (PET) tomography. *Physics in Medicine and Biology*, 51(18):4547–4565.

[Herraiz et al., 2008] Herraiz, J. L., Espana, S., Vicente, E., Herranz, E., Desco, M., Vaquero, J. J., and Udias, J. (2008). Frequency selective signal extrapolation for compensation of missing data in sinograms. In *2008 IEEE Nuclear Science Symposium Conference Record*, pages 4299–4302. IEEE.

[Herraiz et al., 2013] Herraiz, J. L., Lage, E., Parot, V., Dave, S. R., Udías, J. M., Vaquero, J., Muñoz-Martin, A., and Fraile, L. (2013). Production of positron-gamma emitters for multiplexed pet (mpet) imaging. In *2013 IEEE Nuclear Science Symposium and Medical Imaging Conference (2013 NSS/MIC)*, pages 1–3. IEEE.

[Herraiz et al., 2014b] Herraiz, J. L., Moore, S. C., Cervo, M., España, S., Ruiz-Cabello, J., and Lage, E. (2014b). Multiplexed pet in clinical scanners based on triple coincidences. In *IEEE Nuclear Science Symposium & Medical Imaging Conference (NSS/MIC), Oral Presentation M22-3*.

[Herraiz et al., 2011] Herraiz, J. L., Vaquero, J. J., and Udias, J. M. (2011). FBP Reconstruction of Sinograms with Gaps Based on the Inversion of a Perturbed Matrix. *IEEE Nuclear Science Symposium and Medical Imaging Conference*, 1(4):4–5.

[Herzog et al., 2009a] Herzog, B. A., Husmann, L., Valenta, I., Gaemperli, O., Siegrist, P. T., Tay, F. M., Burkhard, N., Wyss, C. A., and Kaufmann, P. A. (2009a). Long-term prognostic value of 13n-ammonia myocardial perfusion positron emission tomography: added value of coronary flow reserve. *Journal of the American College of Cardiology*, 54(2):150–156.

[Herzog et al., 2010] Herzog, H., Iida, H., Weirich, C., Tellmann, L., Kaffanke, J., Spellerberg, S., Caldeira, L., Kops, E. R., and Shah, N. J. (2010). Influence from high and ultra-high magnetic field on positron range measured with a 9.4 tmr-brainpet. In *IEEE Nuclear Science Symposuim & Medical Imaging Conference*, pages 3410–3413. IEEE.

[Herzog et al., 2011] Herzog, H., Langen, K.-J., Weirich, C., Kops, E. R., Kaffanke, J., Tellmann, L., Scheins, J., Neuner, I., Stoffels, G., Fischer, K., et al. (2011). High resolution brainpet combined with simultaneous mri. *Nuklearmedizin*, 50(02):74–82.

[Herzog et al., 2009b] Herzog, H., Tellmann, L., Marx, B., Scheins, J., Michel, C., Byars, L., and Schmand, M. (2009b). First performance tests of the 3tmr-brainpet. *Journal of Nuclear Medicine*, 50(supplement 2):1539–1539.

[Hess et al., 2014] Hess, S., Blomberg, B. A., Zhu, H. J., Høilund-Carlsen, P. F., and Alavi, A. (2014). The pivotal role of fdg-pet/ct in modern medicine. *Academic radiology*, 21(2):232–249.

[Ho et al., 2003] Ho, C.-L., Simon, C., and Yeung, D. W. (2003). 11c-acetate pet imaging in hepatocellular carcinoma and other liver masses. *Journal of Nuclear Medicine*, 44(2):213–221.

[Hoffman et al., 1982] Hoffman, E. J., Ricci, A., Van der Stee, L., and Phelps, M. (1982). Ecat iii: Basic design considerations. Technical report.

[Hofman et al., 2011] Hofman, M. S., Beauregard, J.-M., Barber, T. W., Neels, O. C., Eu, P., and Hicks, R. J. (2011). 68ga pet/ct ventilation–perfusion imaging for pulmonary embolism: a pilot study with comparison to conventional scintigraphy. *Journal of Nuclear Medicine*, 52(10):1513–1519.

[Holdsworth et al., 2001] Holdsworth, C., Levin, C., Farquhar, T., Dahlbom, M., and Hoffman, E. (2001). Investigation of accelerated monte carlo techniques for pet simulation and 3d pet scatter correction. *IEEE transactions on nuclear science*, 48(1):74–81.

[Hudson and Larkin, 1994] Hudson, H. M. and Larkin, R. S. (1994). Accelerated image reconstruction using ordered subsets of projection data. *IEEE transactions on medical imaging*, 13(4):601–609.

[Hugdahl et al., 1999] Hugdahl, K., Brønnick, K., Kyllingsbrk, S., Law, I., Gade, A., and Paulson, O. B. (1999). Brain activation during dichotic presentations of consonant-vowel and musical instrument stimuli: a 15o-pet study. *Neuropsychologia*, 37(4):431–440.

[Hugdahl et al., 2000] Hugdahl, K., Law, I., Kyllingsbæk, S., Brønnick, K., Gade, A., and Paulson, O. B. (2000). Effects of attention on dichotic listening: An 15o-pet study. *Human brain mapping*, 10(2):87–97.

[Irene Virgolini, 2010] Irene Virgolini, Valentina Ambrosini, J. B. B. R. P. B. S. F. M. G. N. D. P. G. P. W. O. C. D. C. . A. C. (2010). Procedure guidelines for pet/ct tumour imaging with 68ga-dota-conjugated peptides: 68ga-dota-toc, 68ga-dota-noc, 68ga-dotatate. *European Journal of Nuclear Medicine and Molecular Imaging*, 37:2004–2010.

[Iriarte, 2017] Iriarte, A. (2017). System models for PET statistical iterative reconstruction: A review. *Computerized Medical Imaging and Graphics*, 91:399–404.

[Ito et al., 2011] Ito, M., Hong, S. J., and Lee, J. S. (2011). Positron emission tomography (pet) detectors with depth-of-interaction (doi) capability. *Biomedical Engineering Letters*, 1(2):70.

[Jakoby et al., 2011] Jakoby, B., Bercier, Y., Conti, M., Casey, M., Bendriem, B., and Townsend, D. (2011). Physical and clinical performance of the mct time-of-flight pet/ct scanner. *Physics in Medicine & Biology*, 56(8):2375.

[Jakoby et al., 2007] Jakoby, B., Long, M., Carr, C., and Townsend, D. (2007). Physical performance of a new combined pet/ct scanner. *Journal of Nuclear Medicine*, 48(supplement 2):46P–46P.

[James, 1980] James, F. (1980). Monte carlo theory and practice. *Reports on progress in Physics*, 43(9):1145.

[James et al., 2011] James, O. G., Christensen, J. D., Wong, T. Z., Borges-Neto, S., and Koweek, L. M. (2011). Utility of fdg pet/ct in inflammatory cardiovascular disease. *Radiographics*, 31(5):1271–1286.

[Jan et al., 2004] Jan, S., Santin, G., Strul, D., Staelens, S., Assie, K., Autret, D., Avner, S., Barbier, R., Bardies, M., Bloomfield, P., et al. (2004). Gate: a simulation toolkit for pet and spect. *Physics in Medicine & Biology*, 49(19):4543.

[Jentzen et al., 2008] Jentzen, W., Freudenberg, L., Eising, E. G., Sonnenschein, W., Knust, J., and Bockisch, A. (2008). Optimized 124i pet dosimetry protocol for radioiodine therapy of differentiated thyroid cancer. *Journal of Nuclear Medicine*, 49(6):1017–1023.

[Jiang and Wang, 2003] Jiang, M. and Wang, G. (2003). Convergence of the simultaneous algebraic reconstruction technique (sart). *IEEE Transactions on Image Processing*, 12(8):957–961.

[Joshi et al., 2014] Joshi, N. V., Vesey, A. T., Williams, M. C., Shah, A. S., Calvert, P. A., Craighead, F. H., Yeoh, S. E., Wallace, W., Salter, D., Fletcher, A. M., et al. (2014). 18f-fluoride positron emission tomography for identification of ruptured and high-risk coronary atherosclerotic plaques: a prospective clinical trial. *The Lancet*, 383(9918):705–713.

[K Nayak and W Brechbiel, 2011] K Nayak, T. and W Brechbiel, M. (2011). 86y based pet radiopharmaceuticals: radiochemistry and biological applications. *Medicinal Chemistry*, 7(5):380–388.

[Kaczmarz, 1937] Kaczmarz, S. (1937). Angenaherte auflosung von systemen linearer gleichungen: Bulletin international de l'académie polonaise des sciences et des lettres.

[Kalman, 1996] Kalman, D. (1996). A Singularly Valuable Decomposition: The SVD of a Matrix. *The College Mathematics Journal*, 27(1):2–23.

[Kalos and Whitlock, 2009] Kalos, M. H. and Whitlock, P. A. (2009). *Monte carlo methods*. John Wiley & Sons.

[Kang et al., 2018] Kang, H., Kim, W.-G., Yang, G.-S., Kim, H.-W., Jeong, J.-E., Yoon, H.-J., Cho, K., Jeong, Y.-J., and Kang, D.-Y. (2018). Vgg-based bapl score classification of 18f-florbetaben amyloid brain pet. *Biomedical Science Letters*, 24(4):418–425.

[Kao et al., 2008] Kao, C.-M., Dong, Y., Xie, Q., and Chen, C.-T. (2008). Accurate image reconstruction with computed system response matrix for a high-sensitivity dual-head pet scanner. *IEEE Trans. Med. Imag.*

[Kapoor et al., 2004] Kapoor, V., McCook, B. M., and Torok, F. S. (2004). An introduction to pet-ct imaging. *Radiographics*, 24(2):523–543.

[Karlberg et al., 2016] Karlberg, A. M., Sæther, O., Eikenes, L., and Goa, P. E. (2016). Quantitative comparison of pet performance—siemens biograph mct and mmr. *EJNMMI physics*, 3(1):1–14.

[Katsikis et al., 2011] Katsikis, V. N., Pappas, D., and Petralias, A. (2011). An improved method for the computation of the Moore-Penrose inverse matrix. *Applied Mathematics and Computation*, 217(23):9828–9834.

[Kinahan and Rogers, 1988] Kinahan, P. E. and Rogers, J. (1988). Analytic 3d image reconstruction using all detected events. Technical report, Triumf.

[Kinahan et al., 1998] Kinahan, P. E., Townsend, D., Beyer, T., and Sashin, D. (1998). Attenuation correction for a combined 3d pet/ct scanner. *Medical physics*, 25(10):2046–2053.

[Knoll, 2010] Knoll, G. F. (2010). *Radiation detection and measurement.* John Wiley & Sons.

[Krane et al., 1987] Krane, K. S., Halliday, D., et al. (1987). *Introductory nuclear physics.*

[Krishnamoorthy et al., 2018] Krishnamoorthy, S., Blankemeyer, E., Mollet, P., Surti, S., Van Holen, R., and Karp, J. S. (2018). Performance evaluation of the molecubes β-cube—a high spatial resolution and high sensitivity small animal pet scanner utilizing monolithic lyso scintillation detectors. *Physics in Medicine & Biology*, 63(15):155013.

[Lage et al., 2015] Lage, E., Parot, V., Moore, S. C., Sitek, A., Udías, J. M., Dave, S. R., Park, M.-A., Vaquero, J. J., and Herraiz, J. L. (2015). Recovery and normalization of triple coincidences in pet. *Medical physics*, 42(3):1398–1410.

[Landweber, 1951] Landweber, L. (1951). An iteration formula for fredholm integral equations of the first kind. *American journal of mathematics*, 73(3):615–624.

[Latham, 1999] Latham, G. (1999). Asymptotic l-based comparison of tikhonov regularization and landweber iteration. *Applied mathematics letters*, 12(8):45–51.

[Lau et al., 2019] Lau, J., Jacobson, O., Niu, G., Lin, K.-S., Bénard, F., and Chen, X. (2019). Bench to bedside: albumin binders for improved cancer radioligand therapies. *Bioconjugate chemistry*, 30(3):487–502.

[LeCun et al., 2015] LeCun, Y., Bengio, Y., and Hinton, G. (2015). Deep learning. nature 521 (7553), 436-444. *Google Scholar Google Scholar Cross Ref Cross Ref.*

[Lee et al., 2013] Lee, S., Gregor, J., and Osborne, D. (2013). Development and validation of a complete gate model of the siemens inveon trimodal imaging platform. *Molecular Imaging*, 12(7):7290–2013.

[Leitão and Svaiter, 2016] Leitão, A. and Svaiter, B. (2016). On projective landweber–kaczmarz methods for solving systems of nonlinear ill-posed equations. *Inverse Problems*, 32(2):025004.

[Lemaréchal, 2012] Lemaréchal, C. (2012). Cauchy and the gradient method. *Doc Math Extra*, 251(254):10.

[Lesniak et al., 2016] Lesniak, W. G., Chatterjee, S., Gabrielson, M., Lisok, A., Wharram, B., Pomper, M. G., and Nimmagadda, S. (2016). Pd-l1 detection in tumors using [64cu] atezolizumab with pet. *Bioconjugate chemistry*, 27(9):2103–2110.

[Leung et al., 2020] Leung, K. H., Marashdeh, W., Wray, R., Ashrafinia, S., Pomper, M. G., Rahmim, A., and Jha, A. K. (2020). A physics-guided modular deep-learning based automated framework for tumor segmentation in pet. *Physics in Medicine & Biology*, 65(24):245032.

[Levin et al., 1995] Levin, C. S., Dahlbom, M., and Hoffman, E. J. (1995). A monte carlo correction for the effect of compton scattering in 3-d pet brain imaging. *IEEE Transactions on Nuclear Science*, 42(4):1181–1185.

[Lewellen, 1998] Lewellen, T. K. (1998). Time-of-flight pet. In *Seminars in nuclear medicine*, volume 28, pages 268–275. Elsevier.

[Lima et al., 2020] Lima, T. V., Gnesin, S., Nitzsche, E., Ortega, P. G., Müller, C., and van der Meulen, N. P. (2020). First phantom-based quantitative assessment of scandium-44 using a commercial pet device. *Frontiers in Physics*, 8.

[Liu et al., 2018] Liu, F., Jang, H., Kijowski, R., Zhao, G., Bradshaw, T., and McMillan, A. B. (2018). A deep learning approach for 18 f-fdg pet attenuation correction. *EJNMMI physics*, 5(1):1–15.

[Liu et al., 2011] Liu, H., Zhao, S., Zhang, B., and Zhou, S. (2011). Penelopet: a pet-dedicated monte carlo simulation toolkit. *Nuclear Electronics and Detection Technology*, 31(10):1143–1146.

[Liu and Zhao, 2014] Liu, H. J. and Zhao, S. J. (2014). Overview of penelopet: A pet-dedicated monte carlo simulation toolkit. In *Applied Mechanics and Materials*, volume 602, pages 3565–3569. Trans Tech Publ.

[Liu et al., 2019] Liu, L., Jiang, H., He, P., Chen, W., Liu, X., Gao, J., and Han, J. (2019). On the variance of the adaptive learning rate and beyond. *arXiv preprint arXiv:1908.03265*.

[Liu et al., 1999] Liu, X., Defrise, M., Michel, C., Sibomana, M., Comtat, C., Kinahan, P., and Townsend, D. (1999). Exact rebinning methods for three-dimensional PET. *IEEE transactions on medical imaging*, 18(8):657–664.

[Lopez-Montes et al., 2017] Lopez-Montes, A., Galve, P., Udias, J., and Herraiz, J. (2017). Real-time accurate rebinning of pet data based on the pseudo-inverse of the axial system matrix. In *2017 IEEE Nuclear Science Symposium and Medical Imaging Conference (NSS/MIC)*, pages 1–4. IEEE.

[López-Montes et al., 2020] López-Montes, A., Galve, P., Udias, J. M., Cal-González, J., Vaquero, J. J., Desco, M., and Herraiz, J. L. (2020). Real-time 3d pet image with pseudoinverse reconstruction. *Applied Sciences*, 10(8):2829.

[López-Montes et al., 2019] López-Montes, A., Galve, P., Udias, J. M., and Herraiz, J. L. (2019). Application of the pseudoinverse for real-time 3d pet image reconstruction. In *15th International Meeting on Fully Three-Dimensional Image Reconstruction in Radiology and Nuclear Medicine*, volume 11072, page 110720J. International Society for Optics and Photonics.

[Lopez-Montes et al., 2019] Lopez-Montes, A., Herraiz, J. L., Galve, P., España, S., Vicente, E., Cal-Gonzalez, J., and Udias, J. M. (2019). Penelopet v3. 0, an improved multiplatform pet simulator. In *2019 IEEE Nuclear Science Symposium and Medical Imaging Conference (NSS/MIC)*, pages 1–3. IEEE.

[López-Sánchez et al., 2019] López-Sánchez, M., Pérez-Fernández, M., Fandiño, J. M., Teijeiro, A., Luna-Vega, V., Gómez-Fernández, N., Gómez, F., and González-Castaño, D. M. (2019). An egs monte carlo model for varian truebeam treatment units: Commissioning and experimental validation of source parameters. *Physica Medica*, 64:81–88.

[Lougovski et al., 2015] Lougovski, A., Hofheinz, F., Maus, J., Schramm, G., and Van Den Hoff, J. (2015). On the relation between Kaiser-Bessel blob and tube of response based modelling of the system matrix in iterative PET image reconstruction. *Physics in Medicine and Biology*, 60(10):4209–4224.

[Lövqvist et al., 2001] Lövqvist, A., Humm, J. L., Sheikh, A., Finn, R. D., Koziorowski, J., Ruan, S., Pentlow, K. S., Jungbluth, A., Welt, S., Lee, F. T., et al. (2001). Pet imaging of 86y-labeled anti-lewis y monoclonal antibodies in a nude mouse model: comparison between 86y and 111in radiolabels. *Journal of Nuclear Medicine*, 42(8):1281–1287.

[Lubberink et al., 2002] Lubberink, M., Schneider, H., Bergström, M., and Lundqvist, H. (2002). Quantitative imaging and correction for cascade gamma radiation of 76br with 2d and 3d pet. *Physics in Medicine & Biology*, 47(19):3519.

[MacDonald et al., 2011] MacDonald, L. R., Harrison, R. L., Alessio, A. M., Hunter, W. C., Lewellen, T. K., and Kinahan, P. E. (2011). Effective count rates for PET scanners with reduced and extended axial field of view. *Physics in Medicine and Biology*, 56(12):3629–3643.

[MacDonald et al., 2008] MacDonald, L. R., Schmitz, R. E., Alessio, A. M., Wollenweber, S. D., Stearns, C. W., Ganin, A., Harrison, R. L., Lewellen, T. K., and Kinahan, P. E. (2008). Measured count-rate performance of the Discovery STE PET/CT scanner in

2D, 3D and partial collimation acquisition modes. *Physics in Medicine and Biology*, 53(14):3723–3738.

[Mackie et al., 1988] Mackie, T., Bielajew, A., Rogers, D., and Battista, J. (1988). Generation of photon energy deposition kernels using the egs monte carlo code. *Physics in Medicine & Biology*, 33(1):1.

[Maecke H.R., 2007] Maecke H.R., A. J. (2007). 68ga-pet radiopharmacy: A generator-based alternative to 18f-radiopharmacy. *Proceeding Schubiger P.A., Lehmann L., Friebe M. (eds) PET Chemistry. Ernst Schering Research Foundation Workshop*, 64.

[Makris et al., 2014] Makris, N. E., Boellaard, R., Visser, E. P., de Jong, J. R., Vanderlinden, B., Wierts, R., van der Veen, B. J., Greuter, H. J., Vugts, D. J., van Dongen, G. A., et al. (2014). Multicenter harmonization of 89zr pet/ct performance. *Journal of Nuclear Medicine*, 55(2):264–267.

[Manabe et al., 2009] Manabe, O., Yoshinaga, K., Katoh, C., Naya, M., Dekemp, R. A., and Tamaki, N. (2009). Repeatability of rest and hyperemic myocardial blood flow measurements with 82rb dynamic pet. *Journal of Nuclear Medicine*, 50(1):68–71.

[McBride et al., 2006] McBride, W. J., Zanzonico, P., Sharkey, R. M., Norén, C., Karacay, H., Rossi, E. A., Losman, M. J., Brard, P.-Y., Chang, C.-H., Larson, S. M., et al. (2006). Bispecific antibody pretargeting pet (immunopet) with an 124i-labeled hapten-peptide. *Journal of nuclear medicine*, 47(10):1678–1688.

[McCarthy, 1998] McCarthy, J. (1998). What is artificial intelligence?

[Melo et al., 2010] Melo, M. F. V., Winkler, T., Harris, R. S., Musch, G., Greene, R. E., and Venegas, J. G. (2010). Spatial heterogeneity of lung perfusion assessed with 13n pet as a vascular biomarker in chronic obstructive pulmonary disease. *Journal of Nuclear Medicine*, 51(1):57–65.

[Merriman, 1877] Merriman, M. (1877). *A List of Writings Relating to the Method of Least Squares: With Historical and Critical Notes*, volume 4. Academy.

[Mitchell et al., 2013] Mitchell, R., Michalski, J., and Carbonell, T. (2013). *An artificial intelligence approach.* Springer.

[Miyaoka et al., 1998] Miyaoka, R., Lewellen, T., Yu, H., and McDaniel, D. (1998). Design of a depth of interaction (doi) pet detector module. *IEEE Transactions on Nuclear Science*, 45(3):1069–1073.

[Moses and Derenzo, 1990] Moses, W. and Derenzo, S. (1990). Effect of depth-of-interaction measurement resolution on radial elongation in pet. *Journal of Nuclear Medicine*, 31:749.

[Moses, 2010] Moses, W. W. (2010). Recent advances and future advances in time-of-flight pet. In *AIP Conference Proceedings*, volume 1204, pages 119–125. American Institute of Physics.

[Moses and Derenzo, 1999] Moses, W. W. and Derenzo, S. (1999). Prospects for time-of-flight pet using lso scintillator. *IEEE Transactions on Nuclear Science*, 46(3):474–478.

[Moskal et al., 2019] Moskal, P., Kisielewska, D., Curceanu, C., Czerwiński, E., Dulski, K., Gajos, A., Gorgol, M., Hiesmayr, B., Jasińska, B., Kacprzak, K., et al. (2019). Feasibility study of the positronium imaging with the j-pet tomograph. *Physics in Medicine & Biology*, 64(5):055017.

[Müller et al., 2014] Müller, C., Bunka, M., Haller, S., Köster, U., Groehn, V., Bernhardt, P., van der Meulen, N., Türler, A., and Schibli, R. (2014). Promising prospects for 44sc-/47sc-based theragnostics: application of 47sc for radionuclide tumor therapy in mice. *Journal of nuclear medicine*, 55(10):1658–1664.

[Muzik et al., 2013] Muzik, O., Mangner, T. J., Leonard, W. R., Kumar, A., Janisse, J., and Granneman, J. G. (2013). 15o pet measurement of blood flow and oxygen consumption in cold-activated human brown fat. *Journal of Nuclear Medicine*, 54(4):523–531.

[Napieczynska et al., 2017] Napieczynska, H., Severin, G. W., Fonslet, J., Wiehr, S., Menegakis, A., Pichler, B. J., and Calaminus, C. (2017). Imaging neuronal pathways with 52mn pet: toxicity evaluation in rats. *Neuroimage*, 158:112–125.

[National Electrical Manufacturers Association, 2007] National Electrical Manufacturers Association, N. (2007). NEMA NU2 2007 Performance Measurements of Positron Emission Tomography. Technical report.

[National Electrical Manufacturers Association, 2008] National Electrical Manufacturers Association, N. (2008). NEMA Standards Publication NU 4 – 2008 Performance Measurements of Small Animal Positron Emission Tomographs. Technical report.

[Natterer, 2001] Natterer, F. (2001). *The mathematics of computerized tomography.* SIAM.

[Nayak et al., 2011] Nayak, T. K., Garmestani, K., Baidoo, K. E., Milenic, D. E., and Brechbiel, M. W. (2011). Pet imaging of tumor angiogenesis in mice with vegf-a–targeted 86y-chx-a -dtpa-bevacizumab. *International journal of cancer*, 128(4):920–926.

[NDS, 2020] NDS (2020). Live Chart of Nuclides.

[Nesterov et al., 2014] Nesterov, S. V., Deshayes, E., Sciagrà, R., Settimo, L., Declerck, J. M., Pan, X.-B., Yoshinaga, K., Katoh, C., Slomka, P. J., Germano, G., et al. (2014). Quantification of myocardial blood flow in absolute terms using 82rb pet imaging: the ruby-10 study. *JACC: Cardiovascular Imaging*, 7(11):1119–1127.

[Nikazad et al., 2017] Nikazad, T., Abbasi, M., and Elfving, T. (2017). Error minimizing relaxation strategies in landweber and kaczmarz type iterations. *Journal of Inverse and Ill-posed Problems*, 25(1):35–56.

[Nilsson, 2014] Nilsson, N. J. (2014). *Principles of artificial intelligence*. Morgan Kaufmann.

[Nutt, 2002] Nutt, R. (2002). The history of positron emission tomography. *Molecular Imaging Biology*, 4(1):11 – 26.

[O'Donoghue et al., 2011] O'Donoghue, J. A., Smith-Jones, P. M., Humm, J. L., Ruan, S., Pryma, D. A., Jungbluth, A. A., Divgi, C. R., Carrasquillo, J. A., Pandit-Taskar, N., Fong, Y., et al. (2011). 124i-hua33 antibody uptake is driven by a33 antigen concentration in tissues from colorectal cancer patients imaged by immuno-pet. *Journal of Nuclear Medicine*, 52(12):1878–1885.

[Ordonez et al., 2019] Ordonez, A. A., Carroll, L. S., Abhishek, S., Mota, F., Ruiz-Bedoya, C. A., Klunk, M. H., Singh, A. K., Freundlich, J. S., Mease, R. C., and Jain, S. K. (2019). Radiosynthesis and pet bioimaging of 76br-bedaquiline in a murine model of tuberculosis. *ACS Infectious Diseases*, 5(12):1996–2002.

[Oyama et al., 2002] Oyama, N., Akino, H., Kanamaru, H., Suzuki, Y., Muramoto, S., Yonekura, Y., Sadato, N., Yamamoto, K., and Okada, K. (2002). 11c-acetate pet imaging of prostate cancer. *Journal of Nuclear Medicine*, 43(2):181–186.

[Panin et al., 2006] Panin, V. Y., Kehren, F., Michel, C., and Casey, M. (2006). Fully 3-D PET reconstruction with system matrix derived from point source measurements. *IEEE Transactions on Medical Imaging*, 25(7):907–921.

[Parot et al., 2013] Parot, V., Herraiz, J., Dave, S., Udias, J., Moore, S., Park, M., Vaquero, J., and Lage, E. (2013). A new approach for multiplexed pet imaging. In *IEEE NSS-MIC*, volume 2013.

[Pauwels et al., 1998] Pauwels, E., Ribeiro, M., Stoot, J., McCready, V., Bourguignon, M., and Maziere, B. (1998). Fdg accumulation and tumor biology. *Nuclear medicine and biology*, 25(4):317–322.

[Pepin et al., 2004] Pepin, C. M., Bérard, P., Perrot, A.-L., Pépin, C., Houde, D., Lecomte, R., Melcher, C. L., and Dautet, H. (2004). Properties of lyso and recent lso scintillators for phoswich pet detectors. *IEEE Transactions on Nuclear Science*, 51(3):789–795.

[Pérez Liva, 2017] Pérez Liva, M. (2017). *Time domain image reconstruction methods for transmission ultrasound computed tomography*. PhD thesis, Universidad Complutense de Madrid.

[Perez-Liva et al., 2018] Perez-Liva, M., Viel, T., Yoganathan, T., Garofalakis, A., Sourdon, J., Facchin, C., Tanter, M., Provost, J., and Tavitian, B. (2018). Performance evaluation of the pet component of a hybrid pet/ct-ultrafast ultrasound imaging instrument. *Physics in Medicine & Biology*, 63(19):19NT01.

[Perez-Liva et al., 2020] Perez-Liva, M., Yoganathan, T., Herraiz, J. L., Porée, J., Tanter, M., Balvay, D., Viel, T., Garofalakis, A., Provost, J., and Tavitian, B. (2020). Ultrafast ultrasound imaging for super-resolution preclinical cardiac pet. *Molecular imaging and biology*, 22(5):1342–1352.

[Petrosyan et al., 2003] Petrosyan, A., Ovanesyan, K., Shirinyan, G., Butaeva, T., Derzyan, M., Pedrini, C., Garnier, N., Dujardin, C., and Kamenskikh, I. (2003). Luap/luyap single crystals for pet scanners: effects of composition and growth history. *Optical Materials*, 24(1-2):259–265.

[Phelps, 2002] Phelps, M. E. (2002). History of pet. In *Practical FDG Imaging: A Teaching File*, pages 1–17. Springer.

[Phelps et al., 1976] Phelps, M. E., Hoffman, E. J., Mullani, N. A., Higgins, C. S., and Ter Pogossian, M. M. (1976). Design considerations for a positron emission transaxial tomograph (pett iii). *IEEE Transactions on Nuclear Science*, (1):516–522.

[Popescu and Lewitt, 2004] Popescu, L. and Lewitt, R. (2004). Ray tracing through a grid of blobs. *IEEE Symposium Conference Record Nuclear Science 2004.*, 6(C):3983–3986.

[Pratt et al., 2020] Pratt, E. C., Isaac, E., Stater, E. P., Yang, G., Ouerfelli, O., Pillarsetty, N., and Grimm, J. (2020). Synthesis of the pet tracer 124i-trametinib for mapk/erk kinase distribution and resistance monitoring. *Journal of Nuclear Medicine*, 61(12):1845–1850.

[Pratx et al., 2008] Pratx, G., Chinn, G., Olcott, P. D., and Levin, C. S. (2008). Fast, accurate and shift-varying line projections for iterative reconstruction using the gpu. *IEEE transactions on medical imaging*, 28(3):435–445.

[Press et al., 2007] Press, W. H., William, H., Teukolsky, S. A., Saul, A., Vetterling, W. T., and Flannery, B. P. (2007). *Numerical recipes 3rd edition: The art of scientific computing*. Cambridge university press.

[Pruszyński et al., 2012] Pruszyński, M., Majkowska-Pilip, A., Loktionova, N. S., Eppard, E., and Roesch, F. (2012). Radiolabeling of dotatoc with the long-lived positron emitter 44sc. *Applied Radiation and Isotopes*, 70(6):974–979.

[Qi and Leahy, 2006] Qi, J. and Leahy, R. M. (2006). Iterative reconstruction techniques in emission computed tomography. *Physics in Medicine and Biology*, 51(15).

[Qi et al., 1998] Qi, J., Leahy, R. M., Cherry, S. R., Chatziioannou, A., and Farquhar, T. H. (1998). High-resolution 3D bayesian image reconstruction using the microPET small-animal scanner. *Physics in Medicine and Biology*, 43(4):1001–1013.

[Qian et al., 2017] Qian, H., Rui, X., and Ahn, S. (2017). Deep learning models for pet scatter estimations. In *2017 IEEE Nuclear Science Symposium and Medical Imaging Conference (NSS/MIC)*, pages 1–5. IEEE.

[Rabinovici et al., 2007] Rabinovici, G., Furst, A., O'neil, J., Racine, C., Mormino, E., Baker, S., Chetty, S., Patel, P., Pagliaro, T., Klunk, W., et al. (2007). 11c-pib pet imaging in alzheimer disease and frontotemporal lobar degeneration. *Neurology*, 68(15):1205–1212.

[Rafecas et al., 2004a] Rafecas, M., Böning, G., Pichler, B. J., Lorenz, E., Schwaiger, M., and Ziegler, S. I. (2004a). Effect of noise in the probability matrix used for statistical reconstruction of PET data. *IEEE Transactions on Nuclear Science*, 51(1 I):149–156.

[Rafecas et al., 2004b] Rafecas, M., Mosler, B., Dietz, M., Pögl, M., Stamatakis, A., McElroy, D. P., and Ziegler, S. I. (2004b). Use of a monte carlo-based probability matrix for 3-D iterative reconstruction of MADPET-II data. *IEEE Transactions on Nuclear Science*, 51(5 II):2597–2605.

[Rahmim et al., 2013] Rahmim, A., Qi, J., and Sossi, V. (2013). Resolution modeling in pet imaging: theory, practice, benefits, and pitfalls. *Medical physics*, 40(6Part1):064301.

[Ramachandran et al., 2017] Ramachandran, P., Zoph, B., and Le, Q. V. (2017). Swish: a self-gated activation function. *arXiv preprint arXiv:1710.05941*, 7:1.

[Rausch et al., 2015] Rausch, I., Cal-González, J., Dapra, D., Gallowitsch, H. J., Lind, P., Beyer, T., and Minear, G. (2015). Performance evaluation of the biograph mct flow pet/ct system according to the nema nu2-2012 standard. *EJNMMI physics*, 2(1):1–17.

[Reader et al., 2020] Reader, A. J., Corda, G., Mehranian, A., da Costa-Luis, C., Ellis, S., and Schnabel, J. A. (2020). Deep learning for pet image reconstruction. *IEEE Transactions on Radiation and Plasma Medical Sciences*, 5(1):1–25.

[Reader et al., 2003] Reader, A. J., Julyan, P. J., Williams, H., Hastings, D. L., and Zweit, J. (2003). EM Algorithm System Modeling by Image-Space Techniques for PET Reconstruction. *IEEE Transactions on Nuclear Science*, 50(5 II):1392–1397.

[Reader and Zaidi, 2007] Reader, A. J. and Zaidi, H. (2007). Advances in pet image reconstruction. *PET clinics*, 2(2):173–190.

[Reddin et al., 2018] Reddin, J. S., Scheuermann, J. S., Bharkhada, D., Smith, A. M., Casey, M. E., Conti, M., and Karp, J. S. (2018). Performance evaluation of the sipm-based siemens biograph vision pet/ct system. In *2018 IEEE Nuclear Science Symposium and Medical Imaging Conference Proceedings (NSS/MIC)*, pages 1–5. IEEE.

[Reske et al., 2006] Reske, S. N., Blumstein, N. M., Neumaier, B., Gottfried, H.-W., Finsterbusch, F., Kocot, D., Möller, P., Glatting, G., and Perner, S. (2006). Imaging prostate cancer with 11c-choline pet/ct. *Journal of Nuclear Medicine*, 47(8):1249–1254.

[Reske and Kotzerke, 2001] Reske, S. N. and Kotzerke, J. (2001). Fdg-pet for clinical use. *European journal of nuclear medicine*, 28(11):1707–1723.

[Rezaei et al., 2014] Rezaei, A., Defrise, M., and Nuyts, J. (2014). Ml-reconstruction for tof-pet with simultaneous estimation of the attenuation factors. *IEEE transactions on medical imaging*, 33(7):1563–1572.

[Roesch, 2012] Roesch, F. (2012). Scandium-44: benefits of a long-lived pet radionuclide available from the 44ti/44sc generator system. *Current radiopharmaceuticals*, 5(3):187–201.

[Roger L. Easton,] Roger L. Easton, J. *Fourier Methods in Imaging.*

[Rogers and Bielajew, 1984] Rogers, D. W. O. and Bielajew, A. F. (1984). *The use of EGS for Monte Carlo calculations in medical physics.* National Research Council Canada, Physics Division.

[Ronneberger et al., 2015] Ronneberger, O., Fischer, P., and Brox, T. (2015). U-net: Convolutional networks for biomedical image segmentation. In *International Conference on Medical image computing and computer-assisted intervention*, pages 234–241. Springer.

[Rösch and Qaim, 1993] Rösch, F. and Qaim, S. (1993). Nuclear data relevant to the production of the positron emitting technetium isotope 94mtc via the 94mo (p, n)-reaction. *Radiochimica Acta*, 62(3):115–122.

[Rosenhain et al., 2018] Rosenhain, S., Magnuska, Z. A., Yamoah, G. G., Kiessling, F., Gremse, F., et al. (2018). A preclinical micro-computed tomography database including 3d whole body organ segmentations. *Scientific data*, 5(1):1–9.

[Rossin et al., 2007] Rossin, R., Berndorff, D., Friebe, M., Dinkelborg, L. M., and Welch, M. J. (2007). Small-animal pet of tumor angiogenesis using a 76br-labeled human recombinant antibody fragment to the ed-b domain of fibronectin. *Journal of Nuclear Medicine*, 48(7):1172–1179.

[Rudd et al., 2002] Rudd, J. H., Warburton, E., Fryer, T. D., Jones, H., Clark, J., Antoun, N., Johnstrom, P., Davenport, A. P., Kirkpatrick, P. J., Arch, B. N., et al. (2002). Imaging atherosclerotic plaque inflammation with [18f]-fluorodeoxyglucose positron emission tomography. *Circulation*, 105(23):2708–2711.

[Rukiah et al., 2018] Rukiah, A., Meikle, S. R., Gillam, J. E., and Kench, P. L. (2018). An investigation of 68 ga positron range correction through de-blurring: A simulation study. In *2018 IEEE Nuclear Science Symposium and Medical Imaging Conference Proceedings (NSS/MIC)*, pages 1–2. IEEE.

[Salvat et al., 2006] Salvat, F., Fernández-Varea, J. M., and Sempau, J. (2006). Penelope-2006: A code system for monte carlo simulation of electron and photon transport. In *Workshop proceedings*, volume 4, page 7. Universitat de Barcelona.

[Salvat et al., 2008] Salvat, F., Fernández-Varea, J. M., Sempau, J., et al. (2008). Penelope-2008: A code system for monte carlo simulation of electron and photon transport. In *the Workshop Proceedings, June.*

[Sanaat and Zaidi, 2020] Sanaat, A. and Zaidi, H. (2020). Depth of interaction estimation in a preclinical pet scanner equipped with monolithic crystals coupled to sipms using a deep neural network. *Applied Sciences*, 10(14):4753.

[Santin et al., 2003] Santin, G., Strul, D., Lazaro, D., Simon, L., Krieguer, M., Martins, M. V., Breton, V., and Morel, C. (2003). Gate: A geant4-based simulation platform for pet and spect integrating movement and time management. *IEEE Transactions on nuclear science*, 50(5):1516–1521.

[Sato et al., 2019] Sato, R., Iwamoto, Y., Cho, K., Kang, D.-Y., and Chen, Y.-W. (2019). Comparison of cnn models with different plane images and their combinations for classification of alzheimer's disease using pet images. In *Innovation in Medicine and Healthcare Systems, and Multimedia*, pages 169–177. Springer.

[Schneider et al., 2009] Schneider, D. W., Heitner, T., Alicke, B., Light, D. R., McLean, K., Satozawa, N., Parry, G., Yoo, J., Lewis, J. S., and Parry, R. (2009). In vivo biodistribution, pet imaging, and tumor accumulation of 86y-and 111in-antimindin/rg-1, engineered antibody fragments in lncap tumor–bearing nude mice. *Journal of Nuclear Medicine*, 50(3):435–443.

[Schwartz et al., 2012] Schwartz, J., Humm, J. L., Divgi, C. R., Larson, S. M., and O'Donoghue, J. A. (2012). Bone marrow dosimetry using 124i-pet. *Journal of nuclear medicine*, 53(4):615–621.

[Selivanov et al., 2001] Selivanov, V., Lepage, M., and Lecomte, R. (2001). Real-time PET image reconstruction based on regularized pseudo-inverse of the system matrix. *IEEE Nuclear Science Symposium and Medical Imaging Conference*, 3:1738–1742.

[Selivanov, 2002] Selivanov, V. V. (2002). *Topics in Image Reconstruction For High Resolution Positron Emission Tomography.* PhD thesis.

[Selivanov and Lecomte, 2001] Selivanov, V. V. and Lecomte, R. (2001). Fast PET image reconstruction based on SVD decomposition of the system matrix. *IEEE Transactions on Nuclear Science*, 48(3 II):761–767.

[Selivanov et al., 2006] Selivanov, V. V., Lepage, M. D., and Lecomte, R. (2006). List-mode image reconstruction for real-time pet imaging. *Journal of Visual Communication and Image Representation*, 17(3):630–646.

[Sempau and Andreo, 2006] Sempau, J. and Andreo, P. (2006). Configuration of the electron transport algorithm of PENELOPE to simulate ion chambers. *Physics in Medicine and Biology*, 51(14):3533–3548.

[Sempau et al., 2011] Sempau, J., Badal, A., and Brualla, L. (2011). A PENELOPE-based system for the automated Monte Carlo simulation of clinacs and voxelized geometries—application to far-from-axis fields. *Medical Physics*, 38(11):5887–5895. _eprint: https://aapm.onlinelibrary.wiley.com/doi/pdf/10.1118/1.3643029.

[Sempau et al., 2003] Sempau, J., Fernández-Varea, J. M., Acosta, E., and Salvat, F. (2003). Experimental benchmarks of the Monte Carlo code PENELOPE. *Nucl. Instrum. Meth. Phys. Res. B*, 207:107 – 123.

[Sgouros et al., 2004] Sgouros, G., Kolbert, K. S., Sheikh, A., Pentlow, K. S., Mun, E. F., Barth, A., Robbins, R. J., and Larson, S. M. (2004). Patient-specific dosimetry for 131i thyroid cancer therapy using 124i pet and 3-dimensional-internal dosimetry (3d-id) software. *Journal of Nuclear Medicine*, 45(8):1366–1372.

[Sham et al., 2014] Sham, J. G., Kievit, F. M., Grierson, J. R., Chiarelli, P. A., Miyaoka, R. S., Zhang, M., Yeung, R. S., Minoshima, S., and Park, J. O. (2014). Glypican-3–targeting f (ab) 2 for 89zr pet of hepatocellular carcinoma. *Journal of Nuclear Medicine*, 55(12):2032–2037.

[Shao et al., 1997] Shao, Y., Cherry, S. R., Farahani, K., Meadors, K., Siegel, S., Silverman, R. W., and Marsden, P. K. (1997). Simultaneous pet and mr imaging. *Physics in Medicine & Biology*, 42(10):1965.

[Sharma et al., 2018] Sharma, S., Kapadia, A., Abadi, E., Fu, W., Segars, W. P., and Samei, E. (2018). A rapid gpu-based monte carlo simulation tool for individualized dose estimations in ct. In *Medical Imaging 2018: Physics of Medical Imaging*, volume 10573, page 105733V. International Society for Optics and Photonics.

[Shepp and Vardi, 1982] Shepp, L. A. and Vardi, Y. (1982). Maximum likelihood reconstruction for emission tomography. *IEEE transactions on medical imaging*, 1(2):113–122.

[Shibuya et al., 2007] Shibuya, K., Yoshida, E., Nishikido, F., Suzuki, T., Tsuda, T., Inadama, N., Yamaya, T., and Murayama, H. (2007). Limit of spatial resolution in fdg-pet due to annihilation photon non-collinearity. In *World Congress on Medical Physics and Biomedical Engineering 2006*, pages 1667–1671. Springer.

[Shimizu et al., 2014] Shimizu, K., Asakawa, T., Harada, N., Fukumoto, D., Tsukada, H., Asai, T., Yamada, S., Kan, T., and Oku, N. (2014). Use of positron emission tomography for real-time imaging of biodistribution of green tea catechin. *PLoS One*, 9(2):e85520.

[Siemens, 2019a] Siemens (2019a). Biograph scanners. `https://www.siemens-healthineers.com/en-us/molecular-imaging/petlink-documents`. Accessed: 2021-05-27.

[Siemens, 2019b] Siemens (2019b). Biograph vision pet/ct. `https://www.siemens-healthineers.com/molecular-imaging/pet-ct/biograph-vision`. Accessed: 2021-05-27.

[Sitek et al., 2011] Sitek, A., Andreyev, A., and Celler, A. (2011). Reconstruction of dual isotope pet using expectation maximization (em) algorithm. In *2011 IEEE Nuclear Science Symposium Conference Record*, pages 4323–4326. IEEE.

[Slomka et al., 2012] Slomka, P. J., Alexanderson, E., Jácome, R., Jiménez, M., Romero, E., Meave, A., Le Meunier, L., Dalhbom, M., Berman, D. S., Germano, G., et al. (2012). Comparison of clinical tools for measurements of regional stress and rest myocardial blood flow assessed with 13n-ammonia pet/ct. *Journal of Nuclear Medicine*, 53(2):171–181.

[Spinks et al., 1988] Spinks, T., Jones, T., Gilardi, M., and Heather, J. (1988). Physical performance of the latest generation of commercial positron scanner. *IEEE Transactions on Nuclear Science*, 35(1):721–725.

[Strulab et al., 2003] Strulab, D., Santin, G., Lazaro, D., Breton, V., and Morel, C. (2003). Gate (geant4 application for tomographic emission): a pet/spect general-purpose simulation platform. *Nuclear Physics B-Proceedings Supplements*, 125:75–79.

[Tamura et al., 2013] Tamura, K., Kurihara, H., Yonemori, K., Tsuda, H., Suzuki, J., Kono, Y., Honda, N., Kodaira, M., Yamamoto, H., Yunokawa, M., et al. (2013). 64cu-dota-trastuzumab pet imaging in patients with her2-positive breast cancer. *Journal of Nuclear Medicine*, 54(11):1869–1875.

[Teymurazyan et al., 2013] Teymurazyan, A., Riauka, T., Jans, H.-S., and Robinson, D. (2013). Properties of noise in positron emission tomography images reconstructed with filtered-backprojection and row-action maximum likelihood algorithm. *Journal of digital imaging*, 26(3):447–456.

[Timmers et al., 2009] Timmers, H. J., Chen, C. C., Carrasquillo, J. A., Whatley, M., Ling, A., Havekes, B., Eisenhofer, G., Martiniova, L., Adams, K. T., and Pacak, K. (2009). Comparison of 18f-fluoro-l-dopa, 18f-fluoro-deoxyglucose, and 18f-fluorodopamine pet and 123i-mibg scintigraphy in the localization of pheochromocytoma and paraganglioma. *The Journal of Clinical Endocrinology & Metabolism*, 94(12):4757–4767.

[Todorov et al., 2008] Todorov, T. I., Margrave, G. F., and Bancroft, J. C. (2008). Radon transforms via truncated singular value decomposition. *CREWES Research Report*, 20(2):1–9.

[Torigian et al., 2013] Torigian, D. A., Zaidi, H., Kwee, T. C., Saboury, B., Udupa, J. K., Cho, Z.-H., and Alavi, A. (2013). Pet/mr imaging: technical aspects and potential clinical applications. *Radiology*, 267(1):26–44.

[Tsuda et al., 2004] Tsuda, T., Murayama, H., Kitamura, K., Yamaya, T., Yoshida, E., Omura, T., Kawai, H., Inadama, N., and Orita, N. (2004). A four-layer depth of interaction detector block for small animal pet. *IEEE Transactions on Nuclear Science*, 51(5):2537–2542.

[Tsui et al., 1981] Tsui, B. M., Beck, R. N., Doi, K., and Metz, C. E. (1981). Analysis of recorded image noise in nuclear medicine. *Physics in Medicine & Biology*, 26(5):883.

[Udias et al., 2018] Udias, J., Gutierrez Fernandez, C., Herraiz, J., Perez-Benito, D., Galve, P., Lopez-Montes, A., Lopez-Longas, J., Arco, J., Desco, M., and Vaquero, J. (2018). Performance evaluation of the pet subsystem of the extended fov superargus 6r preclinical scanner. In *Proceedings of the IEEE Nuclear Science Symposium and Medical Imaging Conference, Sydney, Australia*, pages 10–11.

[Umbricht et al., 2017] Umbricht, C. A., Benešová, M., Schmid, R. M., Türler, A., Schibli, R., van der Meulen, N. P., and Müller, C. (2017). 44 sc-psma-617 for radiotheragnostics in tandem with 177 lu-psma-617—preclinical investigations in comparison with 68 ga-psma-11 and 68 ga-psma-617. *EJNMMI research*, 7(1):1–10.

[Van Sluis et al., 2019] Van Sluis, J., De Jong, J., Schaar, J., Noordzij, W., Van Snick, P., Dierckx, R., Borra, R., Willemsen, A., and Boellaard, R. (2019). Performance characteristics of the digital biograph vision pet/ct system. *Journal of Nuclear Medicine*, 60(7):1031–1036.

[van Velden et al., 2008] van Velden, F. H., Kloet, R. W., van Berckel, B. N., Wolfensberger, S. P., Lammertsma, A. A., and Boellaard, R. (2008). Comparison of 3d-op-osem and 3d-fbp reconstruction algorithms for high-resolution research tomograph studies: effects of randoms estimation methods. *Physics in Medicine & Biology*, 53(12):3217.

[Vandenberghe et al., 2016] Vandenberghe, S., Mikhaylova, E., D'Hoe, E., Mollet, P., and Karp, J. S. (2016). Recent developments in time-of-flight pet. *EJNMMI physics*, 3(1):1–30.

[Vandenberghe et al., 2006] Vandenberghe, S., Staelens, S., Byrne, C. L., Soares, E. J., Lemahieu, I., and Glick, S. J. (2006). Reconstruction of 2D PET data with Monte Carlo generated system matrix for generalized natural pixels. *Physics in Medicine and Biology*, 51(12):3105–3125.

[Vardi et al., 1985] Vardi, Y., Shepp, L., and Kaufman, L. (1985). A statistical model for positron emission tomography. *Journal of the American statistical Association*, 80(389):8–20.

[Venkatesan et al., 2011] Venkatesan, A. M., Kadoury, S., Abi-Jaoudeh, N., Levy, E. B., Maass-Moreno, R., Krücker, J., Dalal, S., Xu, S., Glossop, N., and Wood, B. J. (2011). Real-time fdg pet guidance during biopsies and radiofrequency ablation using multimodality fusion with electromagnetic navigation. *Radiology*, 260(3):848–856.

[Verel et al., 2003] Verel, I., Visser, G. W., Boellaard, R., Stigter-van Walsum, M., Snow, G. B., and Van Dongen, G. A. (2003). 89zr immuno-pet: comprehensive procedures for the production of 89zr-labeled monoclonal antibodies. *Journal of nuclear medicine*, 44(8):1271–1281.

[Vicente Torrico, 2013] Vicente Torrico, E. (2013). *Caracterización, mejora y diseño de escáneres PET preclínicos.* PhD thesis, Universidad Complutense de Madrid.

[Voss et al., 2007] Voss, S. D., Smith, S. V., DiBartolo, N., McIntosh, L. J., Cyr, E. M., Bonab, A. A., Dearling, J. L., Carter, E. A., Fischman, A. J., Treves, S. T., et al. (2007). Positron emission tomography (pet) imaging of neuroblastoma and melanoma with 64cu-sarar immunoconjugates. *Proceedings of the National Academy of Sciences*, 104(44):17489–17493.

[Vugts et al., 2013] Vugts, D. J., Visser, G. W., and van Dongen, G. A. (2013). 89zr-pet radiochemistry in the development and application of therapeutic monoclonal antibodies and other biologicals. *Current topics in medicinal chemistry*, 13(4):446–457.

[Wagenknecht et al., 2013] Wagenknecht, G., Kaiser, H.-J., Mottaghy, F. M., and Herzog, H. (2013). Mri for attenuation correction in pet: methods and challenges. *Magnetic resonance materials in physics, biology and medicine*, 26(1):99–113.

[Wang et al., 2006] Wang, F. Y., Chi, C. Y., Chan, T. H., and Wang, Y. (2006). Blind separation of positive dependent sources by non-negative least-correlated component analysis. *Proceedings of the 2006 16th IEEE Signal Processing Society Workshop on Machine Learning for Signal Processing, MLSP 2006*, (November 2017):73–78.

[Watanabe et al., 2010] Watanabe, S., Hanaoka, H., Liang, J. X., Iida, Y., Endo, K., and Ishioka, N. S. (2010). Pet imaging of norepinephrine transporter–expressing tumors using 76br-meta-bromobenzylguanidine. *Journal of Nuclear Medicine*, 51(9):1472–1479.

[Watson et al., 2008] Watson, C., Hayden, C., Casey, M., Hamill, J., and Bendriem, B. (2008). Prompt gamma correction for improved quantification in 82rb pet. *Journal of Nuclear Medicine*, 49(supplement 1):64P–64P.

[Watson et al., 1996] Watson, C. C., Newport, D., and Casey, M. E. (1996). A single scatter simulation technique for scatter correction in 3d pet. In *Three-dimensional image reconstruction in radiology and nuclear medicine*, pages 255–268. Springer.

[Weber et al., 2003] Weber, S., Christ, D., Kurzeja, M., Engels, R., Kemmerling, G., and Halling, H. (2003). Comparison of luyap, lso, and bgo as scintillators for high resolution pet detectors. *IEEE transactions on nuclear science*, 50(5):1370–1372.

[Wei, 2015] Wei, Q. (2015). Intrinsic radiation in lutetium based pet detector: Advantages and disadvantages. *arXiv preprint arXiv:1501.05372.*

[Wellman et al., 2010] Wellman, T. J., Winkler, T., Costa, E. L., Musch, G., Harris, R. S., Venegas, J. G., and Melo, M. F. V. (2010). Measurement of regional specific lung volume change using respiratory-gated pet of inhaled 13n-nitrogen. *Journal of Nuclear Medicine*, 51(4):646–653.

[Woodcock et al., 1965] Woodcock, E., Murphy, T., Hemmings, P., and Longworth, S. (1965). Techniques used in the gem code for monte carlo neutronics calculations in reactors and other systems of complex geometry. In *Proc. Conf. Applications of Computing Methods to Reactor Problems*, volume 557.

[Wooten et al., 2017] Wooten, A. L., Aweda, T. A., Lewis, B. C., Gross, R. B., and Lapi, S. E. (2017). Biodistribution and pet imaging of pharmacokinetics of manganese in mice using manganese-52. *PLoS One*, 12(3):e0174351.

[Xie et al., 2020] Xie, K., Chen, Y., Wang, X., Xie, G., Cao, J., and Wen, J. (2020). Accurate and fast recovery of network monitoring data: A gpu accelerated matrix completion. *IEEE/ACM Transactions on Networking*, 28(3):958–971.

[Yamagishi et al., 2003] Yamagishi, H., Shirai, N., Takagi, M., Yoshiyama, M., Akioka, K., Takeuchi, K., and Yoshikawa, J. (2003). Identification of cardiac sarcoidosis with 13n-nh3/18f-fdg pet. *Journal of nuclear medicine*, 44(7):1030–1036.

[Yamamoto et al., 2008] Yamamoto, Y., Nishiyama, Y., Kameyama, R., Okano, K., Kashiwagi, H., Deguchi, A., Kaji, M., and Ohkawa, M. (2008). Detection of hepatocellular carcinoma using 11c-choline pet: comparison with 18f-fdg pet. *Journal of Nuclear Medicine*, 49(8):1245–1248.

[Yan, 2010] Yan, M. (2010). Convergence Analysis of SART by Bregman Iteration and Dual Gradient Descent. *UCLA CAM report*, pages 10–27.

[Yuan et al., 2006] Yuan, H., Schroeder, T., Bowsher, J. E., Hedlund, L. W., Wong, T., and Dewhirst, M. W. (2006). Intertumoral differences in hypoxia selectivity of the pet imaging agent 64cu (ii)-diacetyl-bis (n4-methylthiosemicarbazone). *Journal of Nuclear Medicine*, 47(6):989–998.

[Zaidi, 1999] Zaidi, H. (1999). Relevance of accurate monte carlo modeling in nuclear medical imaging. *Medical physics*, 26(4):574–608.

[Zaidi and Montandon, 2007] Zaidi, H. and Montandon, M.-L. (2007). Scatter compensation techniques in pet. *PET clinics*, 2(2):219–234.

[Zeng, 2015] Zeng, G. L. (2015). Revisit of the Ramp Filter. *IEEE Transactions on Nuclear Science*, 62(Ramp Filter).

[Zhang et al., 2019] Zhang, M. R., Lucas, J., Hinton, G., and Ba, J. (2019). Lookahead optimizer: k steps forward, 1 step back. *arXiv preprint arXiv:1907.08610*.

[Zhou and Qi, 2011] Zhou, J. and Qi, J. (2011). Fast and efficient fully 3d pet image reconstruction using sparse system matrix factorization with gpu acceleration. *Physics in Medicine & Biology*, 56(20):6739.

[Zhou et al., 2018] Zhou, Z., Siddiquee, M. M. R., Tajbakhsh, N., and Liang, J. (2018). Unet++: A nested u-net architecture for medical image segmentation. In *Deep learning in medical image analysis and multimodal learning for clinical decision support*, pages 3–11. Springer.

10 List of publication and conference contributions related to this thesis

10.1 Publications:

Galve, P., Udias, J. M., Lopez-Montes, A., Arias-Valcayo, F., Vaquero, J. J., Desco, M., Herraiz, J. L. (2021). Super-iterative image reconstruction in PET. IEEE Transactions on Computational Imaging, 7, 248-257.

Herraiz, J. L., Bembibre, A., López-Montes, A. (2021). Deep-Learning Based Positron Range Correction of PET Images. Applied Sciences, 11(1), 266.

Benito, J., Fraile, L. M., Korgul, A., Piersa, M., Adamska, E., Andreyev, A. N., ... Borge, M. J. G. (2020). Detailed spectroscopy of doubly magic Sn 132. Physical Review C, 102(1), 014328.

López-Montes, A., Galve, P., Udias, J. M., Cal-González, J., Vaquero, J. J., Desco, M., Herraiz, J. L. (2020). Real-Time 3D PET Image with Pseudoinverse Reconstruction. Applied Sciences, 10(8), 2829.

Sánchez-Jiménez, J., López-Montes, A., Núñez-Martínez, L., Villa-Abaunza, A., Fraile, L. M., Sánchez-Tembleque, V., Udías, J. M. (2017). 223Ra-dichloride spectrometric characterization: Searching for the presence of long-lived isotopes with radiological protection implications. Physica Medica, 35, 97-101.

10.2 Conference contributions and proceedings:

Conference: III Jornadas de Física Médica. RSEF/IFIMED. 14-15 December 2020. Madrid. Spain. Talk: "Positron Range Correction based on Deep-Learning". Authors: Alejandro López-Montes, Adrián Bembibre and Joaquín L. Herraiz.

Conference: 2020 IEEE Nuclear Science Symposium and Medical Imaging Conference (NSS/MIC). Authors: Alejandro Lopez-Montes, Kai Giesen, Lutz Tellmann, Stefan Spellerberg, Ingo Spahn, Jose M. Udias, Christoph Lerche, Joaquin L. Herraiz. Talk: Multiplexed PET using 52Mn.

Conference: 2019 IEEE Nuclear Science Symposium and Medical Imaging Conference (NSS/MIC). Authors: Lopez-Montes, A., Herraiz, J. L., Galve, P., España, S., Vicente, E., Cal-Gonzalez, J., Udias, J. M. Poster: PeneloPET v3. 0, an improved multiplatform PET Simulator.

Conference: The 15th International Meeting on Fully Three-Dimensional Image Reconstruction in Radiology and Nuclear Medicine. 2-6 June 2019. University of Pennsylvania.

Philadelphia. PA. United States of America. Talk: “Application of the pseudoinverse for real-time 3D PET image reconstruction”. Authors: Alejandro López Montes, Pablo Galve Lahoz, José Manuel Udías, Joaquín López Herraiz.

Conference: The 15th International Meeting on Fully Three-Dimensional Image Reconstruction in Radiology and Nuclear Medicine. 2-6 June 2019. University of Pennsylvania. Philadelphia. PA. United States of America. Poster: “Super-iterative image reconstruction in PET”. Authors: Pablo Galve Lahoz, José Manuel Udías, Alejandro López Montes, Joaquín López Herraiz.

Conference: International Scientific Meeting on Nuclear. La Rábida 2018. Basic concept son nuclear physics: theory, experiments and applications. 18-22 June 2018. Universidad Internacional de Andalucía. La Rábida. Huelva. Spain. Talk: “Iterative algorithm for optimal super resolution sampling”. Authors: Pablo Galve Lahoz, Alejandro López Montes, José Manuel Udías, Joaquín López Herraiz.

Conference: International Scientific Meeting on Nuclear. La Rábida 2018. Basic concept son nuclear physics: theory, experiments and applications. 18-22 June 2018. Universidad Internacional de Andalucía. La Rábida. Huelva. Spain. Poster: “Real Time Tomographic Image Reconstruction in PET Using the Pseudoinverse of the System Response Matrix”. Authors: Alejandro López Montes, Pablo Galve Lahoz, José Manuel Udías, Joaquín López Herraiz.

Conference: 2018 EEE Nuclear Science Symposium and Medical Imaging Conference (NSS/MIC). 10-17 November 2018, Sydney, Australia. Poster: “Effect of incomplete acquisitions on the image of high resolution preclinical scanners”. Authors: Pablo Galve Lahoz, Alejandro López Montes, Joaquín López Herraiz, José Manuel Udías.

Conference: II Jornadas de Física Médica. SEFM. 14-15 June 2018. Madrid. Spain. Poster: “Detectability Limit of Ultra Low Activity Acquisitions in LYSO/LSO versus LYSO/GSO Preclinical PET Scanners”. Authors: Alejandro López Montes, Pablo Galve Lahoz, Joaquín López Herraiz, José Manuel Udías.

Conference: II Jornadas de Física Médica. SEFM. 14-15 June 2018. Madrid. Spain. Talk: “Effect of incomplete acquisitions on the image of high resolution preclinical scanners”. Authors: Pablo Galve Lahoz, Alejandro López Montes, Joaquín López Herraiz, José Manuel Udías.

Conference: European Molecular Imaging Meeting. 20-23 Mach 2018. San Sebastián, Spain. Poster: “An Iterative Algorithm for Sampling Recovery in PET”, Authors: Pablo Galve Lahoz, Alejandro López Montes, Joaquín López Herraiz, José Manuel Udías.

Conference: Second ySMIN Meeting. 26 February 2018. Madrid, Spain. Talk: “An Iterative Algorithm for Sampling Recovery in PET”, Authors: Pablo Galve Lahoz, Alejandro López Montes, Joaquín López Herraiz, José Manuel Udías.

Conference: IX CPAN Days. Meeting on Nuclear Physics. 23-25 October 2017. Santander, Spain. Talk: "PET Sinogram Restoration for Uniform Spatial Resolution with FBP". Authors: Alejandro López Montes, José Manuel Udías, Joaquín López Herraiz.

Conference: 2017 IEEE Nuclear Science Symposium and Medical Imaging Conference (NSS/MIC). 21-28 October 2017, Hyatt Regency, Atlanta, Georgia, USA. Poster: "Data-driven Improved Sampling in PET". Authors: Pablo Galve Lahoz, Alejandro López Montes, Joaquín López Herraiz, José Manuel Udías.

Conference: 2017 IEEE Nuclear Science Symposium and Medical Imaging Conference (NSS/MIC). 21-28 October 2017, Hyatt Regency, Atlanta, Georgia, USA. Poster: "Real-Time Accurate Rebinning of PET Data Based on the Pseudo-Inverse of the Axial System Matrix". Authors: Alejandro López Montes, Pablo Galve Lahoz, Joaquín López Herraiz, José Manuel Udías.

Conference: XXXVI Biennial Meeting of the Royal Society of Physics of Spain (RSEF). 17-21 July 2017. Santiago de Compostela, Spain. Poster: "Resolution Recovery in PET using Maximum Likelihood-based Sub-Crystals". Authors: Pablo Galve Lahoz, Alejandro López Montes, Joaquín López Herraiz, José Manuel Udías.

Conference: XXXVI Biennial Meeting of the Royal Society of Physics of Spain (RSEF). 17-21 July 2017. Santiago de Compostela, Spain. Poster: "Real-Time PET Data Rebinning Based on the Pseudoinversion of the Axial Part of the System Response Matrix". Authors: Alejandro López Montes, Pablo Galve Lahoz, Joaquín López Herraiz, José Manuel Udías.

Conference: First ySMIN Meeting (ESMI). 30 January 2017. Madrid, Spain. Talk: "Ultra Fast PET Image Reconstruction with the Pseudoinverse". Authors: Alejandro López Montes, Joaquín López Herraiz, José Manuel Udías.

Conference: VIII CPAN Days. Meeting on Nuclear Physics. 28-30 November 2016. Zaragoza, Spain. Talk: "Ultra Fast PET Rebining Data and Image Reconstruction Based on Pseudoinversion". Authors: Alejandro López Montes, Joaquín López Herraiz, José Manuel Udías.